Predictive modelling of the form and development of bone fracture healing

Damien Comiskey, B.Eng.

2009

Predictive modelling of the form and development of bone fracture healing

By

Damien Peter Comiskey, B.Eng.

This thesis is submitted to Dublin City University as the partial fulfilment of the requirement for the award of the degree of

Doctor of Philosophy

Supervisor: Dr. Bryan Mac Donald, B.Eng., M.Sc., Ph.D.
External supervisor: Dr. Billy McCartney, MVB, Ph.D.
Head of School: Professor M.S.J. Hashmi, Ph.D., D.Sc.

School of Mechanical and Manufacturing Engineering
Dublin City University

August 2009

To my parents

Declaration

I hereby certify that this material, which I now submit for assessment on the programme of study leading to the award of Ph.D. is entirely my own work and has not been taken from the work of others save and to the extent that such work has been cited and acknowledged within the text of my work.

Signed:____________________________ ID No.: 51743422

Damien Comiskey

Date: _______________________

Acknowledgements

I would like to thank Dr. Bryan Mac Donald for seeing potential in my abilities to undertake a Ph.D. and for recommending me for a scholarship. He gave me the latitude to explore my own ideas and to develop autonomously, yet he was always at my beck and call to provide guidance and encouragement.

I also wish to thank Dr. Billy McCartney, orthopaedic surgeon at the Marie Louise Veterinary Hospital, for taking many hours out of his busy schedule to discuss ideas and provide a much-needed source of background knowledge of medical science. He always dutifully responded to my many annoying text message questions about bone healing and plate fixation. Many thanks to Mr Keith Synnott, orthopaedic surgeon at the Mater Hospital, for constantly raising the bar and for pushing me to make this project as applicable and practical as possible for orthopaedic surgery. This was a man who had no interest in stress contours or as he called them, “pretty colours”. Thanks to Flavia Lyons at Smith & Nephew for kindly donating implants to aid this study. I would also like to thank Professor John O’Byrne, consultant orthopaedic surgeon at Cappagh Hospital, for his kind words, enthusiasm and involvement with this study. Thanks to Professor Patrick Prendergast and Dr. Damien Byrne for allowing me to use their bone models. A special thanks to Cathal Magner for taking the time to proof read this thesis.

I am also grateful for the technical support from Michael May, Keith Hickey, Frank Byrne, Liam Domican, Cian Merne, Chris Crouch, Martin Johnson and Jim Barry. Thanks to all my family and friends who have supported me throughout my studies, for their advice, and for listening to all my woes. I would also like to convey my sincere thanks to my parents for their unending patience, support and encouragement.

This study was kindly funded by the Irish Research Council for Science Engineering and Technology (IRCSET) under the postgraduate research awards scheme, funded by the Irish Government’s National Development Plan. Scholarship Reference Number: RS/2005/25

Publications resulting from this study

Peer Reviewed Publications

McCartney, W.T., Comiskey, D., Mac Donald, B.J., 2007. Use of transilial pinning for the treatment of sacroiliac separation in 25 dogs and finite element analysis of repair methods. Veterinary and comparative orthopaedics and traumatology 20, 38-42.

McCartney, W.T., Comiskey, D., Mac Donald, B.J., 2007. Fixation of humoral intercondylar fractures using a lateral plate in fourteen dogs supported by finite element analysis of repair. Veterinary and comparative orthopaedics and traumatology 20, 285-90.

Conference Presentations/Publications

Comiskey, D., McCartney, W.T., Mac Donald, B.J., Finite element modelling of in-service behaviour of orthopaedic fracture fixation devices, in Proc. IMC'22, 2005, Dublin, Ireland.

Comiskey, D., McCartney, W.T., Mac Donald, B.J., Experimental and finite element analysis of the mechanical behaviour of orthopaedic fracture fixation devices, in Proc. AMPT'06, 2006, Las Vegas, USA.

Comiskey, D., Mac Donald, B.J., Finite Element and parametric analysis of orthopaedic fracture fixation stiffness, in Proc. Bioengineering in Ireland Conference, January 26-27th, 2007, Fermanagh, Ireland.

Comiskey, D.P., McCartney, W.T., Mac Donald, B.J., Numerical modelling and analysis of orthopeadic screw pull-out, in Proc. European Society of Biomechanics, 26-28th August, 2007, University of Dublin, Ireland.

McCartney, W.T., Comiskey, D.P., Mac Donald, B.J., Fracture fixation choice for distal humerus and sacroiliac separation: a clinical and retrospective finite element study, in Proc. European Society of Biomechanics, 26-28th August, 2007, University of Dublin, Ireland.

Comiskey, D.P., McCartney, W.T., Mac Donald, B.J., Prediction of interfragmentary strain in long-bone plate fixated fractures, in Proc. European Society of Biomechanics, 26-28th August, 2007, University of Dublin, Ireland.

Campbell, R., Comiskey, D.P., Mac Donald, B.J., McCartney, W.T., Finite element simulation of bone fracture callus development during flexible fracture fixation, in Proc. European Society of Biomechanics, 26-28th August, 2007, University of Dublin, Ireland.

Comiskey, D., Mac Donald, B.J., McCartney, W.T., Synnott, K., Finite element modelling of the load sharing mechanics of a healing bone fracture callus and the supporting implant: A pre-operative planning tool, in Proc. NIBES, 2nd April, 2008, University of Ulster, Ireland.

List of figures

List of tables

Nomenclature

Symbol	Definition	Dimension
a	Coefficient	
d	Width	m
D	Hydrostatic stress	
e	Elimination Coefficient	
E	Young's modulus	MPa
f	Force	N
F	Concentrated force	N
h	Thickness	m
i	Iteration	
J	Energy	Nm
k	Stiffness	N/m
K	Concentration factor	
l	Length	m
m	Exponent	
n	Number of samples	
r	Radius of a circle	m
R^2	Correlation coefficient	
s	Sample standard deviation	
S	Deviatoric stress	
u	Strain energy density	J
U	Displacement	m
V	Volume	m^3
$\bar{x}$, $\bar{y}$	Mean/average	
Greek		
σ	Stress	Pa
$\sigma_1, \sigma_2, \sigma_3$	Principal stresses	Pa
ε	Strain	
$\varepsilon_1, \varepsilon_2, \varepsilon_3$	Principal strains	
Subscripts		
e	Equivalent	
E	Element	
i	Iteration	
IF	Interfragmentary	
max	Maximum	

t	Time
y	Yield

Abbreviations

AO/ASIF	Association for the Study of Internal Fixation
AvRE	Average relative error
CS	Critical Strain
CAD	Computer-aided Design
DoF	Degrees of Freedom
ESO	Evolutionary Structural Optimization
FE	Finite Element
IF	Interfragmentary
IFM	Interfragmentary motion
IFS	Interfragmentary strain
LCP	Locking Compression Plate
LISS	Less Invasive Skeletal Stabilization
LVDT	Linear Variable Displacement Transducer
MIPO	Minimally Invasive Plate Osteosynthesis
RE	Relative Error
SD	Standard Deviation
SED	Strain Energy Density

Abstract

It is the contention of this study that the rate and formation of bone healing can be modelled mathematically and computationally, respectively, based on mechanical stimuli induced by the relative motion between bone fragments. To argue this case, the following hypotheses are tested; 1) the relationship between temporal rate of bone healing, measured in terms of callus stiffening per week, and the percentage of interfragmentary strain, can be described mathematically, and 2) the spatial distribution of callus tissue around a fracture can be modelled computationally based on compressive principal strains experienced by the immature healing tissues caused by interfragmentary motions.

To test the first hypothesis, a comparative analysis of empirical relationships between rate of healing and level of mechanical stimulus found in the literature was conducted. Based on this, a mathematical phenomenological model was derived. To test the second hypothesis, the finite element method was employed to determine how bone-fixator position, fracture geometry, loading and the consequent strains experienced by the healing tissues, influence callus formation. An algorithm was proposed which iteratively removed lowly strained soft tissue from a large domain at the fracture site, thus producing a more efficient callus formation. The premise of this algorithm was based on the adage that 'form follows function', and a callus will inevitably strive to remodel itself to the point where greatest mechanical efficiency is achieved.

The results of the comparative literature review and the proposed mathematical model revealed a positive correlation between the rate of callus stiffening and the initially applied interfragmentary strain. The results of computational models showed direct agreement with experimental findings and clinical observations which reinforces the hypothesis that compressive principal strains are the dominant driving force behind callus formation. Furthermore, it was shown that the proximity of a unilateral fixator to the fractured bone has a greater influence over asymmetric callus formation than the physical presence of the fixator itself. Finally, the implications of the proposed strategies show potential in pre-clinical testing of fixation devices and configurations, which was demonstrated using simulated comparisons with clinical case studies of healing bones under unilateral fixation.

Contents

Chapter 1 - Introduction 1

The issue of bone healing and the influence of mechanical stimulus are introduced. Commentary on the current knowledge and knowledge gaps are discussed. It was hypothesized that the compressive principal strains are responsible for the efficient formation of bone callus. Furthermore, it was hypothesised that there is a positive correlation between the rate of bone healing and the initially applied mechanical stimulus. The goals of this study are also discussed here.

Chapter 2 - Literature Review 8

It is argued that the formation of healing bone tissues follow a structurally efficient formation, which is mediated by mechanical strains. To support this argument, clinical cases, experimental findings and computational results are discussed. Based on the review of the literature and contemporary computational methodologies, it was proposed that the efficient formation of callus tissues could be modelled using a specially designed algorithm that captures the formation of tissues based on calculated strain fields. Also, the hypothesis of a causal relationship between the rate of bone healing and mechanical stimulus was strengthened based on experimental observations. From this, it was proposed that a non-linear mathematical model could be derived.

Chapter 3 - Methods 34

The proposed computational and mathematical modelling methods are described here. Firstly, the derivation of a mathematical model of the rate of bone healing is described based on the experimental findings compiled from the literature. Next, the algorithm used to predict the formation of healing tissues is presented, as well as the modelling methods and assumptions. The algorithm was tested under idealised loading conditions, fracture geometries and under unilateral fixation. Finally, the algorithm was further tested against clinical case-specific fractures of the tibia and femur stabilised with internal locking plate fixation.

Chapter 4 - Results **73**

The mathematical and computational findings are presented and analysed. The results of the proposed mathematical model were quantitatively compared with experimental findings, while the outcome of the mechano-regulated algorithm is discussed for the various fractures and loading scenarios.

Chapter 5 - Discussion **102**

The computationally predicted callus formations and mathematically predicted rates of healing are compared with *in vivo* findings and their level of congruency is discussed. Inferences are made with regards to the influence of mechanical stimulus on the formation and rate of bone healing and how these relate to the biology of the healing callus.

Chapter 6 - Conclusions **131**

The conclusions and future work is discussed here.

Chapter 1 - Introduction

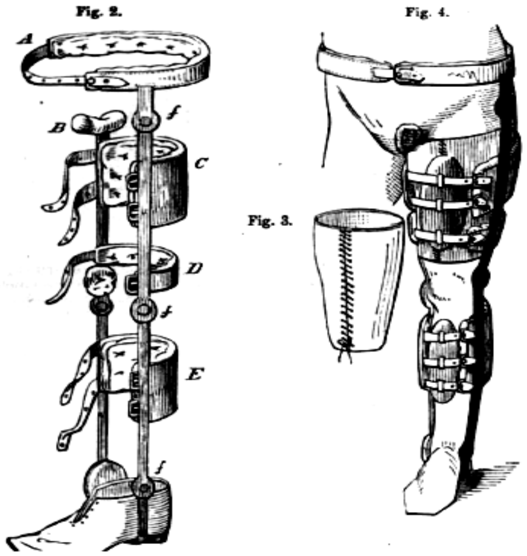

State-of-the-Art:
Treatment of non-union in the 19th century
(from the American journal of Medical
Science, 1885).

Contents

1.1 Mechanical stimulus and bone healing

When a bone breaks, the scar tissues that develop soon after, have merely days or weeks to arrange themselves into a mechanically efficient structure, to stabilise the bone fragments and repair the breakage. Thompson (1942) proposed that the body will naturally attempt to maximise mechanical efficiency by forming tissue in areas where forces are greatest. It is a *communis opinio* that biological tissues, especially bone, have the capacity to respond to mechanical stimulus by forming and resorbing tissues where appropriate (Wolff, 1892). Understanding the means through which stimulus affects tissue differentiation and formation has led to the relatively new field of study known as 'Mechanobiology' (van der Meulen and Huiskes, 2002). It is known that the healing bone tissues, broadly referred to as 'callus tissue', are sensitive to mechanical stimulus (Klein *et al.*, 2003; Schenk, 1986) created by the motion between bone fragments. These relative motions, otherwise known as interfragmentary motions, induce a local mechanical stimulus within the early callus tissue which can influence tissue differentiation and thus influence the rate of healing (Goodship and Kenwright, 1985).

Allowing relative stability at the fracture site, which results in indirect healing by callus formation, is known as 'biological healing' and has become increasingly popular in orthopaedic fracture fixation. This has led to the concept of 'flexible fixation' where bone fragments are surgically fixated with a locking implant that acts as an 'elastic splint' which allows interfragmentary motion to mechanically stimulate the immature callus tissues (Perren, 1999) (see Appendix A). There is a caveat relating to relative stability; too little or too much stimulus can have negative effects. According to Goodship and Cunningham (2001), an overly rigid fixated bone will result in atrophic non-union, while a non-rigidly fixated bone results in hypertrophic non-union. Both of these are failures of the bone to unite; the former through a lack of callus formation which has been suppressed by over-rigid fixation, the latter by an over-proliferation of callus which has failed to unite due to excessive interfragmentary movement. Between these two extremes, it is thought that a mechanical environment will exist at which fracture healing will proceed at an optimal rate (Goodship and Cunningham, 2001).

1.2 Predicting the future of bone healing

Approximately 5-10% of the 5.6 million fractures occurring annually in the United States develop into delayed unions or non-unions (Praemer *et al.*, 1992). Thus, predicting the success of healing by callus formation remains a difficult task for an orthopaedic surgeon due to the influence of biological factors (age, sex, vasculature) and the mechanical environment. Recently, there has been greater focus on computational or *in silico*[1] modelling as a means of simulating or predicting the rate and form of bone healing, thanks to increases in computer power. These methodologies utilise the finite element (FE) method to calculate mechanical stimuli in the early callus tissue to simulate tissue differentiation, which is controlled or modulated using mecho-regulated algorithms (Ament and Hofer, 2000; Lacroix and Prendergast, 2002a; García-Aznar *et al*., 2007). These current simulatory state-of-the-art methodologies have been successfully implemented in idealised fractures and under idealised loading, as a means to better understand the role of mechanical stimuli on bone healing (van der Muelen and Huiskes, 2002). Although impressive in their complexity, to integrate the current technology in a finite element model that represents a specific bone fracture of a specific patient would undoubtedly be a difficult task, and, in the author's opinion, is at present unfeasible. Moreover, the causal relationship between mechanical stimulus and bone healing is still not fully understood, and is therefore difficult to determine the accuracy or predictive power of a computational simulation where no benchmark relationship exists.

Predictive pre-clinical tools which utilise the finite element method have been proposed in other areas such as modelling aseptic loosening of a total hip replacement. On the other hand, no effort has been made in the way of patient specific modelling of bone fractures and healing, despite the prevalence of non-union. This may be ascribed to the complexity of modelling fracture geometries and the formation of callus tissue. Lacroix (2000) suggested that to move forward in FE modelling of bone fracture healing, it is necessary to automate the process of modelling the formation of a fracture callus. According to Lacroix, this will enable the study of patient specific fractures and to compare the effect of one fixator device with another. In the present study, a less complex and more intuitive approach of modelling callus tissue is proposed to facilitate integration with patient specific fractures so that steps towards pre-clinical modelling can be achieved.

1.3 Computational modelling of the form of bone healing

It is evident from clinical observations discussed further in the next chapter that callus tissues form in the most mechanically efficient way and will form differently depending on

---

[1] *In silico* is a relatively new term used to describe experimentation that is conducted on a computer.

the geometry of the fracture and the strain gradient within the interfragmentary space. Under loading, the immature callus tissue will inevitably deform, and it is proposed that these deformations are sensed by the pluripotential cells which react by differentiating. If we consider the adage, ‘form follows function’ then it is logical that the spatial distribution of callus tissue provides mechanical stability where it is most needed. Following this line of thinking, the author hypothesizes that the spatial formation of a healing bone is driven by compressive principal strains in the immature callus tissue which can be calculated using the finite element method. To this end, an algorithm is proposed to control this process by iteratively removing material in areas of a discrete structure that experiences low strains as calculated by finite element analyses.

The motivation for the development of an algorithm is three-fold; 1) to explain why callus tissue forms in a structurally efficient manner, 2) to determine the mechanical stimulus that drives this efficient formation and 3) to automatically produce *in silico* callus formation in patient or case specific models.

Until the present study, the immature callus tissues that form immediately post fracture have been modelled as a ready-made structure which was assumed to form automatically after inflammation (Andreykiv *et al.*, 2007; Byrne, 2008; Carter et al., 1988; Claes and Heigele, 1999; Gardner and colleagues, 2000, 2003, 2004; Isaksson *et al.*, 2006; Lacroix and Prendergast, 2002a-b). It was thought that the influence of mechanical factors occurs later in the healing process and mechanical stimulus has no effect on the formation of immature tissues. Thus, the callus has not yet been considered or modelled as a mechanically efficient structure. In fact, to the author’s knowledge, the question of how the callus initially forms has not been studied, nor has it been modelled using the proposed mechanical stimulus and simulatory methods.

Furthermore, it is postulated in the present study, that a unilateral fixator (an implant fixed on one side of the bone) will affect the relative motion between the bone fragments and thus the distribution of callus tissue. Consequently, if there are greater relative motions at a certain area of the same fracture line, then the callus must rearrange itself to minimise these motions to restore stability. It is argued, therefore, in the present thesis, that the tissues will become biased towards areas where relative motion persists and neglect the areas where there is little motion. Moreover, in the present study, special attention is given to locking plate fixation and how callus forms in the presence of the implant. It is further hypothesized that the proximity of the implant will influence the spatial distribution of callus tissue, where an implant located closer to the bone will result in more severe strain gradient and thus a more asymmetric callus and *vice versa* (Fig. 1.1).

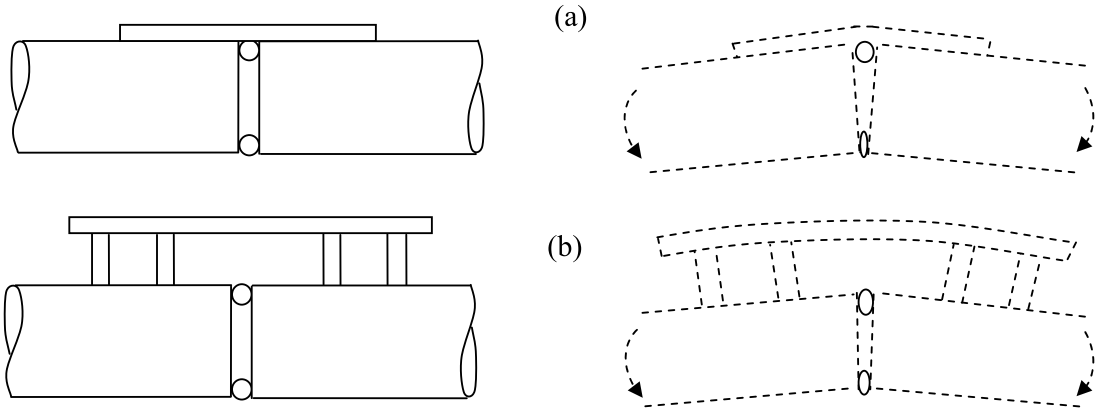

Figure 1.1. Effect of unilateral fixators and their proximity to the bone on inter-cortical strain gradient. (a) Illustration of inter-cortical strain under compression plating (adapted from Perren, 1979), and (b) under external fixation.

1.4 Mathematical modelling of the rate of bone healing

Patterns exist in biology which can in fact be modelled mathematically, such as the geometric pattern of shells or the growth rate of frogs subjected to different temperatures (Thompson, 1942). If in fact, mechanical stimulus does influence the rate of healing, as is widely believed in the scientific community, this would suggest that there is a distinct cause-and-effect relationship. Despite the great effort made in the literature, no such phenomenological relationship exists. What the literature has shown, however, are significant differences in rate of healing for a non-rigidly fixated bone in comparison to a rigidly fixated bone. If the interfragmentary motion or strain does indeed stimulate healing, then one might hope to see a repeatable pattern where intermediate rates of healing can be accounted for.

There is much conflict between experimental studies regarding the significance of mechanical stimulus on the rate of bone healing. Some studies have shown that the stiffness of the callus is not significantly affected by interfragmentary strain whereas other studies have found the opposite. The conflict or ambiguity is most likely due to the lack of consistency between experimental methods. In many cases, completely different fixators were used in different studies, also the level of initial interfragmentary strain was not always known, hence its influence could not be adequately judged. These experimental studies, however, have shown that there is a very noticeable pattern during healing. It may be possible, therefore, to compare and contrast these studies to determine a correlation between mechanical stimulus and the rate of bone healing based on these experiments. Fundamentally speaking, as the callus heals or develops, it increases in structural stiffness. If mechanical stimulus influences bone healing, then one should expect to observe a correlation between stimulus and stiffness. In the present study, it is hypothesized that there is a positive correlation between the initially applied interfragmentary motion or strain and the rate of healing. In fact, it is proposed that this causal relationship can be described mathematically.

1.5 Objectives of this study

In the present study, the author will demonstrate that callus formation is driven by mechanical stimulus, and more specifically, compressive principal strains. This argument is based on finite element simulations using a mechano-regulated algorithm which is controlled by strains in the immature callus tissues. To have results of a numerical simulation that can be relied upon, it will be necessary to qualitatively compare the simulated callus formation with that found in the literature of idealised animal experiments. Furthermore, the robustness of the proposed computational methods are put to a more severe test by comparison with non-idealised clinical case studies of human bone fracture calluses to determine the efficacy of the algorithm in a patient specific scenario.

As of yet, no phenomenological model exists to determine how mechanical stimulus relates to the rate of bone healing. Consequently, to find an empirical correlation, it will be necessary to conduct a comparative analysis of the literature and to re-process the experimental findings so that a correlation can be extracted. This will require novel methods of interpretation and presentation of existing experimental results to determine a mathematical model. Following from this, it will be necessary to rigorously compare this mathematical model with as many studies as possible to determine its accuracy and the strength of the hypothesis that there is a causal relationship between interfragmentary motion/strain and the rate of callus stiffening.

Finally, if the proposed methods predict patterns as are evident in nature, then it will be important to determine the predictive power of the said algorithm and mathematical models. At present, simulations can only be used to describe biological realities by comparison with past experimental analyses, but to predict the outcome is still a future goal (van der Meulen and Huiskes, 2002). However, if correspondence with retrospective callus formations and healing patterns can be achieved, then it is more likely that the future of bone healing can be simulated, and more importantly; have results that can be trusted. Thus, every attempt will be made to quantify the percentage accuracy of the simulated healing throughout this study to determine the robustness of the methodologies.

1.6 Summary

The present study attempts to contribute towards modelling of bone healing in two aspects: 1) by developing a robust yet efficient method of predicting callus formation in patient specific fractures using computational mechano-regulated techniques and 2) by determining a mathematical cause-and-effect relationship between the rate of healing and mechanical stimulus at the fracture site.

It is intended that the proposed computational modelling strategies could be used to predict the structural formation of callus tissue based on the interfragmentary motions. If good accuracy can be achieved then it may be feasible to integrate the methodologies in pre-clinical applications. This would constitute a major leap forward in pre-clinical modelling.

Chapter 2 - Literature Review

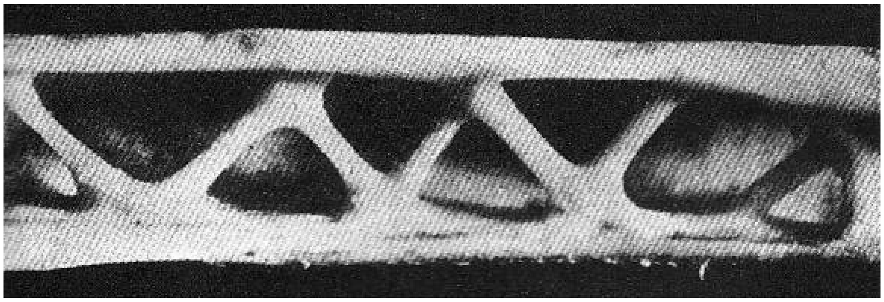

<u>Engineering Nature</u>:
Metacarpal bone from a vulture's wing; stiffened after the manner of a Warren's truss. (After Thompson, 1942)

Contents

2.1 Introduction

It is proposed that the spatio-temporal development of bone healing can be predicted based on the mechanical stimulus at the fracture site using two separate modelling techniques: 1) mechano-regulated algorithm in conjunction with the finite element method to model the efficient formation of healing tissues at a fracture site, and 2) non-linear mathematical modelling to quantitatively determine the rate of healing as an increase in stiffness. If predictive modelling techniques are to be developed, then evidently predictable patterns in nature must also exist. Consequently, an investigation of the literature relating to callus formation at the fracture site and rate of healing was undertaken.

To begin, a discussion of the physiology, form and mechanical efficiency of bone healing is provided. It is argued that the form of a fracture callus directly corresponds to mechanical efficient design; hence many comparisons with *in vivo* callus formations are made with reference to structural mechanics. Next, to investigate the hypothesis that a cause-and-effect relationship exists between mechanical stimulus at the fracture site and rate of healing, a review and comparative analysis of healing rates found in clinical studies from the literature will be examined.

To conclude, a critical review of the published work relating to mechano-regulation of tissue differentiation, bone remodelling and callus healing modelling methods will be conducted. This will provide a comprehensive knowledge of the past and current methods which will allow for determination of the best approach to model the spatio-temporal development of bone fracture healing.

2.2 Callus formation and mechanical efficiency

This section reviews the experimental and clinical evidence of the efficient formation of bone healing tissues and how they are influenced by mechanical stimulus.

2.2.1 Stages of bone healing

There are two types of healing; primary and secondary. Primary healing occurs when the bone fragments are realigned and compressed and no fracture gap exists. Ossification occurs directly from one fragment to the other by cells (osteons) crossing the fracture line (Perren, 2002). This type of healing is generally a result of surgical intervention and rigid fixation and is also known as direct healing because of the direct union.

Secondary healing occurs when the fragments are not compressed and a fracture gap is present. Immediately after fracture, the severed blood vessels in the bone cause a haematoma to form in the localized region where fibroblasts and undifferentiated mesenchymal stem cells arrive at the periosteum via the circulation (Nakahara *et al*., 1990). After a few days post-fracture the red blood cells of the haematoma become resorbed, leaving the fibroblasts which form a loose aggregate of cells, interspersed with small blood vessels, known as granulation tissue (Fig. 2.1b). At this point, the granulation tissue provides some mechanical support. Osteoprogenitors arriving from the vasculature differentiate into chondrocytes which team with the fibroblasts to produce collagenous and fibrous tissue that forms around the outside of the fracture and internally within the medullary cavity (Wornom and Buchman, 1992).

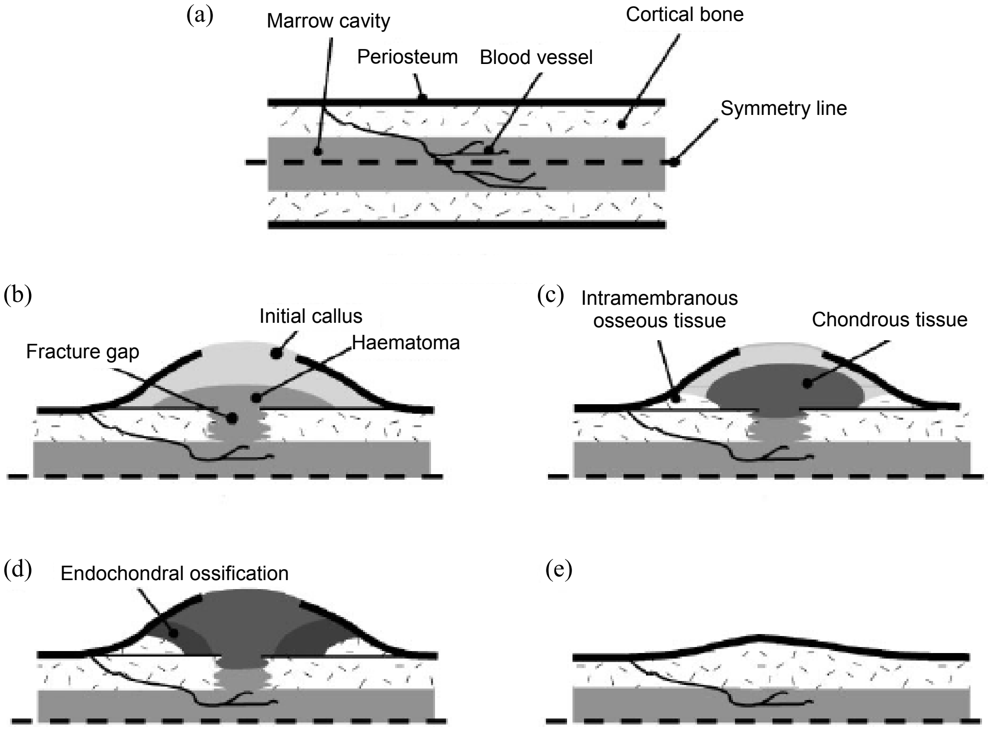

Figure 2.1. The stages of bone healing (adapted from Bailón-Plaza and van der Meulen, 2001). (a) Intact bone, (b) post fracture, (c) intramembranous ossification and cartilage formation, (d) endochondral ossification, and (e) remodelling.

The periosteal cells proximal and distal to the fracture site develop into an adjacent callus through the process of intramembranous ossification, where, the periosteal membrane lifts from the bone surface which expands filled with woven bone. The granulation tissue within the central callus also develops into cartilage through a process known as chondrogenesis (Fig. 2.1c). The replacement of the cartilage with lamellar bone, known as endochondral ossification, occurs beneath the intramembranous tissue. These new tissues grow in size on both sides of the gap until they unite with their counterparts from other pieces of the fracture (Fig. 2.1d). The fracture gap is then bridged by the cartilage and woven bone, restoring some of its original strength. Eventually, the fracture callus is remodelled into a new shape which closely duplicates the bone's original shape and strength (Fig. 2.1e).

It is interesting to note, that for many years the AO/ASIF (Arbeitsgemeinschaft für Osteosynthesefragen /Association for the Study of Internal Fixation) suggested that best healing can be achieved by rigidly compressing the fracture surfaces together thus inducing direct healing. If the implant were to fail, however, and somehow lose its rigid bonding of fracture surfaces, a minute gap will disrupt the osteons and lead to non-union. For this reason, the AO/ASIF has recently put a greater emphasis on indirect healing by callus formation. In this case, the surfaces of the fracture are not compressed together; hence micro-motion between the fragments will not disrupt healing. Allowing healing by callus formation is also a more natural way for the bone to heal, as the repaired bone will be superior to a bone mended by direct healing.

2.2.2 Influence of fracture geometry on efficient callus formation

During the healing process a large callus forms outside the bone (periosteal formation) and a smaller callus forms a bridge within the medullary cavity within the bone (endosteal formation) (Fig. 2.2). It can be observed that the mass of granulation tissue that surrounds a fractured bone is greater than the diameter of the bone itself. The granulation tissue has a lower material stiffness than the bone it is mending but compensates with an increased outer diameter which increases the area and polar moment of inertia. Moreover, the intramembranous ossification and endochondral ossification adds further support by creating an expansion on either side of the fracture which serves to distribute pressure over the central callus area (Fig. 2.2a), which is akin to the metaphyseal expansions found in the knee joint which serve to distribute pressure over the meniscus.

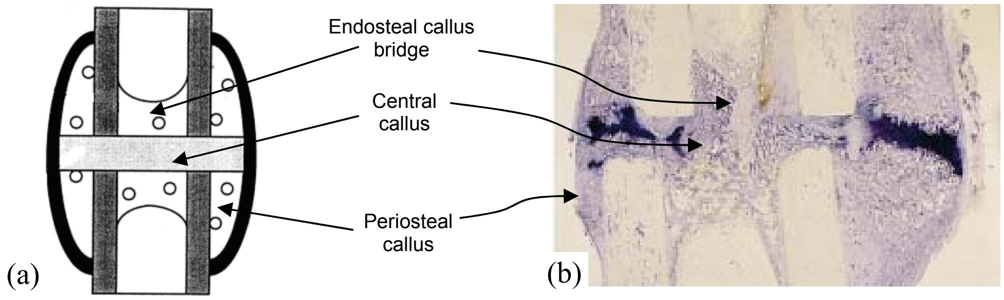

Figure 2.2. (a) Schema of an ovine tibial osteotomy and the three regions of callus tissue (Gardner at al., 1998). (b) In vivo callus formation around a transversal fracture under pure axial loading (Claes and Heigele, 1999).

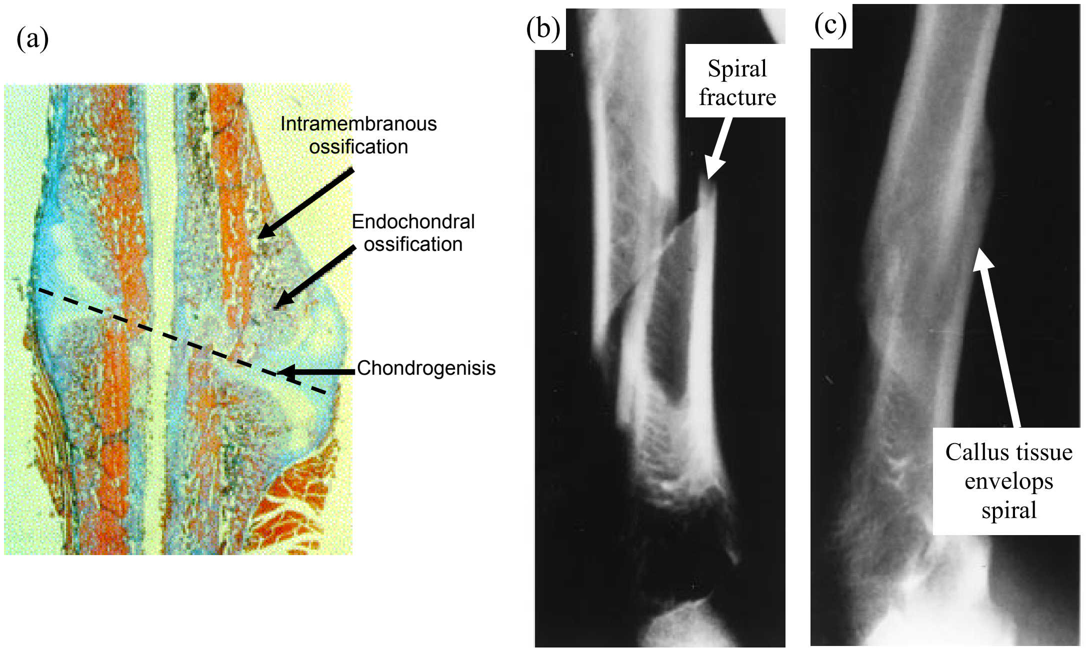

Figure 2.3. (a) Callus formation around oblique fractures (adapted from Einhorn, 1998). Note that the black broken line represents the central line of chondrogenesis. (b) Radiographic image showing lateral view of a spiral fracture of the humerus and (c) anteroposterior radiograph taken 10 months after the fracture which reveal bony union (adapted from Soeda et al., 2002). It can be seen that the tissues envelop the fracture line.

The formation of callus tissue around the healing fracture is typically asymmetric which can be attributed to the fracture pattern itself (Wade *et al*., 2001). For example, *in vivo*, it is observed that when the fracture is oblique ($\geq 30^{o}$), the callus becomes skewed to deposit the healing bone tissues at the same angle at the fracture line. From figure 2.3a it can be seen that the central line of chondrogenisis (cartilage formation) in an oblique fracture shifts to the angle of the fracture plane. It is important to note that intramembranous and endochondral ossification now takes place asymmetrically and at the angle of the fracture line. From a structural view point, by distributing the callus tissue to the fracture line, mechanical stability is reached with the greatest efficiency.

The efficient callus tissue distribution can also be seen in spiral fractures (Fig. 2.3b), where the callus tissue forms at the fracture line (Fig. 2.3c), thus stabilizing the fracture in a similar manner as the oblique fracture (Fig. 2.3a). The callus tissues follow the line of the fracture which envelops the fragments at their ends. These cases exemplify the efficiency of callus formation, where the tissue is deposited and forms so that mechanical stability is maximized but tissue use is minimized. These examples agree with the 'maximum-minimum design principal' proposed by Roux (1881) for bone formation.

2.2.3 Influence of the unilateral fixation on callus formation

It was hypothesized, in the present study, that the presence of a unilateral fixator will alter the strain gradient within the interfragmentary space thus resulting in a greater level of callus formation on the elevated strained side (see Fig. 1.1). This is often seen in radiographic images of fractures under unilateral fixation, where the side furthest from the plate (far-plate cortex) shows significantly greater callus expansion than the side closest to the plate (near-plate cortex) (Fig. 2.4). There are other reasons for this lack of callus growth on the side closest to the plate: 1) the presence of the plate would impede the growth of tissue under the implant, 2) the osteogenic potential is lower due to the lack of contact with soft tissues such as muscles (McKibbon, 1979), and 3) the stress shielding effect of the plate (Wade *et al*., 2001).

In the present study, however, it is contended that the inter-cortical strain gradient, induced by the presence of the implant, is the overriding cause of the lack of near-plate callus. For example, it was found in a clinical case of unilateral fixation that marked far-side callus formation was found whereas no near-side callus formed, despite the fact that the surgeon intentionally altered the implant to prevent impedance of circulation, and thus allow callus formation (Fig. 2.4c).

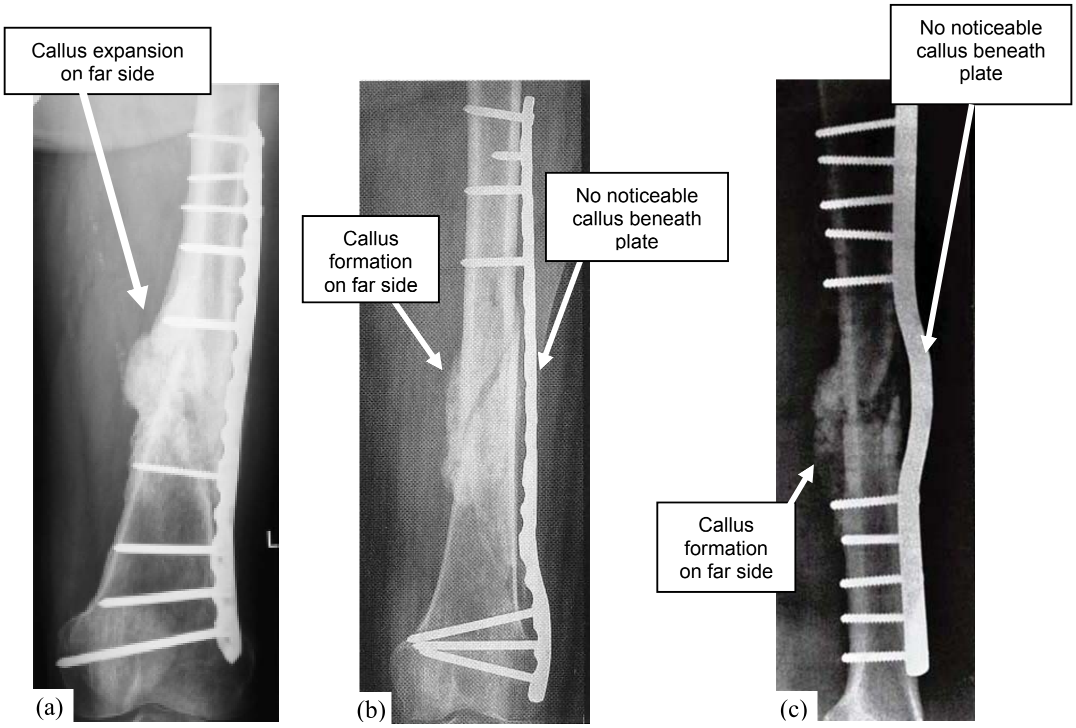

Figure 2.4. Callus formation on far-plate cortex under unilateral fixation. (a) Antero-posterior view of locking plate fixation with significant callus growth and ossification after 1 year (adapted from Sommer et al., 2004). (b) Callus formation on medial side under locking plate fixation but with no callus beneath locking plate after 4 months (adapted from Wagner and Frigg, 2006). (c) Bridging plate altered to prevent periosteal contact at the fracture site to improve circulation. Sourced and adapted from www.aofoundation.org (Website 1).

Importantly, experimental studies of bone healing under unilateral external fixation with motion control have shown an increased callus formation on the side of the fracture/bone where the compressive strains were greatest (Goodship *et al*., 1998) (Fig. 2.5). A similar observation was found by Hente *et al*. (2004) who showed that a fracture subjected to cyclic bending resulted in a significantly greater formation of callus tissue on the compression side of the fracture (Fig. 2.10). Furthermore, it has been shown that a healing bone callus is also sensitive to the number of applied loading cycles and the strain rate, where a profound effect on the formation of callus can be clearly observed (Figs. 2.5-2.6).

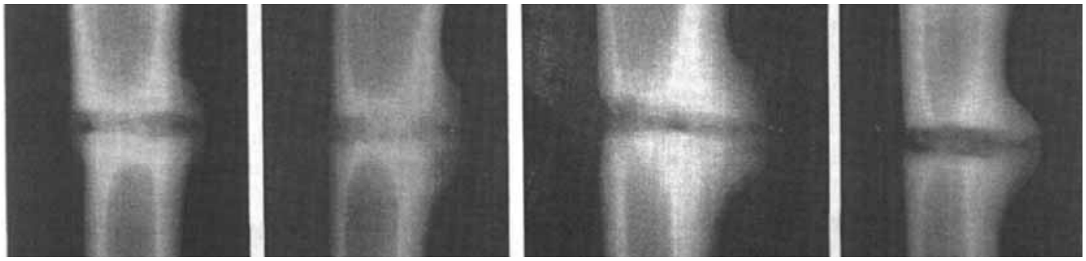
SR = 2mm/sec
SR = 40mm/sec
SR = 400mm/sec
SR = 400mm/sec (late start)

Figure 2.5. Callus asymmetry observed with external fixation and with differing strain rates (Goodship et al., 1998). The stimulus was actively applied on the right side of the images corresponding to increased callus formation.

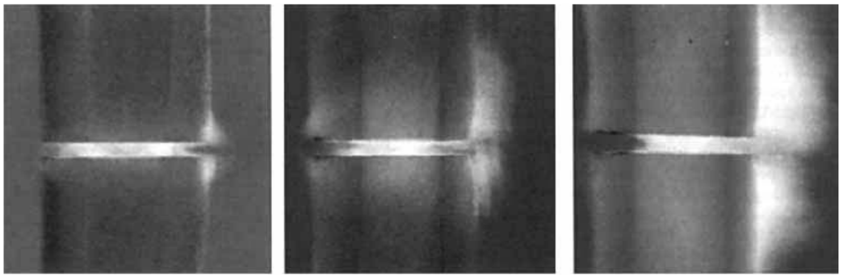
0 cycles
10 cycles
1000 cycles

Figure 2.6. Radiographic imagery of callus asymmetry caused by cyclic bending and with differing number of load cycles (Hente et al., 2004). Greater callus formation can be observed on the right side of the images where compressive strains were imparted.

2.3 Mechanical development of the fracture callus

It was hypothesized in the present study that there is a causal relationship between the rate of bone healing and the mechanical stimulus at the fracture site. This section reviews the existing experimentation to determine whether such a relationship is plausible.

2.3.1 Mechanical patterns in bone healing

Christel *et al.* (1981) identified two distinct mechanical phases in the healing process of rate fracture calluses; a rubbery-like soft tissue phase where up to the first 6 weeks of healing the callus exhibits low strength, low stiffness and large elongation, which was followed by a harder stiffer material phase. Between these two phases, a sudden increase in structural stiffness can be observed which produces a sigmoidal curve (Fig. 2.7a). The upper and lower horizontal portions of the curve represents the remodelling and reparative stages of healing, respectively, while the intermediary phase (sudden shift in stiffness) represents bridging of the fracture gap. The rate of increase in the initial portion of the sigmoidal curve is related to the rate at which intramembranous ossification, chondrogenesis and endochondral ossification occurs. Importantly, the rate at which these tissues advance towards to fracture gap is likely to determine the rate of healing (Lacroix, 2001).

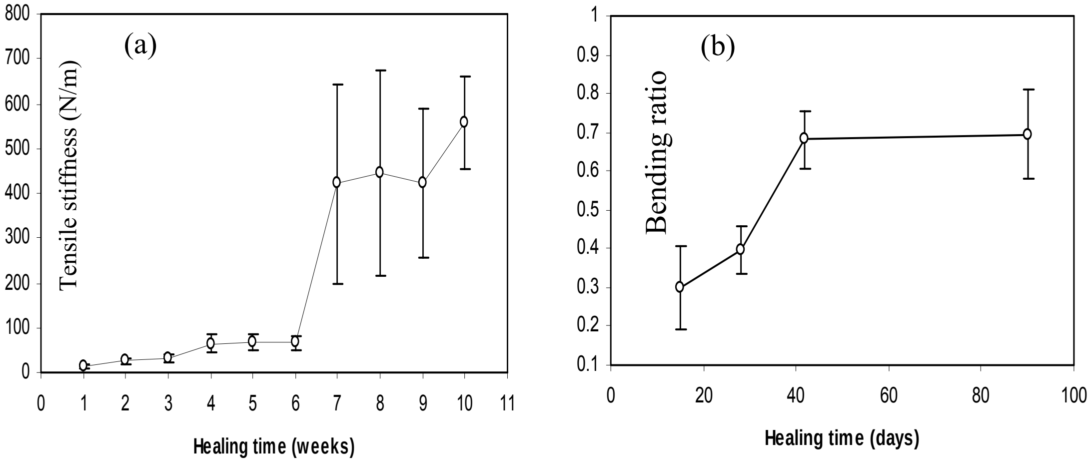

Figure 2.7. (a) Tensile stiffness vs healing time in rat calluses (Christel et al., 1981). The tensile stiffness increased from 35% to 85% of the final value between weeks 6 and 7. (b) Ratio between flexural rigidities vs healing time (Akkus et al., 1998).

Akkus *et al.* (1998) found a similar sigmoidal relationship between healing time and callus bending stiffness in rabbits (Fig. 2.7b). There was a more gradual increase in stiffness between the reparative and remodelling phases in comparison to the results found by Christel *et al.* (1981). This, however, may be due to the method employed in bone fracturing, the size of the fracture gaps themselves and the difference in metabolic rates. In ovine fractures, a similar exponential increase in stiffness can be observed between weeks 2-8 before the remodelling process begins (Gardner *et al.*, 1998).

2.3.2 Influence of mechanical factors on the rate of bone healing

From these initial observations shown above, it is clear that a distinct healing pattern exists. What is more important, however, is whether this pattern alters depending on the applied mechanical stimulus. Animal studies have been conducted to clarify the influence of mechanical factors on bone healing by quantifying the effect of interfragmentary motion

(IFM) or interfragmentary strain (IFS) on the quality of healing, from a histological and mechanical view-point. All of the following studies, discussed in this section, used idealised fractures in sheep tibiae, such as mid-shaft gap-osteotomized transversal fractures. Specially designed external fixators were also utilised to induce a specific IFM for a given fracture gap size, thus producing a specific IFS:

$$IFS = \frac{\text{IFM}}{\text{Gap size}} \tag{2.1}$$

The standard practice *in vivo* was to compare a rigid fixator, which allows some interfragmentary strain (because no fixator is infinitely rigid), and a semi- or non-rigid fixator which allows a greater magnitude of IFS or IFM. A measuring device, such as a Linear Variable Displacement Transducer (LVDT), would then be used to quantify an increase in callus stiffness by the reduction of IFM during the evolution of bone healing. It should be noted that a reduction in IFM data correlates with the increase in axial stiffness as the callus heals and becomes ossified.

It has been shown that the application of IFS in the early stages of healing has a significant influence on the future rate of healing (Goodship and Kenwright, 1985; Mora and Forriol, 2000). This was further exemplified by Klein *et al*. (2003) who showed that the initial phase of fracture healing is specifically sensitive to mechanical conditions, where advanced fracture healing was found in fixators that allowed more interfragmentary motion. This advanced healing presented itself as a stiffer more efficiently sized (smaller) callus. This, according to Klein *et al*., demonstrates that the initial motion or strains in the fracture have a significant influence on the outcome of bone healing.

Conversely, Hente *et al*. (1999) found that there was no clear difference between the effects of a dynamically or rigidly fixated bone and thus concluded that the dynamic fixator provided no further benefit to the healing callus. It should be noted, however, that the dynamic fixator was kept rigid until the fourth week of healing, after which axial motions were permitted. Importantly, Goodship *et al*. (1998) had shown that callus development is inhibited when the strain is applied late in the healing process. This agrees with the previous findings (Klein *et al*., 2003; Mora and Forriol, 2000) where it was known that the future of the healing outcome is sensitive to early mechanical stimulus. It is suspected that if perhaps Hente *et al*. (1999) allowed interfragmentary motion to be permitted earlier in the experiment for the dynamic fixator then a greater rate of healing would have been found.

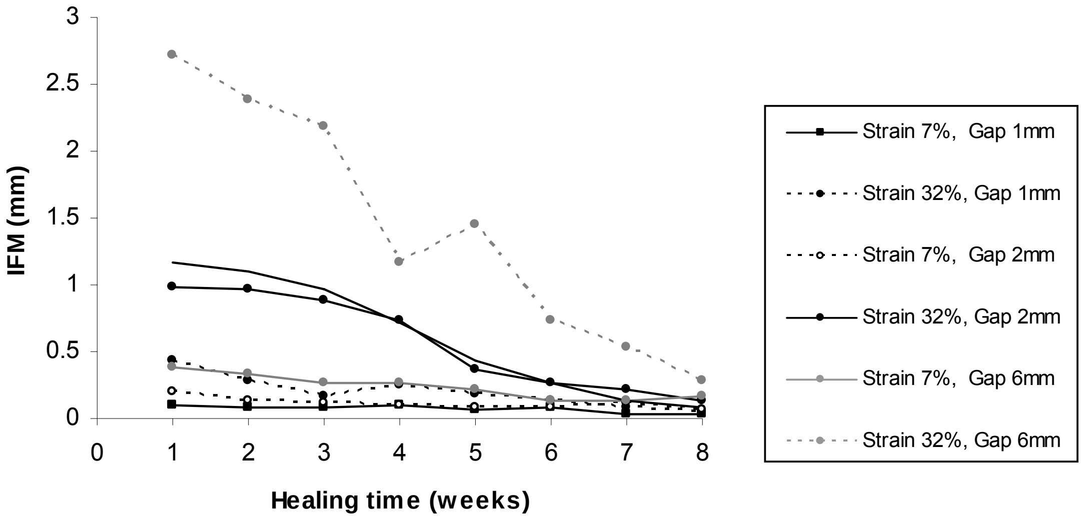

Figure 2.8. Reduction in interfragmentary motions during bone healing for differing interfragmentary strains and gap sizes (adapted from Claes et al., 1997).

Claes *et al*. (1997) compared the reduction in interfragmentary motions (IFMs) during bone healing, for an initially low interfragmentary strain (IFS = 7%) in comparison to an initially high strain (IFS = 31%), to determine whether mechanical stimulus affects the rate of healing (Fig. 2.8). Claes *et al*. concluded that there was no significant difference in IFM between the strain cases after the 7th week of healing. Claes and coworkers, however, presented the evolution in callus stiffening as a reduction in IFM, as measured by the displacement transducers. By analyzing the reduction in interfragmentary motion, it would have been difficult to decipher the rate of healing as the results (IFMs) appear to converge at the 7th week of healing (Fig. 2.8). In the present study, however, it is suspected that an important oversight may have occurred.

2.3.3 A re-investigation of Claes and coworkers (1997, 1999)

To extract new meaningful results from Claes and coworkers' (1997, 1999) experimental findings, and to determine whether a relationship between the initially applied IFS and the rate of healing existed, it was necessary to re-evaluate the original data. Firstly, the data sets which represented the reduction in IFM for each fracture gap size and initially applied IFS (Fig.2.8) was separated into individual graphs (Fig. 2.9). Next, the initial IFM (recorded at week one) was divided by the final IFM (recorded at week 8) for each individual strain case (Fig. 2.9). This approach effectively produces a *stiffness ratio* quantity which normalizes the results and therefore expresses the influence of IFS on healing as a relative increase in axial stiffness between week one and week eight:

$$\text{Stiffness Ratio} = \frac{\text{Initial IFM}}{\text{Final IFM}} \tag{2.2}$$

Consequently, by using a normalized ratio quantity, the effects of fracture gap size, loading, and individual callus size can be eliminated. Based on this novel approach, it was shown that in the low strain cases (IFS = 7%), the initial IFM reduced by an average of 2.85 (SD 0.48) times at week eight (Figs. 2.9a-c), however, in the higher strain groups (IFS = 32%) the initial IFM reduced by an average of 8.5 (SD 1.36) times at week eight (Figs. 2.9d-f). Furthermore, a later study by Claes and Heigele (1999), using the same external fixator, quantified the reduction in IFM for a 3mm fracture gap with an even greater interfragmentary strain of 40%. It was found that the initial IFM decreased by a factor of approximately 12.8 times at week 8 (Fig. 2.9g). By comparing these stiffnesses for the 7%, 31% and 40% strain cases, one can observe a noticeable demarcation between the relative increases in axial stiffness for these strain cases (Fig. 2.10).

This stiffness ratio has provided a new way of analyzing this experimental data to help compare and contrast the stiffness of callus and their relationship to initial gap size and IFS. Interestingly, the fracture gap size did not appear to have an effect on the above findings despite the fact that a larger gap will result in lower bending and tensile stiffness (Augat *et al*., 1998; Claes *et al*., 1997). This is because the *stiffness ratio* is a normalized value and thus it is independent of the initial structural stiffness of the callus as defined by the gap size. Importantly, this novel re-evaluation of Claes and coworkers (1997, 1999) agrees with the hypothesis that there is a positive correlation between the initially applied IFS and the rate of healing. It should be noted that other researchers failed to highlight this phenomenon and is therefore being examined for the first time in the present study.

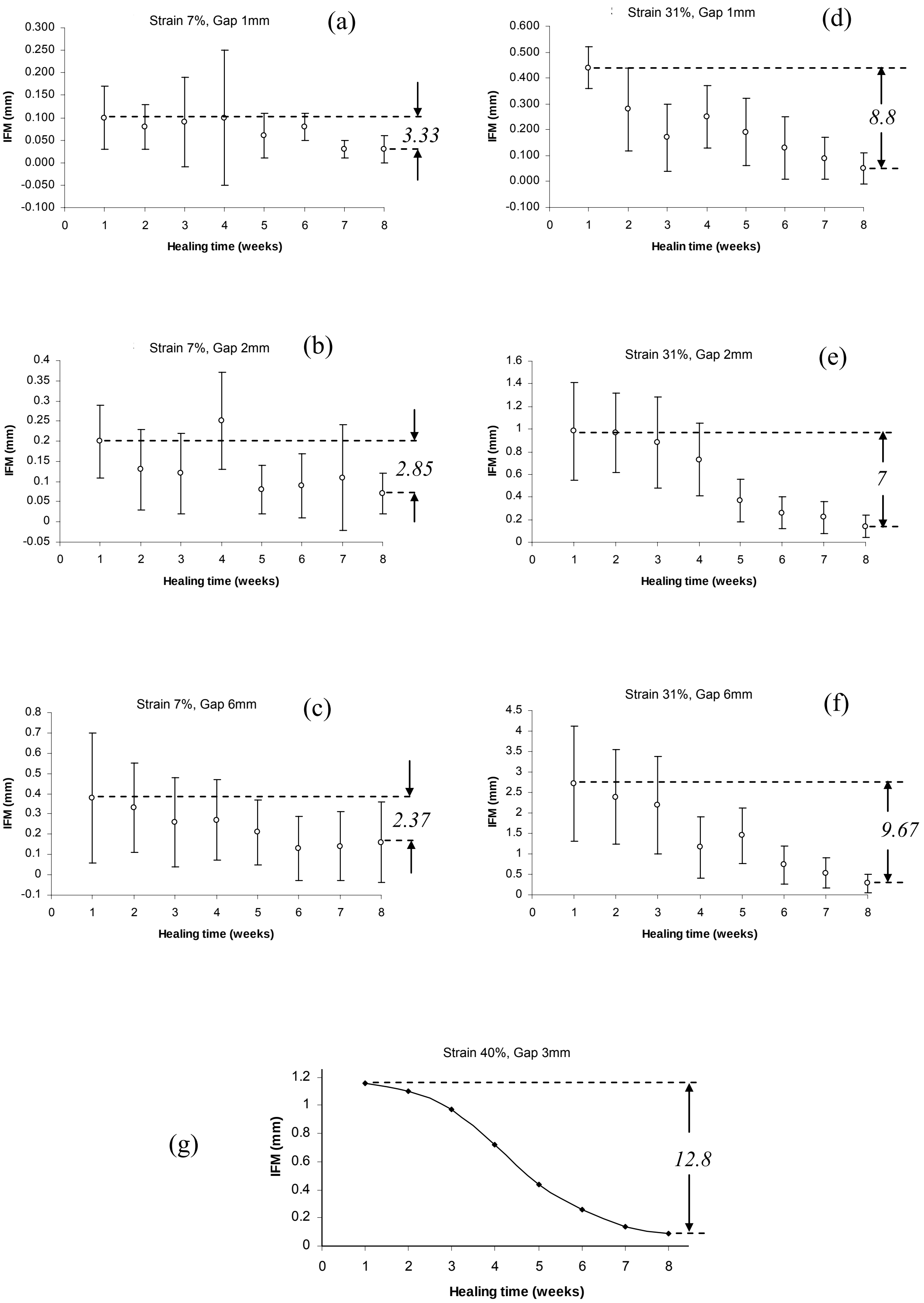

Figure 2.9. Re-evaluation of raw IFM data adapted from Claes and co-workers (1997,1999). The factor reduction in initial IFM is represented in italics.

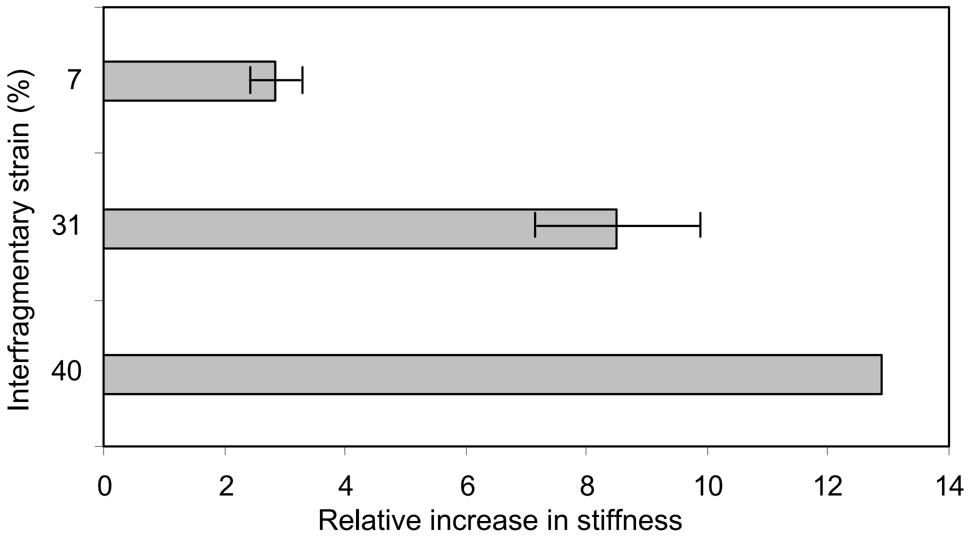

Figure 2.10. Relative increase in stiffness between week one and week eight of healing for three initial interfragmentary strains cases (adapted from Claes and coworkers, 1997, 1999).

What confounds these results, however, was that the tibiae were later excised and were tested mechanically and found no significant difference in tensile stiffness between small sections of the callus subjected to the low (7%) and high (31%) strain cases (Augat *et al.*, 1998). It should be noted, however, that the above reinterpretation was based on an increase in compressive stiffness. The author suspects that compression tests on the full excised calluses may have yielded results similar to above. Furthermore, Augat *et al.* (1998) had found significantly more ($p<0.05$) bone within the 7% strain case in comparison to the 31% cases. However, it may be the case that the formation of these new bone tissues within the general callus also determines the structural stiffness, and not just the percentage of new bone.

2.3.4 The effects of excessive interfragmentary strain

It has been shown that 'too much' IFS may in fact inhibit the rate of healing, often caused by an unstable fixation. This was exemplified by Schell *et al.* (2008) who showed that an unstable fixator with high axial strains (47%) and shearing motions inhibits healing and leads to non-union. Furthermore, Epari *et al.* (2006) have shown that instability prolongs the chondral phase (cartilage to bone) of healing. Epari *et al.* found that the calluses which healed under the rigid fixation were in fact mechanically stiffer (in bending) than the less rigid fixator after the 6th week of healing. A histological examination showed that the remodelling process began earlier in the rigidly fixated calluses while cartilage persisted in the semi-rigid fixator. The actual difference in level of IFM or IFS before or during the experimentation was not known. Nevertheless, Lienau *et al*. (2005) also found that a semi-rigid fixator delayed healing in comparison to a rigidly fixated bone. Goodship and Cunningham (2001) propose that it is possible to influence healing by manipulating the mechanical environment at the fracture site, but for this to be successful the gap must not be too large and the initial fracture site strains have to be of a reasonable value (approximately 10% to 50%) and repeatedly applied.

2.4 Stimulus for callus formation

This section critically analyses the mechanical stimuli that have been theorised to drive tissue differentiation during bone healing. It was hypothesised in the present study that the compressive principal strains are the dominant driving force behind the efficient formation of callus tissue. This hypothesis is argued based on computational and experimental findings from the literature.

2.4.1. The Interfragmentary Strain Theory

Perren and coworkers (Perren, 1979; Perren and Cordey, 1980) proposed the "interfragmentary strain theory" which suggests that bone healing tissues cannot form if the fracture gap experiences strains greater than the tissues rupture strain, as calculated by equation 2.1. Therefore, bone cannot form if the IFS is greater than 2%, endochondral ossification occurs when the IFS is between 2-10% and the formation of granular tissue is present where strain is 100% (Perren 1979).

The interfragmentary strain theory is not considered to be the unified theory of tissue differentiation (Lacroix, 2000). Nevertheless, it does have the merit of simplicity, and it is perhaps for this reason, that many researchers used interfragmentary strain in experimental tests as a quantitative comparison to determine if strain does indeed influence the rate of healing. Consequently in the present study, IFS is also used to determine, mathematically, the cause-and-effect relationship between mechanical stimulus and the rate of healing.

2.4.2 Octahedral and deviatoric shear stresses/strains

The granulation tissue formed in the early stages of healing are interspersed with pluripotential stem cells which have the ability to differentiate into any tissue type. It is widely believed that mechanical factors influence the differentiation of these stem cells. This has sparked many theories of tissue differentiation based on mechanical stimulus. Pauwels (1960) proposed the first theory of mechanical stimulus on tissue differentiation, where it was theorised that deviatoric (shear) stresses, *S*, are the specific stimuli for bone or fibrous connective tissue, whereas hydrostatic (volumetric) stresses, *D*, control the formation of cartilaginous tissues (Eqs. 2.3-2.4).

$$S = \frac{1}{3}\sqrt{(\sigma_1 - \sigma_2)^2 + (\sigma_2 - \sigma_3)^2 + (\sigma_3 - \sigma_1)^2} \tag{2.3}$$

$$D = \frac{1}{3}(\sigma_1 + \sigma_2 + \sigma_3) \tag{2.4}$$

Carter and Beaupré (2001) and Prendergast *et al*. (1997), agree that shear stress/strain influences tissue differentiation. Prendergast *et al*. (1997) further proposed that fluid flow in conjunction with shear strain is the direct stimulus for tissue differentiation. One should note that the flow of fluid is a direct result of the flow of material, or in other words, the strains experienced by the tissues as it deforms. Carter and Beaupré, 2001, agree with Pauwels (1960) and thus maintain that mechanical stresses/strains are the direct stimulus for differentiation. Importantly the above equations are calculated from the stress or strain invariants (principal stresses/strains – scalar quantities that are independent of a co-ordinate system). It has been shown, however, that the cyclic maximum principal strains are critically important to whether intramembranous ossification can occur (Perren and Rhan, 1980) and also in controlling type I collagen synthesis (Giori *et al*., 1993; Wren *et al*., 1998). In the context of compression loading on callus tissue, it is intuitive that the magnitude of the compressive principal strains would negate the effects of other principal strains (radial or hoop) (see Appendix B for a comparison). Consequently, Carter *et al*. (1988) suggested that in fact tissue differentiation is caused by a combination of maximum principal strain and hydrostatic stress.

Claes and Heigele (1999) describe the direction of healing as shown below (Fig. 2.11a), where the origins of bone apposition begin at the periosteal and endosteal surfaces and proceeds towards to the fracture gap. Interestingly, Carter *et al*. (1988) analysed the compressive principal stress vectors in a callus FE model, and showed that the greatest stresses were within the fracture gap and the lower stresses were observed in the adjacent tissue (Fig. 2.11b). In the present study, by comparing Claes and Carter (Figs. 2.11a-b), it can be seen that the advancing ossified callus tissue avoids these high stress gradients at the cortical gap by forming tissues around them. Furthermore, the direction of the stress vectors appear to follow the same path of intramembranous and endochondral ossification. Also, when bending was applied to Carter's model, the compressive stress vectors became skewed to compression side of the fracture (Fig. 2.11c) which correlates with the asymmetric callus formation demonstrated in the *in vivo* callus bending study by Hente *et al*. 2004 (see Fig. 2.6).

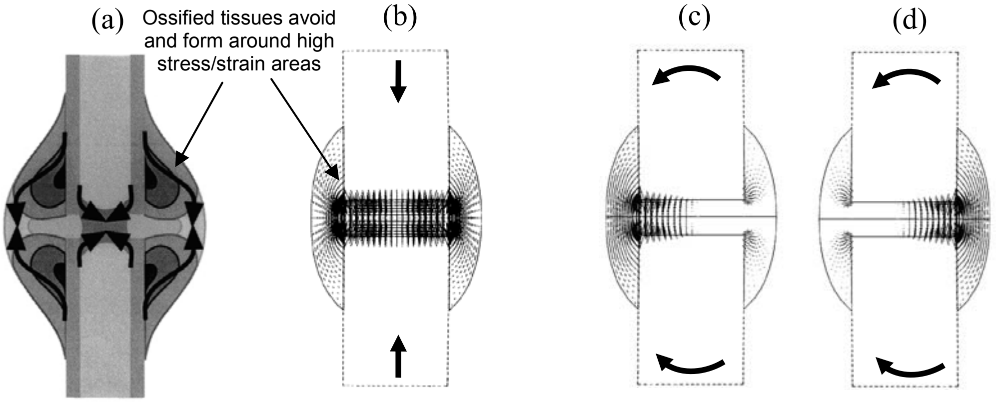

Figure 2.11. (a) Schema of callus healing where arrows indicate the direction of bone apposition (adapted from Claes and Heigele, 1999). (b) Compressive principal stress vectors in the FE model under compression, (c) compressive principal stress vectors under bending loads on the compression side of the fracture, and (d) equal but opposite tensile principal strains on the tension side of the fracture (adapted from Carter et al., 1988).

Furthermore, under bending loads, Carter *et al*. (1988) found an equal but opposite compressive (negative) and tensile (positive) principal strain vector pattern on the corresponding sides of the fracture gap (Figs. 2.11c-d). Carter and Beaupré (2001) postulated that the positive tensile principle stresses will show a trend toward greater bone and/or fibrous on the side of the fracture where the bending moment creates tensile stress. This also agrees with the interpretations of Pauwels (1960) who conjectures that a callus will have a predominantly fibrous character under tensile stretching and a cartilaginous character under compression. According to Carter this was verified based on the experiments by Wurmbach (1928). However, to re-iterate, more recent experimentation has shown that a healing bone subjected to bending moments with equivalent compressive and tensile strain, had conclusively shown that the callus favours the compressive strains over tensile ones (Hente *et al*., 2004).

Furthermore, under tension, fibrous connective tissue (often found in the early stages of healing) is highly compliant, and would do little to resist tensile stretching as was shown experimentally by Christel *et al.* (1981). Thus, from a structural engineering perspective, to locate fibrous tissue on the tension side of a fracture would be inefficient. Under compressive loads, on the other hand, it would be more logical to distribute fibrous or cartilaginous tissue, which contains fluid and is nearly incompressible, on the side of a fracture where compressive loads dominate. Moreover, the eventual formation of harder tissues (bone) will further aid in the resistance to compressive loading. Consequently, it was hypothesised that the compressive principal strains drive the efficient formation of callus tissue.

2.5 Computational simulation of bone healing

A number of methodologies have been presented to simulate tissue differentiation by way of computational FE modelling. The merits and disadvantages of these methodologies are discussed.

2.5.1 A fixed domain approach

Ament and Hofer (2000) were the first to simulate the form of a callus using Strain Energy Density (SED) as a means to calculate, or determine the differentiation of tissues during healing within a fixed rectangular domain. The model was based on the rules of fuzzy logic to determine the tissue differentiation pattern. Ament and Hofer used a fixed scale of Strain Energy Density to control the tissue differentiation caused by interfragmentary compression (Fig. 2.12a). Importantly, the SED field surrounding the bone fragments show a similar pattern to the stress vectors found by Carter *et al.* (1988) shown above (Fig. 2.11b). Using SED as a stimulus, Ament and Hofer could implement their algorithm to produce a callus form that approximately agrees with the typical *in vivo* callus formations (periosteal expansion and endosteal bridge) (Fig. 2.12b).

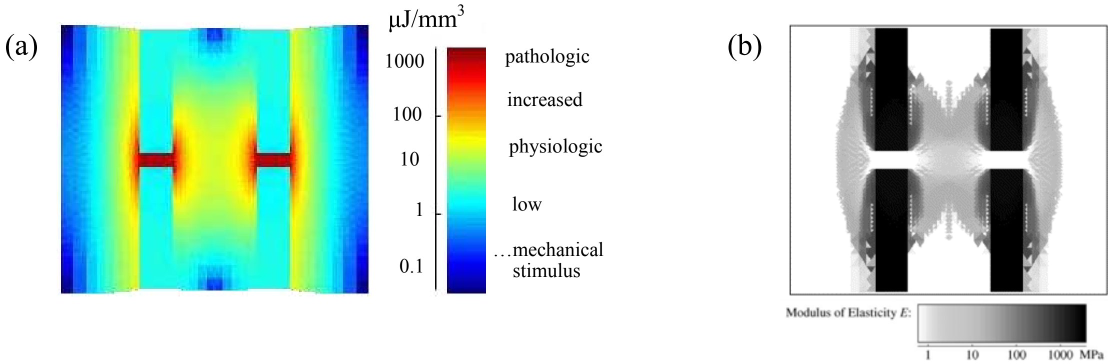

Figure 2.12. (a) Strain energy density field with mechanical stimulus scale and (b) density distribution representing modulus of elasticity of healing tissues at 14 days (adapted Ament and Hofer, 2000).

It should be noted that, due to the assumption of linear-elasticity, the SED field caused by compression of the fragments, will increase in size/intensity as the level of interfragmentary compression increases. This would suggest that the predicted size of the callus would too be equivalent in size. This is of course incorrect, where although there is a link between in IFS and the size of the callus (Claes *et al*., 1997), their relationship is not literally proportional.

Lacroix (2000) notes that the use of so many rules may over constrain the model. Furthermore, this model was verified against only one interfragmentary strain case (IFS = 36%), therefore, one could not determine how Ament and Hofer's proposed methodology behaves under different initial interfragmentary strains and fracture geometries.

2.5.2 A manually generated callus-shaped domain approach

Lacroix and Prendergast (2002a-b) used poroelasticity to model tissue behaviour within a manually generated callus FE model (Fig. 2.13). The assumption of poroelastic material behaviour in FE modelling of healing tissue has been popularised by Prendergast and coworkers who theorise that tissue differentiation is mediated by the drag flow of interstitial fluids over cells and octahedral shear strain in the tissues (Prendergast *et al*., 1997). This type of modelling is also known as biphasic due to the solid phase and the fluid phase, and according to Lacroix (2000), is a more accurate method of modelling the behavior of soft tissues.

Using the FE method, Lacroix (2000) could simulate tissue differentiation based on cellular diffusion and proliferation based on cellular location and the local mechanical stimuli. Also, remodelling was simulated by removing elements later in the healing process. In one such study or simulation, axial loading was applied which induced initial interfragmentary strains that ranged between 19.4 – 35.8% (Lacroix and Prendergast, 2002a). Interestingly, based on these simulations Lacroix predicts a somewhat negative correlation between IFS and the rate of healing (Fig. 2.14). On the contrary, according to the analysis of the literature and the new observations made in the present study, (Fig. 2.10), one would expect a positive correlation between the applied interfragmentary strain and the rate of healing.

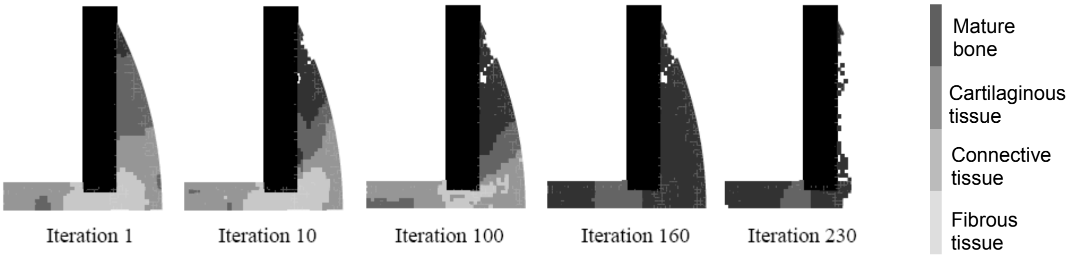

Iteration 1 Iteration 10 Iteration 100 Iteration 160 Iteration 230

Figure 2.13. One-quarter symmetric model of callus during iterative simulation of tissue differentiation (adapted from Lacroix, 2000).

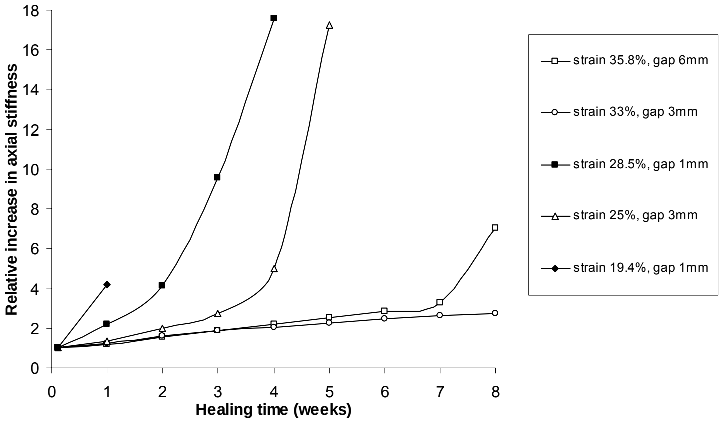

Figure 2.14. Numerically simulated rate of healing for a given level of interfragmentary strain (adapted from Lacroix and Prendergast, 2002a by means of a methodology developed in Section 3.2).

What was most interesting was that the above healing simulations were based on a fixed range of strain and fluid flow which theoretically determined the range at which certain tissues differentiate or become resorbed at. However, Lacroix and Prendergast (2002a) were required to alter the Young's modulus of the initial connective tissue (granulation tissue) (0.2 - 0.02MPa) to achieve the required interfragmentary strains for specific loads and fracture gap sizes. This practice, however, will inevitably alter the strain contours in a FE simulation. For the purposes of the present study, it may be necessary to normalise the strain contours to achieve consistency between loading scenarios and/or interfragmentary strains.

2.5.3 An expanding domain approach

García-Aznar *et al*. (2007) later simulated callus tissue formation and differentiation, also using the theoretical basis proposed by Prendergast *et al*. (1997). Unlike Lacroix above, the callus was modelled as an expanding formation from an initial cylindrical geometry using thermal diffusion to simulate cellular diffusion (Fig. 2.15). Although this modelling technique did capture the periosteal expansion of a callus, it did not take account of the initial immature callus tissue that surrounds the fragments which acts as a domain through which differentiation occurs. Furthermore, García-Aznar had also predicted a negative correlation between the initially applied interfragmentary strain and the rate of healing (Fig. 2.16).

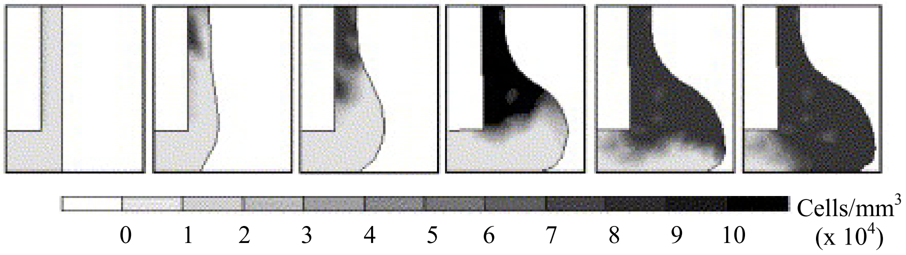

Figure 2.15. Time evolution of numerically simulated callus (García-Aznar et al. 2007). Note, one-quarter symmetry used.

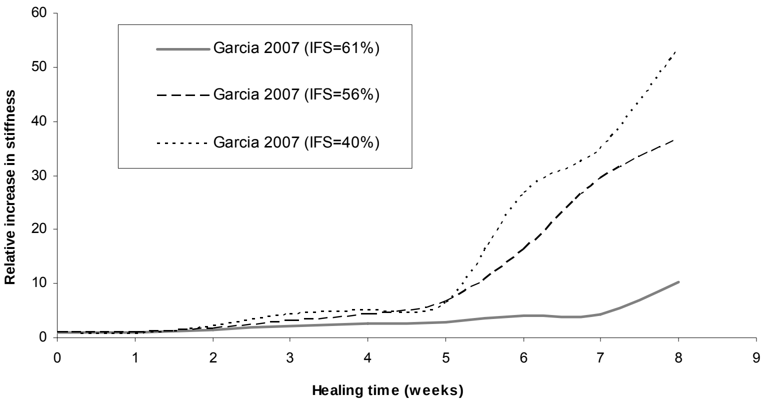

Figure 2.16. Numerically simulated rate of healing for a given level of interfragmentary strain (adapted from García-Aznar et al., 2007 by means of a methodology devolved in Section 3.2).

2.5.4 Predictive capabilities of current simulations

The current mechano-regulated models are impressive in their complexity, however, one must be cognizant that complexity does not always equate to accuracy. What was perhaps most perplexing about the aforementioned mechano-regulated modelling methods, was the variety of FE techniques and stimuli used to determine tissue differentiation and callus growth. Nevertheless, all of the above authors qualitatively verified their simulated reduction in interfragmentary motion with the same experimental findings from Claes *et al.* (1997) despite the diversity of the modelling methods. It should be re-iterated that Claes had not deciphered a relationship between IFS and the rate of healing, nevertheless, the above computational studies used these results to verify their simulations. Logically, to truly verify a computationally simulated relationship between mechanical factors and a simulated rate of healing, a well defined cause-and-effect relationship must firstly exist through which comparisons can be made.

Furthermore, the new interpretation of Claes' experimental results, as described in the present study, now appear to contradict the output of the computational simulations that they were initially intended to verify. Therefore, it is uncertain as to the predictive power of the aforementioned computational simulations. Despite this, simulating healing using mechano-regulated computational methods is still in its infancy and relies on qualitative comparisons. According to Rüberg (2003), regarding the simulation of bone remodelling, the current state of research is still in a trial-and-error phase and postulating a quantitative precision in a simulation is a future task. Understandably, the current callus simulations can afford permissible discrepancies if directly compared with experimental results. van der Muelen and Huiskes (2002) at the time described the current simulations as attempts to model nature through a method of trial-and-error to achieve the desired results. To complicate this task, Lacroix (2000) pointed out the difficulty in finding reliable initial parameters to use in his mechano-regulated model.

Thus, the above critical analyses exemplify the necessity of a phenomenological model to clarify the cause-and-effect relationship between rate of healing and the initially applied interfragmentary strain. Therefore, if a phenomenological model existed that related temporal increase in callus stiffness for a given initially applied interfragmentary strain, then the mechano-regulated simulations discussed above may have been able to parametrically alter the inputs so that the numerically predicted results could have better matched a benchmark solution.

2.6 Design optimization techniques in bone remodelling

It is known that bone tissue is a self-organizing material, where the density distribution is optimized with respect to the external loads (Carter *et al*., 1987; Harrigan and Hamilton, 1994; Mullender *et al*., 1994). Thus, the bone remodelling process can be thought of as an optimization procedure, forming or resorbing bone to minimize the material mass (Chen *et al*., 2007). Based on the clinical observations of callus formation shown previously, it is evident that the regenerative tissues also correspond to a mechanically efficient self-organised 'design'. The self-organizing process of living tissue is similar to the computational topology optimisation idea proposed by Xie and Stephen (1997) for structural engineering applications, which has since been used to predict the external shapes of hard bone structures (Xinghua *et al*., 2005). These computational design methods work on the basis that material of a structure can be iteratively eliminated and redistributed depending on the stresses experienced by that structure to obtain an optimum arrangement of material. Some mechano-regulated algorithms produce a grey scale in bitmap representation, which represents the changing density throughout the discrete structure (Ament and Hofer, 2000; Huiskes *et al*., 2000). In those simulations, however, no tissue is physically removed but is rather designated with a lower density and therefore a low Young's modulus (see Fig. 2.12b). Other studies literally remove material from a discrete structure by deleting finite elements that experience low von Mises stress (Xie and Stephen, 1993).

Huiskes *et al*. (1987) introduced a remodelling algorithm which includes a 'lazy zone' where it was assumed that bone remodelling could occur if the stimulus was either above a certain level or below a certain threshold and in between these two levels the bone structure was maintained. In the present study, a similar method of tissue maintenance and removal could also be applied to the soft tissues of the callus.

It should be noted, however, that the aforementioned studies were concerned with hard tissues and hence stress were considered to be the specific stimulus for adaptation. In the present study, since strain is conjectured to be the driving force behind tissue differentiation in compliant immature callus tissues, a new algorithm or methodology will be required to manage the optimization process.

In terms of capturing the mechanically efficient 'design' of callus tissues, it is proposed in the present study, that the compressive principal strains will predict the spatial pattern of bone healing. In design optimization, it is standard practice to determine the distribution of material based on a single stimulus. For example, trabecular bone formation was modelled using strain energy density (Chen *et al*., 2007; Huiskes et al., 2000) or octahedral shear strain (Shefelbine *et al*. 2005), while cortical bone was formed *in silico* by von Mises stress (Xie and Stephen, 1993). It is logical that hard tissues, such as bone, experience high stresses but low strains, whereas the opposite applies in soft tissues, such as the immature callus, which is highly compliant and thus experiences high strains but low stresses. For this reason, Ament and Hofer (2000) used strain energy density (SED) to simulate bone healing throughout the soft tissue stage to the remodelling of hard tissue stage because SED, u, calculates both stresses and strains

$$u = \frac{1}{2}\sigma\varepsilon \tag{2.5}$$

Consequently, in the present study, it is conjectured that the callus form is determined by the initial strains in the highly compliant soft tissues, which are known to be sensitive to mechanical stimulus which influence the later stages of healing (Klein *et al*., 2003). It is therefore logical to use strain as a means to predict the areas of future tissue deposition (or bone apposition) and tissue resorption.

2.7 Discussion

A brief analysis of the spatial distribution of callus tissue appears to agree with the maximum-minimum design principle proposed by Roux (1881) for bone adaptation. To the author’s knowledge, no studies have as yet investigated the influence of complex loading and fracture geometry on the gross or macroscopic formation of bone healing tissues based on the peak strains experienced by the early healing tissues during cyclic loading. Based on the observations of this chapter, it can be postulated that callus tissue differentiates and deposits in areas of the initial callus tissues where the strains are greatest due to the micro-motions within the interfragmentary space. The corollary of this is that tissue resorbs in lowly strained areas. It is therefore theorized that the flow or deformation of material, as calculated by the compressive principal strains, is sensed by the pluripotential stem cells in the immature callus tissue. These stem cells then react by depositing and/or resorbing the tissue to maximize the callus stiffness whilst minimizing the amount of tissue needed. Furthermore, the review of computational modelling techniques shows that the mechano-regulation and design optimization methods lend themselves to the hypothesis that callus tissues formation follows an efficient ‘design’ as calculated by mechanical stimulus. Consequently, to predict the spatial formation an algorithm will need to be specially developed to simulate the influence of strains on the compliant immature healing tissues.

The comparative analysis of the literature relating to IFS and the rate of bone healing strongly suggests that there is a cause-and-effect relationship with a positive correlation. It appears that for IFS to appropriately influence the rate of healing, it is necessary to allow strain early on in the healing process. Importantly, it was also found that no model, mathematical or otherwise, exists to describe the rate of healing based on the initial IFS. The re-evaluation of Claes and coworkers (1997, 1999) had shown a cause-and-effect relationship between the relative increase in axial stiffness and IFS, which provide impetus for the establishment of a mathematical model. However, to add further credence to the hypothesis that a relationship not only exists, but can be modelled mathematically, requires further comparative investigation with additional experimental results, and quantitative reinforcement by means of error and statistical analyses.

On a final note, with regards to the predictive power of the proposed methodologies, it will be necessary to determine how accurate or how well they simulate nature. As a result, if the proposed algorithm and mathematical model is to be relied upon, then rigorous quantitative and qualitative comparisons with physical evidence is required.

Chapter 3 - Methods

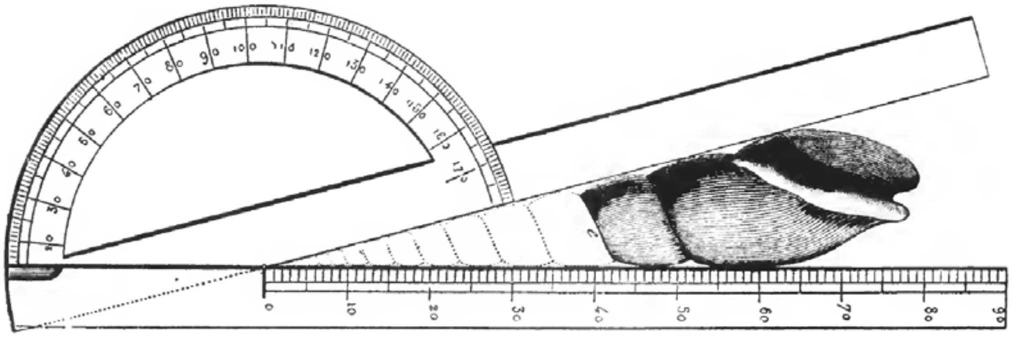

<u>Measuring Nature</u>:
d'Orbigny's helicometer used to measure the apical angle of the turbinate shell (After Thompson, 1942).

Contents

3.1 Introduction

It is hypothesized in the present study that the rate of healing can be predicted based on the initial IFS. This chapter therefore describes methods used to determine a relationship between interfragmentary strain, time and callus stiffness. Clinical studies from the literature were assembled and their quantitative measurements found during healing were re-processed to remove inter-study variability for comparative purposes. Using the empirical correlations found from the literature, a predictive phenomenological mathematical model was derived. Statistical methods and error analyses were employed to determine on a quantitative level the strength of this hypothesis.

It was also hypothesized in this study that the deformations of immature callus tissue, as calculated by the compressive principal strains, are the fundamental driving force behind the efficient formation of callus tissue. A method of automatically modelling the spatial distribution of a callus tissue, using a specially designed mechano-regulated algorithm which utilizes the FE method, was proposed. These simulations would also allow for the analysis of the strain trajectories and how they might contribute to efficient healing and callus formation. The efficacy of the proposed method of predicting the formation of callus tissue was then tested against idealized clinical experiments of bone healing found in the literature.

Next, to determine whether progress in this study has been made in terms of predicting the outcome of bone fracture healing for patient specific studies, three clinical case studies of bone healing under locking plate fixation were modelled. The proposed mechano-regulation algorithm was implemented in these non-idealised retrospective patient specific cases.

Finally, it should be noted that, for the sake of clarity in the present study, the term ‘interfragmentary strain’ (IFS), is used to describe the relative motion between bone fragments based on *in vivo* experimental studies. Whereas, the term ‘inter-cortical strain’ is used to describe the compressive principal strains calculated from *in silico* experimentation. Fundamentally speaking, these terms ‘interfragmentary’ and ‘inter-cortical’ mean the exact same thing but are used, nevertheless, for delineation between mathematical and computational modelling methods, respectively.

3.2 Mathematical modelling of the rate of bone healing

In the present study, a quantitative comparative analysis of the literature was conducted to determine whether a relationship between IFS and rate of healing exits. To this end, a closer inspection of the literature and specifically the reduction in IFM or increase in stiffness for each individual case study was carried out. Following in the field of mathematical biology it is envisaged that a mathematical relationship can be derived to describe the rate of healing for a given initial IFS.

Importantly the relative increase in axial stiffness as described previously only indicates the outcome of healing at one time point, t, for a specific initial IFS (Eq. 2.3). It does not, however, provide information about how the callus stiffness increases over time. Thus, it was necessary to reanalyze the experimental data by comparing the relative increase in stiffness over time.

3.2.1 Study design

This comparative study was based on the combined findings and analysis of other studies found in the literature. Hence, for the sake of reliable comparison, only studies that met the following criteria were analysed: 1) the fracture was transversal and created in ovine tibiae, 2) the stiffness and/or interfragmentary motions were recorded during the experiments, 3) the initial interfragmentary strain was known or could be calculated, and finally, 4) the study lasted, or the results were collected, for at least 7 weeks. This effectively reduced the possible candidates to thirteen studies which are tabulated in table 3.1. Despite the severity of the candidacy choice method, variability still existed between these studies specifically in the type or fixator, IFM measurement technique and fracture gap size. Furthermore, other uncontrollable factors that make it difficult to differentiate the influence of IFM between studies will influence the outcome were: callus size, initial callus material stiffness and fixator stiffness.

As mentioned previously, the initial stiffness of a callus will differ in most cases due to loading, fracture gap size and material stiffness of initial connective tissue. If, therefore, the entire stiffness of the callus, k, is thought of as a spring which resists axial loading (Nolte *et al.*, 2007) and increases in stiffness over time, it is possible to convert the interfragmentary motions (mm), into values of stiffness (N/mm) as they are both intrinsically connected. In many studies the interfragmentary motions were not converted into values of stiffness since the exact loads (N) applied to the bone for each animal was not known (Claes and coworkers 1995, 1997, 1999; Schell *et al*., 2008).

Table 3.1. Studies under comparison

Strain (%)	Gap (mm)	Duration of study (weeks)	Fixation method	Measurement method	Measurement	Reference
7	1	8	External Spatial frame, adjustable stiffness, motion limited, uniaxial (1 DoF)	Displacement transducer	Interfragmentary motion (mm)	Claes *et al*. (1997)
7	2	8				
7	3	8				
31	1	8				
31	2	8				
31	3	8				
21	0.7	8				Claes *et al*. (1995)
42	0.5	7				
40	3	8				Claes and Heigele (1999)
10	3	9	Unilateral, adjustable, (3 DoF)	Displacement markers	Displacement (mm)	Schell *et al*. (2008)
46.6	3	9				
33	2	8	External Spatial frame, adjustable stiffness, motion limited, uniaxial (1 DoF)	Displacement transducer	Interfragmentary motion (mm)	Goodship and Kenwrigth (1985)
45	3	8	Unilateral, pneumatic, uniaxial (1 DoF)	Displacement transducer	Stiffness (N/mm) derived from interfragmentary displacement	Gardner *et al*. (1998)

However, in the present study, since the relative rate of increase of callus stiffness was sought rather than the exact stiffnesses themselves, the actual loads were not required. It was therefore possible to disregard the loads and therefore invert the IFM data into a stiffness value for a given time point, k_t (mm^{-1}) (Eq. 3.1). It was then possible to normalize the stiffness by dividing the stiffness at each time interval, k_t, by the initial stiffness, $k_{t=1}$, so that a relative increase in stiffness could be expressed (Eq. 3.2).

$$k_{\mathrm{t}} = \frac{1}{\mathrm{IFM}_{\mathrm{t}}} \tag{3.1}$$

$$\text{Relative increase in stiffness} = \frac{k_{\mathrm{t}}}{k_{\mathrm{t=1}}} \tag{3.2}$$

3.2.2 Comparative re-investigation of the experimental data

The IFM data conversion process described above was applied to the experimental results found by Claes *et al*. (1997) and Claes and Heigele (1999) (Fig. 3.1) which had shown a positive correlation between IFS and the callus stiffness at week 8 (see Section 2.3.1). The original IFM data (Fig. 3.1a) was firstly inverted, which showed that there is in fact a significant difference between the test groups (Fig. 3.1b). This graph, however, did not indicate the difference in rate of callus evolution between strain cases. The callus stiffness, k (mm^{-1}) was therefore converted into a relative increase in stiffness by dividing the stiffness at each week by the stiffness at week one, $k_{\mathrm{t=1}}$, so that all cases began at a baseline value of 1. This provided a clearer comparison between the groups with different initial IFS (Fig. 3.1c).

As expected, the relative increase in stiffness at week eight showed a distinct demarcation between strain groups as was originally observed earlier in this study (see Fig. 2.10). The re-evaluated experimental results showed a trend which suggests that the relative increase in callus stiffness follows a linear progression when the initial IFS is low (7%), but when the initial IFS is increased (31- 40%), the rate of callus stiffening grows in an exponential fashion (Fig. 3.1c). It should be noted that from this initial finding, the fracture gap size did not appear to affect the rate of healing. However, the gap sizes will not affect the relative increase in axial stiffness by the proposed calculation methods.

3.2.3 Statistical analysis

To determine the level of statistical significance of the relative increase in stiffness for the 7% and 31% interfragmentary strain cases (Fig. 3.1c), an independent two-sample t-test was conducted to determine the statistical significance between data sets at each weekly healing point (Eq. 3.3). These interfragmentary strain cases were chosen since their sample sizes ($n = 3$) were greater than one.

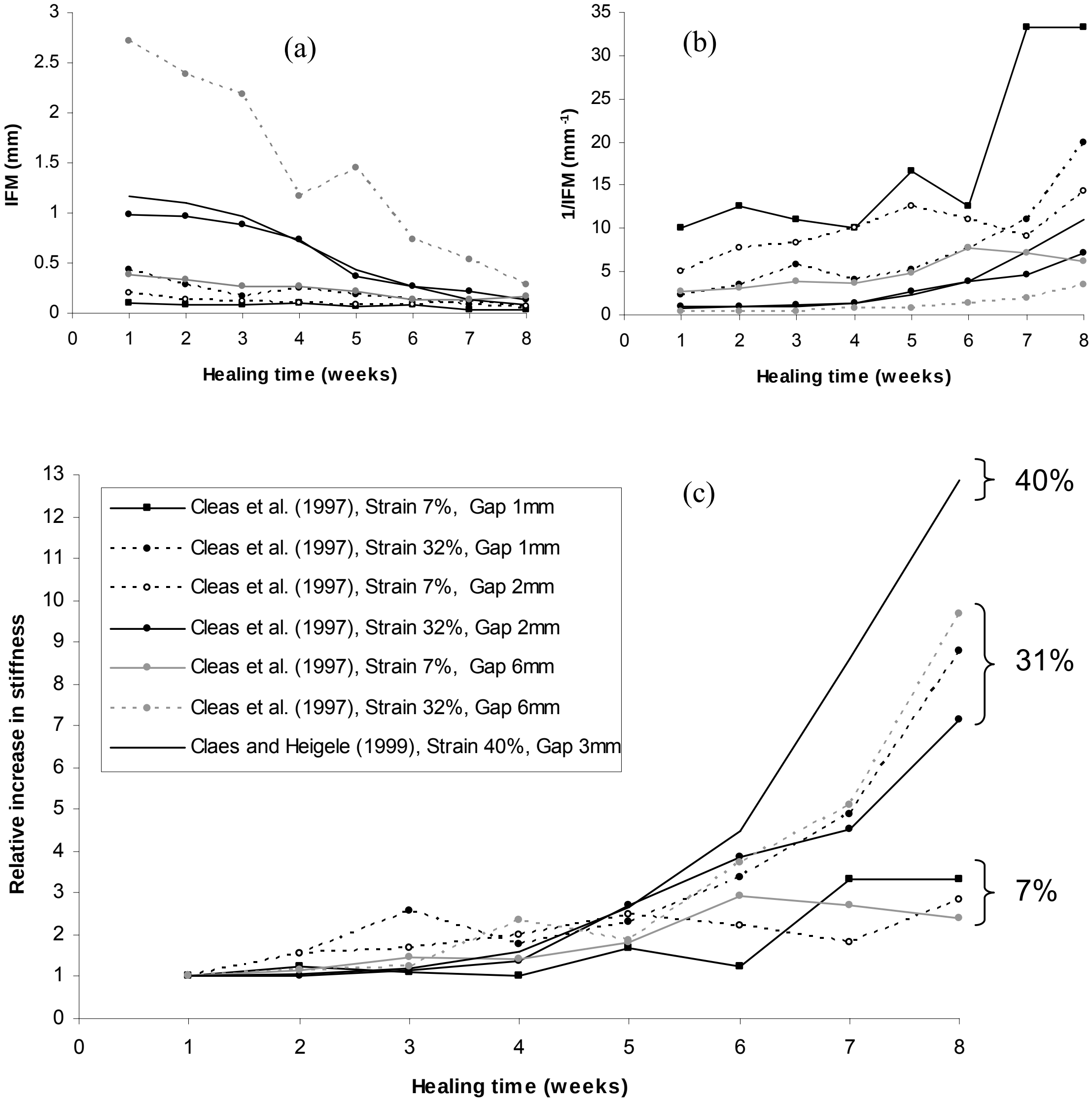

Figure 3.1. (a) Temporal evolution in IFM, (b) inverted IFM and (c) the relative increase in stiffness. The influence of strain on the relative increase in callus stiffness is clearly seen (adapted from Claes and coworkers, 1997, 1999).

$$t-value=\frac{\bar{x}-\bar{y}}{\sqrt{\frac{{s_x}^2}{n}+\frac{{s_y}^2}{n}}} \tag{3.3}$$

$$DoF = 2n-2 \tag{3.4}$$

The degree of freedom (DoF) and the *t*-value were then calculated (Eqs. 3.3-3.4), the *t*-distribution was then consulted to determine the *p*-value. Statistical significance was set at $p < 0.05$, thus anything greater than this was considered not significant (NS).

3.2.4 Derivation of a mathematical expression

Based on the relationship shown above, it was possible to generate a mathematical model which describes the strain-stiffness relationship. Firstly, a concise two-parameter mathematical expression, with only one coefficient, *a*, and one exponent, *m*, was chosen as a general expression to fit with the experimental data (Eq. 3.5). With this general expression, the values of coefficient and exponent were derived to correspond with each IFS case using curve fitting software (LAB FIT) (Eqs. 3.6-3.8) (Fig. 3.2).

General expression: $$f(t) = a\left(t^{m} - 1\right) + 1 \quad (3.5)$$

IFS = 7%: $$f(t) = 0.13\left(t^{1.3} - 1\right) + 1 \quad (3.6)$$

IFS = 31%: $$f(t) = 0.0041\left(t^{3.6} - 1\right) + 1 \quad (3.7)$$

IFS = 40%: $$f(t) = 0.0013\left(t^{4.4} - 1\right) + 1 \quad (3.8)$$

The three functions shown above (Eqs. 36-3.8) account for specific interfragmentary strains, however, a unified expression that accounts for the intermediary strains was required. Therefore, it was necessary to find expressions that describes the relationship between IFS and the coefficient, *a*, and exponent, *m*. Consequently, *a*, and, *m*, were individually plotted against IFS (ε_{IF}) so that a relationship between these datum points could be achieved using a trend line with a high correlation coefficient ($R^2 \approx 1$).

The relationship between the coefficient, *a*, and ε_{IF} was found to be non linear (Fig. 3.4a). This nonlinearity was moved into a linear domain by transformation of the model formulation into a logarithmic scale/formula. Thus, the relationship with coefficient, *a*, and ε_{IF}, was linearized (Fig. 3.3b). A linear trend line was then fitted between the datum points (Fig. 3.3b), to provide a succinct expression for the coefficient, *a* (Eq. 3.9). The exponent, *m*, was found to have a linear relationship with the ε_{IF} (Fig. 3.4). This linear trend line provided an expression for the exponent, *m*, as a function of ε_{IF} (Eq. 3.10).

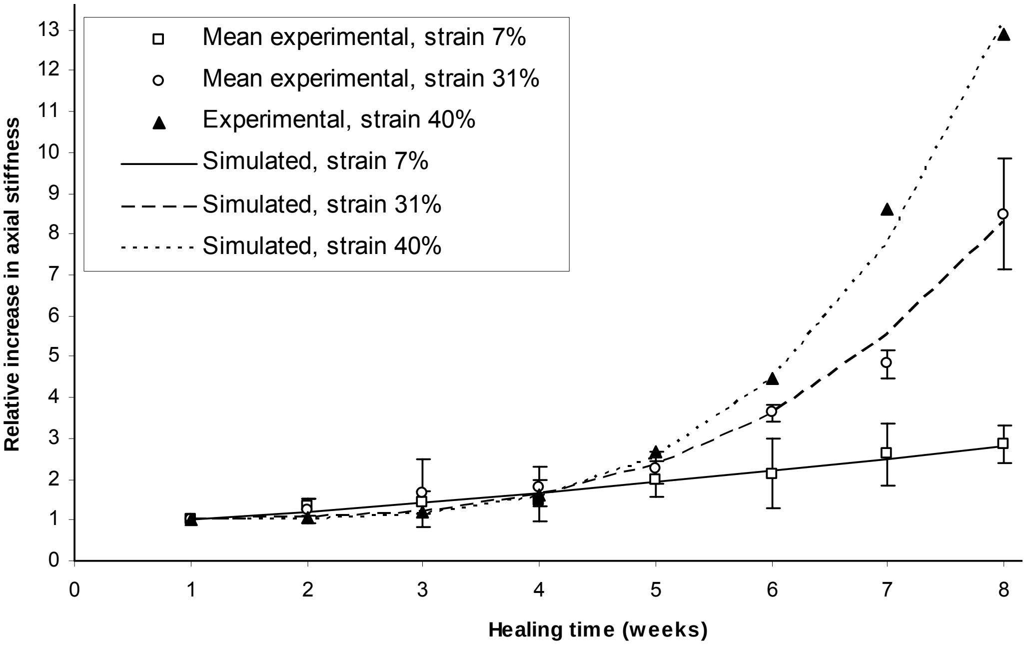

Figure 3.2. Simulated model using equations 3.6-3.8 fit with averaged experimental findings (adapted from Claes and coworkers, 1997, 1999).

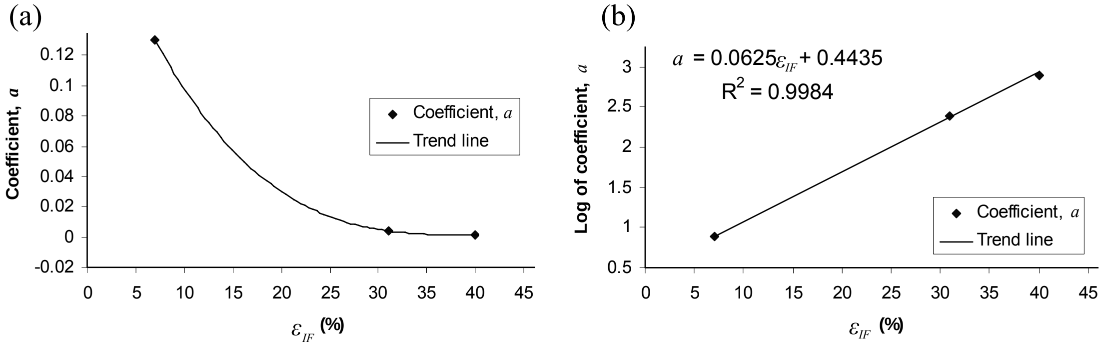

Figure 3.3. (a) Relationship between percentage of ε_{IF} and coefficient, a, and (b) linearized transformation.

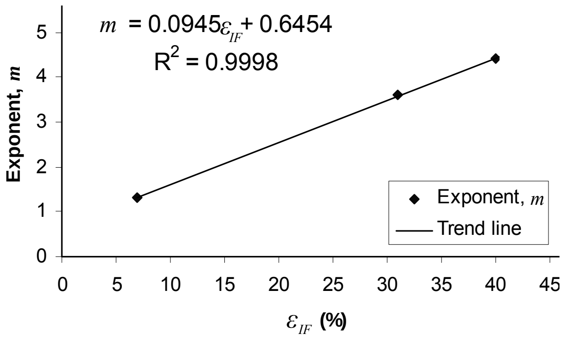

Figure 3.4. Relationship between percentage of ε_{IF} *and exponent, m.*

$$a = 10^{-(0.0625\varepsilon_{IF}+0.4435)} \tag{3.9}$$

$$m = 0.0945\varepsilon_{IF} + 0.645 \tag{3.10}$$

The above expressions could then be substituted into the general expression (Eq. 3.5) that relates time (t) and IFS (ε_{IF}), thus

$$f(\varepsilon_{IF}, t) = \left(10^{-0.0625\varepsilon_{IF}-0.4435}\right)\left(t^{0.0945\varepsilon_{IF}+0.645} - 1\right) + 1 \tag{3.11}$$

3.2.5 Verification of mathematical model

The proposed mathematical model was created based on the experimental findings of Claes and coworkers (1997, 1999), however, to ensure that the model and hypothesis is acceptable, further comparisons of the mathematical model (Eq. 3.11) were made with other experimental findings *i.e.* the remainder of studies shown in table 3.1. The rates of healing in these cases were re-processed into a relative increase in stiffness according to equations 3.1-3.2 and compared with the mathematical expression (Eq. 3.11).

To determine congruency on a quantitative level, the mathematical model was compared with the experimental datum points for each IFS case by calculating the average relative error (AvRE) using equation 3.12.

In some of the cases the processed datum points showed scatter which would inevitably incur problems with error analysis. In these cases best-fit lines were set through the results using Excel. The datum points of these best-fit trend lines were then used to compare with the proposed mathematical model. In other cases, where data at certain time points were missing, extra datum points were interpolated.

$$\text{Average relative error} = \frac{1}{n}\sum_{i=1}^{n}\left[1 - \frac{\text{data measured}(i)}{\text{data calculated}(i)}\right] \tag{3.12}$$

Lastly, it should be noted that the grand mean of all the average errors was as calculated:

$$\text{Grand Mean } = \frac{1}{n}\sum_{i=1}^{n} AvRE \tag{3.13}$$

3.3 Computational modelling of callus formation

Following methods used in mechanobiology (van der Muelen and Huiskes, 2002) and structural evolutionary optimisation (Xie and Stephen, 1993), a mechano-regulated algorithm was proposed to predict the steady-state homeostatic formation of callus tissue for specific bone fractures and loading scenarios (Fig. 3.5). The algorithm was based on an iterative time-independent process of tissue maintenance and removal. Hence, a subtractive approach was proposed, where lowly strained tissue is removed from a large tissue domain while the highly strained areas are maintained. This is typically the premise of many structural optimization techniques and mechano-regulated models. As a result, the proposed algorithm combines aspects of mechanobiological and structural optimization.

The strains experienced by the granulation tissues within and around the interfragmentary space are a result of the compressive forces or motions between bone fragments. Calculating these strains or tissue deformations would be immensely difficult using hand calculations; hence the finite element method was employed to numerically calculate these strains in a discrete structure. The mechano-regulated algorithm begins by conducting a finite element analysis to calculate the compressive principal strains in the granulation tissue which dominates in early callus formation. Using a Critical Strain (CS) parameter, the tissue is either resorbed or maintained based on whether the strains fall above or below this parameter. The algorithm was iterated until eventually, no appreciable change in mass of material was removed, at which point the algorithm was assumed convergent (Weinans *et al.* 1992). Since the FE elements were either maintained or were rejected, the optimisation method therefore produced ‘0-1’ design. Hence, the material was removed from the structure and what remained was a voxel-based mesh with discontinuous surfaces.

3.3.1 Design domain

In vivo the initial immature callus tissue (A.K.A. granulation tissue or initial connective tissue) provides a domain through which ossification can occur by a process of cellular differentiation. It is known that the initial tissues, found approximately at week one, are sensitive to mechanical stimulus. It is conjectured in the present study that the strains experienced by these tissues will determine the spatial formation of the callus during the reparative phase of healing.

In the present study, this soft tissue domain was computationally modelled as a discrete domain comprised of finite elements which was generated around the fragments of a bone fracture. This domain was composed of highly compliant elements which represent granulation tissue which can undergo or experience large strains due to interfragmentary motions.

Importantly, the domain does not have any specific shape or does not give the algorithm any ‘clues’ as to where the callus tissue should be appropriately distributed. Thus no prior knowledge of the shape of the predicted callus formation is required. This was perhaps the most severe yet fairest assessment of the predictive power of the algorithm and compressive principal strain as a driving force for callus tissue distribution. Often a rectangular domain is specified in 2D structural optimization problems (Bendsøe and Sigmund, 2003; Huiskes *et al*., 2000; Xie and Stephen, 1993) but realistically any size or shape can be used.

3.3.2 Material behaviour

Callus tissues contain fluid and as a result these tissues often exhibit viscoelastic behaviour such as hysteresis/energy loss (Moukoko *et al*., 2007; Moorcroft *et al*., 2001; Leong and Morgan, 2008) and stress relaxation (Loboa *et al*., 2004). If, however, continuous cyclical loading and unloading is applied to biological soft tissues, then a repeatable ‘pseudoelastic’ response can be observed after 3-10 cycles (Humfrey and Delance, 2004). This is known as the pre-conditioning effect, and is common in soft tissues due to the presence of fluid in the porous solid matrix. For example, it has been shown that hysteresis can be removed from arterial tissue after only 3-5 cycles (Fung, 1993). Although this has never been studied in early callus tissues *per se*, it is intuitive that the tissue will also experience some preconditioning response due to the viscous nature of the tissue.

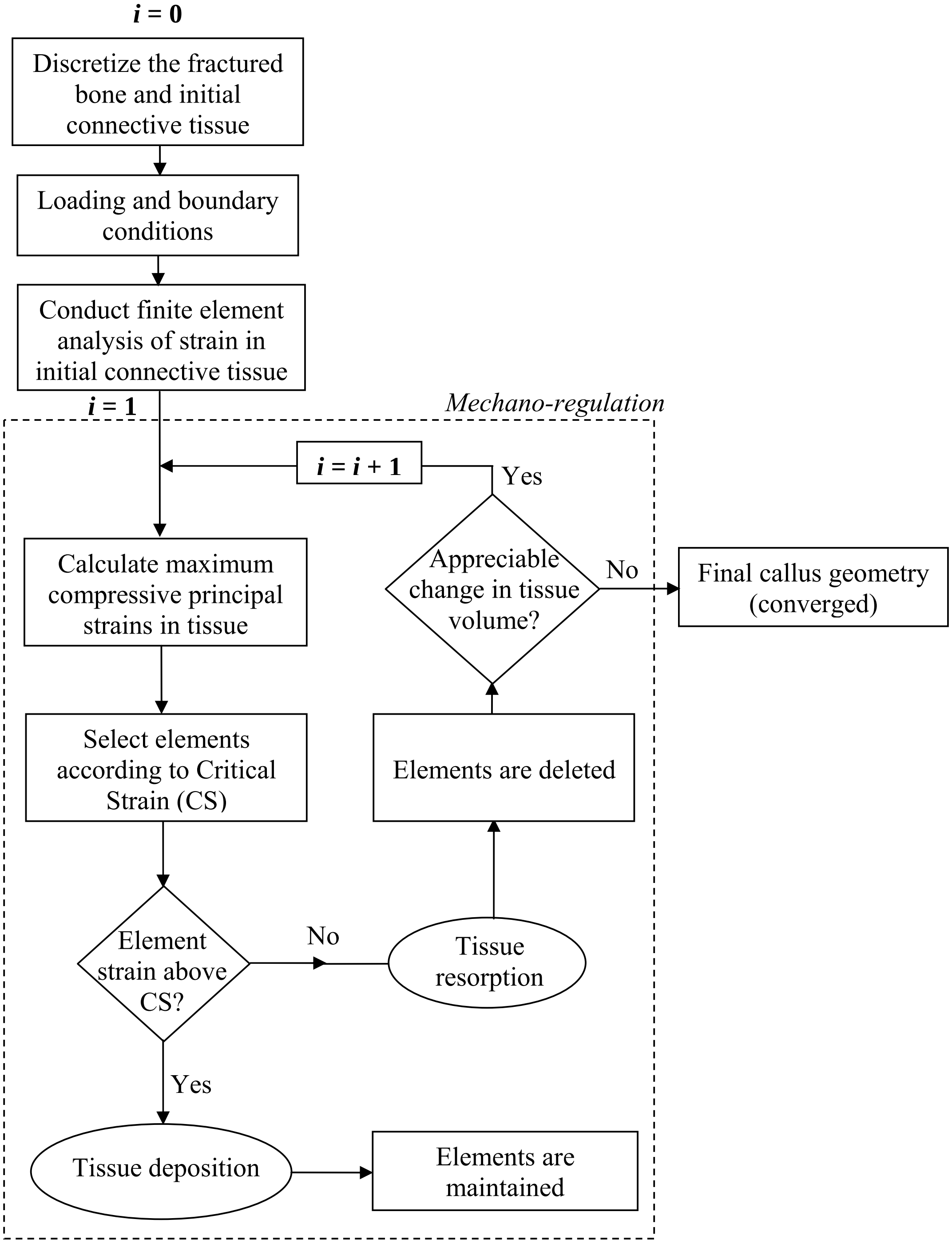

Figure 3.5. Algorithm for the mechano-regulated process of callus formation.

According to Humfrey and Delance (2004), pseudoelasticity is often exploited not only due to the simplicity of its mathematical description but also because it appears to be more physiologic due to the periodic loading experienced by many soft tissues. As a result, it was assumed in the present study that the granulation tissue behaved as a pseudoelastic material. Furthermore, callus tissue is compliant in the early stages of healing, and undergoes large strains, where the force-displacement relationship is linear up until the point of tensile failure (Christel *et al.*, 1981; Moukoko *et al.*, 2007). For this reason it was fitting that the callus tissue was assumed to behave as a solid elastic material (Boccaccio *et al.*, 2006; Carter *et al.*, 1988; Lacroix and Prendergast, 2002b; Loboa *et al.*, 2005). Also, due to the large strains that the immature callus tissues are capable of undergoing, the finite strain method was utilized (Cheal *et al.*, 1991). In the present study, this was implemented in FE code by assuming large displacements and deformations, where essentially the callus tissue material behaviour acted as a hyperelastic material with a linear relationship between stress and strain. To model the compliant behaviour of the granulation tissue, a Young's modulus of E = 1MPa (Leong and Morgan, 2008) and a Poisson's ratio of v = 0.17 (Lacroix, 2001) were assigned[1].

It was also assumed that the initial callus tissue behaved as a homogeneous and isotropic material (Ament and Hofer, 2000; Lacroix and Prendergast, 2002a-b; Loboa *et al.*, 2001). This assumption was based on histological examinations which show that granulation tissue is dominant in the early stages of healing and can be assumed homogeneous and isotropic in a finite element representation (Claes and Heigele, 1999). Moreover, recent experimental studies by Leong and Morgan (2008) showed there was good consistency of the material properties (Young's modulus) of granulation tissues (mean = 0.99MPa, SD = 0.2MPa), between differing locations in the same callus, even 35 days post fracture when the callus tissues becomes highly heterogeneous.

With regards to the modelling of cortical bone in the finite element model, it was assumed that these hard tissues behaved as an isotropic homogenous material. It should be noted that cortical bone is highly anisotropic and inhomogeneous, nevertheless, during early stages of bone healing, loading is transferred to the compliant callus tissues and therefore, it is intuitive that the cortical bone will experience low strains in comparison to the immature callus tissues (Carter *et al.*, 1988). As a result the material behaviour of the cortical bone is of less relevance than the granulation tissue. It was therefore assumed that

---

[1] Actual value of E= 0.99MPa and v = 0.166, thus values were rounded.

the material behaviour of the FE cortical bone was liner-elastic and isotropic. This material model assumes that the stress in a body is always proportional to the strain (Hooke's law) and that the direction of loading does not affect this relationship (isotropy).

3.3.3 Loading

The callus experiences cyclic loading during daily exercises. It was assumed, however, that the peak magnitudes of the intermittently applied mechanical stimuli were the most important parameters of the tissue loading history at the initial stages of fracture healing (Carter *et al*., 1988). In the present study, due to the pseudoelastic material assumption, the tissue behaviour did not exhibit time-dependent properties. As a result, transient or cyclical loading would not have any effects on the simulated peak strains in the immature callus tissues in the present analyses. Accordingly, static loading was employed to simulate the peak strains in the FE model where it is hypothesized that these peak strain vectors predict the spatial formation of healing tissues. Furthermore, it was assumed that these peak strains were achieved through the intermittent motion of the bone fragments over a short period of time; approximately 0.5 seconds (Cleas and Heigele, 1999; Lacroix and Prendergast, 2002a). Importantly, Loboa *et al*. (2004) observed from experiments in callus distraction osteogenesis that, during a step strain lasting 0.5 seconds, the tissue responds in a linear fashion after which the tissue exhibits a non-linear stress relaxation response. Based on this, Laboa *et al*. (2005) justified the use of material linearity and static loading in a FE model of immature callus tissue. Hence, in the present study, the effects of time-dependent material behaviour such as viscoelastic effects were not considered pertinent for the purposes of this study, due to the assumption of pseudoelasticity and that peak loading initiates tissue differentiation.

3.3.4 Critical Strain and the Elimination Coefficient

It is known that the majority of the peak strains are to be found in the inter-cortical gap (Carter *et al*., 1988). In the present study, it is conjectured that the lower strain vectors in the surrounding granulation tissue are expected to define the spatial distribution of the callus. Due to the assumption of solid pseudoelastic finite strain tissue behaviour in the present study, a greater magnitude of interfragmentary motion would result in a proportionally larger strain intensity field, and would therefore predict a proportionally larger callus size. In a finite element representation, the problem of strain proportionality can be eliminated by using a normalized strain ratio quantity. This is akin to the *Rejection Ratio* proposed by Xie and Stephen (1993) for 'Evolutionary Structural Optimisation' (ESO). In the present study, however, a percentage of the maximum magnitude of compressive principal strain intensity was used to define the average callus shape (and size) in any given model regardless of level of intercortical strain.

The 3rd principal strain happened to calculate the compressive principal strains, which had the greatest magnitude in comparison to the 1st (radial) and 2nd (circumferential) principal strains (see Appendix B). A Critical Strain (CS) value was calculated by a percentage of the maximum 3rd principal strain ($\varepsilon_{3,max}$) experienced by the tissue domain under peak loading. The percentage or threshold value itself is referred to as the Elimination Coefficient, *e*, which was used to calculate the Critical Strain thus:

$$Critical\ Strain = e\varepsilon_{3,max} \tag{3.14}$$

Therefore, the maximum magnitude of compressive principal strain was obtained from the finite element analyses and was multiplied by the Elimination Coefficient to give a Critical Strain value, where *e* can range between 0 and 1. Hence, a high Elimination Coefficient ($e \leq 1$) will predict a small callus formation localized to the areas of peak strains, whereas a low coefficient ($e > 0$) will predict a large callus based on the lower strains in the surrounding tissues.

The benefit of this was that unlike the 'Topology Homogenization Method' (Bendsøe and Sigmund, 2003), where the final size of an optimised material is based on the size of the design domain, in the proposed method the size of the domain does not influence the size of the callus. Hence, in the proposed method the size of the distributed material relies only on the Elimination Coefficient. A further benefit was that, unlike classic ESO, fewer iterations were required to reach the 'optimal' design. To this end, in any given simulation or case, the algorithm essentially produces the same volume of tissue regardless the magnitude of loading applied and fracture gap size or in other words the magnitude of calculated strain.

3.3.5 Solution procedure

The finite element models presented in this study were generated, solved and post-processed using ANSYS Multiphysics v10, an advanced commercial finite element analysis software package. In certain loading scenarios where the strains and displacements were large; non-linearities in the numerical solution were accounted for by using an incremental solution strategy.

It was intended that the mechano-regulated algorithm was to be employed without any interference or modification of the parameters. Consequently, the algorithm should predict the form of a callus for different fracture geometries and loading conditions without any manipulation. This approach will allow a more rigorous assessment of the predictive power of the proposed methods and will determine how robust the algorithm and Elimination Coefficient parameter is. To this end, a batch file was used to implement the algorithm in the finite element simulations.

The initial iteration of the algorithm proceeds with a finite element analysis of the fracture model under applied loading. The initial maximum compressive principal strains were then collected for an element solution and stored in a table. The greatest magnitude of strain was determined and the Critical Strain was calculated base on the decided Elimination Coefficient parameter. Next, any elements that experienced less than the Critical Strain were selected, counted and subsequently deleted. On the contrary, any elements that experienced strains greater than the Critical Strain were maintained. To actually delete elements from the model, the geometric and the finite element models were detached.

The solution was considered to be convergent if the total mass was convergent (Weinans *et al*., 1992). Consequently, if the volume of material (elements) marked for deletion (V_E) fell below a certain percentage of the previous iteration, then it was considered that no appreciable change in tissue volume (mass) was found and thus the algorithm was convergent. In the present study, if $V_E \geq 10\%$, then the solution was not convergent and further iterations were applied. In this instance, the FE model with the remaining elements were re-loaded and the strain in those elements which experienced less than Critical Strain were again selected, counted and subsequently deleted. The iterative process was continued until convergence was reached ($V_E \leq 10\%$). Although, it should be noted that the number of elements deleted depends on the mesh density, thus the value of V_E is up to the user's discretion.

3.4 Implementation in idealised fractures

The first step in the FE modelling procedure was the idealisation and simplification of the problem. Assumptions were made to simplify the geometry, material behaviour, and loading so that the mechano-regulated algorithm could be implemented in a computational finite element model. The investigation began by approximating/predicting the formation of callus tissue around type-A fractures in long bones (Fig. 3.6). It should be noted that these fractures are uni-planar, that is, there are only two bone fragments which share the same fracture plane. These fracture types were chosen due to their relative simplicity. This aspect of the study also allowed for the investigation of varying the gradient of inter-cortical strains for the analyses of asymmetric callus formation under unilateral fixation.

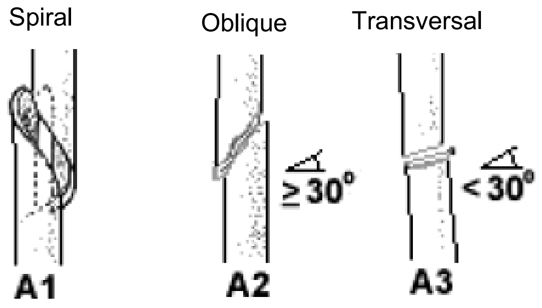

Figure 3.6. AO/ASIF categorization of type-A fractures in long bones (adapted from Müller et al., 1990).

3.4.1 Transversal fractures under compression, bending and torsion

The mechano-regulated algorithm was firstly tested in a perfectly transversal fracture under idealized loading scenarios; compression, bending and torsion. It should be noted that, i*n vivo*, bones will experience a combination of these loading conditions, but in these initial analyses they were modelled individually.

FE modelling

The dimensions of the fracture, bone cortex and interfragmentary gap used in this case were based on the average geometry of ovine tibia as specified by Claes and Heigele (1999). In the present study, a cylindrical tissue domain was generated around the cortical bone geometry which was sufficiently large to allow callus formation of reasonable size (Fig. 3.7). Due to the asymmetry of loading, a full 3D model was generated. The model was meshed with 8-node 3D hexahedral (brick-shaped) elements. Mapped meshing was used to ensure high mesh quality and to control mesh density.

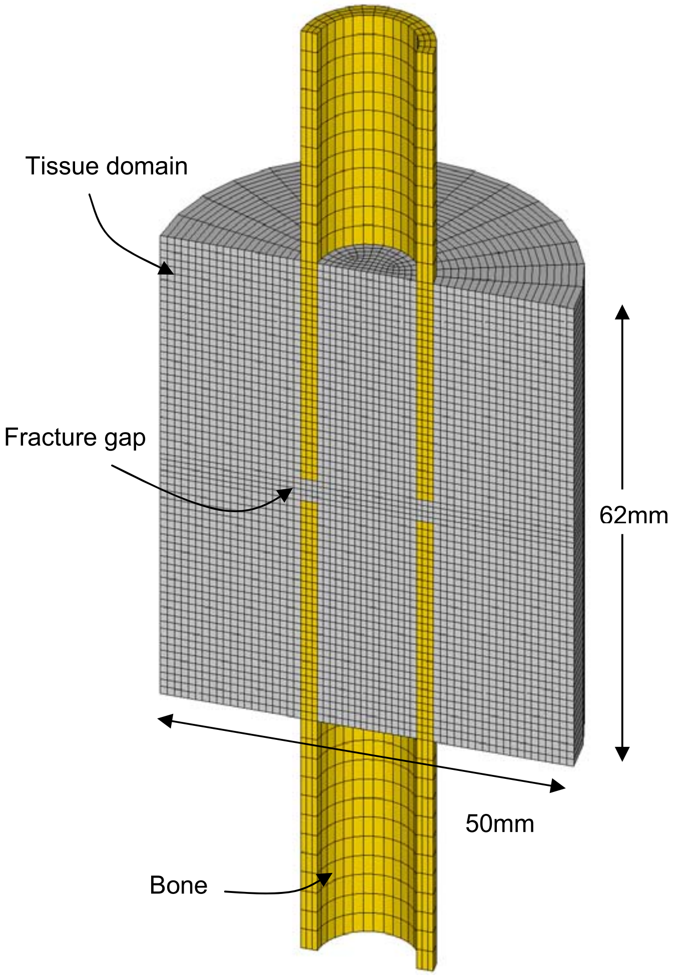

Figure 3.7. FE model of long-bone transversal fracture with cylindrical tissue domain.

Loading and constraints

Three loading scenarios were considered in this investigation. Firstly, a symmetric axial compressive load was applied by defining displacement constraints on the proximal cortex of the bone, while constraining the distal end face in all DoF (Fig. 3.8a). An arbitrary maximum displacement of 0.1mm was applied, which allowed for the assumption of linear-elasticity. The effects of a bending load was investigated by imparting two equal yet opposing displacements of on the periphery of the bone fracture which would then induce compression and tension on either side of the fracture gap (Fig. 3.8b). It should be noted that half-symmetry boundary conditions were exploited in the compression and bending scenarios.

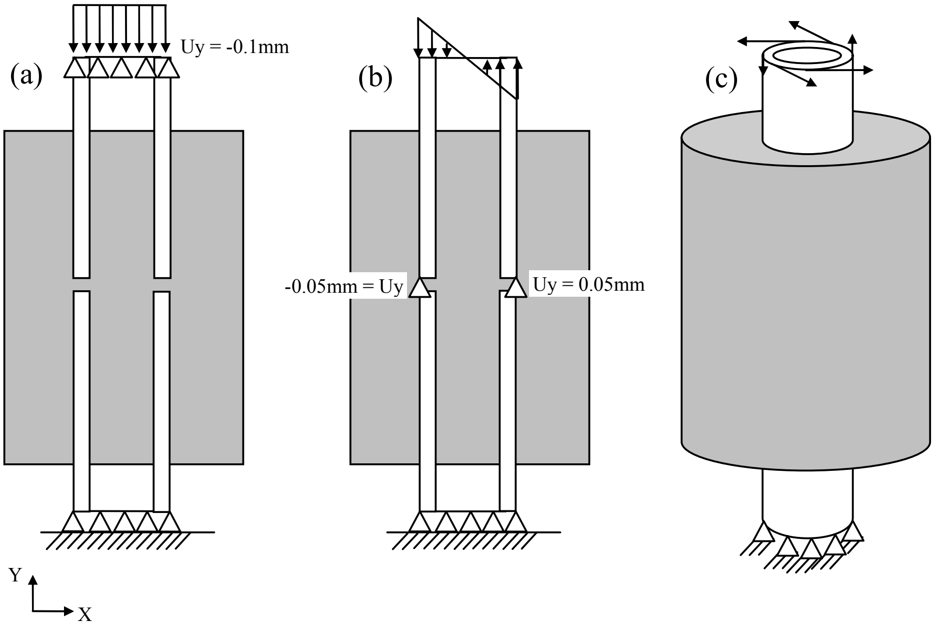

Figure 3.8. Schema of loading of the bone and tissue domain. (a) Symmetric loading with displacement constraints on the upper cortex. (b) Asymmetric loading with two opposing displacement constraints on the periphery of the bone surface representing a bending moment. (c) Application of torsion loading. Note, the arrows represent an idealization of the intended loaded profile.

Torsional loading was simulated by firstly rotating the nodes on the periphery of the proximal end-face of the bone model into a nodal cylindrical coordinate system, loads were then applied to these nodes to induce a rotational force (Fig. 3.8c). A maximum torque of 0.32Nm was arbitrarily applied to the model which was calculated as

$$T = nFr \tag{3.15}$$

where n is the number of nodes on the periphery, F is the force (N) applied at each node and r is the outer radius (m) of the tube (bone). Finally, symmetry boundary conditions in this scenario could not be exploited, thus the full FE model was solved.

3.4.2 Transversal fractures under unilateral fixation

The ability of the proposed algorithm to capture/predict the formation of callus tissue under unilateral internal and external fixation was investigated. The literature review has revealed many experimental studies and clinical observations that have illustrated the influence of a unilateral fixation on bone healing. According to these experimental findings, if one side of a cortical gap were to experience greater strain, then the callus would be larger on that side.

It is conjectured in the present study, that the distance of the implant to the bone affects the inter-cortical strain gradient and thus the distribution of callus tissue. It is contended that a lower strain gradient will produce a less asymmetric callus and *vice versa*. Theoretically, an internal fixator, which is located closer to the bone, should induce a more severe inter-cortical strain gradient than the external fixator which is located further from the bone, as discussed in Section 1.3. It was decided that the internal locking plate fixation method was modelled to determine how the presence a unilateral fixator affects the inter-cortical strain gradient and thus the formation of callus tissue. The locking plate fixator was specifically chosen as it acts as an internal/external fixator, where the locking screws and plate act in a similar manner as the pins and side bar of an external fixator, respectively (see Appendix A). Thus, a sensitivity analysis was conducted by altering the plate-bone distance between 2-60mm in 10mm increments from 10-60mm. Consequently, this required the generation of a full 3D FE models of the bone and implant.

FE modelling of unilateral fixation

The geometry of the unilateral locking plate fixator was loosely based on the Smith & Nephew 10 hole locking plate (Fig. 3.9), the dimensions of which were measured directly from the implant (see Appendix C for further details). As is the case in any finite element model, a number of simplifications were made to solve the numerical problem. With regards to the plate implant; the underside curvature of the locking plate model and ridges were neglected in the FE model and therefore the plate was assumed to be perfectly flat. Also, the staggered screw holes were perfectly aligned. The screw threads were neglected and hence the geometry of the screw shaft was simplified into a solid cylinder (Ferguson *et al*., 1995; Stoffel *et al*., 2003). This assumption is made valid by the study by Chao *et al*. (2006) who showed that the relative importance of the threads in comparison to the root diameter shaft is not a significant factor in screw shaft bending stiffness. Also, the unoccupied screw holes in the implant were neglected as holes tend not to be present in the side bar of an external fixator.

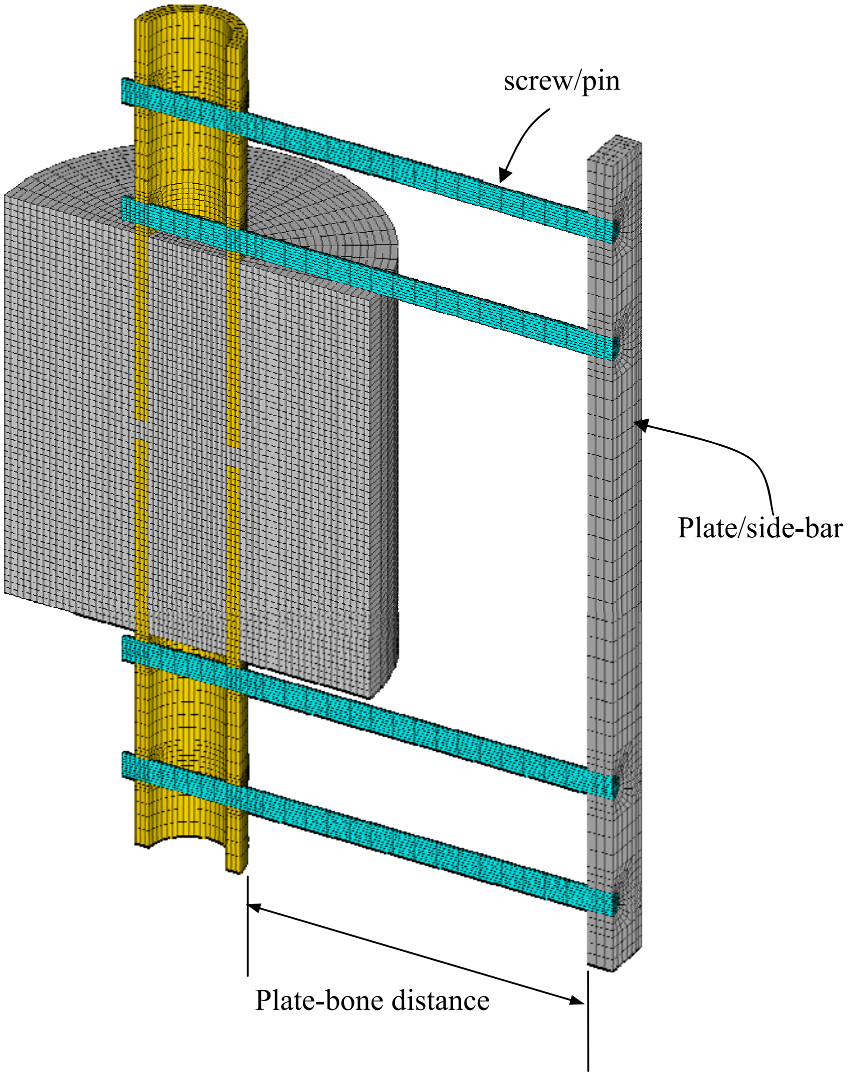

Figure 3.9. Sectional view of solid model of locking plate and bone system. Dimensions of implant given in Appendix C. Dimensions of bone based on Claes and Heigele (1999).

The screw heads were simplified to a solid cylinder, with a diameter of 7mm, which provided a perfect fit with screw holes in the plate model. It was further assumed that the screw shafts were directly bonded to the bone and plate by coincidental nodal contact (Ferguson *et al.*, 1995; Simon *et al.*, 1977; Stoffel *et al.*, 2003). Following from the minimally invasive concept, the locking plate was raised at least 2mm from the bone and therefore frictional contact was not defined between these components (Stoffel *et al.*, 2003). The plate and screws were modelled as 316L stainless steel (E = 190GPa, v = 0.3). A cylindrical tissue domain was modelled around the transversal fracture. The entire model was meshed with 3D 8-node hexahedral elements.

The culmination of the aforementioned assumptions and simplifications will inevitably lead to inaccuracies. In numerical modelling it is vital to know how these assumptions impact on the computational simulations. Consequently, an experimental verification process was undertaken to determine the percentage of error between the physical and numerical plate fixation models. For this, synthetic bone samples were used with actual locking plate fixation. To keep this chapter as short as possible, the details of the verification are given in Appendix C. Importantly, this verification study had revealed that there was a general error of 15.6% between the physical and numerical plate fixation models. Nevertheless, in the present sensitivity analysis, the absolute values of fixator stiffness were of less importance than its physical behavioral properties, which the FE model was capable of matching.

Loading and boundary conditions

One-half symmetry boundary conditions were exploited to reduce computational effort. It should be noted that although the elements of the locking plate and cylindrical tissue domain pass through one another, there was no physical contact defined between these components. In this case the cylindrical tissue domain allows the elements, even the ones within the plate to be chosen to form the final callus geometry. An arbitrary load of 100N was applied to a line of nodes of the proximal cortex of both model while displacement constraints were defined as illustrated below (Fig. 3.10). Large geometric displacements were accounted for using a non-linear solver.

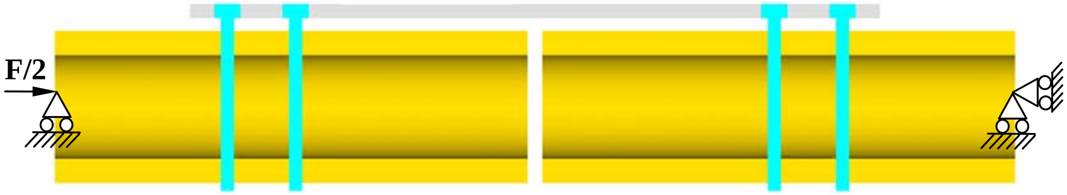

Figure 3.10. Axial loading boundary conditions applied to locking plate FE model.

3.4.3 Oblique fracture

The ability of the proposed mechano-regulated algorithm to capture/predict the shape of a callus in other fracture types was further investigated. The literature review explored the *in vivo* formation of callus tissue which showed asymmetry in oblique fractures, which is postulated to improve mechanical efficiency. The proposed algorithm was further tested by automatically predicting the distribution of callus tissue in an idealized oblique fracture.

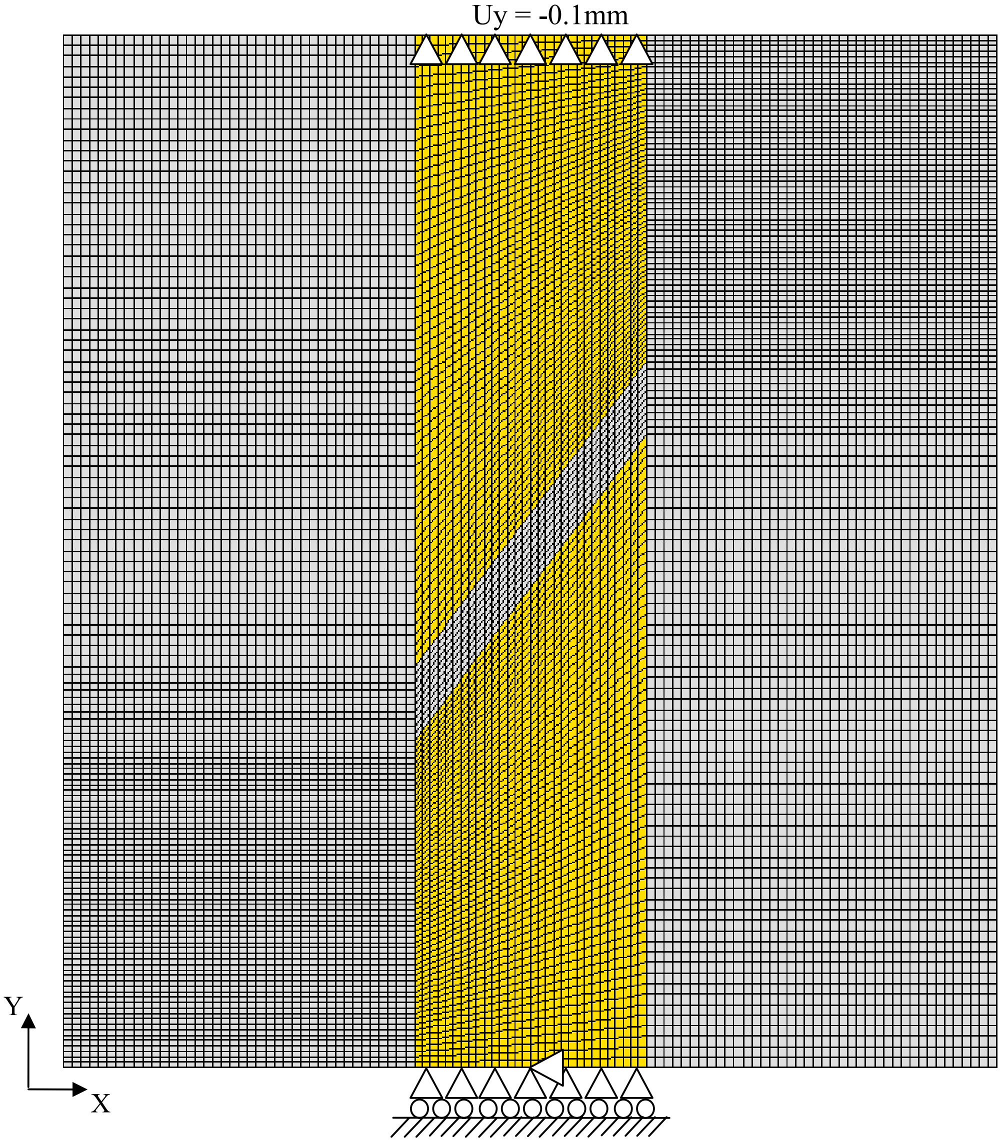

Figure 3.11. Finite element model of idealised oblique fracture (adapted from Loboa et al., 2001) with rectangular tissue domain (grey elements).

FE modelling

The oblique fracture modelled in the present analysis was based on the radiographic imagery from Urist *et al*. (1954), which was later idealized by Loboa *et al*. (2001) for other FE modelling purposes, not related to this study. In Loboa's idealisation, the medulla was not included hence it was not modelled in this case for later comparisons. Due to the asymmetry of the problem, symmetrical boundary conditions could not be utilized and hence the full 2D plane strain model was developed (Fig. 3.11). Loboa *et al*. did not specify the exact dimensions of the oblique fracture thus the model built in this study was replicated using the same scale of dimensions. The model contained 14300 elements and 43381 nodes using 4-node elements. The upper cortex was loaded with an arbitrary displacement of 0.1mm while the lower cortex was constrained in both degrees of freedom, which allowed for the assumption of linear-elasticity.

3.4.4 Spiral fracture

To verify the efficacy of the algorithm in more geometrically complex three dimensional models, a spiral fracture was developed. The FE model of the spiral fracture itself was not based on any specific radiographic image or *in vivo* geometry, but was based on the general shape of a spiral fracture according to Alms (1961). The spiral is typically created from a torsional force which causes the maximum shear strain to be 45^{o} to the central axis. The proximal and distal aspects of the spiral fracture were connected by a linear fracture which detaches from tensile forces (Fig. 3.12a).

FE Modelling

The spiral was modelled using the mathematical formula for a helix in 3D space. The following three parametric equations in rectangular coordinates define a helix

$$x = \cos t\,,\ \ y = \sin t\,,\ \ z = t \tag{3.16}$$

As the parameter t increases, the point (x,y,z) traces a right-handed helix of pitch 2π (360^{o}) about the z-axis, in a right-handed coordinate system. The solid model was therefore created from this equation in a tubular geometry to represent the mid-shaft of a bone (Fig. 3.12a).

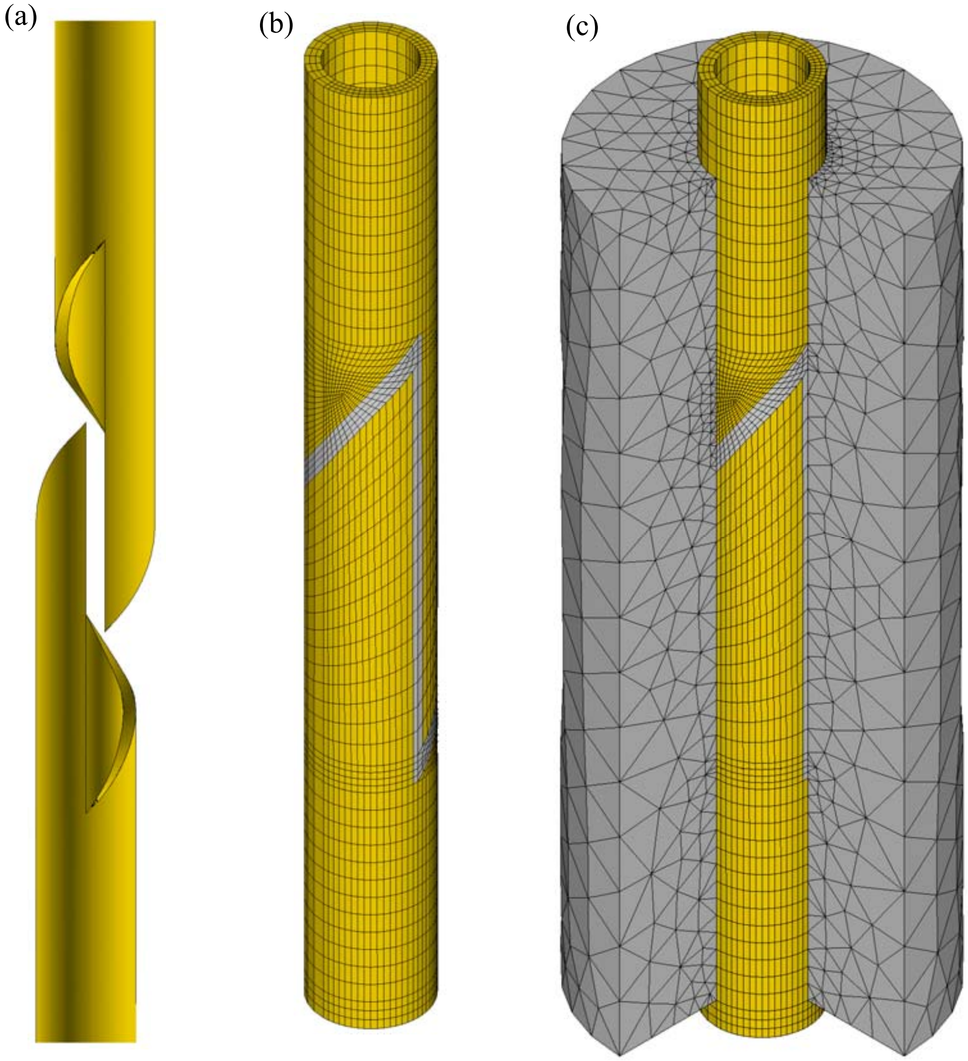

Figure 3.12. (a) Solid model of spiral fracture, (b) FE model of bone and spiral fracture, and (c) cylindrical tissue domain with section removed.

The FE model of a spiral fracture and tissue domain utilized both hexahedral and tetrahedral elements due to the relatively complex geometry of the fracture. The bone itself and the elements occupying the fracture gap were meshed with hexahedral elements (Fig. 3.12b), whereas, the tissue cylinder was composed of tetrahedral (pyramid-shaped) elements (Fig. 3.12c). The inner area of the cylinder was 'glued' to the fractured bone model, which meant that the tetrahedral elements would attempt to merge with the hexahedral elements by converting into square-based pyramids at the interface. These interface pyramids were created from degenerate hexahedral elements. The benefit of tetrahedral elements in this respect was that it was possible to refine the elements at a specified location in the mesh. The software allowed a level of elemental refinement from

1 to 5, where a value of 1 provides minimal refinement, and a value of 5 provides maximum refinement. When a level of 1 was specified, the resulting element edges in the refined region are approximately 1/2 the original edge lengths. In this study, a level of 1 was chosen, as refinement was carried out after each iteration, which would have provided a smooth enough final callus geometry. It should be noted that, unlike the tetrahedral elements, it was not possible for ANSYS to allow hexahedral elements to be refined. In this case, relatively course elements were used in the initial mesh and in the first iteration of the element removal process. Lastly, the model was constrained in all degrees of freedom on the distal cortex, whilst the upper cortex was arbitrarily loaded with displacement of 0.1mm to induce compression.

3.5 Implementation in case-specific fractures

The above simulations were intended to analyse and produce a somewhat idealised callus formation under a variety of idealized loads and fracture geometries. However, for the present study to truly predict or simulate nature, it was necessary to test the algorithm in less idealised bone healing situations. For that reason, it is proposed that the algorithm can capture callus formation in non-idealised case-specific scenarios where the loading magnitude and direction are more complex and realistic. The general technique of modelling the fractured bone was to use the existing radiographic images from the literature or directly from patient records. From this a series retrospective clinical case studies of lower limb fractures were modelled using the FE method. Importantly three of the four cases described here utilized unilateral locking plate fixation, which support biological healing by callus formation.

3.5.1 Case study 1- Oblique fracture of the tibia

Case study 1 presents an oblique fracture of the tibia in a male subject of 20 years of age who had sustained a closed, non-comminuted, oblique diaphyseal fracture of the left tibia. The fractured tibia was stabilized using an external fixator placed on the anterior-medial cortical surface of the bone (Fig. 3.13a). Furthermore, the external fixator was capable of measuring and recording the displacements and interfragmentary motions during healing. The geometry of this fracture was based directly on measurements taken from radiographic images found by Gardner *et al*. (2000, 2003, 2004) (Fig. 3.13b).

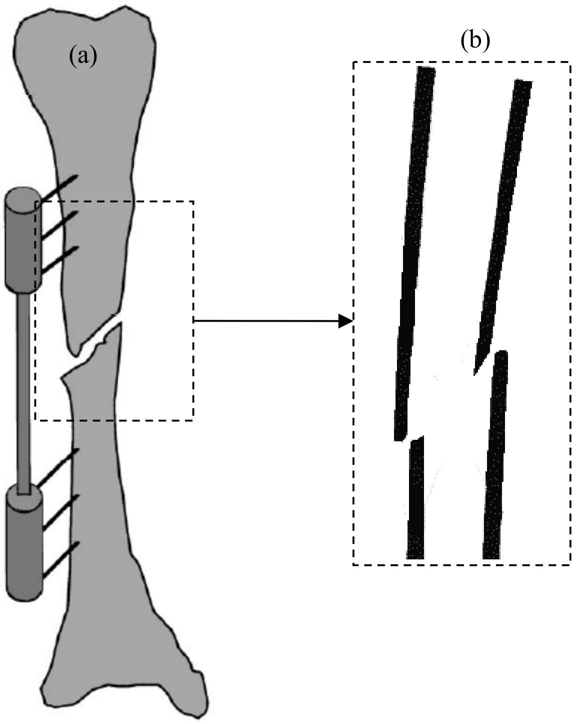

Figure 3.13. (a) Schema of the external fixator which was fixed to the anterio-medial cortical surface of the fractured tibia. (b) Coronal section of the fracture. Adapted from Gardner et al. (2000).

FE modelling

Using the existing data it was possible to replicate a 2D geometry of the bone fracture (Fig. 3.13b) and apply the constraints and displacements in a 2D plane strain FE model (Fig. 3.14). The fractured fragments were modelled based on the radiographic images, and although the actual dimensions were not known, the scale was equivalent. In the present study, the bone fragments were surrounded with a large area of granulation tissue which was meshed with 2D plane strain 4-node elements.

Loading and boundary conditions

A plane strain model was assumed as the three dimensional shape of the fracture or loading was unknown, hence the problem remained two dimensional. Importantly, a comparative two- and three-dimensional finite element analysis of the above oblique fracture had shown little difference between the stress and strain distributions on the mid-longitudinal plane (Mirishra and Gardner, 2001). The lower cortices were constrained in all degrees of freedom, whereas, the upper cortices were applied with displacement constraints to approximately replicate as the interfragmentary motions at the first week of healing (Ux = 0.283mm, Uy = -0.377mm) as described by Gardner *et al.*, (2003).

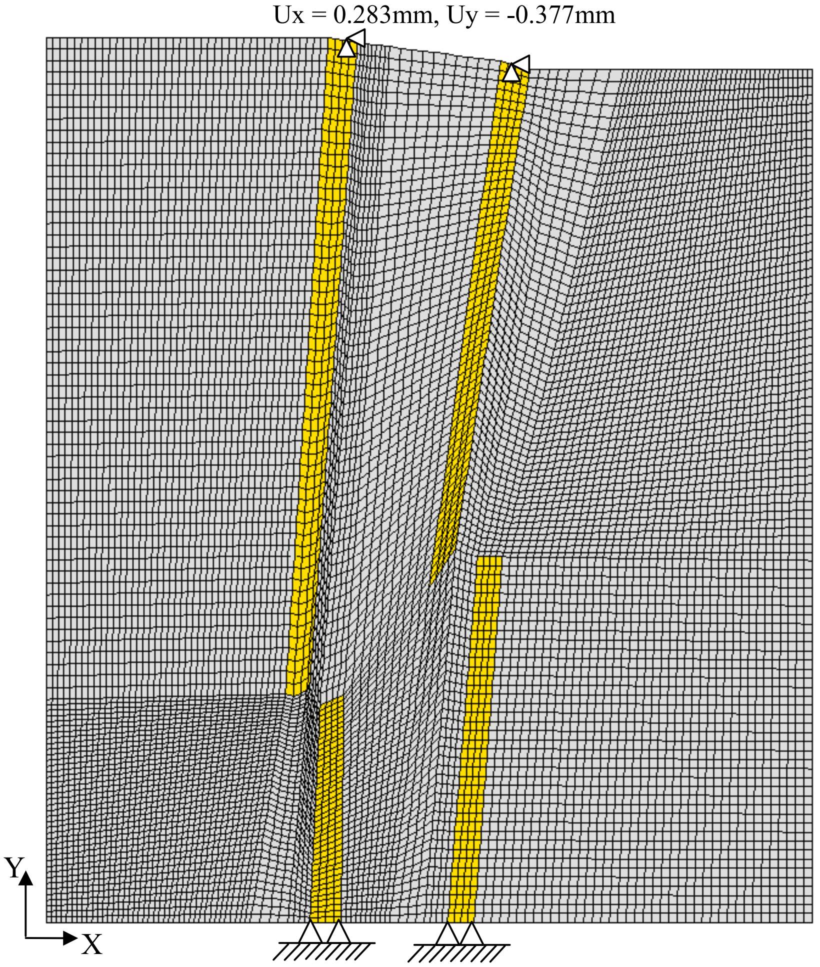

Figure 3.14. FE model of oblique tibial fracture 14 weeks post op (adapted from Gardner et al. 2000, 2003, 2004) with tissue domain (grey coloured elements).

3.5.2 Case study 2 –Transversal fracture of the tibia

Case study 2 presents a diaphyseal transversal fracture of the tibia (AO-42-A3) with an associated fracture of the fibula (Williams and Schenk, 2008) (Fig. 3.15a). This was a closed fracture where the skin was unbroken. An 11-hole stainless steel locking plate (Synthes) was used to stabilize the fracture. In total four screws were used, two on the proximal and distal fragments, respectively. The screws were located at the furthest distance from the fracture gap thus providing the greatest possible working length (Fig. 3.15b).

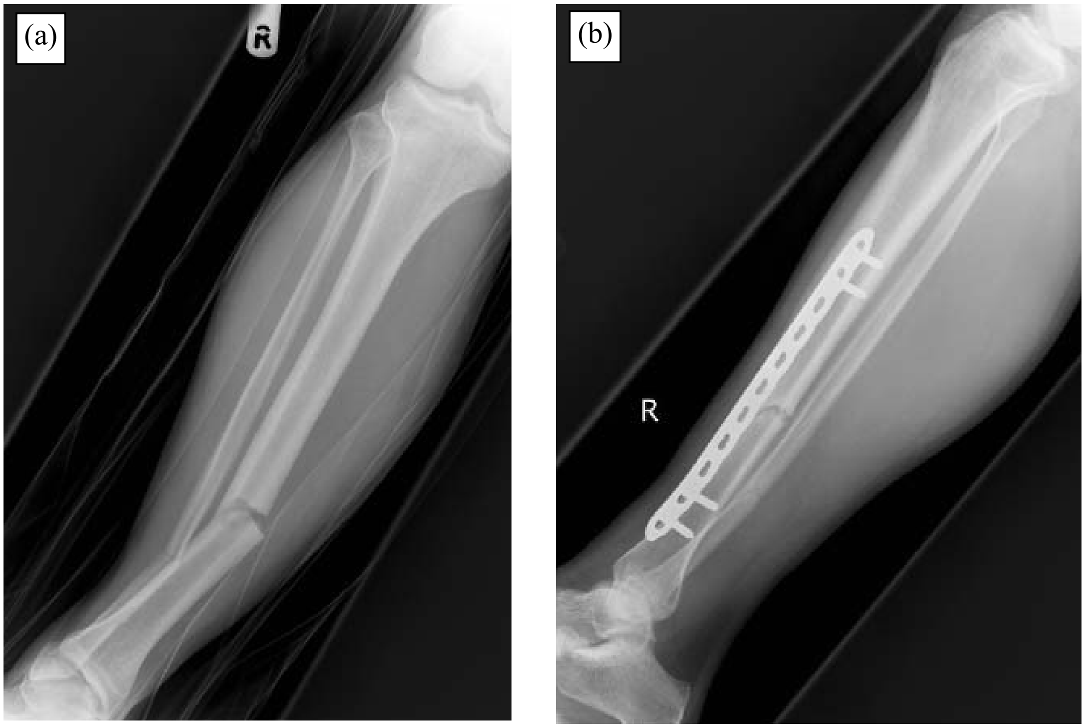

Figure 3.15. (a) Type AO-42-A3fracture of the tibia and (b) immediately post-op with locking plate fixation (courtesy of Mr Willem Schenk and Mr Timothy Williams).

FE modelling of a 3D tibia

The tibia, transversal fracture and locking plate implant were modelled using the finite element method. Due to the fracture of the fibula, it was assumed that it would have provided no additional mechanical support hence it was not modelled (Duda *et al*., 2002; Lacroix and Prendergast, 2002b). Furthermore, due to the load-bearing mechanics of the callus and implant, it was assumed that the cancellous bone had no load-bearing capacity, and hence the mechanical contribution of the cancelllous bone was excluded from the FE model (Cheung *et al*. 2004; El-Shiekh, 2002; Shih *et al*. 2008). In many case-specific studies of intact bone (modelling of bone anatomy), the exact dimensions of the bones are sought so that the stresses/strains can be estimated as accurately as possible in three dimensions (Yosibash and Trabelsi, 2007). In the present study, however, where the bone is fractured, the majority of stresses and strains are experienced by the implant and the callus tissues, respectively. Thus the exact dimensions of the bone were not required.

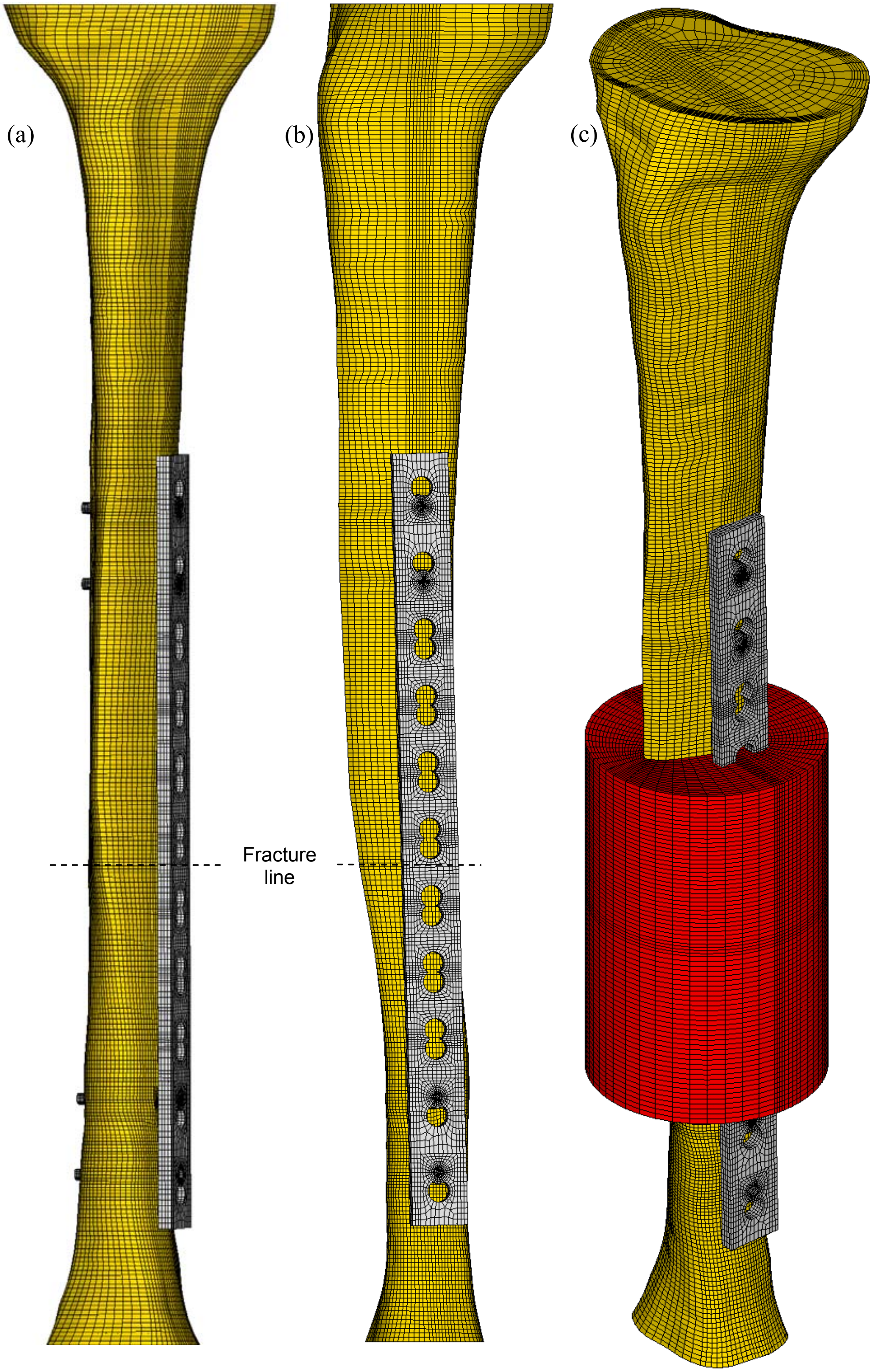

Figure 3.16. Three-dimensional tibia FE model with implant and fracture. (a) Anterior-posterero view, (b) medio-lateral view, (c) implant with cylindrical tissue domain.

Furthermore, in the present study, only 2D x-ray images from the mediolateral and/or anteroposterior views, were relied upon to replicate the geometry of the bone. Since the dimensions of the locking plate were known, it was therefore used as a point of reference so that the bone model could be scaled relative to the size of the implant.

The tibia model was based on the composite tibia (Sawbones) where the inner and outer contour profiles of the compact bone were digitized by Lacroix and Prendergast (2002b) by means of slicing and measuring the synthetic bone at 3mm intervals. In the present study, by using these keypoints, it was possible to regenerate a number transversal rings which captured the profile of the bone cortex at 3mm intervals, similar to a CT scan. Using the rescaled transversal rings, the areas and volumes could then be generated to the size and scale of the real bone and implant (Fig. 3.16a-b). A full cylindrical tissue domain was generated around a 1mm fractured which was assumed to be perfectly transversal (Fig. 3.16c). The model was meshed using 8-node hexahedral elements, where the minimum mesh density of the implant, and especially the screw holes, were found through convergence studies (see Appendix C).

3.5.3 Case study 3 – Fracture of the tibia with fragment misalignment

Case study 3 presents another transversal fracture of the tibia with an associated fracture of the fibula. Importantly, the difference between this case and the previous was that the fragments were not aligned (Fig. 3.17a-b). The surgeon in question used a 10-hole stainless steel locking plate (Synthes). In total 6 screws were used, 3 on each side of the fracture. This case led to non-union 6 months post-op and hence the surgeon removed the inner most screws to dynamize the fracture and allow further interfragmentary motions. This proved successful and the bone went on to unite after another 6 months.

FE modelling of fracture tibia

This model was generated in a similar manner as outlined in Case study 2 above. The main exception was that a 10-hole plate was used with the distal fragment at a 4 degree angle relative the proximal fragment (Fig. 3.18). A 2mm fracture gap was modeled which was assumed to be perfectly transversal. The FE model shown below contains four screws, which corresponds to the configuration that led to bone union. The model was meshed with 8-node hexahedral elements.

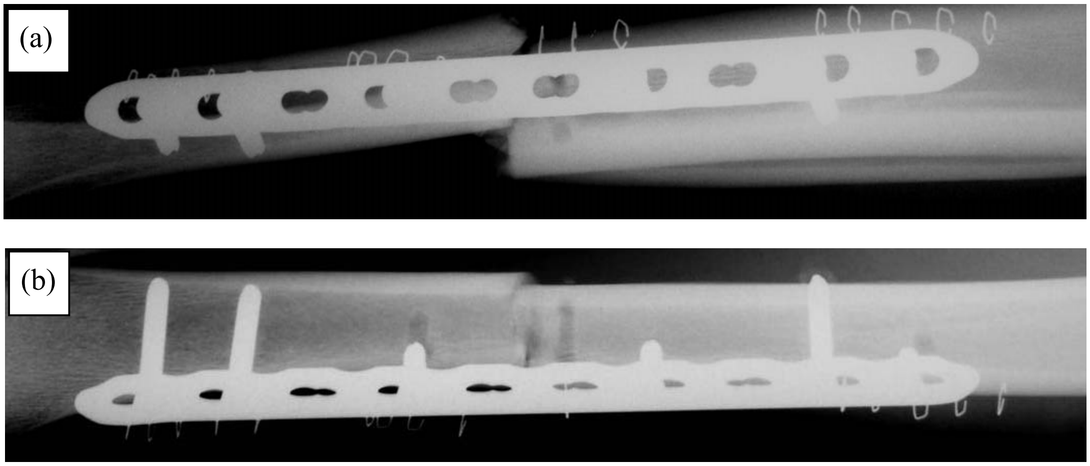

Figure 3.17. Transversal fracture of the tibia stabilised with locking plate with fragments not aligned. (a) Medio-lateral view showing reduction with misalignment and (b) anterior-posterior view. Courtesy of Dr Nassiri and Mr David Cogley.

Loading and boundary conditions

Physiological-like loading of tibia models (Case studies 2-3) was simulated by including muscle and joint contact loads as specified by Duda *et al*. (2001, 2002) for a patient weighing 80kg (Table 3.2 and Fig. 3.19). The locations of the muscle and ligament attachment data, force magnitudes and orientations were scaled to the tibial models in the present study. The model was constrained by fixing three nodes on the distal end of the bone to prevent rigid body motions (Heller *et al*., 1999).

The loading applied to the tibiae represented an instant in gait with maximum muscle activity and high joint contact loading (45% of the whole gait cycle). It should be noted, however, that patients will tend to restrict loading on an injured limb (Koval *et al*., 1998). Thus, in the present FE representation, only 10% of the loading specified by Duda *et al*. was applied to the models, which also corresponds to the FE studies by Byrne, (2008).

Figure 3.19. Physiological-like loading the vectors represent all muscle and joint contact forces (adapted from Duda et al., 2002).

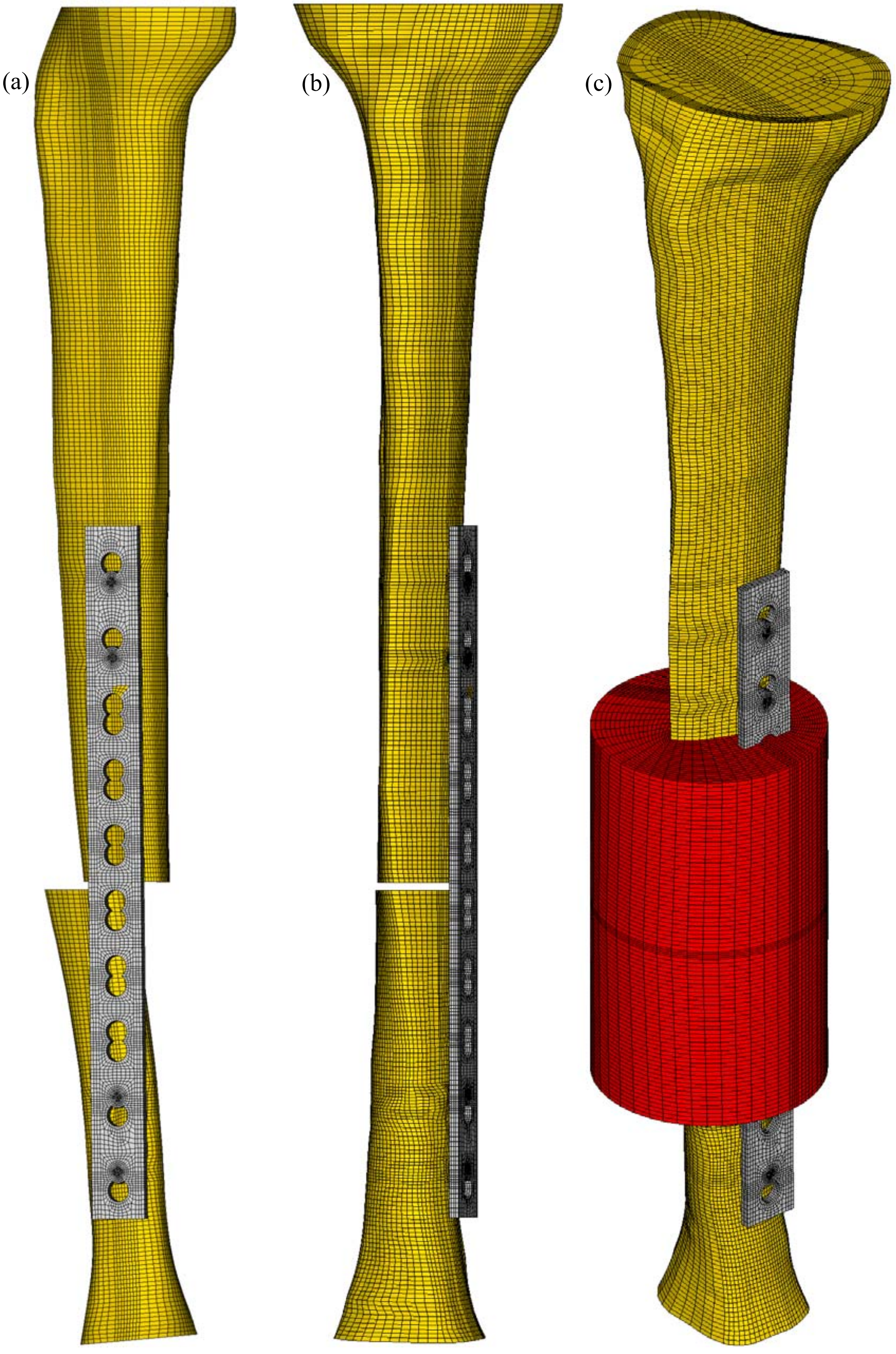

Figure 3.18. Three-dimensional tibia FE model with implant and fracture. (a)anterior-posterero view, (b) medio-lateral view, (c) implant with cylindrical tissue domain.

Table 3.2. Forces and attachment co-ordinates applied to the tibia models (Duda *et al*., 2001, 2002).

Forces	Force (N)			Attachment (mm)		
	X	Y	Z	X	Y	Z
Iliotibial tract I	-8.5	-8.8	61.3	-19.8	39.1	369.9
Iliotobial tract II	-97.4	-64.4	291.5	-27.1	28.2	370.5
Quadraceps femoris m.	13.6	-32.8	303.5	34.8	19.3	353.4
Tibalis anterior m. I	17.2	38.7	-327.7	-4.9	9.9	251.8
Tibialis anterior m. II	25.9	53.6	-191.8	-7.6	9.9	127.9
Soleus m.	-63.1	-47.1	-697	-7.4	15	332.2
Ant. tibiofibular lig.	-132.4	-111.2	-56.8	-7.3	11.1	0.9
Ant. cruciate lig.	87.5	101.5	41.1	10.3	-5	390.5
Deltoid lig.	44.9	9.7	15.7	-1.5	-16.5	-0.3
Knee	232.3	214.9	-1525.1	1.5	-2	388.2
Ankle	-120	-154.4	2070.4	0.8	0.6	0.4

3.5.4 Case study 4 – Spiral fracture of the femur

Case study 4 presents a femoral spiral fracture in an elderly lady (Fig. 3.20a). The fragments were realigned and a 20-hole stainless steel femoral locking plate (Smith & Nephew) was used to stabilize the fracture (Fig. 3.20b). Four screws were used on the proximal fragment while 5 screws were used on the distal fragment (nine in total) where the most proximal screw was mono-cortical.

FE modelling of a 3D femur

The solid femur model was adapted from the 'Standardized Femur' (Viceconti *et al*., 1996). The standardized femur was based on the geometry of the 'composite femur' which was designed as an analogue to mimic the mechanical behaviour of a human femur (Cristofolini *et al*. 1996). The CAD femur model consisted of areas to represent the outer and inner surface of the cortical shell.

The complex topology of the CAD model did not allow Boolean operations to be performed on it and therefore, the model was converted into a number of 2D cross sectional splines (El-Shiekh, 2002; Scannell and Prendergast, 2005). Using these splines, the solid model was rebuilt so that cross sectional segments could be created between the slices which were easier to manipulate, thus allowing the inclusion of the locking implant model. The rebuilt solid model was then divided appropriately to allow mapped meshing techniques to be utilised (Figs. 3.21b-c). The spiral fracture was created in the femur (Fig.

3.21a) as described earlier in Section 3.4.4, with a cylindrical tissue domain generated around the fracture itself (Fig. 3.22).

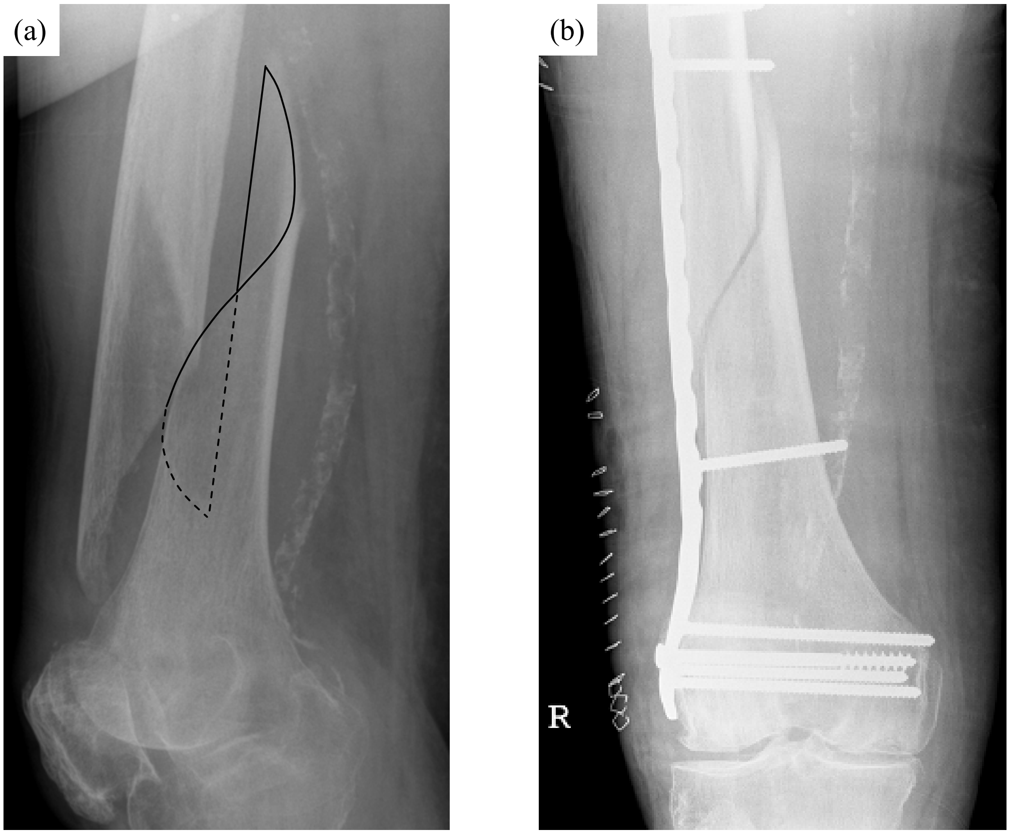

Figure 3.20. (a) Spiral fracture in femur and (b) anterior-postereo view locking plate fixation. Courtesy of Dr Nassiri.

Loading and constraints

The femur was loaded to simulate physiological-like forces which included a joint contact force on the femoral head and an abductor muscle force (Fig. 3.23). The magnitude of the forces was calculated from the percentages of the subject's body weight, which replicates peak loading at the stance phase of gait (Bergmann *et al*., 1993) (Table 3.3), which has since been used in the FE modelling and loading of a femur (Radcliffe and Taylor, 2007). Knee contact was modelled at the distal end face using three nodal constraints to prevent rigid body motion (Speirs *et al*., 2007). In the present study, it was assumed that the subject weighed 154lbs (685N). To coincide with the previous case studies, it was also assumed that the subject will bear only 10% of their weight on the fixated femoral fracture post-op, as they tend to voluntarily limit their weight on the injured limb (Koval *et al*., 1998).

Figure 3.21. FE model of spiral fracture based on radiographic imagery. (a) Mediolateral view of spiral fracture with exaggerated separation, (b) lateromedial view of femur with locking implant and (c) anteroposterior view.

Figure 3.22. Isometric view of femur with cylindrical tissue domain.

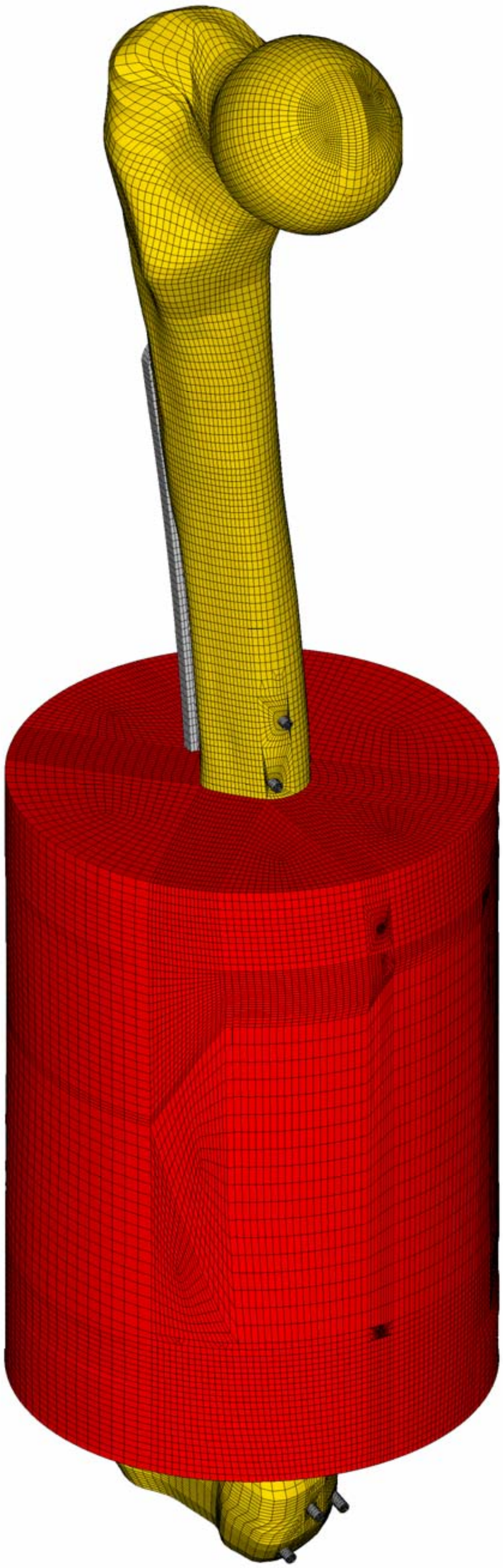

Table 3.3. Normal walking load forces as % of body weight (Bergmann *et al.*, 1993)

	Hip Contact Force	Abductor Force
X axis	-54.0	58.0
Y axis	32.8	-4.3
Z axis	229.2	-89.5
Total Magnitude	238	-104

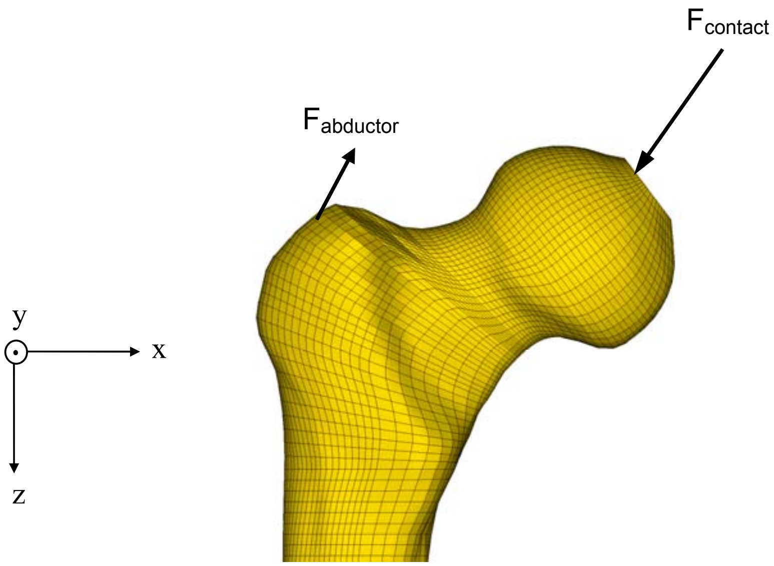

Figure 3.23. Physiological-like loading and constraints on femoral FE model.

3.6 Summary

Methodologies were presented as means to predict or model the rate and spatial formation of bone healing. The hypotheses of this study were tested in idealised bone fractures and less-idealised clinical cases studies. The modelling methods and assumptions applied to these models were outlined in this chapter. The next chapter will analyse the findings of the proposed models and methods.

Chapter 4 - Results

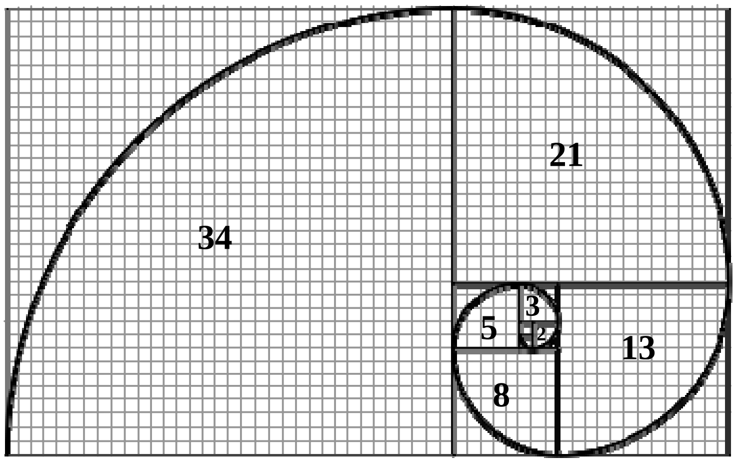

Modelling Nature:
Fibonacci sequence used to mathematically describe the spiral of a nautilus shell using squares of sizes.

Contents

4.1 Introduction

It was hypothesized that there was a cause-and-effect relationship between the magnitude of interfragmentary strain and the rate of bone healing which could be modelled mathematically. To determine the strength of this argument, the proposed mathematical model was compared against further experimental studies using statistical and error analyses. Based on these findings, it was possible to quantify the correlation between mechanical stimulus and the rate of bone healing.

It was also hypothesized in the present study that the compressive principal strains are the dominant driving force behind the efficient formation of healing bone tissues. Furthermore, it was also contended that the proximity of a unilateral fixator to the bone influenced the formation at callus tissues. The findings of the computational modelling of the formation of callus tissue are presented. This includes an analysis of the strain contours and vector plots of the callus tissue under various loading scenarios. The iterative process of the algorithm to produce *in silico* callus formations is also presented and analysed.

4.2 Relationship between rate of healing and IFS

This section analyses the influence of mechanical stimulus (IFS) on the rate of bone healing. The initial observation, as described in Chapter 2, showed that there is a positive correlation between IFS and rate of healing, as quantified by a relative increase in callus stiffness (see Fig. 2.10). This initial observation, however, was based on the data collected by Claes and coworkers (1997, 1999), and was therefore strengthened by further comparisons with other experimental studies found in the literature (see Table 3.1).

4.2.1 Statistical analysis

A statistical analysis was undertaken to determine whether the re-interpreted results of Claes *et al*. (1997) now showed a quantifiable significance between the rate of healing for an initial IFS of 7% or 31%. From this, it was found that there was no significant difference ($p > 0.05$) in the relative increase in stiffness between weeks one to five, whereas, at week 6 and after, there was a significant divergence between the rates of healing between both of the initial IFS cases ($p < 0.05$) (Fig. 4.1).

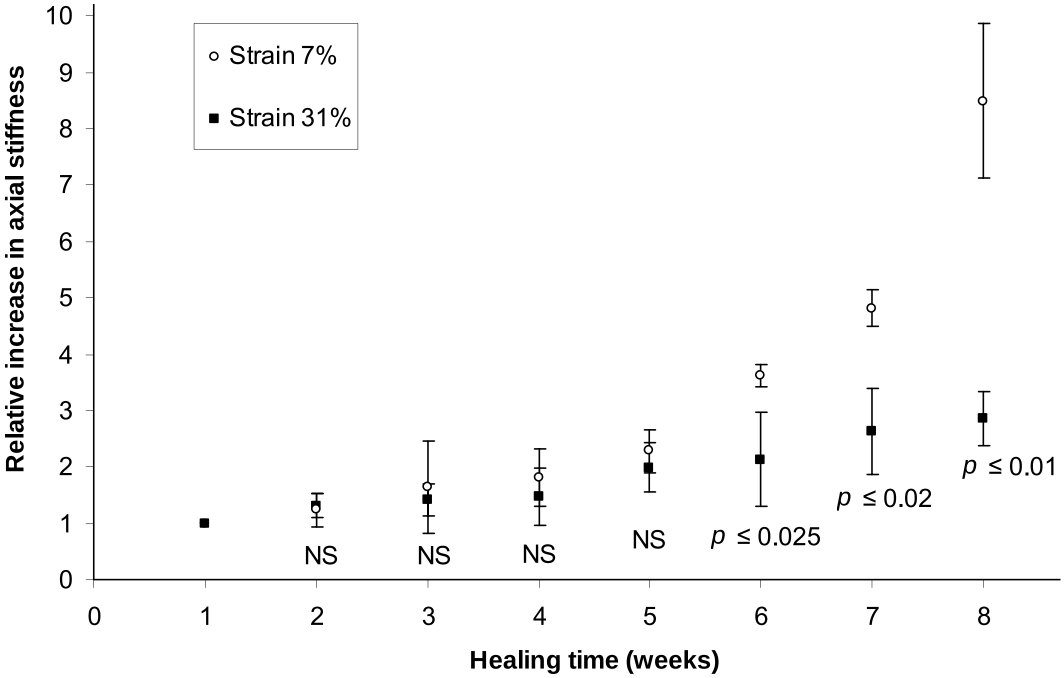

Figure 4.1. Statistical significance found between the 6th to 8th weeks of healing (adapted from Claes et al., 1997). Note, NS means 'not significant' (i.e. p>0.05).

4.2.2 Verification and analysis of the mathematical model

The proposed mathematical model was further compared with the remaining experimental studies found in the literature (Table 3.1). Thus, the interfragmentary strains used in the experimental studies were inputted into the mathematical function to simulate the relative increase in stiffness between weeks 1 to 8 (Fig. 4.2). It should be noted that the proposed mathematical model was based on three interfragmentary strain cases; 7%, 31% and 40% (Claes and coworkers, 1997, 1999), and as expected, the average relative error (AvRE) was low for these three cases; 4.9%, 10.8% and 7%, respectively (Figs. 4.2a, d & f). It should be noted that although the correlation was high ($R^2 \approx 1$) for these simulated rates of healing, error occurred due to deviation of the simulated and scattered experimental datum points at each week of healing.

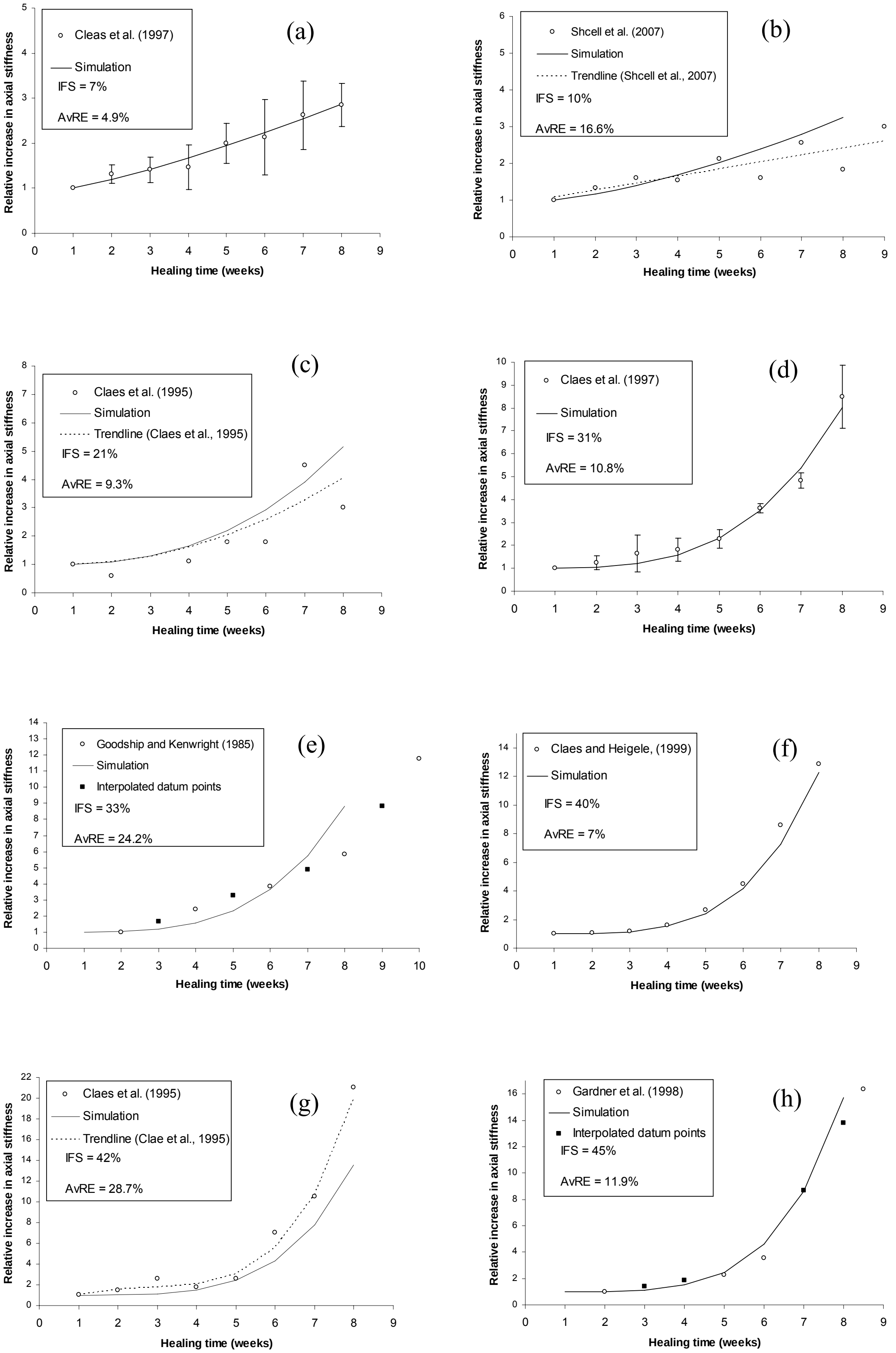

Figure 4.2. Relative increase in simulated and experimental stiffness (adapted from Claes and coworkers, 1995, 1997, 1999; Gardner et al., 1998; Goodship and Kenwright, 1985; Schell et al., 2008).

Importantly, the mathematical model was capable of capturing the rate of healing for intermediary interfragmentary strains; 10%, 21% and 33% with good agreement, where the average relative error ranged between 16.6%, 9.3% and 24.2%, respectively (Figs. 4.2b-c, e). The largest recorded error was 24.2% for the 33% interfragmentary strain case (Fig. 4.2e) which was attributed to the fact that Goodship and Kenwrigth (1985) recorded a linear increase in stiffness between weeks 2-8. Naturally, this will cause error to accumulate between the simulated (non-linear) approximation and the (linear) experimental data. Interestingly, it should be noted that Goodship and Kenwright did record an inflection or increase from week eight onwards which qualitatively agrees with the simulated increase in stiffness for this specific strain case.

More importantly, the proposed model could account for interfragmentary strains that were outside of the range that the mathematical model was based on; 42% and 45% and again showing good agreement with an average relative error of 28.7% and 11.9%, respectively (Figs. 4.2g-h). The large error for the 42% strain was due to the high relative increase in stiffness adapted from Claes *et al*. (1995) at week 8. Nevertheless, the simulated rate of healing qualitatively corresponds to the experimental rate of healing which appears to increase in an exponential fashion. Lastly, it should be noted that the grand mean of all the average errors was 14.2%.

4.2.3 Mathematical representation

The mathematical model was shown to have good agreement with IFS within the range of 7 – 45% and for an increase of stiffness between weeks 1 – 8. When the model was graphed for each IFS within the aforementioned range (Fig. 4.3), it was shown that at a low strain (ε_{IF} = 7%) there was an almost linear progression in the rate of healing. When the initial IFS was increased, (ε_{IF} > 7%) the rate of healing became increasingly non-linear and almost increases in an exponential fashion, especially towards the higher strains ($\varepsilon_{IF} \leq$ 45%). Also, it was found that a non-linear relationship existed between the initially applied IFS and the stiffness at week 8, which corresponded to the initial observation (see Fig. 2.10).

When the model was graphed in 2D for each IFS within the aforementioned range, it was evident that the simulated rate of healing, for all interfragmentary strains diverged after week six and onwards (Fig. 4.4). The statistical analysis shown previously confirms this, where a statistically significant difference ($p \leq 0.025$) after week six as was found for an initial IFS of 7% and 31% (Fig. 4.1). Finally, the proposed mathematical model suggests that there is a positive correlation between IFS and rate of callus stiffening. It should be noted that the computational studies discussed in chapter 2 have found, based on FE simulations, that there is a negative correlation between the initial IFS and the rate of stiffening (García-Aznar *et al.,* 2007; Lacroix and Prendergast*,* 2002a), which directly opposes the findings of the present study.

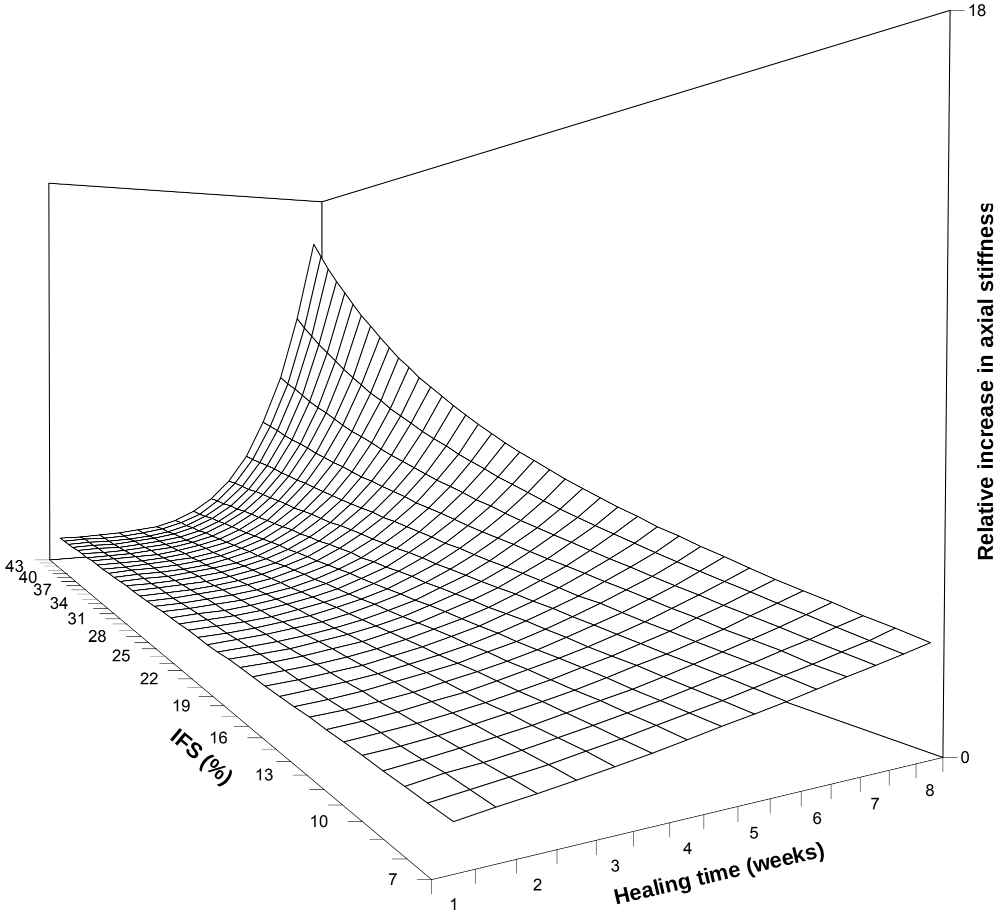

Figure 4.3. Area plot of relationship between IFS, healing time and relative increase in axial stiffness, calculated from the mathematical model (Eq. 3.11).

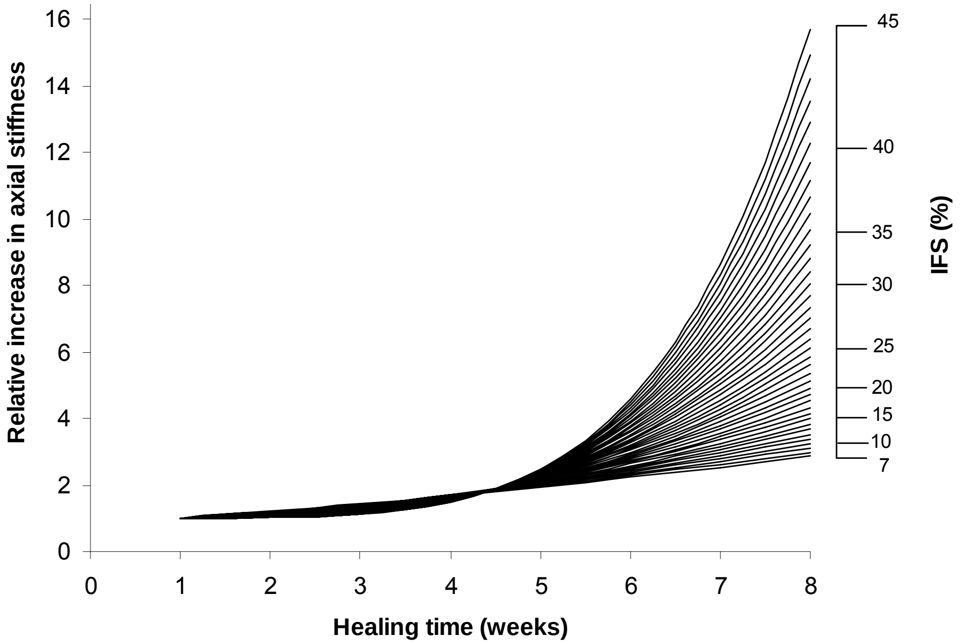

Figure 4.4. Relative increase in callus stiffness for a given IFS presented as 2D graph, calculated from the mathematical model (Eq. 3.11).

4.3 Analysis of *in silico* callus formation in idealized fractures

The influence of compressive principal strains on callus formation was investigated. An important aspect was to analyze how the strains were distributed in the immature tissue under the applied loading of the bone fragments. It was postulated that these strains within the tissue domain were responsible for the efficient formation of healing tissues. Thus, this section analyses the direction and intensity of compressive principal strains experienced by the tissue as calculated by the FE method for idealized fractures and loading scenarios. Using the proposed algorithm, it was intended that these strains and their direction will drive the efficient formation of the *in silico* callus tissue formation by iteratively removing lowly strained areas of tissue.

4.3.1 Transversal fracture – compressive loading

The FE results of the axially loaded (compression) transversal fracture are presented as both vector plots and as contour plots of the compressive principal strains within the tissue domain (Fig 4.5). The vector plot displays the direction and magnitude of the compressive principal strains (Fig. 4.5a), while the contour plots show the intensity of the strains where 100% corresponds to the greatest magnitude of principal strain and 0% corresponds the lowest magnitude of principal strain, which corresponds to the Elimination Coefficient, *e* (Fig. 4.5b).

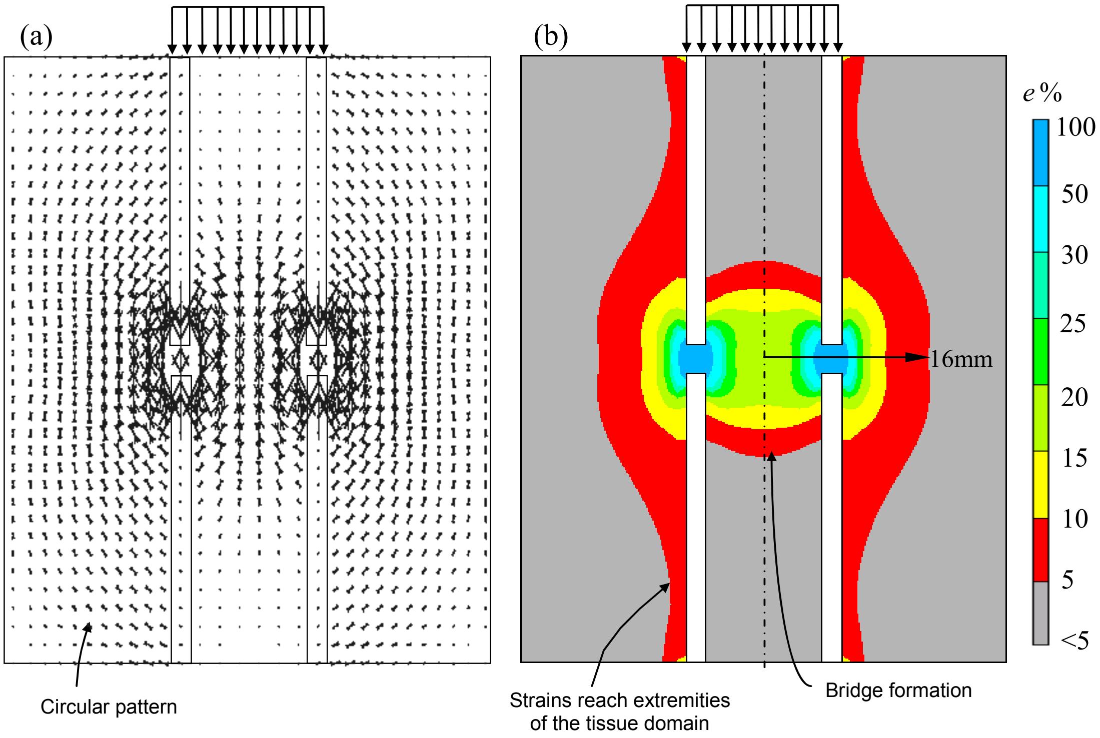

Figure 4.5. Compressive principal strains within a discrete FE structure under compression loading. (a) Vector field of principal strains (magnitude plot x3). The vectors show a circular pattern around the fracture. (b) Undeformed contour plot of principal strains presented as e%. A lower percentage of strain will produce a larger callus and vice versa. A 5% cut-off strain intensity would produce a radial extension of approximately 16mm.

It was found that the principal strain vectors freely follow a circular trajectory around the fracture line, while a similar yet limited pattern was also found within the medullary cavity (Fig. 4.5a). This also appears to correlate with what was found in the study by Carter *et al.* (1988) where the strain followed a circular trajectory about the fracture (see Fig. 2.11b). Also, one can observe based on the contour plot that the highest magnitude of strains (50-100%) were located within the interfragmentary space (Fig. 4.5b). The lower strained areas (<50%) were found adjacent to the inter-cortical gap. These lower strained areas produced contours adjacent to the fracture that followed a bulbous pattern while the strains within the medullary cavity produced a bridge-like pattern. What was most astonishing was their likeness to the general features of callus formations that have been observed *in vivo*, such as periosteal callus and endosteal bridge formations (*cf*. Fig. 2.2 & Fig. 4.5b). However, the strain contours do not show the same dip in the endosteal bridge as can be seen *in vivo*. Furthermore, the strain contour in the exterior domain reached axially towards the extremities of the domain.

Implementation of algorithm

The figure above (Fig. 4.5b) also represents how the Elimination Coefficient (presented as percentages) corresponds with the size of the approximated *in silico* callus formation, where it can be seen that there is an inverse relationship between the *e*% parameter and the size of the approximated *in silico* callus. An Elimination Coefficient of 0.05 (5%) produces a spatial distribution of strain that extends 16mm radially from the fracture site which corresponded directly to the average size observed from histological examinations (Claes and Heigele, 1999). Consequently, the *e*% was set to 5%, thus any elements that experienced strains less than 5% of the maximum magnitude of the compressive principal strains would be iteratively removed during the algorithmic process.

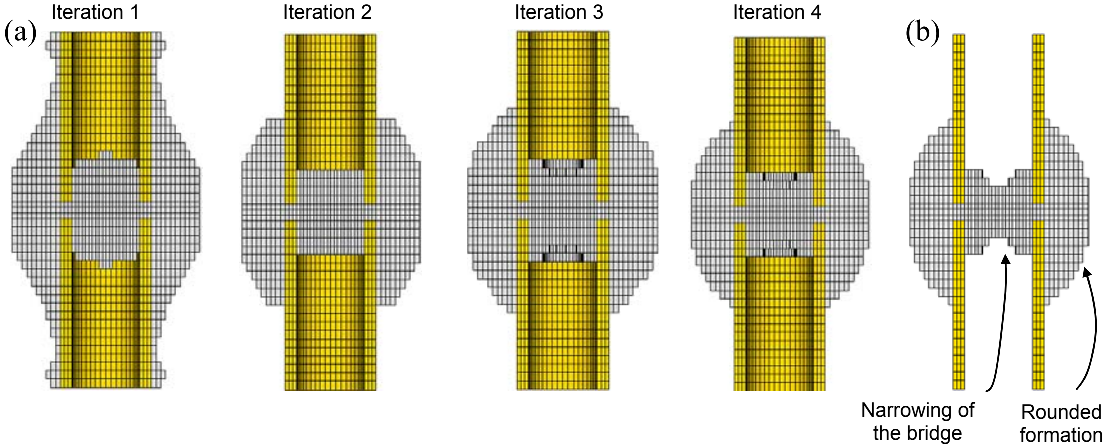

Figure 4.6. (a) Iterative removal of elements of a transversal fracture under compression loading and (b) longitudinal section of tissue domain from the final iteration. e = 0.05.

The first iteration of the algorithm removed a large amount of elements (Fig. 4.6a) leaving only those elements that experienced >5% of the maximum strain which left a pattern of elements equal to the initial strain field (*cf*. Fig. 4.5b). The second iteration had removed the elements that had extended axially to the extremity of the tissue domain. The third iteration removed the lowly strained elements within the medullary canal which produced a narrowing in the bridge. The fourth and final iteration refined the formation at which point the algorithm was convergent where any further iterations would have removed an inappreciable mass or volume of tissue (elements). The converged *in silico* callus formation showed a distribution of elements within the medulla where a bridge formation was found between the bone cortices with a dip in the centre (Fig. 4.6b). Also, adjacent to the fracture showed a rounded formation of elements.

4.3.2 Transversal fracture – torsion loading

The effects of torsional loading on the formation of *in silico* callus tissue were analysed. In this case the highest strains were located within the fracture gap (Fig. 4.7), as was also seen in the previous analysis.

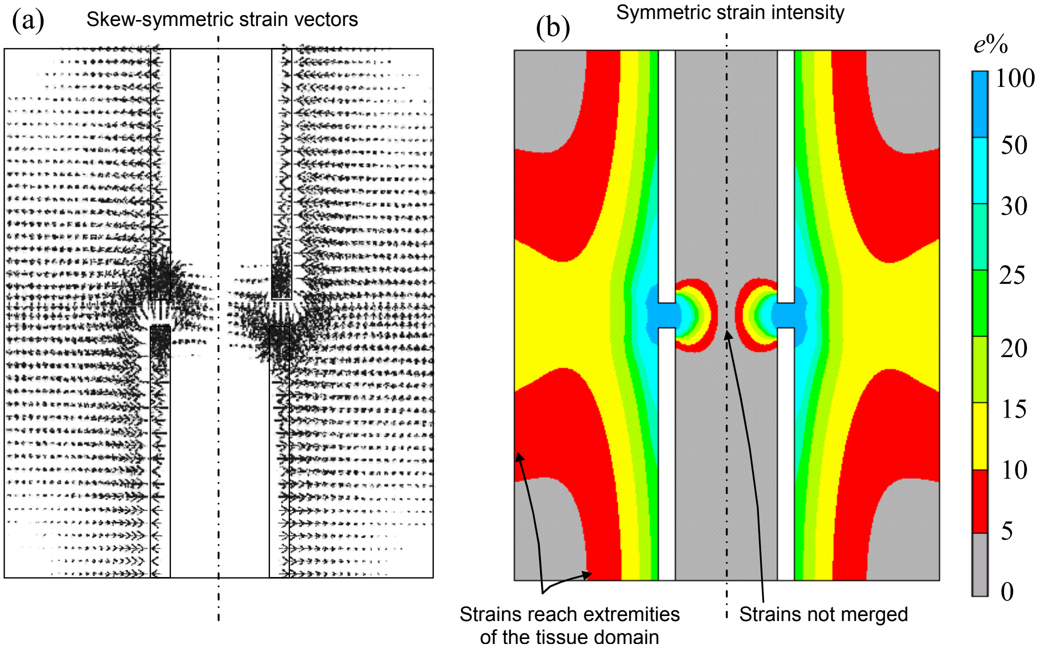

Figure 4.7. Compressive principal strains within a discrete FE structure under torsion loading. (a) Vector plot of compressive principal strains (magnitude plot x3). The vectors show a skew symmetric about the central longitudinal axis. (b) Undeformed contour plot of principal strains presented as e%. The strains extend towards to the radial and axial extremities of the tissue domain.

The vector plot showed that the strains followed a circular trajectory about the fracture line, however, due to the shearing forces, these strains were also acting perpendicular to the image shown (Fig. 4.7a). Also, the vectors were skew-symmetric about the central longitudinal axis due to the torsion loading. The contour plot, on the other hand, showed that the intensity of the strains were symmetric about the longitudinal axis. Also, it was found that the strains did not meet at the centre of the medulla canal, whereas the strains adjacent to the fracture extended to both the radial and axial extremities of the tissue domain (Fig. 4.7b).

Implementation of algorithm

The magnitude of the strain in the above case was greater than the previous compression loading case and thus the majority of the tissue domain experienced at least 5% of the maximum strain (Fig. 4.7b). Therefore, an *e*% of 10% was arbitrarily chosen to reduce the eventual size of the *in silico* callus. The first iteration of the algorithm removed a large amount of elements (Fig. 4.8a) leaving only those elements that experienced >10% strain which left a pattern of elements equal to the initial strain intensity field (*cf*. Fig. 4.7b). The second iteration had removed the elements that had extended radially and axially to the extremities of the tissue domain. The third and final iteration refined the formation at which point the algorithm was convergent where any further iterations would have removed an inappreciable mass or volume of tissue (elements). The converged *in silico* callus formation showed a symmetric formation of elements about the longitudinal axis (Fig. 4.8b). Also, adjacent to the fracture showed a rounded formation of elements while the tissue within the medulla was unconnected in the centre.

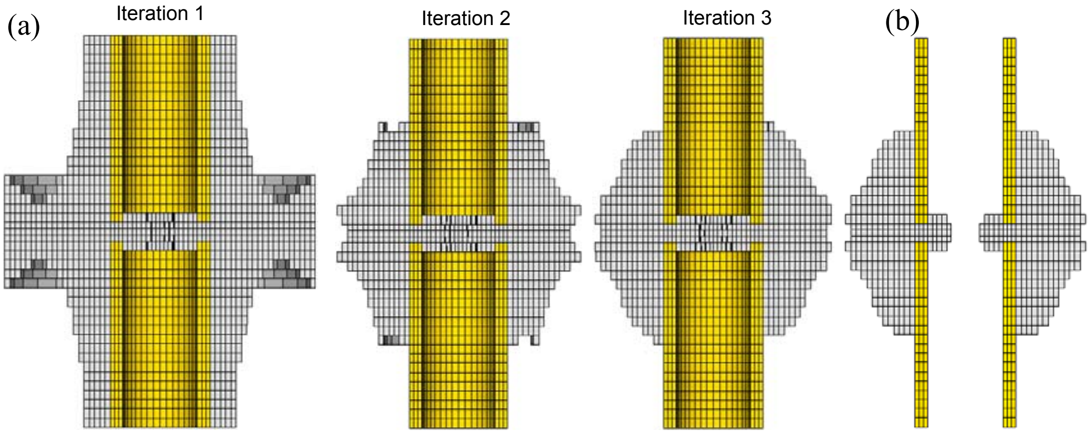

Figure 4.8. Implementation of algorithm under torsional loading in a transversal fracture. (a) Iterative removal of elements and (b) longitudinal section of tissue domain from the final iteration. e = 0.1.

4.3.3 Transversal fracture – bending moment

The ability of the compressive principle strains to drive callus formation under a bending moment was investigated. Importantly, one must remember that a bending moment will induce both tensile and compressive strains on opposing sides of the fracture, where theoretically there is no strain in the centre of these two extremes (neutral axis). Interestingly, it was found that the compression side showed a similar pattern of strain vectors as was seen previously (*cf.* Fig. 4.5a) where there was a circular trajectory of strain vectors (Fig. 4.9a). On the tension side, it was found that the vectors acted radially from the fracture gap. The magnitude of the compressive principal strains was greater on the compression side than the tension side as can be clearly seen from the contour plot (Fig. 4.9b). Also, on the compression side, the strains extended axially and radially to the extremities of the tissue domain. On the tension side, the strains were of a lesser magnitude and thus were experienced by a lesser proportion of the tissue domain. Lastly, the strains within the medulla canal did not form a bridge due to the lack of strain (neutral axis).

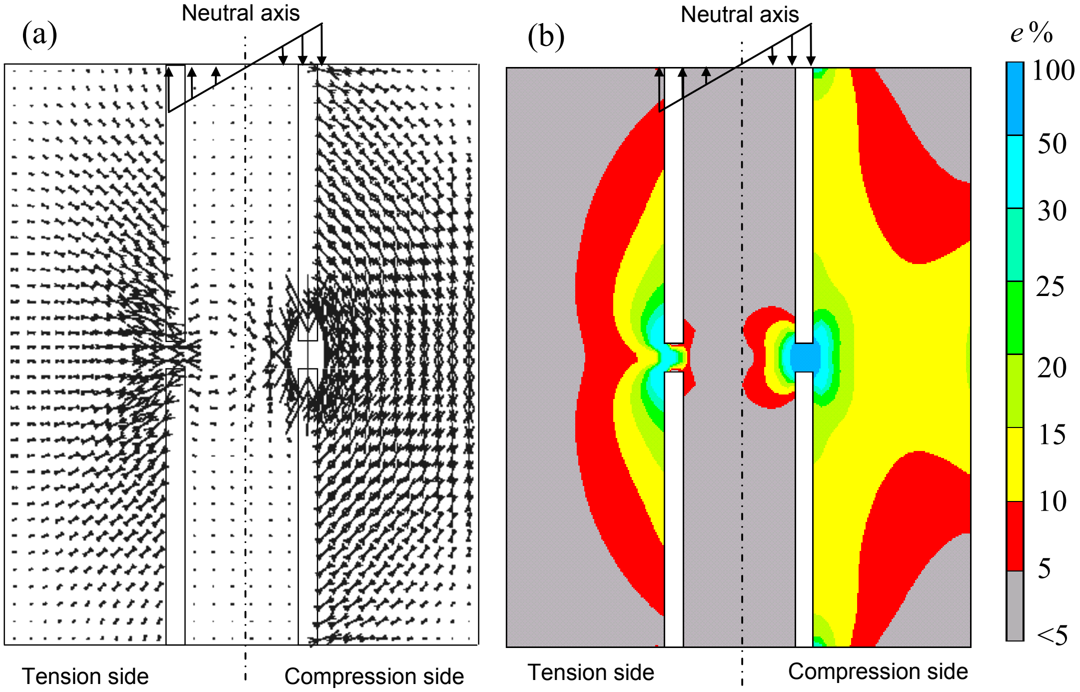

Figure 4.9. Compressive principal strains within a discrete FE structure under a bending moment. (a) Vector plot of compressive principal strains (magnitude plot x3). The vectors show an asymmetry about the central longitudinal axis (neutral axis) where the compressive strains act radially from the fracture gap on the tension side and vice versa. (b) Undeformed contour plot of principal strains presented as e%. The strains extended towards to the radial and axial extremities of the tissue domain on the compression side.

Implementation of algorithm

An Elimination Coefficient of 0.05 (5%) was chosen to coincide with the compression loading case shown earlier. The first iteration of the algorithm removed a large amount of elements (Fig. 4.10a) leaving only those elements that experienced >5% strain which left a pattern of elements equal to the initial strain field (*cf.* Fig. 4.9b). The second and third iterations had removed the majority of elements on the tension side of the tissue domain. The fourth and final iteration refined the formation at which point the algorithm was convergent where any further iterations would have removed an inappreciable mass or volume of tissue. The converged *in silico* callus formation showed an asymmetric distribution of elements about the longitudinal axis with the majority of tissue on the compression side (Fig. 4.10b). Also, adjacent to the fracture on the compression side showed a rounded formation of elements while very few elements occupied the medulla canal.

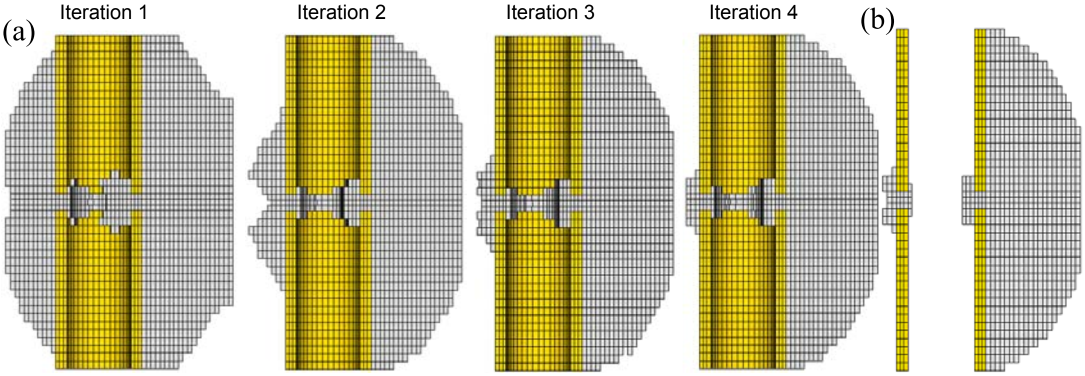

Figure 4.10. Implementation of algorithm under bending loading in a transversal fracture. (a) Iterative removal of elements and (b) longitudinal section of tissue domain from the final iteration. e = 0.05.

4.3.4 Oblique fracture – compressive loading

The influence of fracture type was investigated. This began with an analysis of compressive strains around an oblique fracture under compression. From the vector plot, it was found that the strain vectors follow a circular trajectory about the fracture (Fig. 4.11a). The strain contours also showed that the greatest intensity was found within the inter-cortical gap (30-100%), with lower strains extending to the extremities of the tissue domain (Fig. 4.11b).

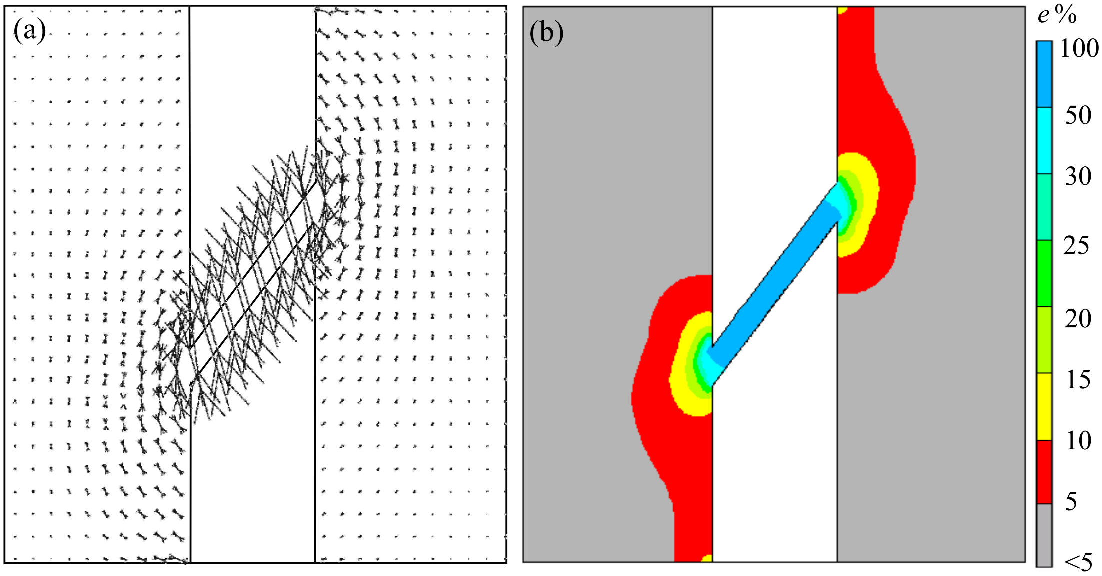

Figure 4.11. Compressive principal strains within a discrete FE structure of an oblique fracture. (a) Vector field of principal strains (magnitude plot x3). (b) Undeformed contour plot of principal strains presented as e%. The strains extend towards to the axial extremities of the tissue domain.

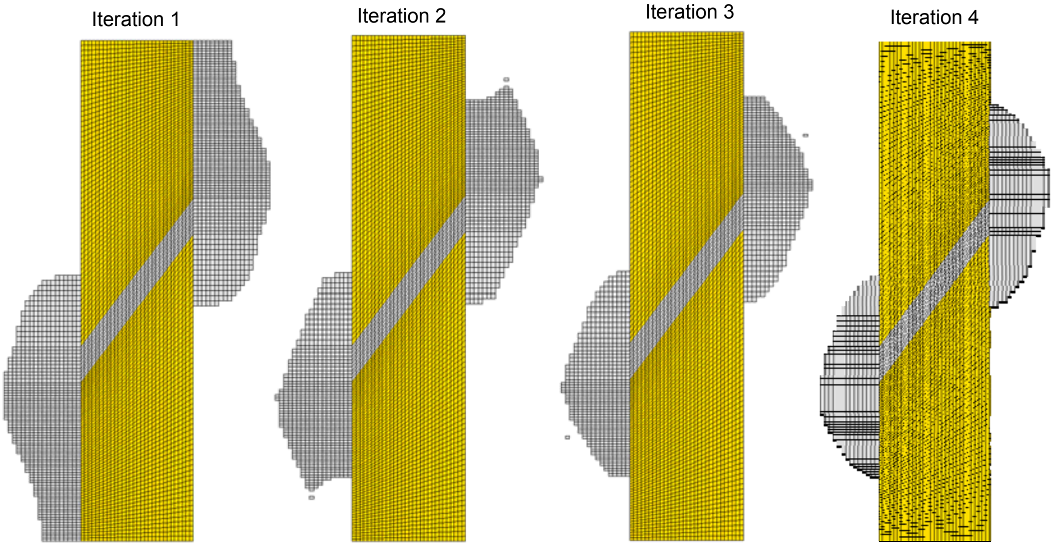

Figure 4.12. Implementation of algorithm under compressive loading in a oblique fracture. Iterative removal of elements under compression loading in an oblique fracture. e =0.05.

Implementation of algorithm

An Elimination Coefficient of 0.05 (5%) was again chosen to coincide with the compression loading case shown earlier. Four iterations were required to achieve convergence (Fig. 4.12). The initial iteration showed the *in silico* tissue forming asymmetrically on the distal and proximal ends of the domain. The second iteration removed these extremities and by the third iteration, the formation of periosteal callus was more rounded. The fourth and final showed that the formation of tissue was localized to the fractured regions with a more refined rounded formation similar to the formations found in the compressive loading scenario (*cf*. Fig. 4.6).

4.3.5 Spiral fracture – compressive loading

The algorithm and compressive principal strain hypothesis was further tested in a more complex 3D spiral fracture (Fig. 4.13a). In this case, relatively course elements were used in the initial mesh. Three iterations and two element refinement stages were used to arrive at the final *in silico* callus formation with an Elimination Coefficient of 0.05 (5%) (Fig. 4.13b).

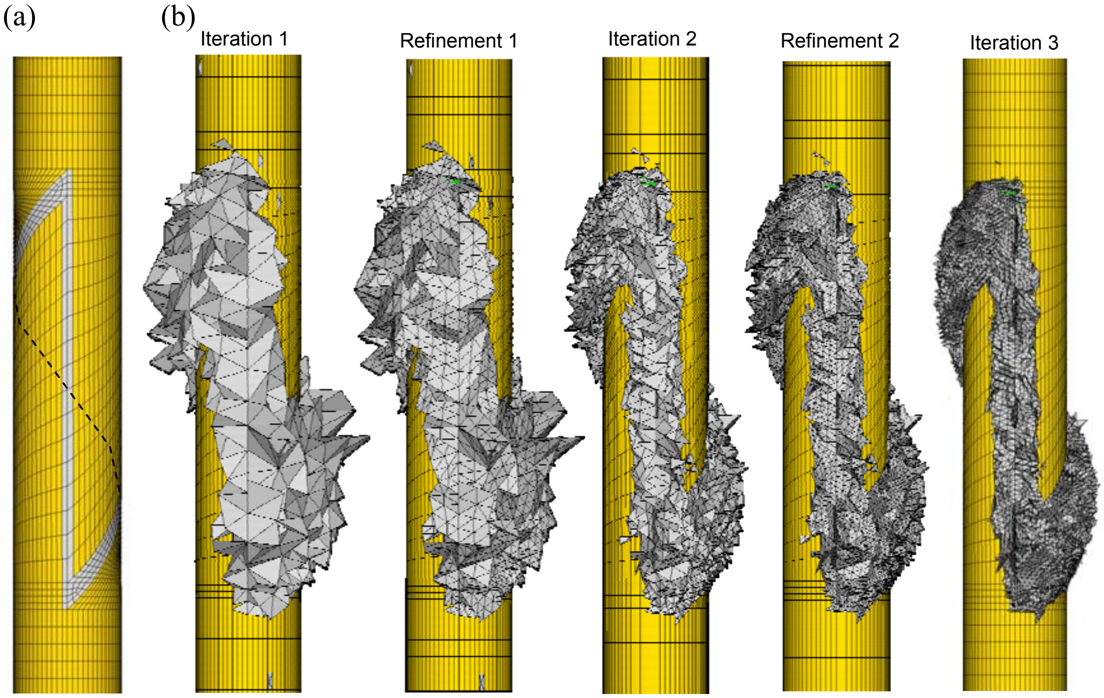

Figure 4.13. (a) FE model of spiral fracture and (b) iterative removal and refinement of elements under compression loading. e=0.05.

The first iteration of the algorithm removed a significant proportion of elements, leaving a relatively coarse formation that enveloped the fracture line. After the first iteration the elements were refined, although it should be noted that the formation remains the same. The second iteration refined the outer formation of the elements showing a closer fit with the fracture line. The third and final iteration further refined the outer geometry of the *in silico* callus formation. The *in silico* formation was found to encapsulate the fracture line as was found in the previous analyses. The tissue (elements) in fact followed the fracture line almost uniformly.

4.3.6 Analysis of *in silico* callus formation under unilateral fixation

The influence of the proximity of implant to the bone was studied to determine how a unilateral fixator influences the inter-cortical strain gradient and thus the resulting *in silico* callus formation. It was postulated that a unilateral fixator located closer to the bone will induce a more severe strain gradient than if the fixator was placed further from the bone. It was further postulated that a larger callus will form on the far cortex for an internal fixator than for an external fixator. Therefore, the interfragmentary strains ($\varepsilon_{IF,}$) on the near- and far-plate peripheries were calculated according to equation 2.1 for the varying plate-bone distances (Fig. 4.14a). When the fixator was located nearer to the bone (2mm) the near-far interfragmentary strain ratio was greatest (Fig. 4.14b). When the fixator was located further from the bone, the ratio began to asymptotically approach a near-far IFS ratio of 1:1. However, it should be noted that since the unilateral fixator is present, an inter-cortical strain gradient will always theoretically be asymmetric thus the ratio will always be greater than 1:1. Furthermore, it should also be reiterated that since the implant will inevitably bend under compressive loading of the bone; the inter-cortical strain will be compressive.

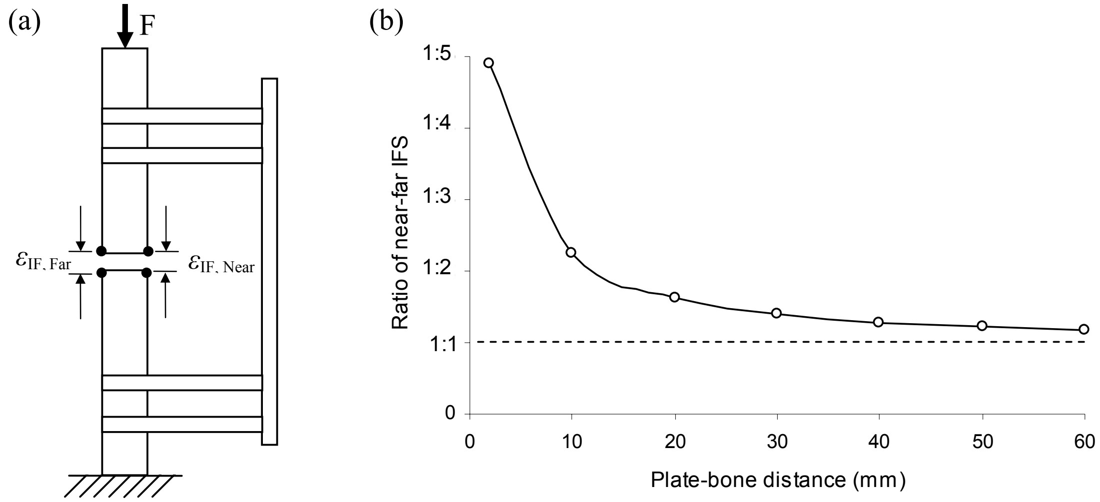

Figure 4.14. (a) Schema of implant and interfragmentary strain gradient measurement method. Note that these strains are measured from the periphery of the cortex. (b) Ratio of near-far interfragmentary strain due to asymmetric loading induced by the presence and proximity of the unilateral fixator. The ratio becomes asymptotic at a further plate-bone distance.

Due to the inherent inter-cortical strain asymmetry caused by the presence of the fixator, the tissue domain experienced significantly greater strain on the far-plate cortex than the near-plate cortex which is demonstrated for the 2mm plate-bone distance shown in figure 4.15. It was found that the principal strain vectors freely follow a circular trajectory around the fracture, while a similar yet limited pattern was also found within the medullary cavity (Fig. 4.15a). The lower strained areas (<50%) were found adjacent to the inter-cortical gap. These lower strained areas produced contours adjacent to the fracture on the far-plate side that followed a bulbous pattern, while the strains within the medullary cavity produced a bridge-like pattern (Fig. 4.15b). Lastly, the strains on the far-plate side reached towards the extremities of the domain.

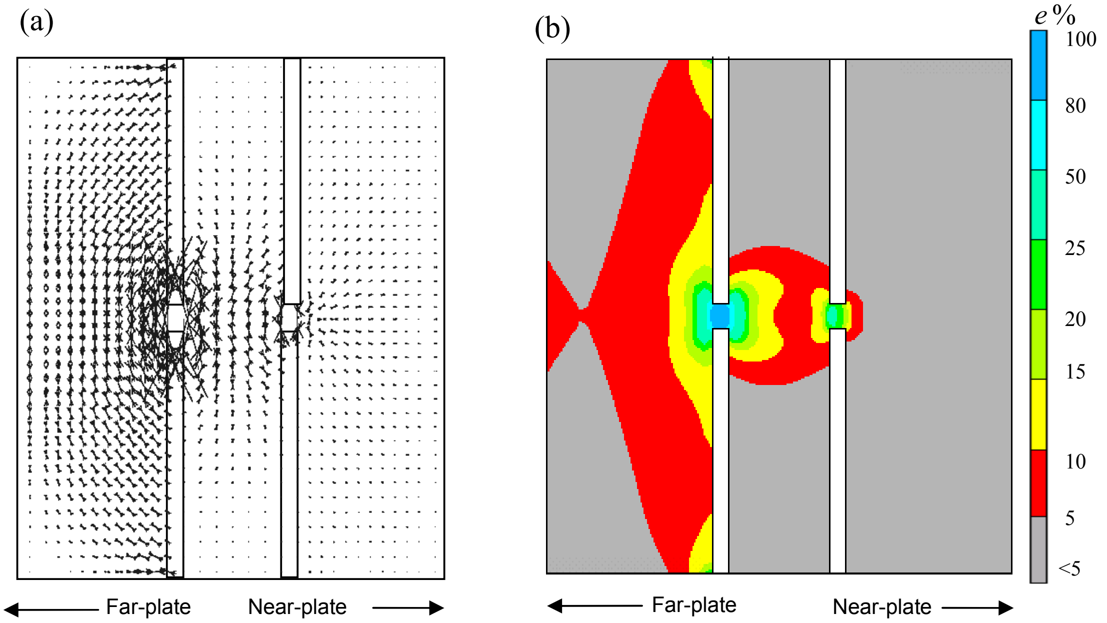

Figure 4.15. Compressive principal strains within a discrete FE structure under unilateral fixation (plate 2mm from the bone). (a) Vector plot of principal strains (magnitude plot x3). The vectors show asymmetry about the central longitudinal axis. (b) Undeformed contour plot of principal strains presented as e%. The strains merge towards to the radial and axial extremities of the tissue domain on the far-plate side.

Implementation of algorithm

An Elimination Coefficient of 0.05 (5%) was chosen for all the plate-bone distances to coincide with the compression loading case shown earlier. In all cases, the algorithm required only four iterations to reach convergence, furthermore, the first iteration produced a formation of *in silico* tissue which extended axially to the extremities of the tissue domain on the far-plate side, as demonstrated for the 2mm plate-bone scenario (Fig. 4.16). Also, in all cases, these were removed after the second iteration, leaving a more rounded *in silico* tissue formation. By the third iteration, the bridging of tissue within the medulla become narrower in the centre, while after the fourth and final iteration, the formation became more refined. See Appendix D for the remaining iterative solutions of the differing plate-bone distance scenarios.

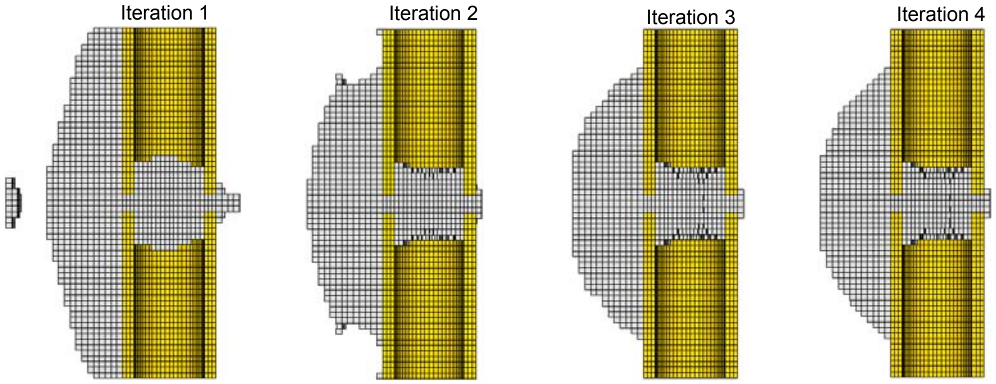

Figure 4.16. Iterative removal of elements under locking plate fixation for a plate-bone distance of 2mm in a transversal fracture. Note, the left side of the images show far-plate callus formation.

The 2mm plate-bone scenario showed the greatest level of asymmetry of *in silico* callus formation (Fig. 4.17a) due to the large inter-cortical strain gradient ratio, whereas the 60mm plate-bone scenario showed almost symmetric formation (Fig. 4.17g). Between these extremes it was found that the level of asymmetry varied gradually and non-linearly as the fixator was located further or nearer to the bone, which was quantified as a percentage of *in silico* callus on either side of the longitudinal axis (Fig. 4.18a).

Furthermore, due to the asymmetric loading, there will never be greater than 50% of the *in silico* callus on the near-plate cortex. Also, the bridge within the medulla was shown to be narrower with a greater level inter-cortical strain gradient and *vice versa*. Lastly, it was found that the near-far callus formation ratio showed an asymptotic relationship with the plate-bone distance (Fig. 4.18b). In fact this was almost equivalent to the near-far inter-cortical strain ratio, where an asymptotic relationship also occurred (Fig. 4.14b).

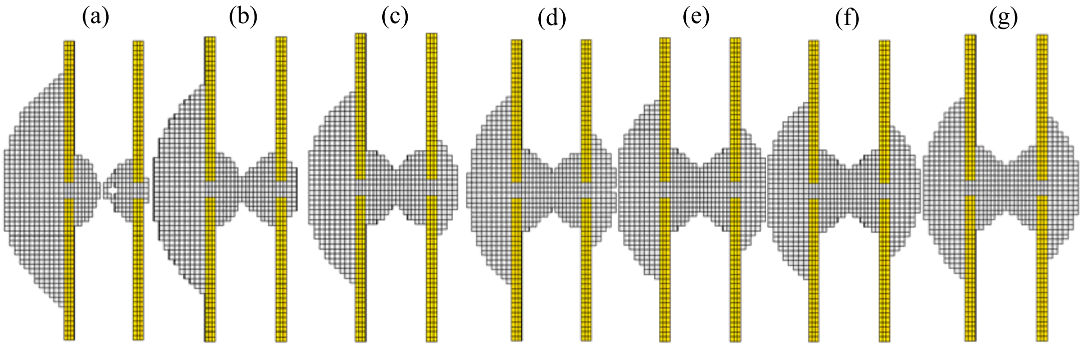

Figure 4.17. Longitudinal section of in silico callus formation under varying plate-bone distances. Asymmetry caused by alteration of proximity of the plate to the bone. Plate-bone distance: (a) 2mm, (b) 10mm, (c) 20mm, (d) 30mm, (e) 40mm, (f) 50mm and (g) 60mm. Note, the left side of the images show far-plate callus formation.

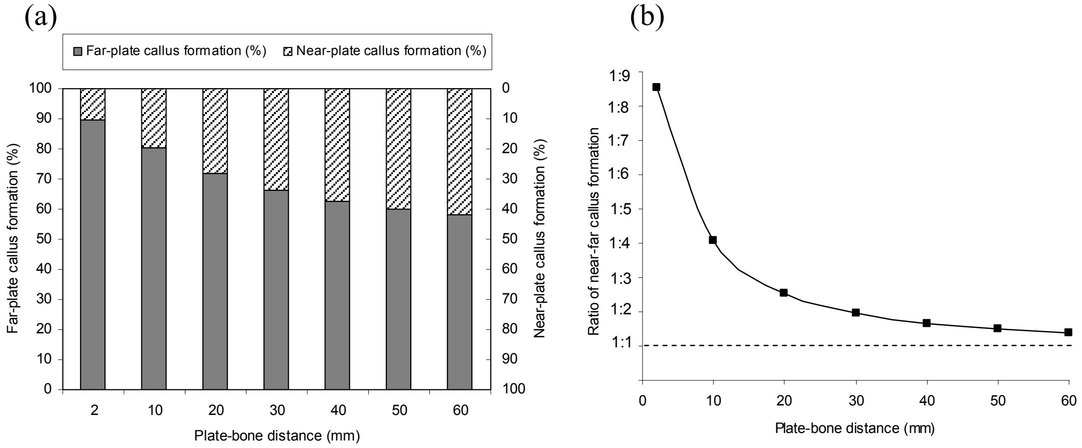

Figure 4.18. (a) Percentage of near-far in silico callus tissue formation due to asymmetric loading induced by the presence and proximity of the unilateral fixator. The closer the proximity of fixator to bone, the greater the level of asymmetry and vice versa. (b) Ratio of near-far callus formation. The ratio becomes asymptotic at a further plate-bone distance.

4.4 Analysis of *in silico* callus formation in case-specific fractures

To fully realize the potential of the proposed methods and to test the hypothesis in the most severe manner possible; the mechano-regulated algorithm was implemented in less-idealized case-specific fractures under physiologic-like loading. Three cases of *in silico* callus formation in tibial fractures and one spiral fracture of the femur are analysed below.

4.4.1 Case study 1 - oblique fracture of the tibia

The oblique fracture geometry and interfragmentary displacements were adapted from Gardner *et al.* (2003). It was found that the compressive principal strain vectors freely followed a circular trajectory around the fracture, while a similar yet limited pattern was also found in within the medullary cavity (Fig. 4.19a).

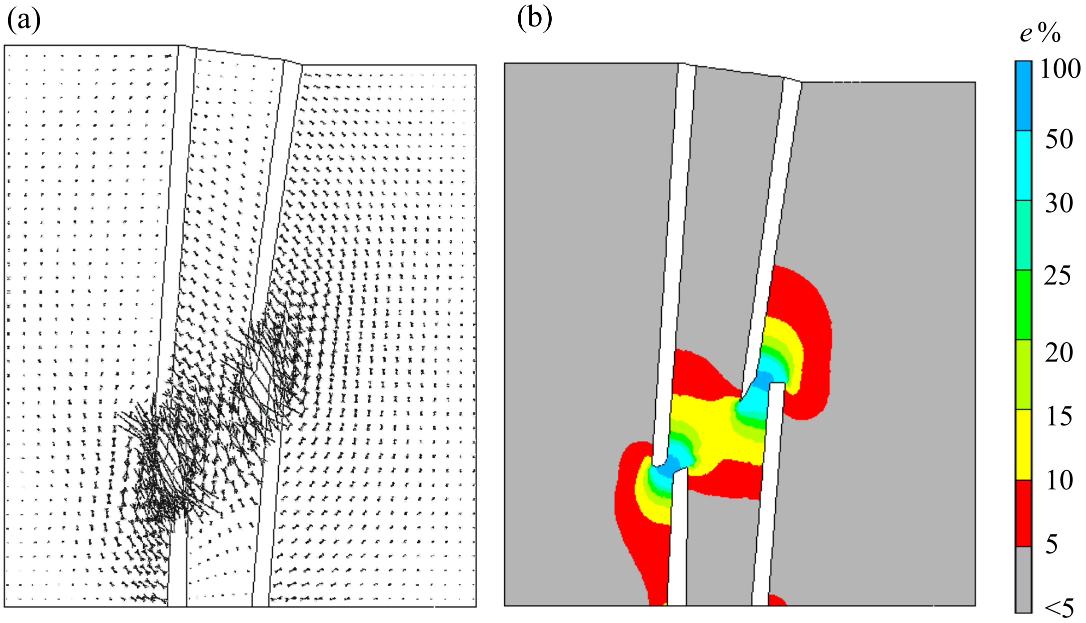

Figure 4.19. Compressive principal strains within a discrete FE structure under physiological displacements in an oblique fracture based on a geometry described by Gardner et al. (2003). (a) Vector plot of principal strains (magnitude plot x3). (b) Undeformed contour plot of principal strains presented as e%. The strains extended towards to the distal extremity of the tissue domain.

The principle strain distribution in the tissue domain showed a skewed strain field (Fig. 4.19a), similar to the idealised oblique fracture (see Fig. 4.12). Also, one can observe based on the contour plot that the highest magnitude of strains (50-100%) were located within the interfragmentary space (Fig. 4.19b). The lower strained areas (<50%) were found adjacent to the inter-cortical gap which produced contours that followed a bulbous pattern while the strains within the medullary cavity produced a bridge-like pattern. Furthermore, the strains reach towards the distal extremity of the tissue domain.

Implementation of algorithm

The algorithm required four iterations to achieve convergence using an Elimination Coefficient of 0.05 (5%). The iterative process of removal of the lowly strained areas of the tissue domain showed the progressive formation of the endosteal and periosteal callus (Fig. 4.20). The first iteration produced a formation exactly equal to the strain distribution shown above (Fig. 4.19b). The second iteration removed the elements that extended towards to the lowest extremity of the tissue domain. The third and fourth iterations revealed the narrowing of the bridge between the cortices while refining the general formation. The final *in silico* formation showed that the callus became skewed to the same angle of the fracture line, as was observed in the idealized oblique case (see Fig. 4.12).

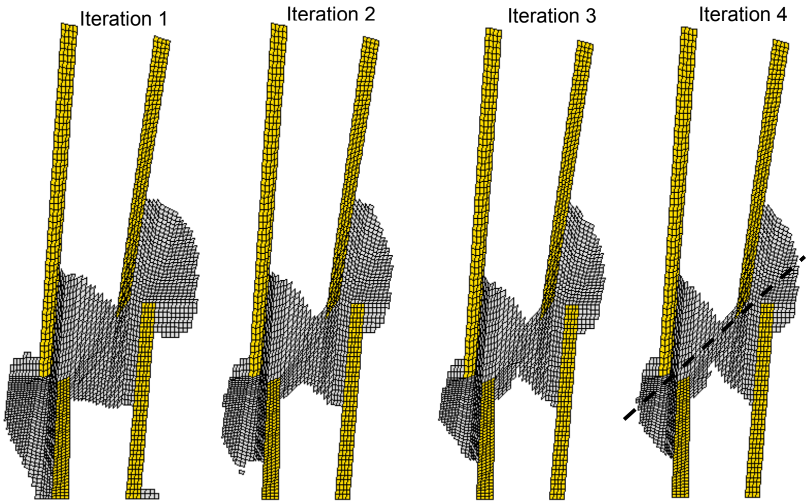

Figure 4.20. Iterative removal of elements for an oblique fracture of the tibia. The in silico tissues became skewed to the angle of the fracture. e = 0.05.

4.4.2 Case study 2 - mid-shaft transversal fracture of the tibia under locking plate fixation

The results of the 3D case-specific model of a tibial fracture fixated with a unilateral implant is analysed here. What was most intriguing in this case was that the physiological-like loading, as described by Duda *et al.* (2002), caused the plate to bend away from the bone surface which resulted in the inter-cortical gap and surrounding tissues to experience tensile strains (Fig. 4.21a). Thus the compressive principal strain vectors were acting radially from the inter-cortical gap (Fig. 4.21b) similar to the strains found on the tensile side of the bending case (see Fig. 4.9).

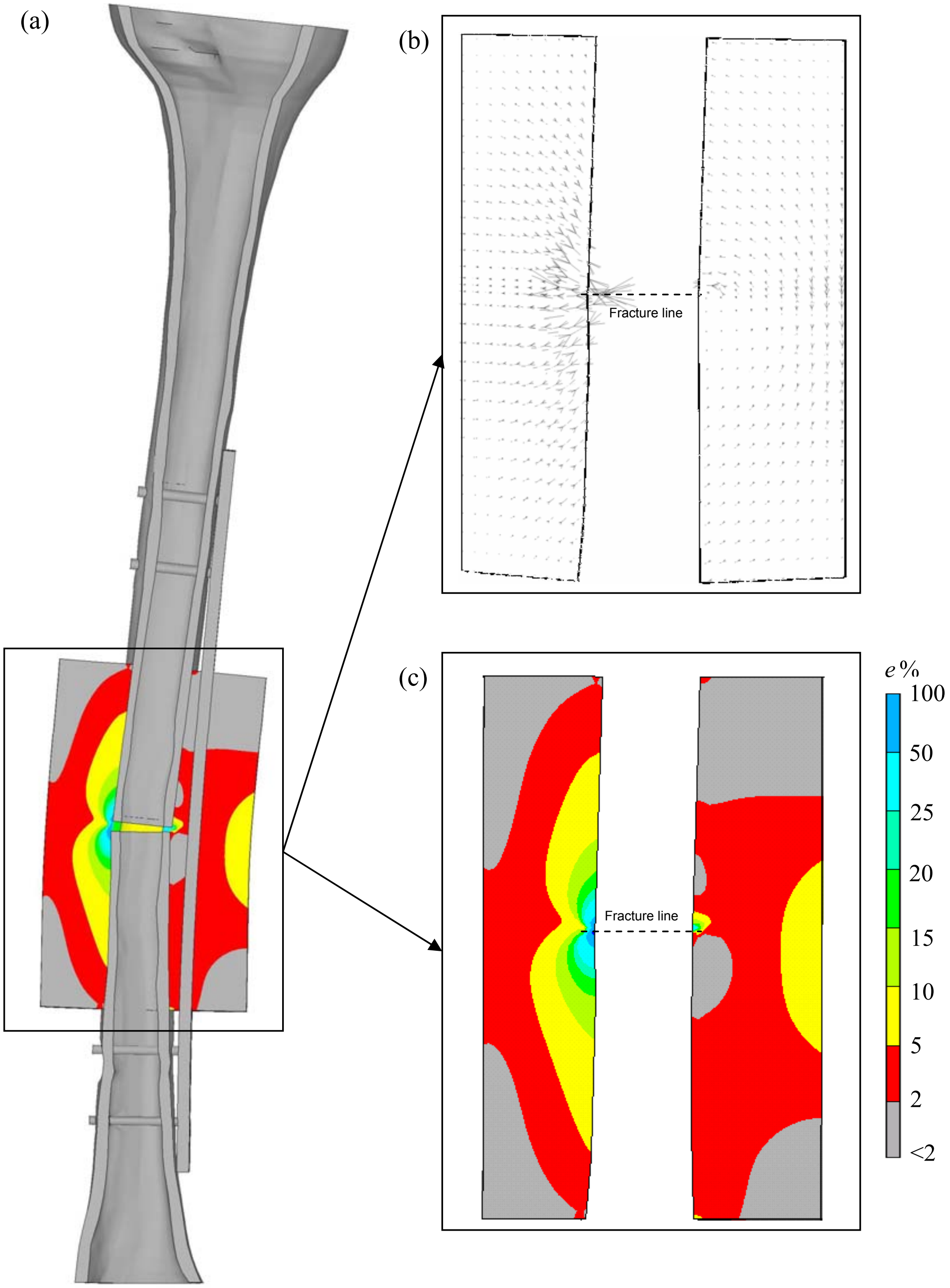

Figure 4.21. Deformed model of the tibia (magnitude x3) and (b) undeformed vector plot of principal strains (magnitude plot x3). (c) Undeformed contour plot of principal strains presented as e%. The highest strains were at the periphery of the fracture gap.

The strain intensity contour plot did not show an obvious correlation with the typical *in vivo* callus formation (Fig. 4.21). The contour plot in this specific analysis had shown that the highest strains (25-100%) were located adjacent to the inter-cortical gap at the periphery of the far-plate cortex (Fig. 4.21c), unlike in the compression loading cases where the highest strains were experienced by the inter-cortical tissues.

Implementation of algorithm

The algorithm was convergent after four iterations (Fig. 4.22), using an Elimination Coefficient of 0.02 (2%), to correspond with the *in vivo* callus formation discussed further in the following chapter. Due to the loading, the formation of elements after the first iteration did not bare any resemblance to the typical *in vivo* formation. For example, a large portion of 'floating' tissue, which was not connected to the other sections in the tissue domain, was found on the near-plate cortex.

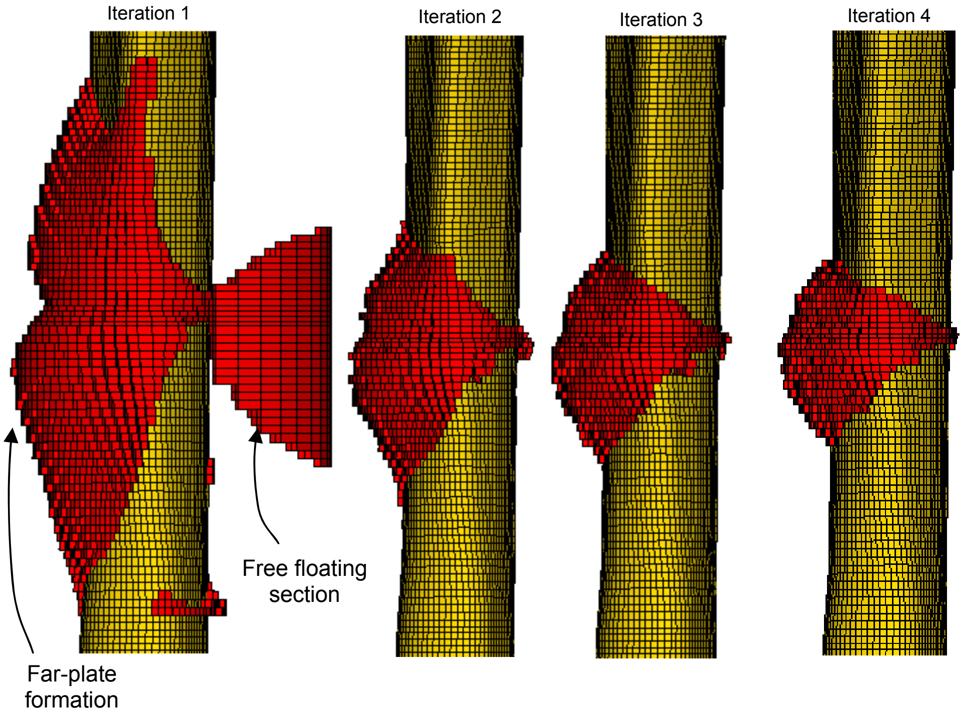

Figure 4.22. Anteroposterior (A-P) view of iterative removal of elements for a transversal fracture of the tibia. e = 0.02.

After the second iteration, however, the tissues at near-plate cortex experienced low strain and therefore became redundant and were removed leaving the majority of the tissues on the far-plate cortex. The third iteration produced a more rounded formation on the far-plate cortex while removing extra elements on the near-plate cortex. The fourth and final iteration refined the *in silico* callus with the majority of tissue on the far-plate cortex as was previously observed in the idealised loading scenario under asymmetric compressive loads caused by unilateral plate fixation (see Fig. 4.17a).

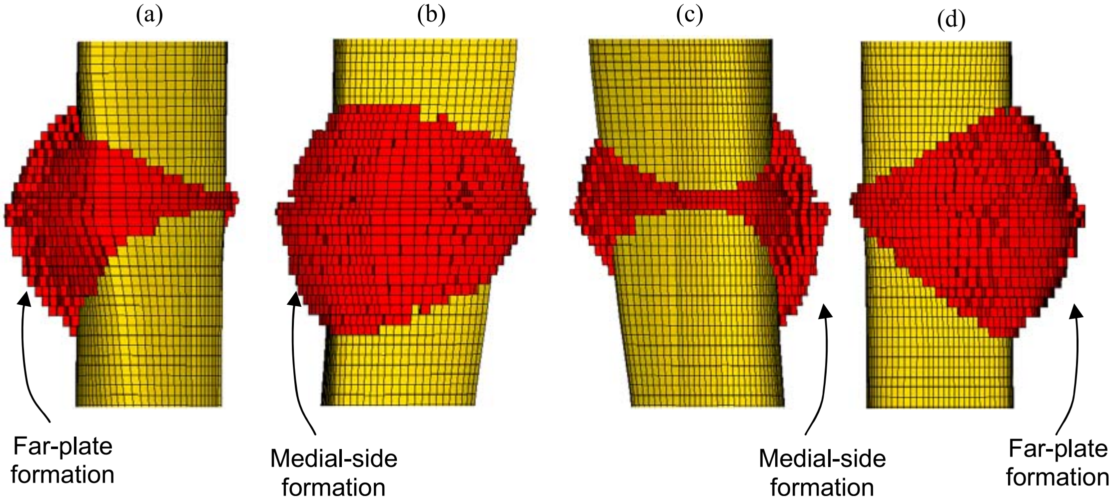

Figure 4.23. In silico prediction of callus formation under physiological-like loading in a transversal fracture of a human tibia. (a) Anteroposterior (A-P) view, (b) mediolateral (M-L) view, (c) lateromedial (L-M) view, and (d) posteroanterior view (P-A). Marked callus was found on the far-plate cortex and the medial aspect of the bone.

A multitude of anatomical views of the converged *in silico* callus formation are shown above (Fig. 4.23). The far-plate cortex had marked callus formation where the strains were highest (Fig. 4.23a & d). Furthermore, it found that the medial aspect of the fracture had a greater formation of tissue than the lateral side (Fig. 4.23b-c). This was attributed to the complex loading and the anterolateral positioning of the implant which affected the inter-cortical strains leading the observed level of asymmetry. Most importantly, the final callus formation produced a distribution of tissue similar to the compression loading scenarios despite the tensile strains within the interfragmentary space.

4.4.3 Case study 3 – mid-shaft transversal fracture of the tibia with misalignment of the fragments under locking plate fixation

This case analyzed how callus forms in a fracture with fragment misalignment and under locking plate fixation. As in the previous case, the tibia and plate underwent bending which caused tensile strains within the interfragmentary gap and tissue domain. This case required four iterations to achieve convergence (Fig. 4.24) with an Elimination Coefficient of 0.05 (5%) to correspond with the *in vivo* callus formation discussed further in the following chapter. The first iteration revealed a formation on the far-plate cortex as was shown previously and also with a free floating section of tissue not connected to the rest of the domain. The second iteration removed the free floating section and rounded the far-plate tissue formation. The third and forth iterations refined the formation.

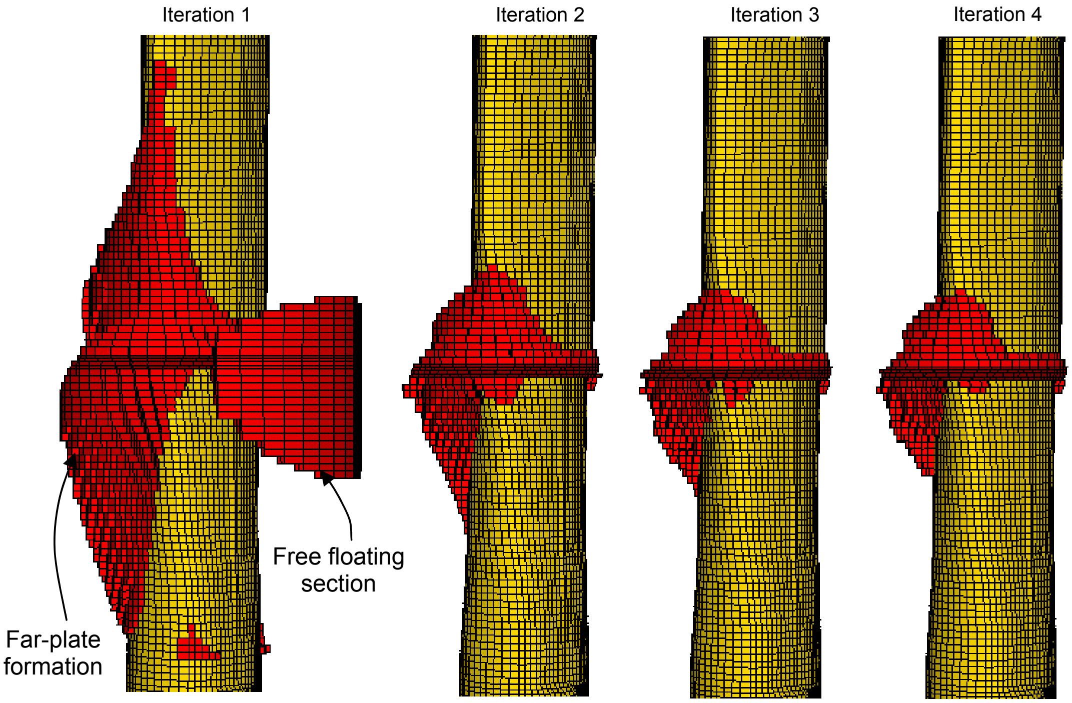

Figure 4.24. Anteroposterior (A-P) view of iterative removal of elements for a transversal fracture of the tibia with fragment misalignment. e = 0.05.

A multitude of anatomical views of the converged *in silico* callus formation are shown below (Fig. 4.25). Due to the misalignment of the bone fragments the *in silico* callus tissue enveloped the fracture, thus bridging the fragments at angle (Figs. 4.25b-c). Furthermore, due to the presence of the implant, as in the previous case above, the tissue was biased towards the far-plate cortex where strains were highest (Figs. 4.25a & d). Also, it was found that there is a grater formation of the callus on the medial side of the fracture in comparison the lateral side (Figs. 4.25b-c) as was also found in the previous case.

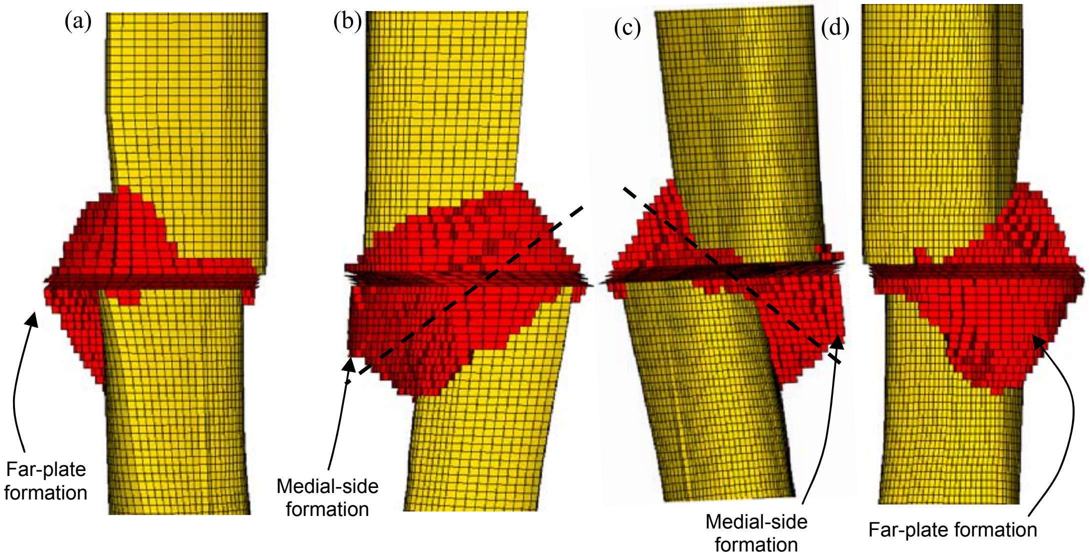

Figure 4.25. In silico prediction of callus formation under physiological-like loading in a transversal tibia fracture with misaligned fragments. (a) Anteroposterior (A-P) view showing marked callus on the far-plate cortex. (b) Mediolateral (M-L) and (c) lateromedial (L-M) views, displaying the angular alignment of the callus and the greater formation on the medial side. (d) Posteroanterior view (P-A) showing greater formation of callus on the far-plate cortex. e = 0.05.

4.4.4 Case study 4 – spiral fracture of a femur under locking plate fixation

The final case presented here is of the femoral spiral fracture with locking plate fixation on the lateral aspect. In this case the physiological-like loading revealed that the greatest magnitude of compressive principal strain was found on the most proximal aspect of the interfragmentary gap. Thus when the algorithm was implemented, there was a bias of callus towards this area (Fig. 4.26). The algorithm was convergent after three iterations using an Elimination Coefficient of 0.01 (1%) to correspond with the *in vivo* callus formation discussed further in the following chapter. The first iteration removed a significant proportion of the tissue domain, which revealed a distribution of tissue about the fracture line. The second iteration removed elements that extended to the proximal extremity of the tissue domain. The third and final iteration refined the formation producing an outer geometry providing a smoother distribution of tissue.

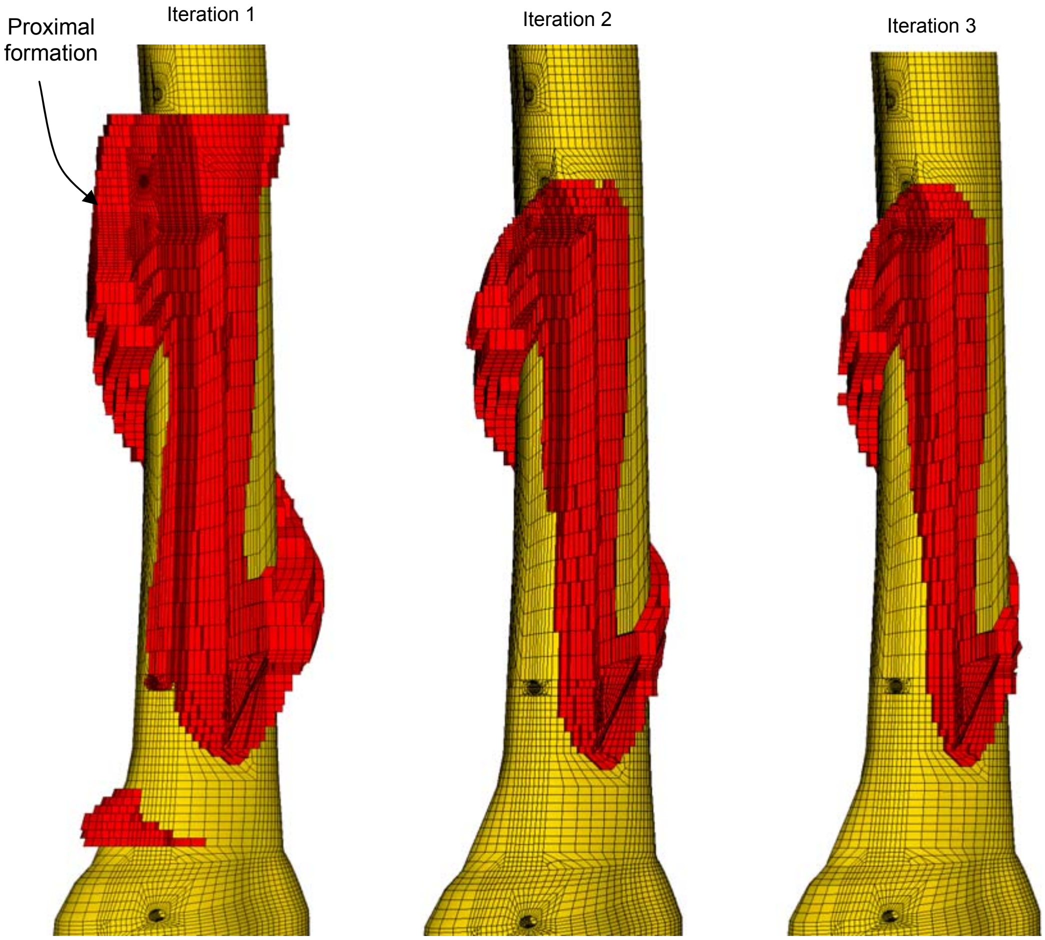

Figure 4.26. Stages of callus refinement and development in a femoral spiral fracture. e=0.01

Importantly, the converged solution produced an *in silico* callus that enveloped the fracture line, as was found in the idealised simulation (see Fig. 4.13). The exception was that in the femoral fracture, the unilateral implant caused the *in silico* callus tissue to become distributed towards to the far-plate cortex, with little or no tissue on the near-plate cortex under the implant (Fig. 4.27a). It was also found that there was a greater formation of tissue on the most proximal aspect of the fracture line in comparison with the distal aspect (Fig. 4.27b). These formations corresponded with the intensity of compressive principal strains within the fracture line.

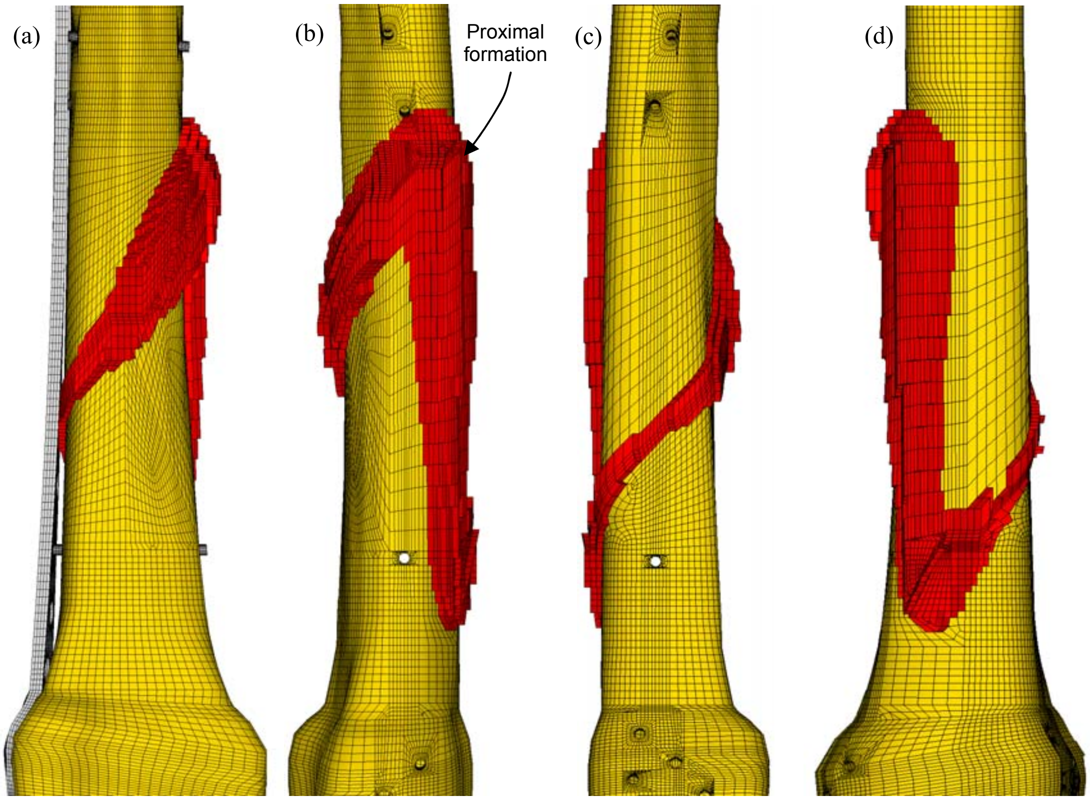

Figure 4.27. In silico prediction of callus formation under physiological-like loading in a femoral spiral fracture under unilateral plate fixation. (a) Anteroposterior (A-P) view with plate. There is little or no callus under the implant. (b) Mediolateral (M-L) view showing a greater formation on the proximal aspect in comparison with the distal aspect of the fracture line. (c) Lateromedial (L-M) view, and (d) posteroanterior view (P-A).

4.5 Summary

Two hypotheses were investigated in this study; 1) that a mathematical cause-and-effect relationship exists for the rate of bone healing and the initially applied interfragmentary strain, and 2) that the efficient formation of callus tissues is mediated by the compressive principal strains in the immature healing tissues. Mathematical and computational methods were proposed to model the temporal and spatial healing of a bone, the results of which were analysed in this chapter. It was paramount to be able to determine the strength of these hypotheses by every possible means available; hence, the robustness of these proposed strategies and models were tested against further experimental data, as in the mathematical modelling case, and analysed in as many fractures and loading scenarios, as in the *in silico* callus formation modelling case. The congruency of the *in silico* callus formations with the *in vivo* formations is discussed in the following chapter.

Chapter 5 - Discussion

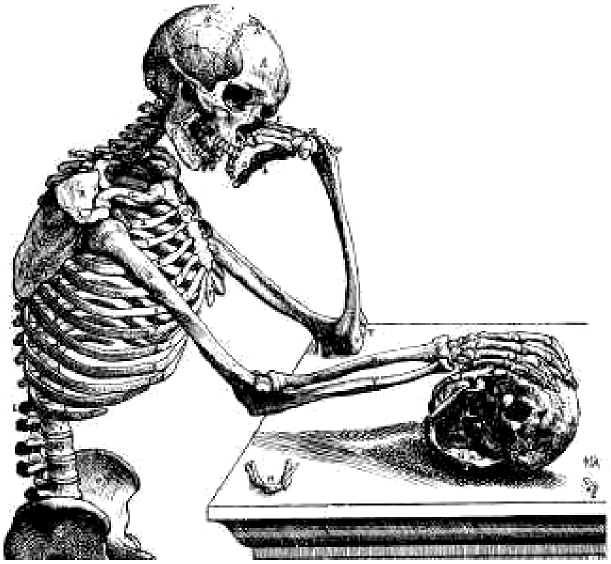

<u>Contemplation of formation</u>:
Drawing by Renaissance physician Vesalius depicting the scientific method.

Contents

5.1 Introduction

The results of this study are discussed to determine the strength of the hypotheses and the predictive power of the proposed models and methods. Furthermore, the mathematical and *in silico* findings are further compared with *in vivo* evidence to determine the level of agreement. Firstly, the strength of the hypothesis, which states that there is a cause-and-effect relationship between the rate of healing and the initially applied interfragmentary strain, is discussed here.

Next, it is argued based on FE simulations, that compressive principal strains drive the efficient formation of callus tissue. It was also postulated that the asymmetric formation of healing tissues under unilateral fixation is caused by the inter-cortical strain gradient induced by bending of the implant. Moreover, it was also contended that the proximity of the fixator to the bone (and its neutral axis) would impart a proportional severity of strain gradient which would then equivalently influence the asymmetry of the callus formation. To determine the strength of these hypotheses, comparative analyses were conducted to find the level of congruency between the *in silico* and *in vivo* formations found in the literature. Furthermore, to determine the predictive power of the proposed simulations and to add further credence to the hypotheses; the *in silico* predicted callus formation in case specific fractures under unilateral fixation were qualitatively compared with radiographic images to determine the ability of the proposed methods for use in patient specific studies.

The assumptions and limitations of the mathematical and computational modelling methods are discussed. It is envisaged that the techniques/strategies proposed in the present study could be incorporated into a pre-clinical tool to aid implant design and/or as a pre-operative planning tool to aid/guide orthopaedic fracture fixation surgery. The implications and limitations of such a symbiosis are discussed here. Lastly, the achievements of this study are outlined.

5.2 On the role of interfragmentary strain on the rate of bone healing

A positive correlation was found between the initially applied interfragmentary strain and the relative increase in callus stiffness which was discovered through a novel interpretation of the *in vivo* experimental data by Claes and coworkers (1997, 1999). To the author's knowledge, this is the first time the results of Claes and coworkers have been presented in this manner. Based on this, a mathematical model was developed to simulate the rate of healing for a range of interfragmentary strains. The robustness of the model was reinforced by comparison with a collection of experimental data spanning two decades of work found from the literature.

5.2.1 Mathematical relationship

The proposed mathematical model represents the rate of healing between weeks 1-8. This time scale represents the reparative phase of healing, i.e. after inflammation and before the fracture gap becomes fully bridged and thus before the remodelling phase. The experimental studies with which the models were based on confirms this as they too did not achieve full ossification or full bony bridging for that matter as the studies were truncated at approximately week eight of healing.

With regards to the accuracy of the mathematical model; the percentage of relative averaged error ranged between 4.86% - 28.7%, with a grand average relative error of 14.2%. It is logical that this level of error be found when comparing independent studies, which have not been compared until now. Furthermore, it should be reminded that, the mathematical model was expressed as a single function and was intended only to account for intermediary interfragmentary strains within the range of 7% - 40%. However, the model was in fact capable of predicting, with good accuracy, the rates of healing for interfragmentary strains above the intended range (up to 45%).

Goodship and Cunningham (2001) hypothesized that the appropriate range of interfragmentary strain should be between 10-50%, where outside of this range may cause atrophic and hypertrophic non-union, respectively. Importantly, the results of this study suggest that the IFS should be within the range of 7 - 45%, which approximately agrees with Goodship and Cunningham’s (2001) hypothesis. Interestingly, Schell *et al.* (2008) found that an initial axial IFS of 47% coupled with shear strain resulted in non-union which suggests that strains up until 47%, healing will progress successfully, but greater than this will lead to non-union. Furthermore, a study by Claes *et al.* (2002) found that an initial strain of 10% yielded greater bone formation than an initial strain of 50%, which, agrees with the postulation that strains greater than 47% will have a negative effect.

Based on the proposed mathematical model, the effect of initially applied interfragmentary strain does not affect the rate of healing until after the 5th week of healing where divergence occurs. This approximately agrees with Hente *et al*. (2003) who found little variation in callus bending stiffness before the 4th week of healing between equivalent ovine fractures (Fig. 5.1). Furthermore, Hente *et al*. found considerable divergence between subjects (Fig. 5.1a), which qualitatively agrees with the level of divergence of the proposed mathematical model (Fig. 5.1b). Unfortunately, Hente *et al*. did not control nor monitor the mechanical stimulus during healing, thus the influence of interfragmentary strain could not be determined and thus could be assumed random. In the present study, however, the variation or divergence in rate of healing was in fact based on controlled stimulus (interfragmentary strain) and thus the relationship was shown to be non-random.

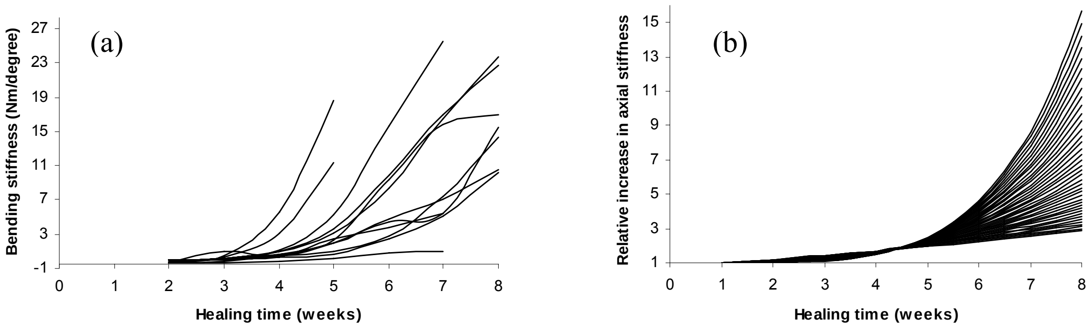

Figure 5.1. (a) Increase in callus bending stiffness between weeks 1-8 in 12 sheep with same facture gap and external unilateral fixator (adapted from Hente et al., 2003). Note the level of mechanical stiffness was unknown. (b) Simulated rate of healing for IFS between 7-45% based on Eq. 3.11.

Cheal *et al*. (1991) also found that, stimulated healing calluses, increase in torsional and bending stiffness after the 4th week of healing, which was measured as a decrease in torisonal and bending strain. Also, after the 4th week of healing calcification was also found from histological examinations. Consequently, one can postulate that the influence of mechanical stimulus does not become apparent until or after week 4, which approximately agrees with the proposed mathematical model, where divergence begins after week five.

It should also be noted that the proposed mathematical model was based on compressive stiffness measurements, whereas Cheal *et al*. (1991) and Hente *et al*. (2003) measured stiffness by means of bending and/or torsion. Furthermore, the internal structure of the callus becomes increasingly anisotropic and inhomogeneous during the healing process which will influence the stiffness based on the direction of loading. As a result, it is likely that the discrepancies in the above comparisons will occur due to the difference in mechanical loading methods used to determine the stiffness of the callus during the healing process. For example, Claes and colleagues (1995, 1997) found that, under pure compressive loads, the callus was capable of supporting the subjects weight after week one. However, the bending measurements by Hente *et al*., (2003) found that in the first 3 weeks of healing an extremely low bending stiffness (<1Nm/^{o}) was found. Therefore, under bending loading where tensile strains exist, the natural ability of a callus to resist compression is compromised, and thus its weakness in tension reduces the structural (bending) support. Importantly, Claes *et al*. (1995) found from histological analyses that the effect of IFS occurred after the 5th week of healing which agrees with the proposed mathematical model.

Based on the proposed mathematical model, when the initially applied interfragmentary strains were high (up to 45%), a greater rate of increase in callus stiffness followed and therefore these initially high strains would decrease correspondingly. Interestingly, it should be noted, that according to the *interfragmentary strain theory* (Perren and Cordey, 1980), ossification or new bone will not be created unless the strains are less than 2%. Thus it can be inferred that the callus increases in stiffness by alteration of its internal and external structures and tissue formations in an attempt to reduce these initially high interfragmentary strains so that the mechanical environment is more conducive to bone formation (ossification). On the contrary, according to the mathematical model, when the initially applied interfragmentary strains were low (7%), the rate of stiffening was lower despite the fact that these initially lower strains were technically more conducive of ossification according to the *interfragmentary strain theory*. It could be conjectured that these initially low strains do not stimulate the adjacent callus to bridge the fracture gap or differentiation within the central callus. Importantly, it has been shown experimentally, that lesser mechanical stimulus (strain rate and number of applied cycles per day) resulted in significantly less callus formation (Goodship *et al*., 1998; Hente *et al*., 2004).

On a final note, the proposed mathematical model directly contradicts the computationally simulated rates of healing found in the literature. In the present study a positive correlation was found between the initially applied interfragmentary strains and the relative increase in callus stiffness, whereas the computational simulations suggest the opposite. Logically speaking, it is intuitive to agree with a model based directly on experimental studies, which one must assume are correct, rather than a computer simulation based on mechano-biological theories. Nevertheless, the proposed mathematical model shows potential as a benchmark solution through which future computational simulations of bone healing could be compared with.

5.3 *In silico* modelling of callus formation

It was argued in the literature review, that *in vivo*, the healing callus tissues distribute themselves about the fracture line in such a manner that the tissue envelopes the fracture. Thus minimizing relative motion between bone-fragments and maximizing stability while minimizing tissue usage. Finite element analyses found in the literature had shown promising patterns of stress and strain energy density around bone fragments that could have been further explored as a means of studying/predicting the formation of callus tissue. Based on these observations, it was hypothesized in the present study that the compressive principal strains experienced by the early immature healing tissue drive and sustain the efficient callus formation through a process of tissue maintenance/deposition and resorption.

The proposed algorithm was tested under a number of loading conditions and fracture geometries to predict the structural formation of callus. To truly determine the predictive power of compressive principal strain and the algorithm; where possible, comparisons of the *in silico* and *in vivo* formations were made. It should be noted that qualitative comparisons are made with the *in vivo* since the formation of a callus can differ slightly between subjects even in controlled circumstances.

5.3.1 On the influence of loading

The influence of the loading (compression, torsion and bending) on the *in silico* callus formation was tested in transversal fracture gaps.

Compression and torsion loading

The compression and torsion loading scenarios produced an axisymmetric *in silico* formation, due to the method of loading which were compared with the average *in vivo* callus geometry as described by Claes and Heigele (1999) (Fig. 5.2). Firstly, it should be noted that the Elimination Coefficient, *e*, was intentionally set to a value of 0.05 in the compression loading scenario to produce a callus that was approximately equal to the average *in vivo* radial extension of the periosteal callus (16mm) (Fig. 5.2a-b). Nevertheless, the *in silico* periosteal axial extension was also found to be almost equal to the average *in vivo* extension for both compression and torsion loading scenarios. The *in silico* endosteal bridge in the compression loading scenario was approximately twice the size of the *in vivo* callus, despite this, the *in silico* callus did however mimic the *in vivo* shape, including the narrowing in the centre of the endosteal bridge (Fig. 5.2b).

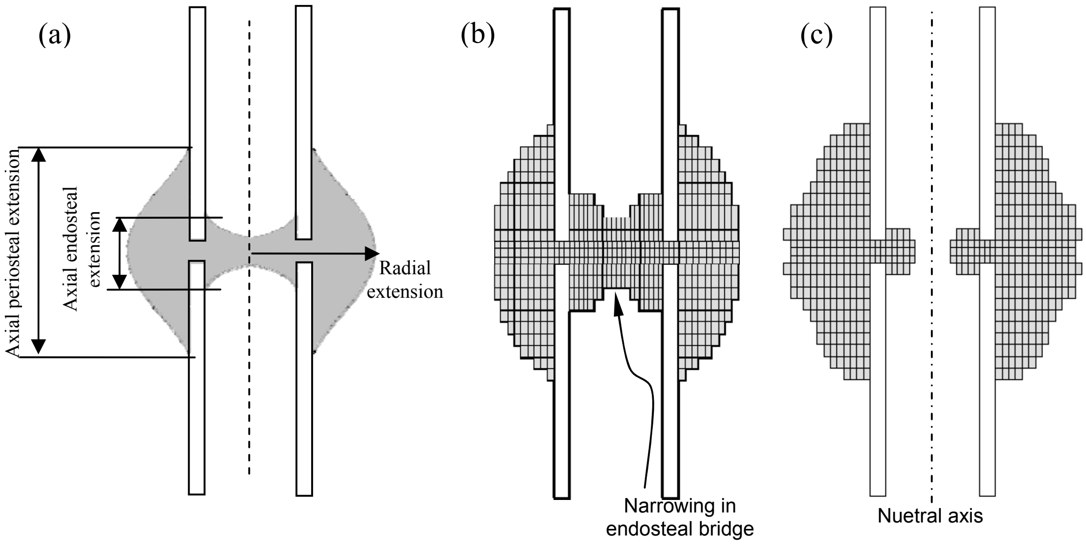

Figure 5.2. Comparison of in vivo and in silico callus formation under axisymmetric compression and torsion. (a) Idealised average geometry of fracture callus formation of a transversal fracture under axial compressive loading (adapted from Claes and Heigele, 1999). In silico callus formation under (b) compression and (c) torsion loading.

One must be cognizant, that it is possible for the proportions of the *in vivo* endosteal bridge and periosteal expansion to alter between subjects. In fact, it has been shown that the endosteal bridge may be larger than the idealized geometry (specifically see Fig. 2.2b) which more closely corresponds with the above *in silico* formation.

The torsional loading scenario produced an *in silico* formation similar to the axisymmetric *in silico* periosteal formation found under axial compression loading, with the exception that the endosteal bridge was not connected (Figs. 5.2b & c). This lack of callus in the centre was due to the theoretically zero strains within neutral axis at the centre of twisting. Finally, it should be noted that, to the author's knowledge, no *in vivo* study has been conducted to determine the affect of torsion on the fracture callus, thus the *in silico* formation was compared with the *in vivo* compression loading case.

Bending moment

Under a bending moment, where both tensile and compressive strains exist, it was found that the algorithm produced a larger formation of *in silico* callus tissue on the compression side of the fracture (Fig. 5.3a). Hente *et al.* (2004) found a similar *in vivo* callus formation by applying a cyclic bending moment to fractured ovine tibiae with equivalent tensile and compressive strains on either side of the fracture gap (Fig. 5.4a). Both *in vivo* and *in silico* formations showed extensive periosteal callus on the compression side, and very little periosteal callus on the tension side (Figs. 5.3a & 5.4a).

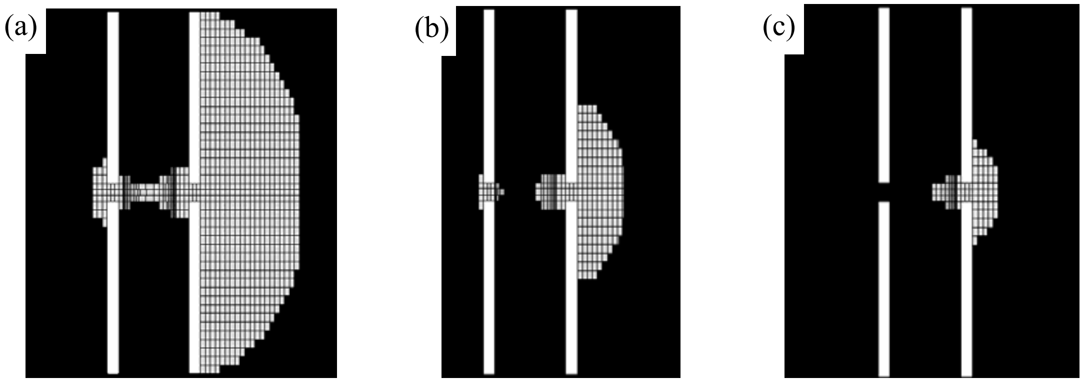

Figure 5.3. In silico callus formation under a bending moment. The majority of tissues become distributed to the compression side of the fracture which can be seen on the right side of the images. The size of the callus can be altered by varying CS%: (a) 'Large' callus predicted for e = 0.05, (b) 'medium' predicted for e = 0.1 and (c) 'small' callus predicted for e = 0.15

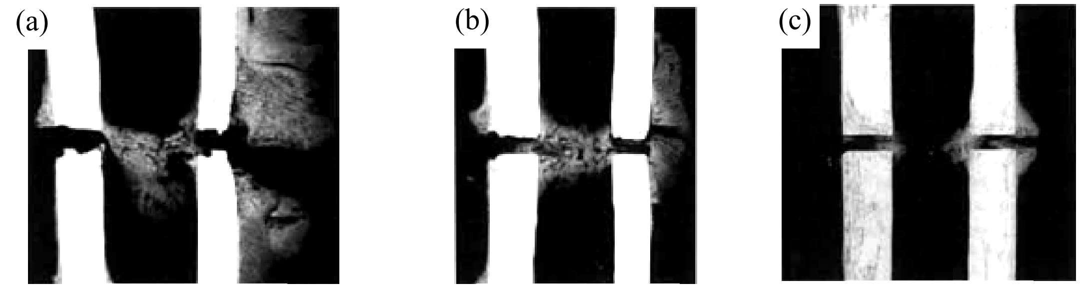

1000 cycles 10 cycles 0 cycles

Figure 5.4. Callus asymmetry observed with external fixation and with differing number of load cycles: (a) 1000 cycles, (b) 10 cycles and (c) 0 cycles (adapted Hente et al., 2004). Greater callus formation can be observed on the right side of the images where compressive strains were imparted.

The *in silico* formation, however, did not produce an endosteal bridge as was found *in vivo* due to the fact that there was theoretically no strain within the neutral axis of bending as calculated in the FE analysis. Interestingly, Hente *et al*. (2004) was able to alter the size of the callus by varying the number of loading cycles per day (Figs. 5.4b-c). Thus, to add further credence to the *in silico* formations and to test the robustness of the algorithm; an *ad hoc* analysis was conducted to generate a proportional *in silico* callus that matched the size of the *in vivo* calluses. This was accomplished by strategically altering the Elimination Coefficient to achieve a proportional *in silico* callus size that was comparable to the *in vivo* size (*cf*. Figs. 5.3b-c & Figs. 5.4b-c). The *in silico* callus sizes were reduced by increasing the *e* from the standard 0.05, to 0.10 and 0.15. Interestingly, in this situation there was an inverse relationship between the *in vivo* number of cycles and the *in silico* Elimination Coefficient. Where, *in silico,* a lower Elimination Coefficient provides a large callus, while *in vivo,* a lower number of loading cycles produces a smaller callus and *vice versa*. It was also interesting to note that when little or no cycles were applied *in vivo*, the mass of tissue became so small that no endosteal bridging forms and the tissues are localized to the inter-cortical spaces (Fig. 5.4c), which corresponds with the *in silico* formation when a high Elimination Coefficient ($e = 0.15$) was used (Fig. 5.3c).

5.3.2 On the influence of fracture geometry

The ability of the compressive principal strains to drive the efficient formation of *in silico* callus was tested in a 2D oblique and a 3D spiral fracture.

Oblique fracture

The geometry of the fracture in this case was based on the idealization of an oblique fracture and callus as described by Laboa *et al*. (2001) (Fig. 5.5a), which itself was based on histological findings by Urist *et al*. (1954). The idealized *in vivo* callus showed that the periosteal formation was skewed to the angle of the fracture. Importantly, the *in silico* formation correlated with the idealized formation, with an almost approximately equivalent axial and radial periosteal extension (Figs. 5.5a-b).

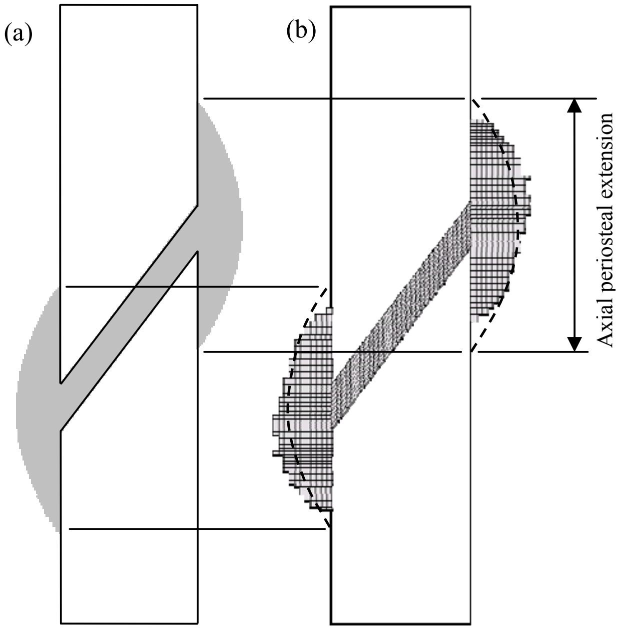

Figure 5.5. Comparison of in vivo and in silico callus formation around an oblique fracture. (a) Idealized fracture and callus geometry (adapted from Loboa et al., 2001) and (b) the predicted in silico callus formation. Note the Elimination Coefficient was increased from 0.05 to 0.08 for this specific comparison.

Spiral fracture

An idiealised model of a spiral fracture was developed to determine how the compressive principal strains predict the *in silico* callus formation. Unfortunately, unlike the above analyses, no experimental studies of spiral fractures could be found in the literature. Therefore, verifying the *in silico* callus formation directly with *in vivo* callus was difficult due to the complexity of the three-dimensional fracture geometry. Nevertheless, the numerical prediction did correspond with clinical observations where the callus would envelope the fracture site[1]. Furthermore, a qualitative comparison with a spiral fracture of the humerus (Soeda *et al*., 2002) showed that the callus formed almost uniformly around the fracture line as was found *in silico* (Fig. 5.6). In the clinical case shown below, there was complete separation of the fragments with some misalignment. Also, the radiographic image was taken 10 months post fracture where at this late stage, remodelling would most likely be underway (Figs. 5.6a). Nevertheless, the radiographic image showed that the callus literately enveloped the fracture and fracture line in a similar fashion as with the *in silico* formation (Fig. 5.6b).

---

[1] Personal communication with Mr Keith Synnott, Fracture Clinic, The Mater Misericordiae University Hospital, Dublin, Ireland.

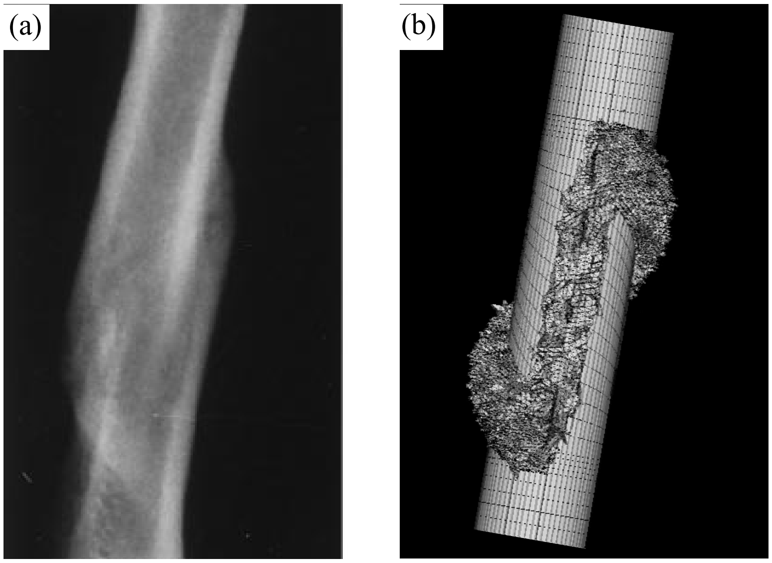

Figure 5.6. Comparison of in vivo and in silico callus formation around a spiral fracture. (a) Radiographic image showing anteroposterior view of a spiral fracture with callus formation 10 months post-fracture (Soeda et al., 2002). It can be seen that the callus envelopes the fracture line. (b) In silico callus formation also showing full envelopment of the fracture line.

5.3.3 On the influence of unilateral fixation

It was found in the literature that the inter-cortical strain gradient influences the asymmetric formation of callus tissue. In the present study, it was further conjectured that the proximity of the unilateral fixation to the bone influences the inter-cortical strain gradient thus proportionately affecting the asymmetric formation of callus tissue.

This was tested by altering the distance of the plate to the bone. Under compressive loading, the implant inevitably deflected, which induced a compressive inter-cortical strain gradient, where a higher strain was experienced on the far side of the fracture gap and *vice versa*. It was found that the unilateral fixator indeed influenced the inter-cortical strain, where an internal implant (located closer to the bone) induced a steeper strain gradient, while an external fixator (located further form the bone) induced a less severe gradient. Consequently, as was originally postulated, *in silico* a greater level of callus formation asymmetry was found under internal fixation, whereas the external fixator induced an almost symmetric formation for a fixator-bone distance of 60mm.

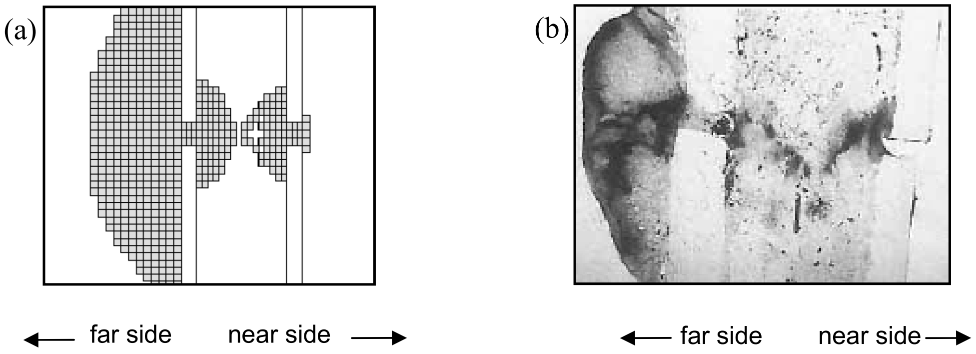

Figure 5.7. (a) Longitudinal section of in silico callus formation under unilateral fixation with a plate-bone distance of 2mm. (b) Histological sample of bone healing under unilateral fixation at week 4 with flexible implant approximately 2mm from the bone (adapted from Cheal et al., 1991). It can be seen that callus formation is significantly greater on the far-cortex where strains were highest.

The *in silico* prediction of callus under internal fixation (2mm plate-bone distance) was compared with the *in vivo* callus formations under a flexible internal plate fixation found by Cheal *et al*. (1991). From this, it was found that both the *in silico* and *in vivo* formations had both shown significant formation on the far plate-cortex, with little or no formation on the near-plate cortex (Fig. 5.7). Also, it was observed that the endosteal bridge as was disconnected in the centre in both cases. The *in silico* callus was not as physically large as the *in vivo* histological section, however, this may be attributed to the fact that the *in vivo* callus size is constrained by blood supply and surrounding soft tissues, whereas the FE model predicts the 'optimal' formation as if no constraints existed.

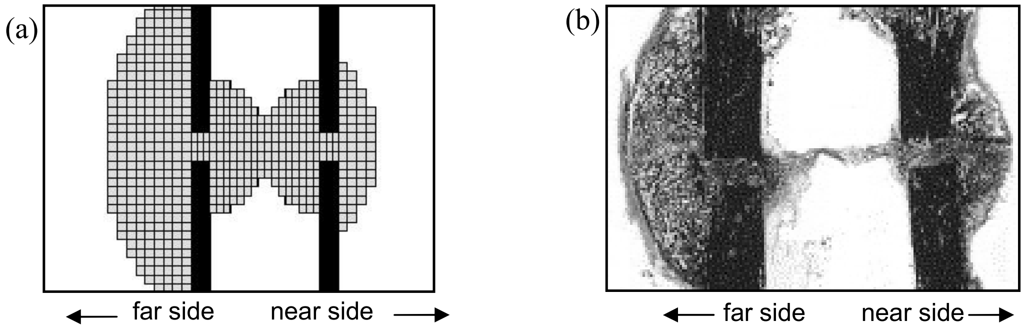

Figure 5.8. Asymmetric callus formation under external fixation. (a) Longitudinal section of in silico callus formation under unilateral fixation with a plate-bone distance of 20mm. (b) Histological sample of bone healing under unilateral external fixation at week 6 with a plate-bone distance of approximately 15mm (adapted from Epari et al., 2006).

Under external unilateral fixation, where a less severe strain gradient existed, the level of asymmetric callus formation was also less severe, with callus forming on the near side of the external fixator, as was found in both *in silico* and *in vivo* formations (Fig. 5.8). Epari *et al*., (2006) showed that a callus that formed under unilateral fixation was larger on the far side of the fixator, in comparison to the callus on the near side (Fig. 5.8b). In this case the less severe strain gradient allowed callus to form on both sides of the fracture. Finally, to surmise, under unilateral external fixation, callus tissues form on both near and far sides (Fig. 5.8) unlike under internal fixation where there was a total absence of callus on the near-cortex (Fig. 5.7).

5.3.4 Callus formation in clinical case-specific fractures

The case-specific modelling tested the robustness of the proposed algorithm and the ability of the compressive principle strains as a driving force under the most severe circumstances: physiological-like loading, misaligned bone fragments, complex fracture and bone geometries, and fixated by unilateral internal locking plates.

Oblique fracture of the tibia

The oblique fracture was based on the radiographic imagery by Gardner *et al*. (2003), who found that the *in vivo* callus tissues were formed in a skewed manner along the oblique fracture line (Fig. 5.9a-d). It could also be seen that, during the healing process, the new tissues formed within the callus, induced small changes in gross geometry over a 12 week period. Under the physiological interfragmentary displacements, as described by Gardner *et al*. (2003), the *in silico* callus was also found to form asymmetrically with the periosteal and endosteal callus skewed to the angle of the fracture line (Fig. 5.9e).

The *in silico* callus in this case does not conform to any specific time point during the healing, but does appear to correlate with the general *in vivo* formation during the reparative phase of healing. One must be cognizant, that there are numerous factors that influence the evolution of callus morphology; sex, age, blood supply etc. Considering these factors, and the continuous variation and morphology of the *in vivo* callus tissue, the *in silico* callus still predicted the general formations found *in vivo*. To re-iterate, the algorithm produces a deterministic *in silico* formation that matches the specific loading, whereas *in vivo*, it is logical that the loading will vary over time, and thus so too does the *in vivo* callus.

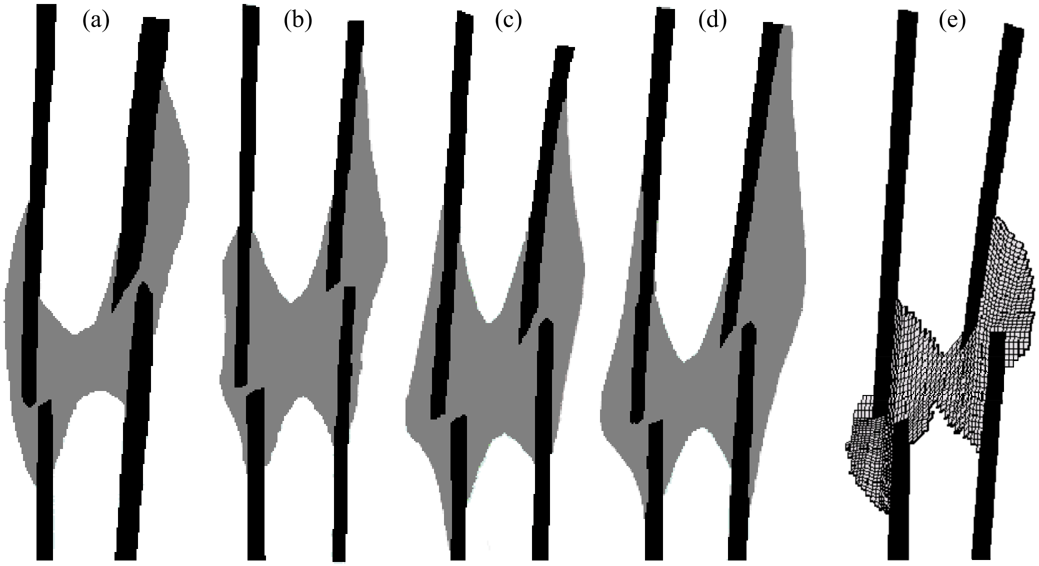

Figure 5.9. 2D representation of the morphology of a healing callus based on radiographic imagery at week (a) 4, (b) 8, (c) 12 and (d) 16 (adapted from Gardner et al. 2000, 2003, 2004). Note, the black regions represent the bone cortex and the grey region represents the callus tissue. (e) Predicted in silico callus shape based on physiological interfragmentary motions.

Transversal fracture of the tibia

The transversal fracture of the tibia was based on radiographic imagery under unilateral plate fixation. It was therefore possible to qualitatively compare the *in vivo* and *in silico* formation of the callus tissues. Figure 5.10a shows an x-ray of the healed bone with marked callus formation 3 months post operation. Importantly, from the radiographic image, it is clear that the callus has become distributed on the far-plate cortex. The *in silico* formation also shows a pattern of callus formation that agrees closely with the *in vivo* formation (Fig. 5.10b). As seen previously, the callus does not form under or near the plate. One would have assumed that this lack of near-plate formation was due to the inhibiting presence of the implant. Yet, it can be clearly seen that the bias of callus tissue can in fact be attributed to the strain gradient within the inter-cortical gap and thus the principal strains experiences by the surrounding immature callus tissues. One must remember that the FE model did not take account of contact between the tissue domain and implant, yet the *in silico* callus still did not form underneath the plate. One might argue, however, that under internal plate fixation, the *in vivo* callus will inevitably not form on the near-plate cortex due to the obstructive presence of the implant. However, in the present study, the *in silico* callus was formed based on compressive principal strains alone.

Importantly, the loading as described by Duda *et al*. (2001, 2002) caused a tensile stretching to occur at the fracture site. Based on the fact that the compressive strains were under investigation, one would have assumed that the theoretical framework would break-down under these circumstances. Nevertheless, the compressive strains produced a similar *in silico* callus under inter-cortical tension as the *in silico* calluses under inter-cortical compression. The tissues in this case were stretched in tension, which caused the compressive principle strains to act radially from the inter-cortical gap, which drove the callus tissue formation.

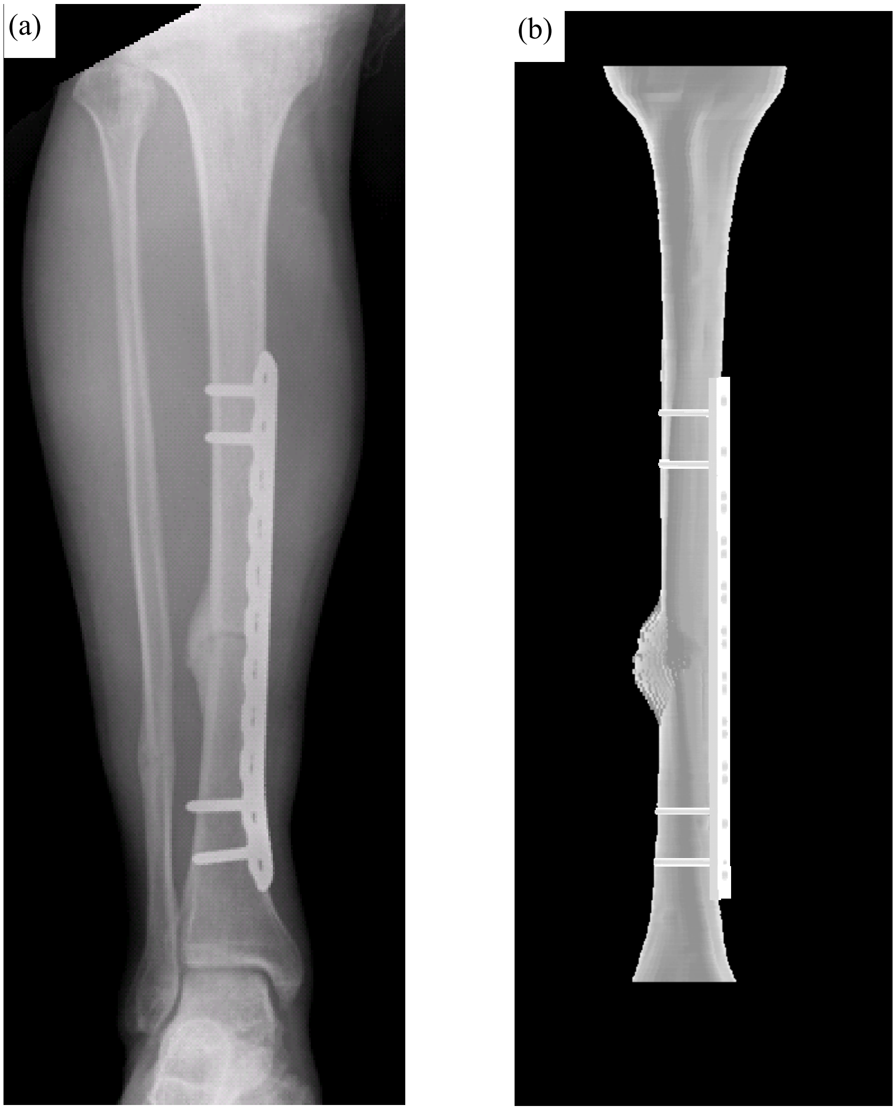

Figure 5.10. (a) Anterio-posterio view of radiographic image of fractured tibia with callus formation 3 months post-op (courtesy of Mr Willem Schenk and Mr Timothy Williams) and (b) in silico callus formation in FE model of same tibial fracture. Note, image of FE model of implant superimposed over bone and callus, also element edge lines are not shown.

Transversal fracture of the tibia with fragment misalignment

In this case, it was found that the *in vivo* fracture showed marked callus on the far-plate cortex after 6 months post operation (Fig. 5.11a). It should also be noted that, at this point the callus did not achieve bony union and so the inner-most screws were removed, soon after when the x-ray was taken. Importantly, the *in silico* prediction also showed marked callus on the far-plate cortex, which corresponds with the gross anatomy of the *in vivo* callus formation. Lastly, in this specific case, The Elimination Coefficient was lowered to produce an *in silico* callus equivalent in size with the *in vivo*.

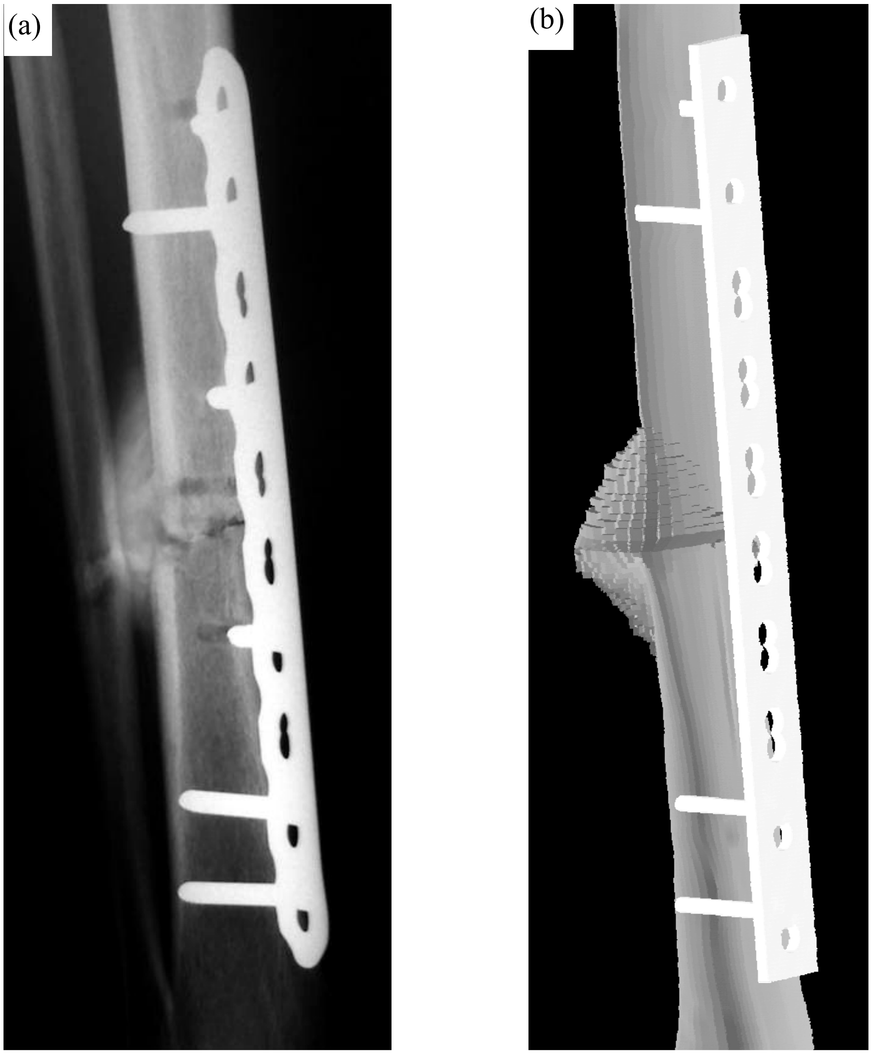

Figure 5.11. (a) Anterio-posterior view of enhanced radiographic image of fracture tibia with callus formation 6 months post-op (courtesy of Dr Nassiri and Mr David Cogley). For details of image enhancement see Appendix E. (b) In silico callus formation in FE model of same tibial fracture ($e = 0.03$). Note, image of FE model of implant superimposed over bone and callus, also element edge lines are not shown.

The mediolateral view of the same fracture which was taken 6 months after the revised operation is shown in figure 5.12a. In this case, bony union was achieved and the callus is likely to be undergoing remodelling. Consequently, the ossified callus was smaller and more efficiently sized. Also, the radiographic image shows that the callus joins the misaligned fragments at an angle. Importantly, the *in silico* formation showed good agreement, where the callus also joined the fragments at an angle (Fig. 5.12b). However, the *in silico* callus was slightly more rounded in formation, whereas the *in vivo* callus was less rounded. This discrepancy was due to the fact that the *in vivo* callus was more developed and was in the remodelling phase, whereas the *in silico* was a representation of the reparative phase. Nevertheless, the *in silico* callus formation captured the skewed formation of the *in vivo* callus.

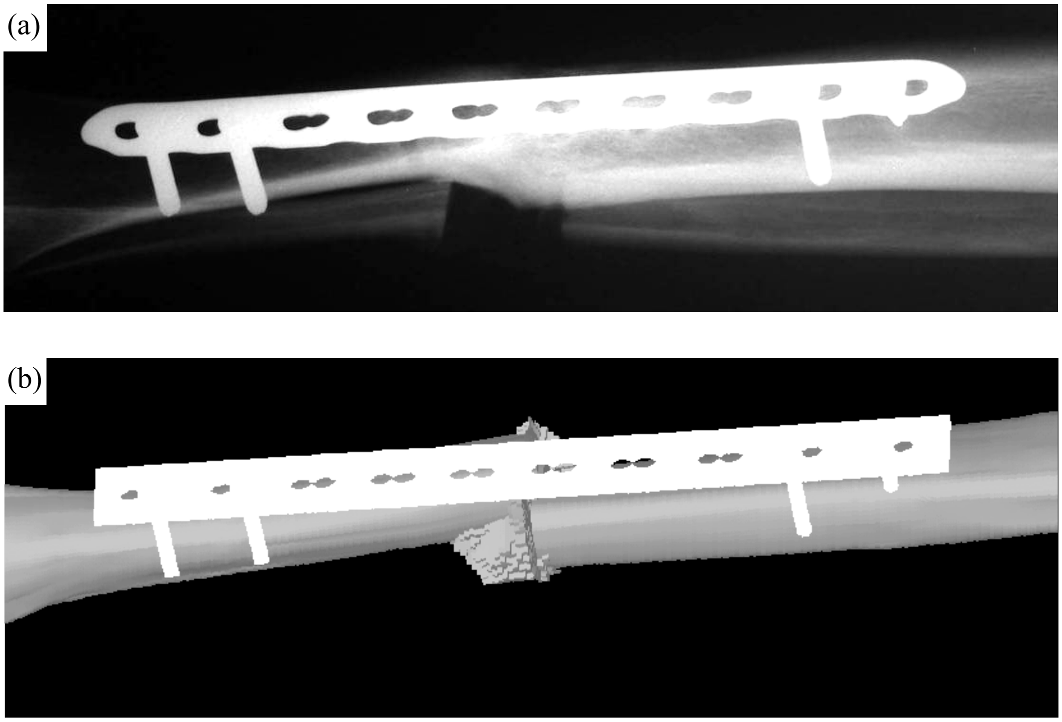

Figure 5.12. (a) Medio-lateral view of radiographic image of fracture tibia with callus formation 12 months post-op (courtesy of Dr Nassiri and Mr David Cogley). (b) In silico formation in FE model of same tibial fracture. Note, image of FE model of implant superimposed over bone and callus, also element edge lines are not shown.

Spiral fracture of the femur

The radiographic images of the femoral spiral fracture with which the FE model was based on, showed callus formation 2 months post operation on the far-plate cortex (Fig. 5.13a).

Furthermore, the formation of the *in vivo* tissue was also biased towards the most proximal aspect of the fracture line. Importantly, the *in silico* callus was also distributed along the fracture gap as had been shown in the previous idealised axial loading spiral analysis (Fig. 5.6), but in this case the *in silico* callus was also biased towards the far-plate cortex and the proximal aspect of the fracture line, which agrees with the *in vivo* formation (Fig. 5.13b). Also, the radiographic image showed that the larger formation of callus on the most proximal aspect of the fracture followed the fracture line in the distal direction, while decreasing in mass as was shown *in silico*.

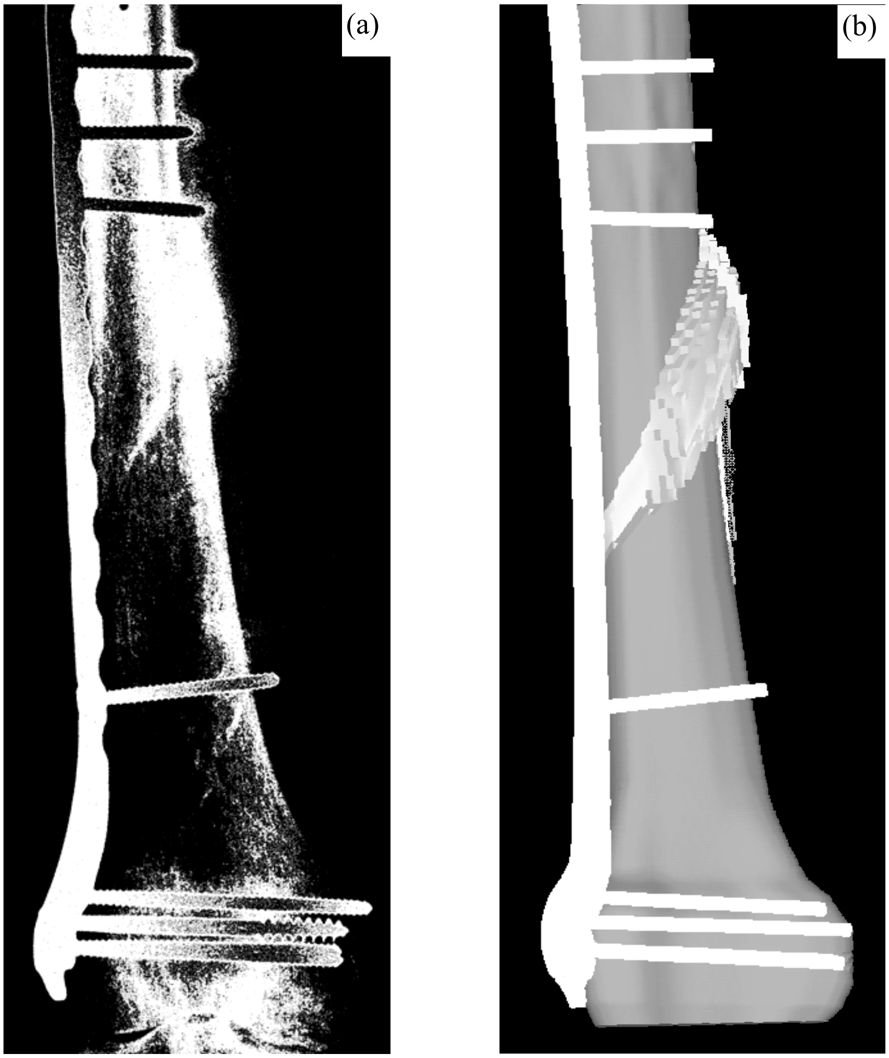

Figure 5.13. (a) Anterio-posterior view of enhanced radiographic image of femur spiral fracture fixated with locking plate fixation, where callus formation is visible 2 months post-op (courtesy of Dr Nassiri). For details of image enhancement see Appendix E. (b) In silico callus formation in FE model of same femoral fracture. Note, image of FE model of implant superimposed over bone and callus, also element edge lines are not shown.

Lastly, the latereo-medial view of the same fracture also shows significant callus on the most proximal aspect of the fracture line (Fig. 5.14a), which was also found in the *in silico* formation (Fig. 5.14b).

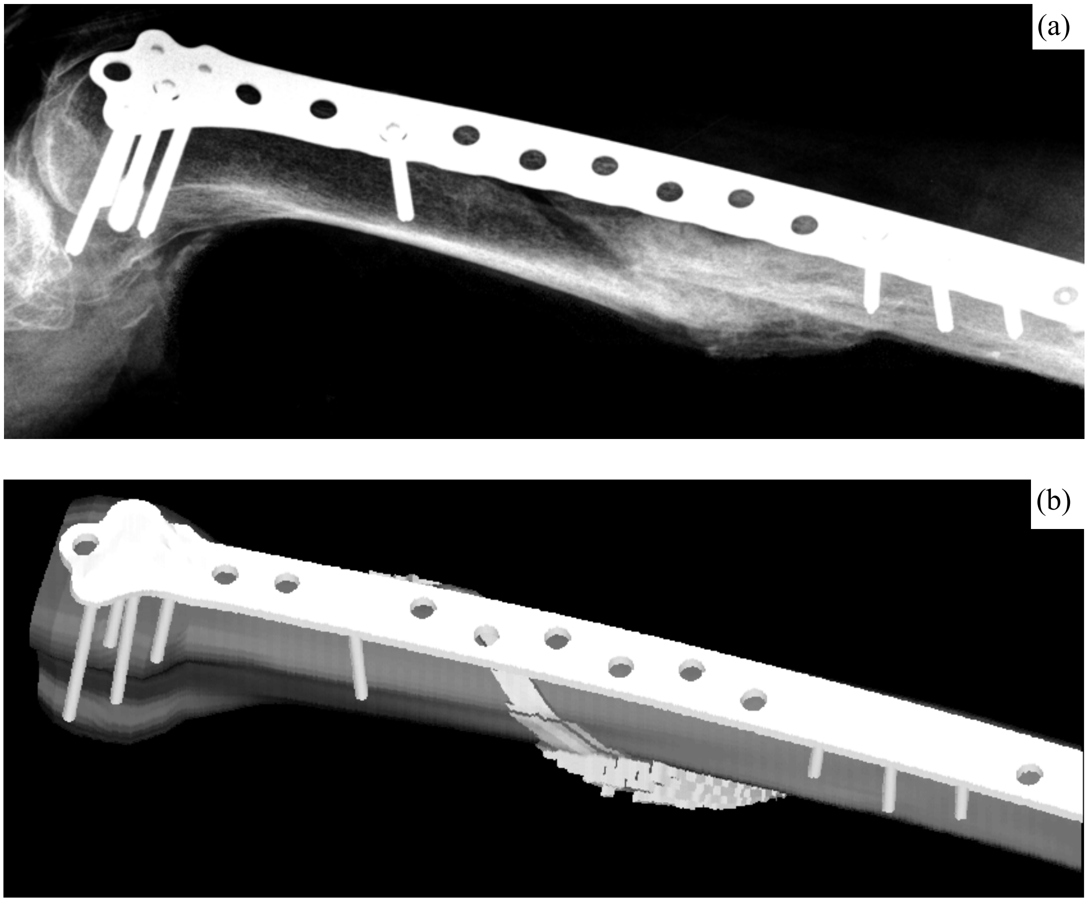

Figure 5.14. (a) Latereo-medial view of enhanced radiographic image of femoral spiral fracture fixated with locking plate fixation, where callus formation is visible 2 months post-op (courtesy of Dr Nassiri). For details of image enhancement see Appendix E. (b) In silico callus formation in FE model of same femoral fracture. Note, image of FE model of implant superimposed over bone and callus, also element edge lines are not shown.

5.4 Mechano-regulated algorithm

The mechano-regulated algorithm was intended to capture the steady state homeostatic formation of the *in silico* callus tissue. This is somewhat of a contradiction, because *in vivo* the callus does not reach 'steady state' and constantly evolves until after the remodelling process when the bone has fully healed. Nevertheless, the *in silico* formation captures a ‘snapshot’ the most efficient formation for a specific loading scenario, fracture, geometry and inter-cortical strain gradient.

What sets the proposed algorithm apart from contemporary callus simulations was that it was based on a single principal strain, requiring only 3-4 iterations to achieve convergence. In the author’s opinion, the swiftness of convergence is a testament to the ability of the compressive principal strain to achieve/drive the optimal *in vivo* callus formation.

5.4.1 Compressive principle strain as a stimulus

The present analyses were based on a static loading, which represented the maximum or peak strains during the ‘down-stroke’ of the bone fragments under cyclic loading. To re-iterate, it is the role of the callus to maintain structural stability, thus the callus will attempt to withstand the applied cyclic loading by distributing the material (callus tissue) where it was most needed to reduce interfragmentary motions. It was therefore postulated that callus tissue forms to envelope the fracture site in a mechanical efficiency manner to stabilize the bone fragments.

Thus, it was hypothesized that the compressive principal strains, caused by the relative motion of the bone fragments, drove the mechanically efficient formation of these tissues. It should be noted that under compression loading the compressive principal strains were found to be the dominant strain; 3.5 times greater than the radial strains, and 20 times greater than the circumferential strains (see Appendix B). Furthermore, the initial compressive principle strains experienced by the tissue domain showed a correspondence with the typical *in vivo* formations *i.e.* periosteal expansion and endosteal bridging.

From the computational analyses in the present study, it was found that the compressive principal strains drove the formation of the tissues during the reparative phase of healing which are known to be sensitive to mechanical loading (Klein *et al*., 2003). It should also be noted that after a bone fracture, the inflammation provides a domain through which other tissues can develop; these include the immature callus tissues or initial connective tissues. In the present study, the low strains adjacent to the fracture gap not only influenced the formation of the initial connective tissues, but also influenced the future of tissue differentiation.

The results of the present computational study have shown that compressive strains are responsible for the formation of the gross formation of callus tissues. If these strains predict the gross formation, then it is logical to infer that they too affect the microstructural formation; including fibrous tissue, cartilage and bone. It should be noted that, the present study remained on a macroscopic level since physiological and cellular mechanisms are not yet fully understood and thus the validity of the continuum mechanics approach for modelling cellular events is not clear (Doblaré *et al*., 2004). Nevertheless, early callus tissues act as a scaffold through which pluripontential cells migrate and differentiate through. Thus, it can be inferred that on a macroscopic level, that the compressive strains influence the various cells to differentiate which results in the observed gross formation of the callus where mechanical stimulus persists.

It has been theorised that the callus is driven by a combination of the three principal strains as calculated by the octahedral shear strain, hydrostatic strain and strain energy density (Carter and coworkers; Ament and Hofer, 2000) as well as interstitial fluid flow (García-Aznar *et al*., 2007; Prendergast *et al*., 1997). However, in the present study, the compressive principal strains have been isolated and identified as the main driving force behind the gross formation of the callus. This does not necessarily negate the aforementioned mechanical stimuli, whose affects may have specific functions by influencing the differentiation of specific aspects of the internal callus formation, but it has been shown that the said stimuli are less relevant to the gross formation.

Lastly, Carter and Beaupré (2001) had suggested that the low strains in the early periosteal callus would have no effect on the initial fibrous tissues. However, the results of the present study would suggest that these low strains adjacent to the fracture gap, experienced within in the immature granulation callus, in fact predicted the *in silico* formation of tissues.

5.4.2 Elimination Coefficient as a parameter

The algorithm proposed in the present study required only one parameter, Elimination Coefficient, which was essentially a percentage value of the maximum magnitude of compressive principal strain. This parameter acts as a threshold which dictated the removal of tissue from the domain which fell below that threshold. This was the only parameter in the algorithm that needed alteration. In the present study, the Elimination Coefficient normalized the strain so the initial material properties did not require alteration for a specific fracture gap, unlike that of Lacroix and Prendergast (2002a).

The Elimination Coefficient was found to produce *in silico* callus of reasonable size similar, to *in vivo* formations with a range of 0.01 – 0.15, where a value of 0.05 was found to adequately capture the formation for the majority of *in vivo* cases. It must be stated that the author is under no illusion that *in vivo* such a parameter exists, but it was necessary *in silico* due to the assumptions and generally the nature of the finite element method. Nevertheless, alteration of the Elimination Coefficient did appear to correspond (inversely) with the level of mechanical stimulus and the resulting *in vivo* callus tissue mass, as was exemplified earlier (see Figs. 5.3-5.4).

5.5 Limitations of the predictive modelling methods

Based on the title of this thesis, it is expected that the proposed modelling methods can predict the natural phenomena found in bone healing. One must be aware that it can be difficult to model nature, and especially bone healing, due to the number of factors which will alter the spatial and temporal aspects of healing between subjects. According to Thompson (1942), there is a principle of negligibility with regards to modelling nature:

> *"The physicist or mathematician can give us perfectly satisfying expressions for the form of a wave, or even of a heap of sand; but we never ask him to define the form of any particular wave of the sea, nor the actual form of any particular mountain-peak or hill."*

Nevertheless in the present study, every attempt was made to correlate the mathematical and computational models with the patterns and formations found in nature. There are of course limitations of these models.

5.5.1 Limitations of the mathematical model

There were a number of limitations and restrictions of the mathematical model. Firstly, the model was restrained to weeks 1-8 of healing and, secondly, the model was based on an initially applied interfragmentary strain at week one. If, for example, the strains *in vivo* were applied later, then it is likely that divergence may not be observed, as was found with Hente *et al*. (1999) who applied the IFS at the fourth week of healing. Furthermore, the mathematical model was based on experimental studies of fracture gap sizes that ranged from 1-6mm, it is therefore uncertain whether the model behaves the same outside of this range.

Furthermore, the mathematical model was based on the mean or average datum points from Claes and coworkers (1997, 1999). To extract meaningful results, the re-interpretation of the datum points assumed that these mean interfragmentary motions were the ‘true’ datum points, thus ignoring the error bars (see Fig. 2.9). In the present study, these ‘true’ datum points between interfragmentary strains cases were averaged for the 7% and 31% cases (see Fig. 3.2). This was essentially an average of an average. Thus that the statistical significance between the 7% and 31% interfragmentary cases, were based upon these doubly averaged datum points (see Fig. 4.1). Consequently, the reliability of the statistical significance is uncertain.

The model itself, describes the relative increase in stiffness, therefore, it does not suggest that the fracture gap size has no influence on healing. Importantly, a larger gap size, will not only induce a mechanical disadvantage, but has shown to delay healing (Claes *et al*., 2003). What this means is that, although the proposed model suggests a greater rate of stiffening for a larger gap size (up to 6mm), it does not suggest improved healing. It should also be noted, that the mathematical model is phenomenological and gives no indication as to the quality of the callus, such as the percentage of new bone cells, or in other words, the level of ossification.

5.5.2 Limitations of the *in silico* callus formation

The callus formation algorithm presented in this study, was intended as a predictive method of modelling *in silico* callus that matched the *in vivo* formation. One must be cognizant that the simulated callus formation can only be of a qualitative character as there are many biological factors that can cause variation. Thus the main goal was to produce numerical results which showed similarities to the *in vivo* structures. In some cases, the critical strain parameter had to be tweaked to achieve the same physical proportions as was observed in the histological examinations and/or radiographic images.

It is uncertain which exact time-point during healing the *in silico* formation best captures the *in vivo* formation. It is proposed, nevertheless, that the *in silico* formation generally best captured the reparative phase of healing. Despite this, it is clear that during this phase the callus morphology, changes in the external structure as was observed from Gardner *et al*. (2003) (see Fig. 5.9).

The *in silico* formation represents an idealised mass of tissue to best cope with the mechanical stimulus, and thus to optimize the structure of the healing tissues to improve mechanical stability. *In vivo* it is clear that a number of mitigating factors will prevent the callus from freely forming, whereas, the *in silico* formation is not restricted by lack of blood supply, age, sex, metabolic rate, surrounding soft tissues, local vasculature and whether the patient smokes or not.

Lastly, it was assumed that the tissue domain, was homogeneous, isotropic, and linearly pseudoelastic, while in reality these tissues are bi-phasic, which implies viscoelasticity (stress relaxation & creep). Nevertheless, one must be aware that these assumptions were appropriate to the approach used to test the hypothesis under investigation, and therefore did not compromise the predictive quality of the compressive principal strains to determine structural tissue formation.

5.6 Clinical implications and limitations

To re-iterate, both the computational and mathematical models were based on mechanical stimulus created by the relative motion between bone fragments; where the former models the formation of healing tissues, while the latter models the rate of healing (tissue stiffening through differentiation).

5.6.1 Combination of modelling strategies

The obvious corollary is to combine the mathematical and computational modelling methods for use in FE modelling for bone healing predictions (Fig. 5.15). For example, the proposed algorithm can be utilised to simulate the callus formation in an FE model, and its initial material stiffness. Then, based on the presumed loading it would be possible to determine the level of initial interfragmentary strain and using the mathematical model, approximately predict the rate of callus stiffening until the 8th week of healing. To determine the feasibility and accuracy of such an approach, an *ad hoc* analysis was conducted which compared the rate of callus stiffening of an existing FE model of callus healing by tissue differentiation (Claes and Heigele, 1999) and the combination of the proposed methods (see Appendix F). The approximated IFS was inputted into the mathematical model which simulated the rate of healing (increase in stiffness) more accurately than if the effort were to be put into modelling the various tissues that become present during healing. Although this only represented one example, it does however show that the proposed modelling strategies can be used as a substitute for simulating tissue differentiation in a FE model.

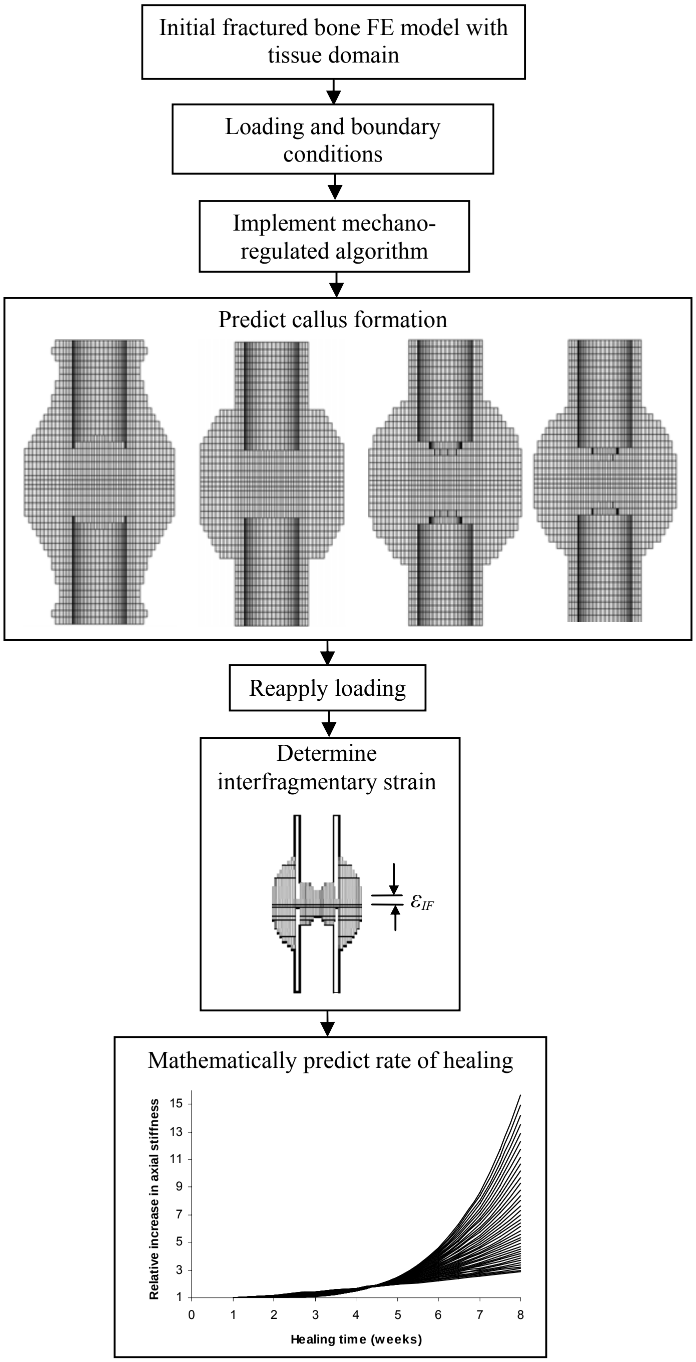

Figure 5.15. Flow chart of combination of computational and mathematical methods.

5.6.2 A pre-clinical testing tool

Based on the results shown in the present study, one could implement the proposed strategies in an expert system used to guide or aid the planning of orthopaedic fracture repair or implant design. For example, the *in silico* formation of callus may be used to aid the design of a bone fixator for pre-clinical testing. Thus, an implant may be designed to account for the healing bone tissues for a given fracture and determine the callus formation under the specific implant design.

Also, in fracture repair, a surgeon must consider a number of factors for successful healing and implantation; the mechanical environment at the fracture site and the stresses experienced by the implant. The former will influence the rate of healing, while the latter may lead to mechanical failure through bending (plastic deformations) and/or catastrophic breakage (fatigue failure) (Sharma *et al.*, 2006). If, however, the interfragmentary strain can be calculated numerically with good accuracy for a given fracture, implant configuration and patient weight, then theoretically, one could determine the rate of healing as an increase in stiffness based on the proposed mathematical model. Consequently, predictions in the implant stress could be analyzed to ensure the implant does not experience stresses that are likely to lead to failure by either fatigue of plastic deformation. The proposed methods, therefore, show potential as a risk assessment tool so that implant failure can be avoided by altering the configuration of the implant to suit the specific patient's attributes. A similar concept was proposed by Lacroix and Prendergast (2002b), based on their modelling methods.

5.6.3 Limitations of a pre-clinical tool

Regarding the application to clinical use, there are a number of caveats that should be noted. Firstly, the mathematical model was based on increase in compressive stiffness in idealised ovine tibial transversal gap-osteotomized fractures, consequently, the ability of the model to predict the rate of healing for other fracture types or loading scenarios is uncertain. Also, when modelling patient-specific bones and implants, it is known that there is much natural variation that needs to be taken into account. Even in controlled circumstances, a 15.6% average error was found in the experimental and FE model of the bone and locking plate (see Appendix C).

5.7 Achievements of this study

The present study investigated the effects of mechanical stimulus on the spatial formation of callus tissue. To the author's knowledge, this has been the most comprehensive study to date, due to the diversity of fractures and loading scenarios that were investigated. Furthermore, the results of the present study were qualitatively compared with an abundance of *in vivo* callus formations. To the author's knowledge, no other study in bone healing simulation, or in mechanobiology for that matter, was capable of providing the same level of *in vivo* evidence to determine the strength of their hypotheses.

More importantly, it was shown that compressive principal strains drove the gross formation of callus tissues, whereas, previous computational studies generated the callus manually, with no consideration to its initial formation, or modelled it as a gradual expansion by excluding the initial granulation tissue formation. Furthermore, the proposed mechano-regulated algorithm proved to be highly robust which could automatically capture the formation of callus tissue in type-A fractures of long bones, as well as asymmetric callus formation under unilateral fixation.

The rate of callus healing and influence of mechanical stimulus has been identified based on a comparative review of experimental data. The mathematical modelling of a causal relationship between rate of healing and the initially applied interfragmentary strain has never before been presented until now. Furthermore, the present study did not rely on purely qualitative comparisons, but was in fact capable of showing direct correlations using error and statistical analyses, over a wide range of interfragmentary strains (7 – 45%).

Patient specific modelling has become more prevalent as computer power and knowledge of the influences of mechanical stimulus on tissue differentiation has increased. The success of patient specific modelling, however, relies on efficient modelling and therefore virtually instantaneous computer solving time. The current trends in callus modelling, as described in Chapter 2, were not conducive to fast solution times[1,2,3]. The proposed methods, however, considerably reduced these times by alternative modelling methods. As a result, there are obvious implications for the proposed strategies in pre-clinical testing or pre-operative planning. One should be mindful that no expert system

---

[1] Correspondence with Prof. Damien Lacroix, Institute of Bioengineering of Catalonia, Barcelona, Spain.

[2] Correspondence with Dr. Damien Byrne, Trinity Centre for Bioengineering, Trinity College Dublin, Ireland.

[3] Correspondence with Dr. Alex Lennon, Trinity Centre for Bioengineering, Trinity College Dublin, Ireland.

currently exists which attempts to simulate bone healing in a practical pre-clinical FE modelling manner. Consequently, this study was the first attempt to move towards efficient case specific modelling of bone healing. Interestingly, Lacroix (2000) suggested that if we are to move forward in callus modelling, it will be necessary to automatically generate the mesh of the immature callus through which differentiation can occur. This study has achieved that goal.

Chapter 6 - Conclusions

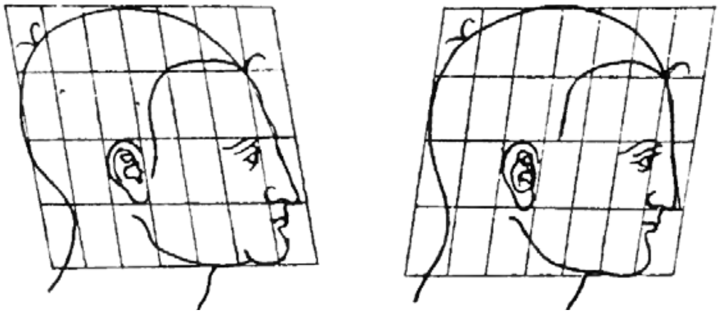

Alteration of perception:
Coordinate geometry used to transform facial features
(After Thompson, 1942).

Contents

6.1 Main results of this study

The aims of this study were to determine the dominant mechanical stimulus that drove the efficient formation of callus tissue and to derive a relationship between stimulus and the rate of healing. Computational and mathematical models and methodologies were devised to predict phenomena that occurred during bone healing. The main conclusions of this thesis are as follows:

1. Experimental data has been re-evaluated and compared in a novel manner which revealed that there is a positive correlation between the rate of callus compressive stiffening and the initially applied interfragmentary strain.

2. The rate of callus compressive stiffening can be described as mathematical function of both healing time and initially applied interfragmentary strain within the range of 7 - 45%.

3. Compressive principle strains caused by inter-cortical motions were found to drive the efficient structural formation of the reparative phase of bone healing.

4. Compressive principle strains also drove the formation of callus tissue under both compressive and tensile inter-cortical strains.

5. The proximity of the unilateral fixator's neutral axis to the fracture gap influences the spatial distribution of tissue, where the closer the implant is to the bone the greater the level of asymmetry and *vice versa*.

6. The lack of inter-cortical strain on the near-plate cortex was found to be the most important factor influencing the lack of callus growth under the plate and not the physical presence of the plate itself.

6.2 Future considerations

If the proposed methodologies were to be implemented into a pre-clinical tool then it would be advisable to introduce uncertainty into the FE model. This is because a FE model is a deterministic system, and will therefore produce the same output unless the inputs are changed. It is known that the initial connective tissue at week one not only can vary in material stiffness (Leong and Morgan, 2008) but also has a significant influence on the structural stiffness. Thus there will be some indeterminacy in its future evolution of callus stiffness. Dar *et al*. (2002) highlighted the importance of introducing uncertainty into a finite element model, especially in biomechanics, where there is a wide variation in the material properties or geometry of living tissues. A probabilistic analysis can be used to randomly choose a number of inputs, according to a Monte Carlo simulation so that the finite element model simulates a spread of values (mean and standard deviation). If a percentage of uncertainty is inputted, then a confidence interval could be sought.

Furthermore, if we were to apply the bone formation algorithm in patient specific studies, then we would need to know how the Elimination Coefficient relates to the *in vivo* size of a callus. For example, if the subject lacked blood supply in the fractured area, then the parameter could be tuned in anticipation for a smaller callus. This, however, will require further study so that a relationship between biological factors and the Elimination Coefficient can be properly defined.

Finally, in the present study, every attempt was made to verify the formation of the *in silico* callus formation using 2D radiographic or histological images. However, three dimensional imagery by MRI or CT scans of healing fractures would better validate the *in silico* calluses, especially the more complex fracture types[1]. Furthermore, it would be necessary to validate the mechano-regulated method using other fracture types such as multi-fragment fractures[2].

---

[1] Personal communication with Professor John O'Byrne, consultant orthopaedic surgeon, Cappagh National Orthopaedic Hospital, Dublin, Ireland.

[2] Personal communication with Dr. Ian Robertson, general surgeon, The Mater Misericordiae University Hospital, Dublin, Ireland.

References

Akkus, O., Korkusuz, F., Akin, S., Akkas, N., 1998. Relation between mechanical stiffness and vibration transmission of fracture callus: an experimental study on rabbit tibia. Proceedings of the I MECH E Part H Journal of Engineering in Medicine 212, 327-336.

Alms, M., 1969. Fracture Mechanics. The journal of bone and bone joint surgery 43, 162-166.

Ament, C.H., Hofer, E.P., 2000. A fuzzy logic model of fracture healing. Journal of biomechanics 33, 961-968.

Andreykiv, A., van Keulen, F., Prendergast, P.J., 2007. Simulation of fracture healing incorporating mechanoregulation of tissue differentiation and dispersal/proliferation of cells. Biomechanics and modeling in mechanobiology 7, 1617-7959.

Augat, P., Margevicius, K., Simon, J., Wolf, S., Suger, G., Claes, L., 1998. Local tissue properties in bone healing: inuence of size and stability of the osteotomy gap. Journal of orthopaedic research 16, 475-481.

Bailón-Plaza, B., van der Meulen, M.C.H., 2001. A mathematical framework to study the effects of growth factor infuences on fracture healing. Journal of theoretical biology 212, 191-209.

Bendsøe, M.P., Sigmund, O., Topology optimization. Springer, Berlin, 2003.

Bergmann, G., Graichen, F., Rohlmann, A., 1993. Hip joint loading during walking and running, measured in two patients. Journal of biomechanics 26, 969-990.

Boccaccio, A., Lamberti, L., Pappalettere, C., Carano, A., Cozzani, M., 2006. Mechanical behaviour of an osteotomized mandible with distraction orthodontic devices. Journal of biomechanics 29, 2907-2918.

Byrne, D., (2008). "Computational modelling of bone regeneration using a three-dimensional lattice approach", Ph.D. Thesis, University of Dublin, Dublin, Ireland.

Carter, D.R., Fyhrie, D.P., Whalen, R.T., 1987. Trabecular bone density and loading history: regulation of connective tissue biology by mechanical energy. Journal of biomechanics 20, 785-794.

Carter, D.R., Blenman, P.R., Beaupré, G.S., 1988. Correlations between mechanical stress history and tissue differentiation in initial fracture healing. Journal of orthopaedic research 6, 736-748.

Carter, D.R., Beaupré, G.S., Skeletal function and form. Cambridge University Press, Cambridge, 2001.

Chao, C-K., Hsu, C.-C., Wang, J.-L., Lin, J., 2006. Increasing bending strength of tibial locking screws: Mechanical tests and finite element analyses. Clinical biomechanics 22, 59-66.

Cheal, E.J., Mansmann, K.A., DiGioia, A.M., Hayes, W.C., Perren, S.M., 1991. Role of interfragmentary strain in fracture healing: ovine model of a healing osteotomy. Journal of orthopaedic research 9, 131-142.

Chen, G., Pettet, G.J., Pearcy, M., McElwain, D.L.S., 2007. Modelling external bone adaption using evolutionary structural optimisation. Biomechanics and modeling in mechanobiology 6, 275-285.

Cheung, G., Zalpal, P., Bhandari, M., Spelt, J.K., Papini, M., 2004. Finite element analysis of a femoral retrograde intramedullary nail subject to gait loading. Medical engineering & physics 26, 93-108.

Christel, P., Cerf, G., Pilla, A., 1981. Time evolution of the mechanical properties of the callus of fresh fractures. Annals of biomedical engineering 9, 383-391.

Claes, L., Wilke, H-J., Augat, P., Rübenacker, S., Margevicius, K.J., 1995. Effect of dynamization of diaphyseal fractures under external fixation. Clinical biomechanics 5, 227-234.

Claes, L., Augat, P., Suger, G., Wilke, H-J., 1997. Influence of size and stability of the osteotomy gap on the success of fracture healing. Journal of orthopaedic research 15, 577-584.

Claes, L.E., Heigele, C.A., 1999. Magnitudes of local stress and strain along bony surfaces predict the course and type of fracture healing. Journal of biomechanics 32, 255-266.

Claes, L., Eckert-Hübner, K., Augat, P., 2002. The effect of mechanical stability on local vascularization and tissue differentiation in callus healing. Journal of orthopaedic research 20, 1099-1105.

Claes, L., Eckert-Hübner, K., Augat, P., 2003. The fracture gap size influences the local vascularization and tissue differentiation in callus healing. Langenbeck's archives of surgery 388, 316-322.

CristofoIini, L., Viceconti, M., Cappelio, A., Toni, A., 1996. Mechanical validation of whole bone composite femur models. Journal of biomechanics 29, 525-535.

Dar, F.H., Meakin, J.R., Aspden, R.M., 2002. Statistical methods in finite element analysis. Journal of biomechanics 35, 1155-1161.

Doblaré, M., García, J.M., Gómez, M.J., 2004. Modelling bone tissue fracture and healing: a review. Engineering fracture mechanics 71, 1809-1840.

Duda, G.N., Mandruzzato, F., Heller, M., Goldhahn, J., Moser, R., Hehli, M., Claes, L., Haas, N.P., 2001. Mechanical boundary conditions of fracture healing: borderline indications in the treatment of undreamed tibial nailing. Journal of biomechanics 34, 639-650.

Duda, G.N., Mandruzzato, F., Heller, M., Kassi, J-P., Khodadadyan, C., Hass, N.P., 2002. Mechanical conditions in the internal stabilization of the proximal tibial defects. Clinical biomechanics 17, 64-72.

Einhorn, T.A., 1998. The cell and molecular biology of fracture healing. Clinical orthopaedocs and related research 355, 7-21.

El-Shiekh, H., (2002), "Finite Element Simulation of Hip Joint Replacement under Static and Dynamic Loads", Ph.D. Thesis, Dublin City University, Dublin, Ireland.

Epari, D.R., Schell, H., Bail, H.J., Duda, G.N., 2006. Instability prolongs the chondral phase during bone healing in sheep. Bone 38, 864-870.

Ferguson, S.J., Wyss, U.P., Pichora, D.P., 1995. Finite element analysis of a hybrid fracture fixation plate. Medical engineering & physics 18, 241-250.

Fung, Y.C., Biomechanics: mechanical properties of living tissues (2nd Ed.). Springer, New York, 1993, pp. 261-262.

García-Aznar, J.M., Kuiper, J.H., Gómez-Benito, M.J., Doblaré, M., Richardson, J.B., 2007. Computational simulation of fracture healing: Influence of interfragmentary movement on the callus growth. Journal of biomechanics 40, 1467-1476.

Gardner, T.N., Evans, M., Simpson, H., 1998. Temporal variation of applied inter fragmentary displacement at a bone fracture in harmony with maturation of the fracture callus. Medical engineering & physics 20, 480-484.

Gardner, T.N., Stoll, T., Marks, L., Mishra, S., Knothe Tate, M., 2000. The influene of mechanical stimulus on the pattern of tissue differentiation in long bone fracture – A FEM study. Journal of biomechanics 33, 415-425.

Gardner, T.N., Mishra, S., 2003. The biomechanical environment of a bone fracture and its influence upon the morphology of healing. Medical engineering & physics 25, 455-464.

Gardner, T.N., Mishra, S., Marks, L., 2004. The role of osteogenic index, octahedral shear stress and dilatational stress in the ossification of a fracture callus. Medical engineering & physics 26, 493-501.

Giori, N.J., Beaurpé, G.S., Carter, D.R., 1993. Cellular shape and pressure may mediate mechanical control of tissue consumption in tendons. Journal of orthopaedic research 11, 581-591.

Goodship, A.E., Kenwright, J., 1985. The influence of induced micromotion upon the healing of experimental tibial fractures. Journal of bone and bone joint surgery (Br) 67, 650-655.

Goodship, A.E., Cunningham, J.L., Kenwrigth, J., 1998. Strain rate and timing of stimulation in mechanical modulation of fracture healing. Clinical orthopaedics 335, 105-115.

Goodship, A.E., Cunningham, J.L., 2001. Pathology of function adaption of bone remodelling and repair in vivo. In: Cowin. S.C., (Ed.), Bone Biomechanics Handbook (2nd Ed.) CRC Press, New York, 2008, pp. 22-25.

Harrigan, T.P., Hamilton, J.J., 1994. Bone remodelling and structural optimization. Journal of biomechanics 27, 323-328.

Heller, M., Mandruzzato, F., Hehli, M., Importance of muscle forces on the loading of fractured tibia after unreamed nailing. Trans. Eur. Orthop. Res. Soc. (1999) 1,O8.

Hente, R., Cordey, J., Rahn, B.A., Maghsudi, M., von Gumppenberg, S., Perren, S.M., 1999. Fracture healing of the sheep tibia treated using a unilateral external fixator – comparison of static and dynamic fixation. Injury 30, 44-51.

Hente, R., Cordey, J., Perren, S.M., 2003. In vivo measurement of bending stiffness in fracture healing. Biomedical engineering online 2, 8.

Hente, R., Füchtmeier, B., Schlehel, U., Ernstberger, A., Perren, S.M., 2004. The influence of cyclic compression and distraction on the healing of experimental tibial fractures. Journal of orthopaedic research 22, 709-715.

Huiskes, R., Weinans, H., Grootenboer, H.J., Dalstra, M., Fudala, B., Sloof, T.J., 1987. Adaptive bone remodelling theory applied to prosthetic-design analysis. Journal of biomechanics 20, 1135-1150.

Huiskes, R., Ruimerman, R., van Lenthe, G.H., Janssen, J.D., 2000. Effects of mechanical forces on maintenance and adaptation of form in trabecular bone. Nature 405, 704-706.

Humfrey, J.D., Delance, S.L., Biomechanics: solids and fluids, analysis and design. Springer-Verlag, New York, 2004, pp.278-279.

Isaksson, H., Wilson, W., van Donkelaar, C.C., Huiskes, R., Ito, K., 2006. Comparison of biophysical stimuli for mechano-regulation of tissue differentiation during fracture healing. Journal of biomechanics 39, 1507-1516.

Koval, K. J., Sala, D. A., Kummer, F.J., and Zuckerman, J. D., 1998. Postoperative weight-bearing after a fracture of the femoral neck of an intertrochanteric fracture. The journal of bone and joint surgery 80, 352-356.

Klein, P., Schell, H., Streitparth, F., Heller, M., Kassi, J-P., Kandziora, F., Bragulla, H., Hass, N.P., Duda., G.N., 2003. The initial phase of fracture healing is specifically sensitive to mechanical conditions. Journal of orthopaedic research 21, 662-669.

Lacroix, D., (2000). "Simulation of tissue differentiation during fracture healing", Ph.D. Thesis, University of Dublin, Dublin, Ireland.

Lacroix, D., Prendergast, P.J., 2002a. A mechano-regulation model for tissue differentiation during fracture healing: analysis of gap size and loading. Journal of biomechanics 35, 1163-1171.

Lacroix, D., Prendergast, P.J., 2002b. Three-dimensional simulation of fracture repair in the human tibia. Computer methods in biomechanics and biomedical engineering 5, 369-376.

Leong, P.L., Morgan, E.F., 2008. Measurement of fracture callus material properties via nanoindentation. Acta biomaterialia 4, 1569-1575.

Lienau, J., Schell, H., Duda, G.N., Seeback, P., Muchow, S., Bail, H.J., 2005. Initial vascularization and tissue differentiation are influenced by fixation stability. Journal of orthopaedic research 23, 639-645.

Loboa, E.G., Beaupré, G.S., Carter, D.R., 2001. Mechanobiology of initial psuedoarthrosis formation with oblique fractures. Journal of orthopaedic research 19, 1067-1072.

Loboa, E.G., Fang, T.D., Warren, S.M., Lindsey, D.P., Fong, K.D., Longaker, M.T., Carter, D.R., 2004. Mechanobiology of mandibular distraction osteogenesis: experimental analyses with a rat model. Bone 34, 336-343.

Loboa, E.G., Fang, T.D., Parker, D.W., Warren, S.M., Fong, K.D., Longaker, M.T., Carter, D.R., 2005. Mechanobiology of mandibular distraction osteogenesis: finite element analysis with a rat model. Journal of orthopaedic research 23, 663-670.

McKibbon, B., 1979. The biology of fracture healing in long bones. The journal of bone and bone joint surgery 60, 150-162.

Mirishra, S., Gardner, T.N., 2001. Comparative two- and three-dimensional finite element techniques for tibial fractures. Proceedings of the institution of mechanical engineers, Part H: Journal of engineering in medicine 215, 255-258.

Moorcroft, C.I., Ogrodnik, P.J., Thomas, P.B.M., Wade, R.H., 2001. Mechanical properties of callus in human tibial fractures: a preliminary investigation. Clinical biomechanics 16, 776-782.

Moorcroft, C., Ogrodnik, P., Thomas, P., 2007. Reliability of fracture stiffness as a measurement of clinical union and visco-elastic properties of callus. Injury extra 38, 164.

Mora, G., Forriol, F., 2000. Mechanical analysis of the healing of different osteotomies fixed externally. International orthopaedics 24, 295–298.

Moukoko, D., Pithioux, M., Charbrand, P., 2007. Temporal evolution of mechanical properties of skeletal tissue regeneration in rabbits: an experimental study. Medical and biological engineering and computing 45, 989-995.

Mullender, M.G., Huiskes, R., Weinans, H., 1994. A physiological approach to simulation of bone remodelling as a self-organizational process. Journal of biomechanics 27, 1389-1394.

Müller M.E., Nazarian, S., Koch, P., Schatzker, J. The comprehensive classification of fractures of the long bones. Springer, Berlin, 1990.

Nakahara, H., Bruder, S.P., Haynesworth, S.E., Holecek, J.J., Baber, M.A., Goldberg, V.M., Caplan, A.I., 1990. Bone and cartilage formation in diffusion chambers by subcultured cells derived from the periosteum. Bone 11, 181-188.

Nolte, D., Urban, K., Niemeyer, F., Claes, L., Simon, U., Simulation and optimization of fracture healing, in Proc. 14th Finite Element Workshop, 18th-19th July, 2007, University of Ulm, Germany.

Pauwels, F., 1960. Eine neue theorie über den einflub mechanischer reize auf die differenzierung der stützgewebe. Z Anat Entwickl. Gesch. 121, 478–515. Translated as A new theory concerning the influence of mechanical stimuli on the differentiation of the supporting tissues. In: Maquet, P., Furlong, R. (Eds.), Biomechanics of the locomotor apparatus, Springer, Berlin, 1980, 375–407.

Perren, S.M., 1979. Physical and biological aspects of fracture healing with special reference to internal fixation. Clinical orthopaedics 138, 175-196.

Perren, S.M, Cordey, J., 1980. Mechanics of interfragmentary compression by plates and screws. In: Uhthoff, H.K. (Ed.), Current concepts of internal fixation of fractures, Springer-Verlag, Berlin, 1980, 184–191.

Perren, S.M., Rahn, B.A., 1980. Biomechanics of fracture healing. Canadian journal of surgery 23, 228-232.

Perren, S.M., 1999. Editorial: Trends in internal fixation - Potential, limits and requirements. Injury 30, 2-4.

Perren, S.M., 2002. Evolution of the internal fixation of long bone fractures. Journal of bone and bone joint surgery (Br) 84, 1093-1110.

Praemer, A., Furner, S., Rice, D. P., 1992. Musculoskeletal Conditions in the United States (The American Academy of Orthopaedic Surgeons (Eds.)), pp. 85-124. American Academy of Orthopaedic Surgeons, Park Ridge, IL.

Prendergast , P.J., Huiskes, R., Søballe, K, 1997. Biophysical stimuli on cells during tissue differentiation at implant interfaces. Journal of biomechanics 30, 539-548.

Radcliffe, I.A.J., Taylor, M., 2007. Investigation into the effect of varus-valgus orientation on load transfer in resurfaced femoral head: A multi-femur finite element analysis. Clinical biomechanics 22, 780-786.

Roux, W., Der züchtende kampf der theile, oder die 'theilauslese' im organismus (The struggle of the components within organisms). W. Englemann, Leipzig, 1881.

Rüberg, T., (2003). "Computer simulation of adaptive bone remodeling". Masters Thesis, Universidad de Zaragoza, Spain.

Scannell, P.T., Prendergast, P.J., 2005. Simulation of changes in bone around hip replacement implants. Engineers Journal 59, 372-377.

Schenk, R.K., 1986. Histophysiology of bone remodelling and bone repair. In: Lin, O.C., Chao, E.Y.S., (Eds.), Perspectives on Biomaterials. Elsevier Science, Amsterdam, pp. 75-94.

Schell, H., Thompson, M.S., Bail, H.J., Hoffmann, J-E., Schill, A., Duda, G.N., Linenau, J., 2008. Mechanical induction of critically delayed bone healing in sheep: radiological and biomechanical results. Journal of biomechanics 41, 3066-3072.

Sharma A.K., Kumar, A., Joshi, G.R., John, J.T., 2006. Retrospective study of implant failure in orthopaedic surgery. Medical journal of armed forces of India 62, 70-72.

Shefelbine, S.J., Augat, P., Claes, L., Simon, U., 2005. Trabecular bone fracture healing simulation with finite element analysis and fuzzy logic. Journal of biomechanics 38, 2440-2450.

Shih, K-S., Tseng, C-S., Lee, C-C., Lin, S-C., 2008. Influence of muscular contractions on the stress analysis of distal femoral interlocking nailing. Clinical biomechanics 23, 38-44.

Simon, B.R., Woo, S. L-Y., Stanley, G.M., Olmstead, S.R., McCarty, M.P., Jemmott, G.F., Akeson, W.H., 1977. Evaluation of one-, two-, and three-dimensional finite element and experimental models of internal fixation plates. Journal of biomechanics 10, 79-86.

Soeda, T., Nakagawa,Y., Suzuki, T., Nakamura, T., 2002. Recurrent throwing fracture of the humerus in a baseball player. The American journal of sports medicine 30, 900-902.

Sommer, C., Babst, R., Müller, M., Hanson, B., 2004. Locking compression plate loosening and plate breakage – A report on four cases. Journal of orthopaedic trauma 18, 571-577.

Speirs, A.D., Heller, M.O., Duda, G.N., Taylor, W.R., 2007. Physiologically based boundary conditions in finite element modeling. Journal of biomechanics 10, 2318-2323.

Stoffel, K., Dieter, U., Stachowiak, G., Gächter, A., Kuster, M.S., 2003. Biomechanical testing of the LCP – how can stability in locked internal fixators be controlled? Injury 34, 11-19.

Thompson, D.W., On growth and form (2nd Ed.). Cambridge University Press, Cambridge, 1942.

Urist, M.R., Mazet, R., McLean, F.C., 1954. The pathogenesis and treatment of delayed union and non-union. Journal of bone joint surgery 36, 931-967.

van der Meulen, M.C.H., Huiskes, R., 2002. Why mechanobiology? Journal of biomechanics 35, 401- 414.

Viceconti, M., Casali, M., Massari, B., Cristofolini, L., Bassini, S., Toni, A., 1996. The 'Standardised Femur Program'. Journal of biomechanics 29, 1241.

Wade, R.H., Moorecroft, C.I., Thomas, P.B.M., 2001. Fracture stiffness as a guide to the management of tibial fractures. Journal of bone and bone joint surgery (Br) 83, 533-535.

Wagner, M., Frigg, R., AO manual of fracture management – Internal fixators: Concepts and cases using LCP and LISS. Thieme Medical Publishers, Davos, 2006.

Wang, X., Zhang, X., Li, Z., Yu, X., 2005. A first order system model of fracture healing. Journal of Zhejiang University science, 6, 926-930.

Weinans, H., Huiskes, T., Grootenboer, H.J., 1992. The behaviour of adaptive bone-remodelling simulation models. Journal of biomechanics 25, 1317-1324.

Wolff, J., Das Gesetz der Transformation der Knochen*,* Hirchwild, Berlin, 1892; translated as The law Bone Remodelling (trans. Maquet, P. & Furlong, R.), Springer, Berlin, 1986.

Williams, T.H.D., Schenk, W., 2008. Bridging-minimally invasive locking plate osteosynthesis (Bridging-MILPO): Technique description and prospective series of 20 tibial fractures. Injury 39, 1198-1203.

Wornom, I., Buchman, S., 1992. Bone and cartilaginous tissue. In: Cohen, K., Diegelmann, R., Lindglad, W., (Eds). Wound healing: Biochemical and clinical apects. WB Saunders, Philadelphia, p. 356.

Wren, T.A., Beaupré, G.S., Carter, D.R., 1998. A model for loading-dependent growth, development, and adaption of tendons and ligaments. Journal of biomechanics 31, 107-114.

Wurmbach, H., 1928. Histologische Unteruschengen uber die hilung von knochenbruchen bei saugern. Z wiss zool 132, 200-256, as cited by Carter and Beaupré, 2001.

Xie, Y.M., Stephen, G.P., 1993. Simple evolutionary procedure for structural optimization. Computers and structures 49, 885-896.

Xie, Y.M., Stephen, G.P., Evolutionary structural optimization. Springer, Berlin, 1997.

Xinghua, Z., He, G., Bingzhoa, G., 2005. The application of topology optimization on the quantitative description of the external shape of bone structure. Journal of biomechanics 38, 1612-1620.

Yosibash, Z., Trabelsi, N., Reliable patient-specific high-order FE analysis of the proximal femur, In Proc. European Society of Biomechanics, 26-28th August, 2007, University of Dublin, Ireland.

Website 1
http://www.aofoundation.org/wps/portal/!ut/p/c0/04_SB8K8xLLM9MSSzPy8xBz9CP0os3hng7BARydDRwN39yBTAyMvLwOLUA93I4MQE_2CbEdFAF3RnT4!/?segment=Malleoli&bone=Tibia&soloState=true&popupStyle=diagnosis&contentUrl=srg/popup/further_reading/PFxM2/12_44_Fx_w_abs_stability.jsp
(Last accessed 01/07/09)

Appendix A

Locking plate fixation

Contents

A.1 Locking plate technology

The locking plate is known as an internal external-fixator. This is because the threaded screw heads can be locked to the threaded holes in the plate and therefore the plate does not rely on frictional contact with the bone to maintain stability (Fig. A.1a). Hence, the screws act as though they were pins and the plate acts as a support bar, similar to a unilateral external fixator. Another variation is the locking compression plate (LCP), which accommodates both locking and dynamic compression screws (Fig. A.1b).

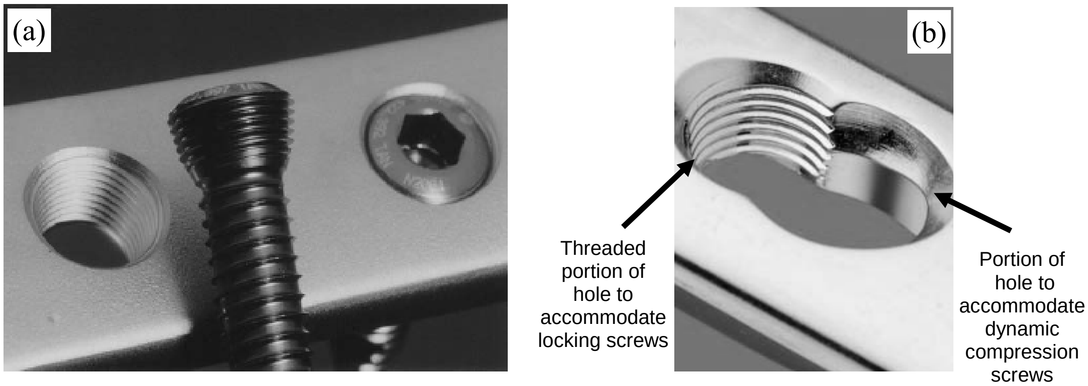

Figure A.1. (a) The standard locking screw with threaded screw head (Shütz and Südkamp, 2003) and (b) locking plate with both locking and dynamic compression options (Website 1).

A.1.1 Minimally invasive plate osteosynthesis (MIPO)

Minimally invasive surgery helps to reduce damage to the injured zone thus preventing complications such as bone devitalisation, infection, delayed union, and non-union (Wagner and Frigg, 2006). Using locking technology and methodology, the incisions are smaller and therefore damage to soft tissue is minimized in comparison with compression plating. Since the plate can be raised from the bone, interference with the callus can be avoided in most cases.

The method of installing a locking plate is considered minimally invasive. Initially, the plate is inserted through a single incision in the skin. A special jig, which remains outside of the body, is connected to the plate and allows a surgeon to locate the position of the screw holes whilst the plate is under the skin (Fig. A.2).

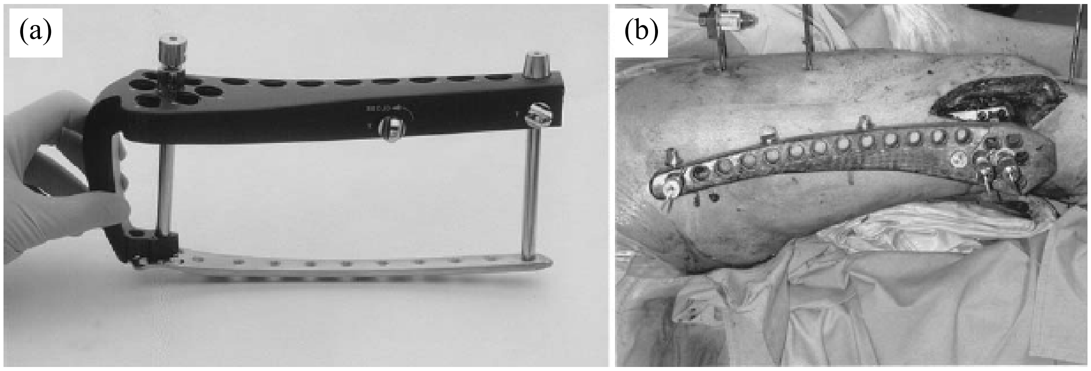

Figure A.2. (a) Jig used to locate the holes in the plate when (b) inserted under the skin (Shütz and Südkamp, 2003)

When the surgeon has chosen the appropriate screw holes to utilise, small 'stab' incisions are made to allow entry of the screws (Fig. A.3a). Unlike, the compression plate, the locking fixator is not required to maintain stability by friction and consequently, the threaded screw shaft may only be required to penetrate through a single cortex (Fig. A.3b). These features of the locking plate help reduce the damage to healthy bone stock by using less drilling, as every screw added in surgery results in extra damage to healthy intact bone (iatragenic trauma).

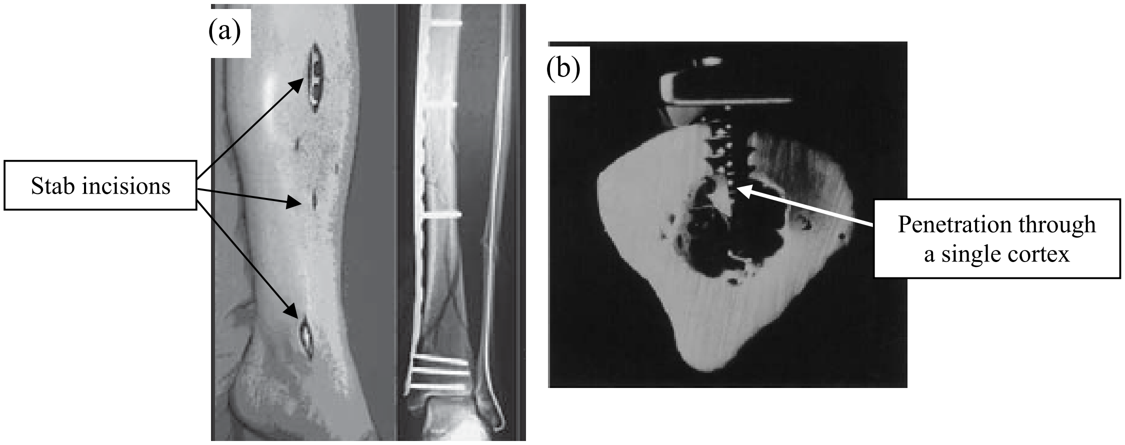

Figure A.3. (a)The minimal incisions used to implant a tibial locking plate and screws (Sommer, 2006) and (b) mono-cortial screws (Shütz and Südkamp, 2003)

A later feature of the locking plate system was the pre-contoured plate design (Fig A.4), which meant that the implant did not need to be intentional contoured by the surgeon to match the patient’s anatomy. Numerous locking plates have therefore been designed for specific regions of a bone.

Figure A.4. Pre-contoured locking plate on distal femur model.

A.2 Flexible splinting and relative stability

The locking fixator can act as a splint to bridge multiple fractures or large fracture gaps. This supports the concept of relative stability, as the locking plate may act as a ‘flexible elastic splint’, which is defined by the stiffness of the implant system, the fracture gap size and the load (Perren, 1999). Elasticity indicates that the implant will deform under a specific load and return to its original form during un-loading. Relative stability is defined as the motion between bone fragments, and is applicable to indirect healing and callus formation. This however, indicates that the implant is load-bearing in the early stages of healing before the callus can share the load.

Appendix B

Comparison of mechanical stimuli

Contents

B.1 Comparison of principal strains experienced by tissue domain under compression loading

Under compression loading, the compressive principal strains experienced by the tissue domain were found to be the dominant strain; 3.5 times greater than the radial strains, and 20 times greater than the circumferential strains (Figs, B.1-B.3). It should be noted that the negative compressive strain value is a convention, where negative represents compression while tension is positive.

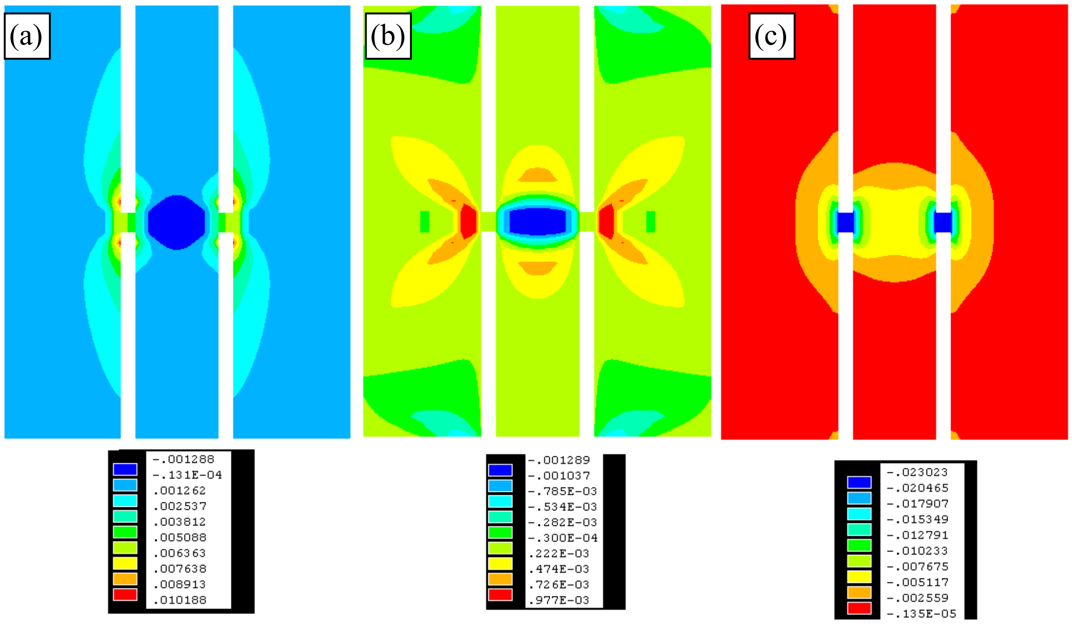

Figure B.1. Principal strains experienced by the inter-cortical tissues under compression loading. (a) First (radial), (b) second (circumferential) and (c) third (axial).

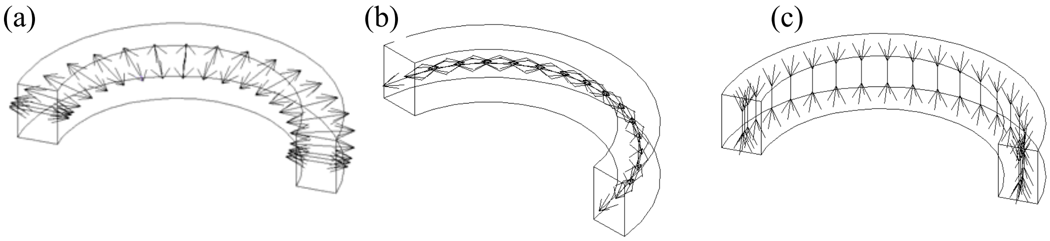

Figure B.2. Principal strains experienced by the inter-cortical tissues under compression loading. (a) First (radial), (b) second (circumferential) and (c) third (axial). Note, tension (⟷) and compression (≻—≺).

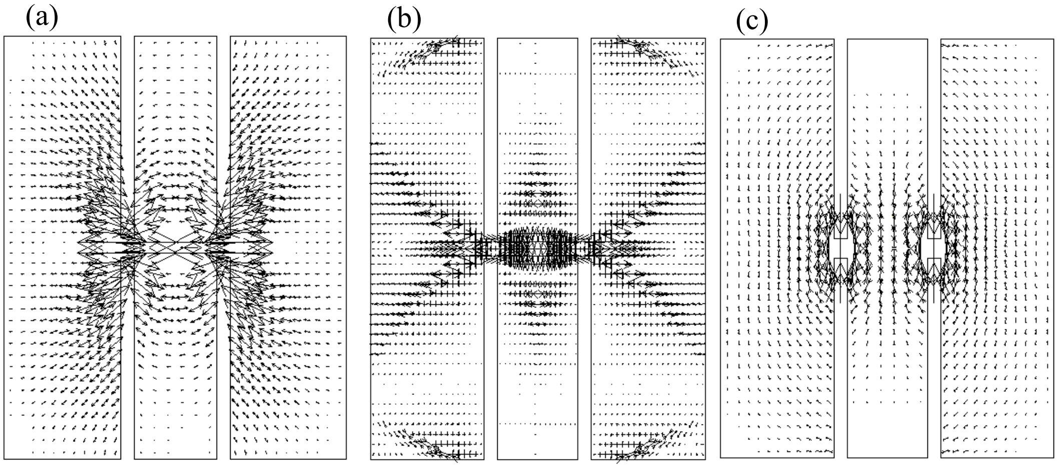

Figure B.3. Principal strains experienced by the tissue domain under compression loading. (a) First (radial), (b) second (circumferential) and (c) third (axial) (magnitude x3). Note, tension (⟷) *and compression* (>—<).

B.1.1 Comparison of compressive principal strain, strain intensity and strain energy density experienced by tissue domain under compression loading

Importantly, equivalent or von Mises strains (Eq. B.1), which is a similar calculation of the octahedral shear strain (*cf.* Eqs. B.1-B.2), calculated an equal strain intensity as the compressive principal strains alone (Figs. B.4a-b). The reason why the von Mises strain is positive is due to the method of calculation which effectively normalizes the values or creates and absolute values (Eq. B.1). The strain energy density (SED) was calculated from stress and strains, and thus the very low stress calculations reduced the energy values in the highly compliant tissues (Fig. B.4c).

$$\varepsilon_e = \frac{1}{\sqrt{2}}\sqrt{(\varepsilon_1-\varepsilon_2)^2+(\varepsilon_2-\varepsilon_3)^2+(\varepsilon_3-\varepsilon_1)^2} \tag{B.1}$$

$$\varepsilon_{oct} = \frac{1}{\sqrt{3}}\sqrt{(\varepsilon_1-\varepsilon_2)^2+(\varepsilon_2-\varepsilon_3)^2+(\varepsilon_3-\varepsilon_1)^2} \tag{B.2}$$

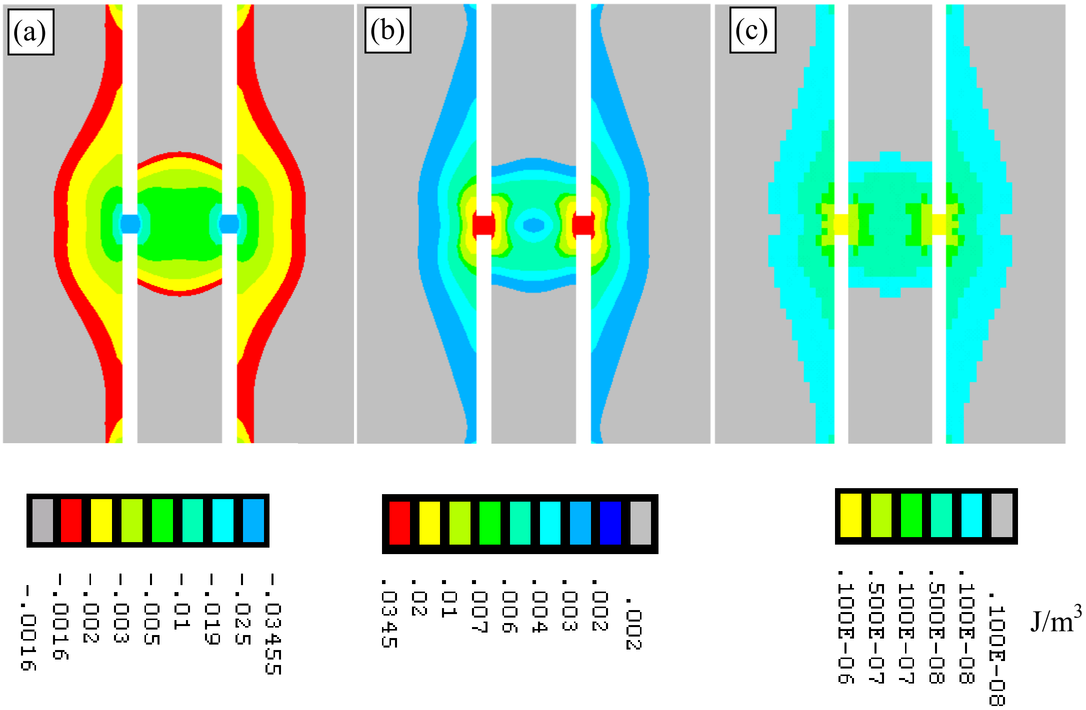

Figure B.4. Illustration and comparison of strain distributions; (a) 3rd or compressive principal strain, (b) octahedral shear strain/von Mises strain and (c) strain energy density. The coloured contours represent different quantities of strain in each case. The boundary of interest is between the grey and coloured regions.

Appendix C

Verification of numerical locking plate fixation

Contents

C.1 Introduction

This chapter presents the details of the methodology used to generate the FE models and experimental testing of the locking plate implants. The numerical and experimental locking plate constructs were tested under idealised loading conditions (axial, bending and torsion). The FE method was tested to validate the accuracy of assuming linearity in a locking plate model. The FE models were also tested to predict the alteration in structural stiffness when changes were made to the implant screw configuration.

According to Mac Donald (2007) there are a number of uncertainties that can exist in a FE model; geometric because no exact dimensions can be machined, loads and boundaries are assumed constant when in nature they never are, assuming linearity when in fact no material truly behaves this way and then finally uncertainties about the mesh quality. In the present study, other assumptions regarding the contact mechanics of the thread connections was also assumed thus adding further uncertainty (Eq. C.1).

$$U_{total} = U_{geom} + U_{mat} + U_{load+BC} + U_{mesh} + U_{cont} \tag{C.1}$$

This chapter therefore attempts to evaluate the appropriateness of the assumptions made in the FE modelling and the impact of these assumptions.

C.2 Study design

The method of validation was to build experimental models of the locking plate system and then build representative FE models, load both numerical and experimental models and then compare the stiffness results. The implants and bone constructs were to be validated under, compressive, bending and torsion loading, as the implant is prone to experiencing such loads *in vivo*.

C.2.1 Locking plate

The implant of choice was the 4.5mm, 10-hole Smith & Nephew periloc plate (Fig. C.1a). The indications for use of a periloc plate is for fractures above the periarticular surface of the bone, or in other words, mid-shaft fractures. This specific plate was chosen due to its relatively simple design which made comparison with FE models easier. The plate was designed to accommodate both locking and non-locking screws, however, in this study only the locking option was of interest (Fig. C.1b). The under side of the plate was designed with a ridged surface between each screw hole, so that if the non-locking (compression) screws were to be used, there would be reduced pressure on the periosteal surface of the bone, much like a Low- Contact DCP (Fig. C.1c). The screw holes are staggered in the plate to allow more screws per length which also results in a wider plate (15mm). The plate was made from 316L stainless steel.

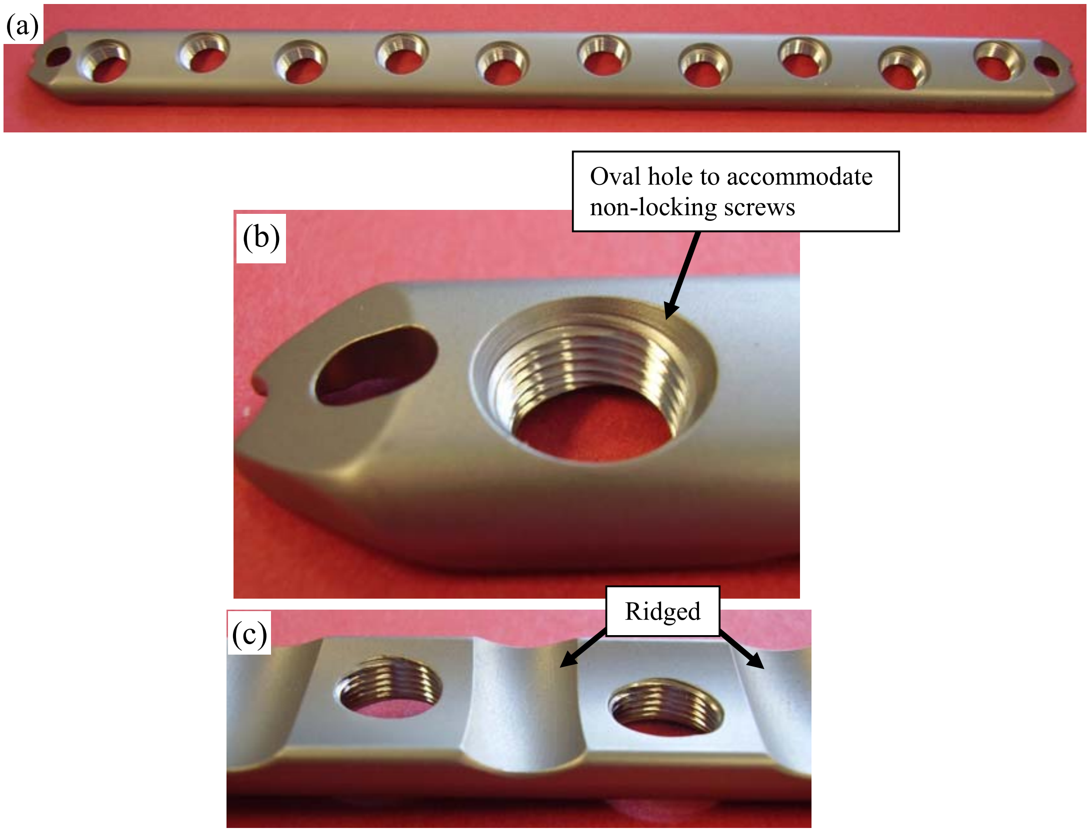

Figure C.1. (a) Smith & Nephew 4.5mm locking plate, (b) details of screw holes and (c) ridged under side of plate.

C.2.2 Locking screw

The screws were 4.5mm cortex locking screws and were 42mm long (Fig. C.2a). The 4.5mm relates to the thickness of the plate they are designed to fit. The root diameter of the screw is 3.5mm and the outside thread diameter is 4.5mm. The screw head has the shape of a an inverted frustum of a cone, where the cone is 3.5mm high, the upper diameter is 8mm and the lower diameter is 7mm (Fig. C.2b). The fully inserted screw does not sit flush with the plate which results in an approximately 1mm gap between plate and screw head (Fig. C.2c). The screws were also made from 316L stainless steel.

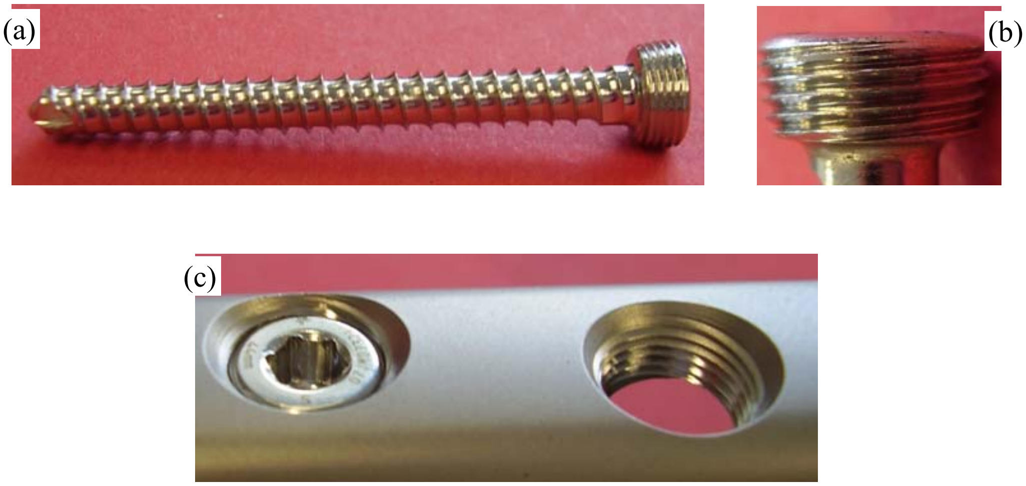

Figure C.2. (a) Locking screw, (b) details of screw head and (c) head is approximately 1mm below the plate when screw is fully inserted.

C.2.3 Synthetic bone

The implant was installed on synthetic bone samples for biomechanical testing. Rigid, non-cellular, epoxy resin tubes (Pacific Research Laboratories), with a Young's modulus similar to that of cortical bone (12.4Gpa), was used as a substitute for hollow long bones (Ahmad *et al*., 2007). The synthetic bone was made of a mixture of short glass fibers and epoxy resin that has been pressure molded into hollow cylinders. The synthetic bone was used to replicate the tubular shape of the mid-shaft of a long bone (40mm OD with a 6mm wall thickness).

C.2.4 Specimen preparation

In the biomechanical tests the fracture was modelled using a 4mm gap at the centre of the bone to represent a mid-shaft transversal fracture (Ahmad *et al*., 2007; McCartney *et al*., 2005; Stoffel *et al*., 2003). The bone tubes were therefore sectioned into two 150mm long pieces, where each piece represented a separate bone fragment. The plate was mounted flush with the bone sample in a vice so that the drill holes could be centred. Firstly, a countersink was used to centre and guide the smaller drill bit (3.5mm) to provide holes through which the self-tapping cortical screws were inserted. A series of 2mm spacers were used between the underside of the plate and the bone to ensure uniform plate-bone distance in all tests when the screws were inserted and fully tightened (Fig. C.3).

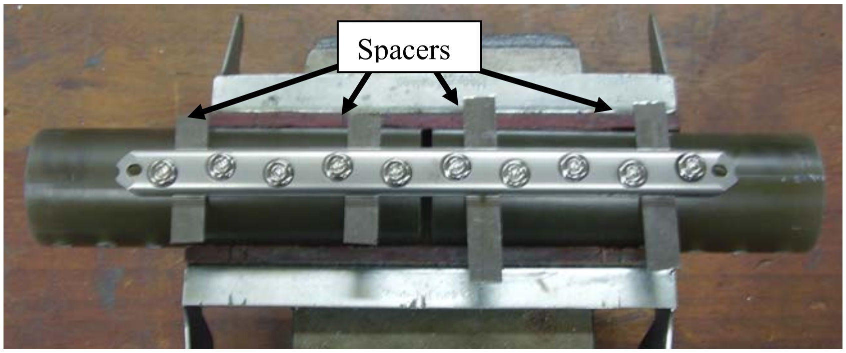

Figure C.3. Preparation of test sample with spacers to ensure consistent plate bone distance.

C.3 Experimental testing of locking plate fixation

C.3.1 Axial and four-point bending loading

Axial and four-point loading was applied to the fixation constructs using an electromechanical materials testing machine (Instron) (Fig. C.4a). Four-point loading was carried out with a load span of 150mm and a support span of 225mm (Fig C.4b). For axial loading, the proximal and distal ends of the bone were located in knife-edged supports (Fig. C.4c). The constructs were subjected to a quasi-static load at a rate of 0.5mm/min and measurements were taken at a sampling rate of 10Hz. A maximum load of 200N was applied to both axial and four-point bending tests. Load and displacement results were then logged and analysed using a Microsoft Excel spreadsheet.

C.3.2 Torsion loading

Torsion was applied to the constructs by rigidly clamping the distal and proximal ends of the bone substitute in a custom made three-jaw chuck. The distal end was constrained in all degrees of freedom, while the proximal end was housed in a bearing which only allowed rotary motion about its own central axis and no longitudinal motion (Fig. C.5). A lever arm was attached to the rotating end and 0.5N loads were hung from the end of the lever arm until a torque of 5.5Nm was reached. The torque (Nm) was calculated from the applied force (N) and length (m) of the lever arm. A displacement gauge with a digital display was used to measure the displacement of the lever arm as weights were applied, so that the angle of twist could be calculated according to the following equation

$$\theta = \sin^{-1}(A/B) \tag{C.2}$$

where A is the downward displacement recorded by the displacement gauge and B is the distance from the central axis of rotation to the displacement gauge.

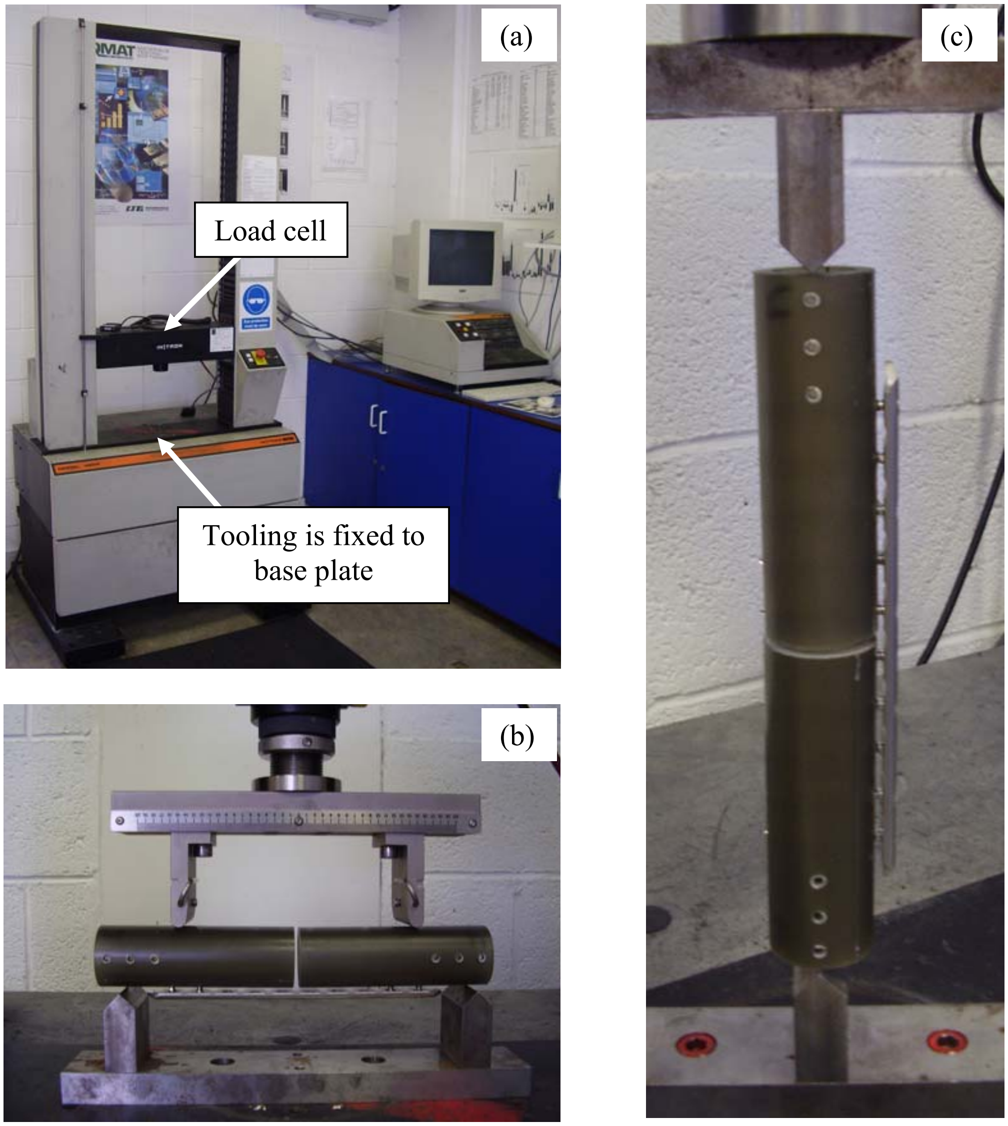

Figure C.4. (a) Electro-mechanical materials testing rig, (b) four-point bending jig, and (c) axial loading jig.

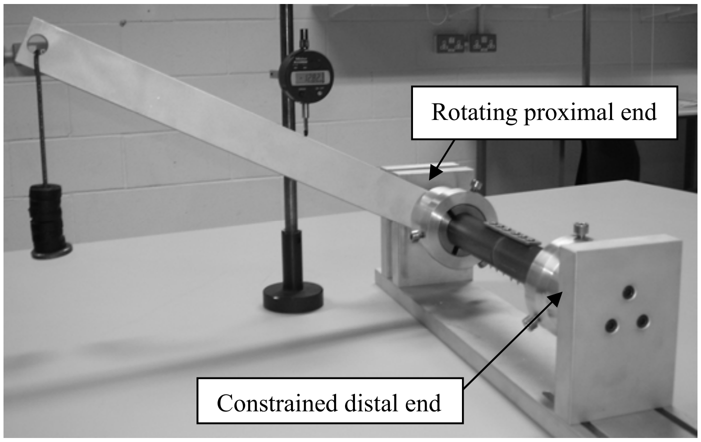

Figure. C.5. Torsion loading rig used in experimental investigations.

C.3.3 Data processing

The loads applied to all experimental tests were only required to induce elastic deformation and hence obtain elastic stiffness results from the load-displacement graphs. The load and displacement results were logged using an Excel spreadsheet. Since the load was sufficiently low to capture elastic deformation, there was a linear relationship between load and displacement. Fitting a trend line between the data points allowed the slope of the load-displacement graph to be obtained, which provided the stiffness (kN/mm) values. Since five experimental samples were used, the average of all five samples was obtained.

C.4 Finite element modelling

The first step in the FE modelling procedure is the idealisation and simplification of the problem. Assumptions were made to simplify the geometry, material behaviour, loads and boundary conditions, and contact mechanics. The FE models presented in this study were based on the geometries, material properties and boundary conditions used in the implant and synthetic bone testing.

C.4.1 Generating solid models for discretisation

There are two main types of 3D solid elements; tetrahedral (pyramid) and hexahedral (brick) shaped elements. It was decided that hexahedral elements would be used in this study, as tetrahedral elements can overestimate bending stiffness in a model. The benefit of hexahedral elements is that they can be used in mapped meshing, which is a technique of meshing which forces the elements into a more regular and consistent pattern, where a more consistent mesh results in greater solution accuracy (Mac Donald, 2007). The disadvantage of this method of discretisation is that it requires that the volumes in the models be divided into regular shapes. Although more complex to implement, this method allows for reduced element and node numbers and hence reduced computational effort than the more easily implemented method of using tetrahedral elements. Even if a volume is of a regular shape it must meet the following criteria to be map meshed:

1. An area must contain 3 or 4 lines (triangle or quadrilateral).
2. A volume must contain 4, 5 or 6 areas (tetrahedral, triangular prism or hexahedral).
3. Element divisions on opposite sides must match. (Fig. C.6b)

The screw holes in the plate and bone were therefore sub-divided into more regular volumes that satisfy the aforementioned conditions (Fig. C.6a). Map meshing helps to produce a highly regular arrangement of brick shaped elements around curved edges and volumes (Fig. C.6c-d).

The screw holes in the bone model were created by subtracting cylinders from the bone model, thus leaving a set of screw holes. The bone model was strategically divided by re-orientating the working plane so that the segments surrounding the holes of the solid model could be map-meshed (Fig. C.7).

The screw heads and shafts were built from cylindrical volumes which were divided through the central axis into eight sections using a Boolean volume-divide operation (Fig. C.8a) so that map-meshing could be used (Fig. C.8b). The screw shafts were divided by the inner and outer areas of the bone volume (Fig. C.8c) using Boolean operations, so the nodes in the bone and screw shafts would be coincident.

The screw-head holes in the plate were created by building a series of cylinders positioned along the length of the plate using the working plane, which were then subtracted from the plate thus, producing cylindrical holes. The plate was then divided into several 10x10mm segments by rotating and re-positioning the working plane (Fig. C.9a-b). The plate was divided up into a series of map-meshable cross sections at 45 degree angles around the holes, thus producing a consistent mesh (Fig. C.9c). The side volumes produced the final plate width (Fig. C.9d).

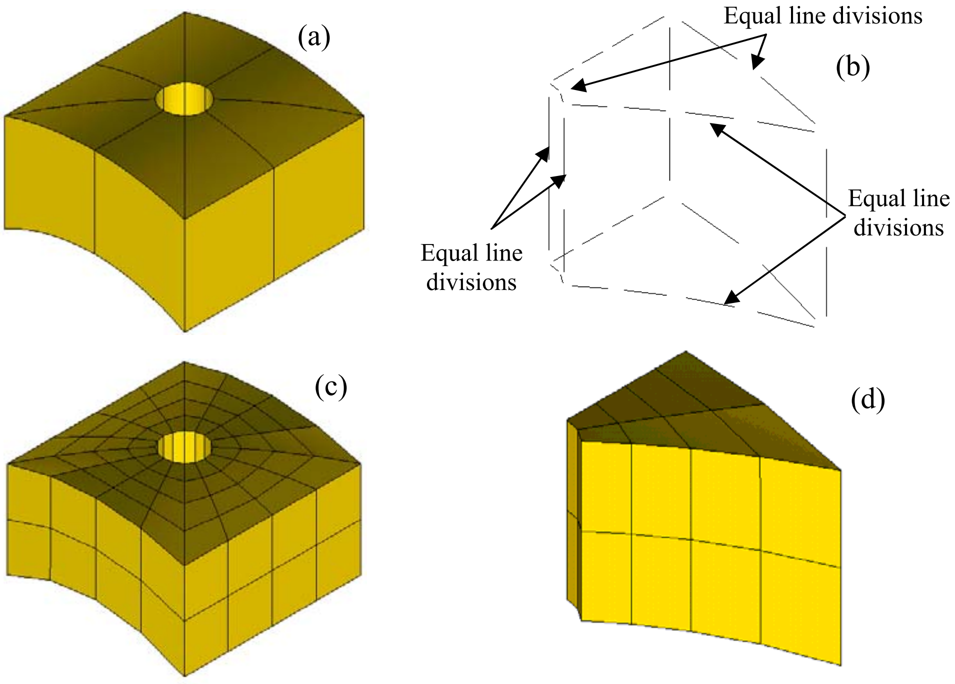

Figure C.6. (a) Section of bone volume with screw hole, (b) smaller segment of bone volume with line divisions to allow map meshing, (c) fully meshed section of bone and (b) map meshed segment.

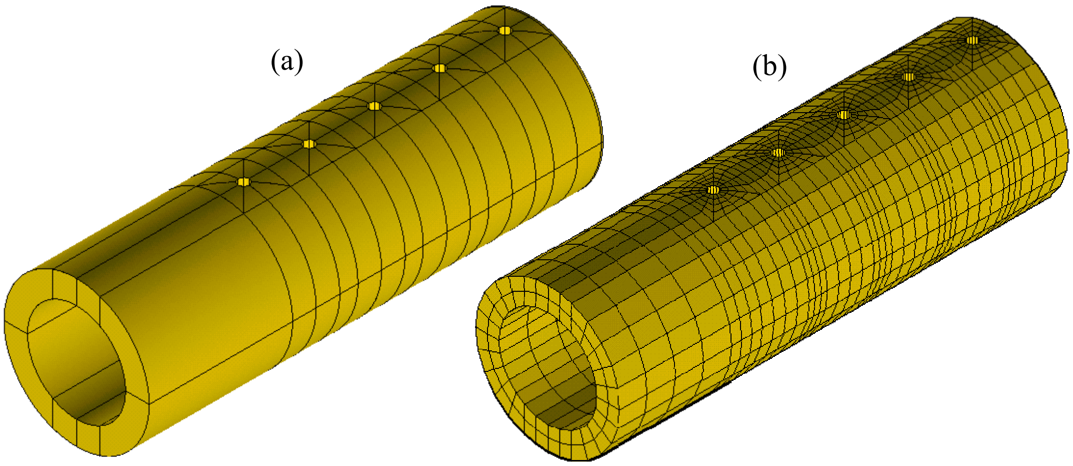

Figure C.7. (a) segmented solid model of bone with screw holes and (b) discretised model.

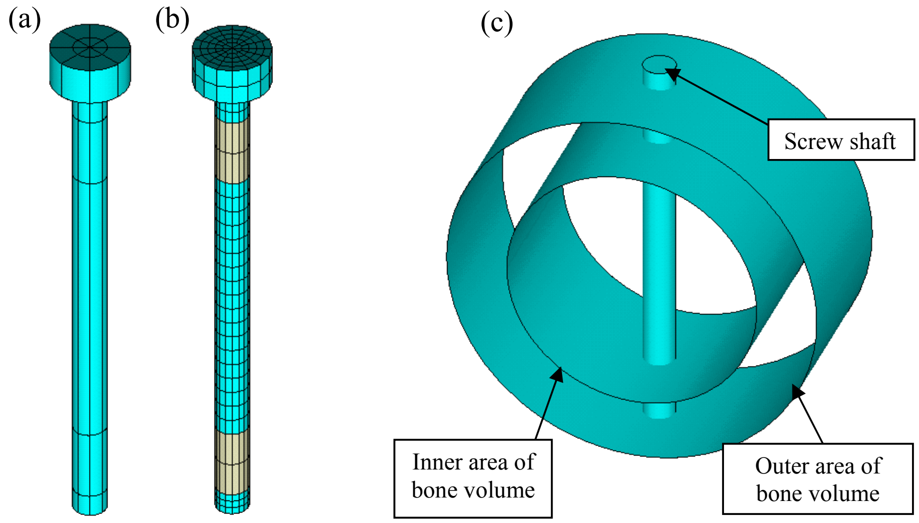

Figure C.8. (a) Segmented screw model, (b) meshed screw and (c) method of dividing screw shaft by areas of bone volume.

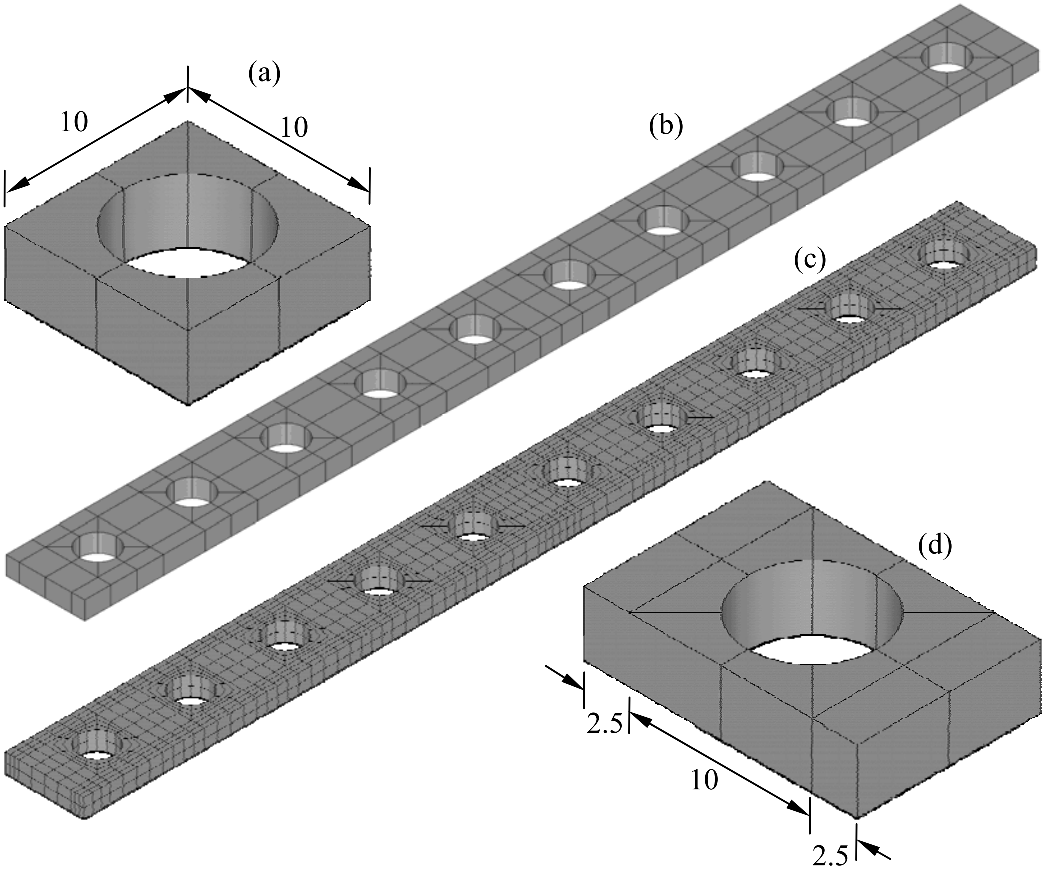

Figure C.9. (a) Square section of plate with 45^o segments, (b) full segmented solid plate mode, (c) map meshed plate, and (d) plate section with side volumes.

C.4.2 Material behaviour

The material properties of the bone model were set equal to the properties of epoxy resin (E = 12.4GPa, v = 0.33). The plate and screws were modelled as 316L stainless steel (E = 190GPa, v = 0.3).

C.4.3 Loads and boundary conditions

Torsional loading was simulated by firstly rotating the nodes on the periphery of the proximal end-face of the bone model into a nodal cylindrical coordinate system (Fig. C.10a-b). Loads and constraints were then applied to these nodes to induce a rotational force and also to prevent radial displacements (Fig. C.10c).

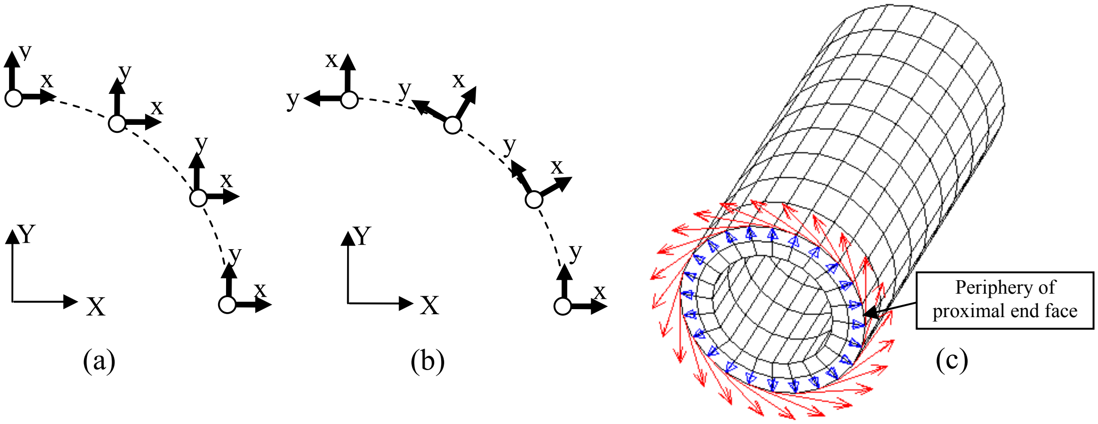

Figure C.10. (a) Conversion of Cartesian co-ordinate system into (b) cylindrical co-ordinate system. (c) Constraints were applied in the cylindrical x-direction and forces were applied cylindrical y-direction. Note: upper and lower case represent global Cartesian and local nodal co-ordinate systems, respectively.

Radial constraints would ensure that the end-face would only rotate about its own central axis, as in experimental testing. The proximal end-face was not constrained from longitudinal motion as this was found to overestimate the torsional stiffness approximately five times greater than the experimental stiffness. It was assumed that the periphery of the distal end-face of the bone was constrained in all degrees of freedom. Symmetry boundary conditions could not be used due to the nature of the problem. The bone itself was built 20mm shorter than the experimental model as the experimental model was loaded 10mm into clamps at each end. The torque applied to the models was calculated as

$$T = nFr \tag{C.3}$$

where n is the number of nodes on the periphery, F is the force (N) applied at each node and r is the outer radius (m) of the tube. Nodal displacements at the load points were then obtained from the FE model to calculate torsional rigidity (Nm/^{o}).

Four-point bending was simulated using quarter symmetry boundary conditions to simplify the FE model and reduce computational effort (Fig. C.11). Therefore, only one quarter of the load was applied to a single point. The support point was simulated by applying a constraint in the vertical direction. The bending stiffness (N/m) was calculated by the displacement recorded from the load point.

Axial loading was simulated using half-symmetry boundary conditions and hence, only half the force was applied to a central line of nodes in the perpendicular direction, parallel to the plate on the proximal end-face (Fig. C.12). The same nodes were constrained in a direction perpendicular to the forces. A line of nodes on the distal end-face were constrained in both the vertical and horizontal directions to simulate the lower edge-support to mimic the experimental set-up. Axial and bending stiffness (N/m) was calculated using the nodal displacements at the load points.

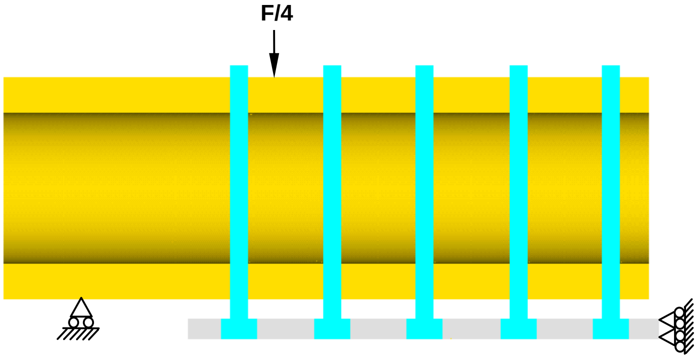

Figure C.11. Four- point bending applied to locking plate FE model.

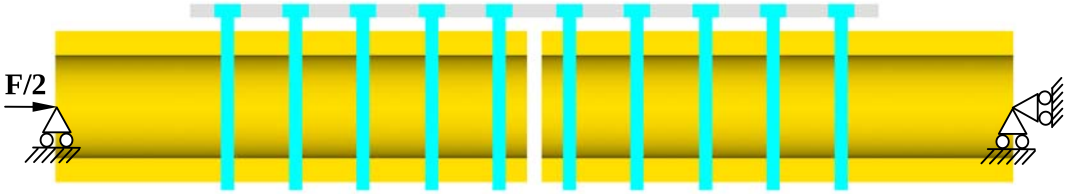

Figure C.12. Axial loading boundary conditions applied to locking plate FE model.

C.5 Mesh convergence

In a FE model, the accuracy of the solution depends on the ability of the elements to accurately represent the geometry of the problem. The quality and consistency of the FE model meshes were ensured by using map meshing techniques. Another important factor to consider was the density of the mesh. In general, increasing the number of elements should result in an improvement in solution accuracy. There are two ways of ensuring solution accuracy, by comparing the results to 1) experimental data or 2) analytical results. In the present study, both methods were used.

C.5.1 Analytical stress concentration

The analytical approach was initially used to find the most appropriate element to use in the mesh and to find the appropriate element type and density to obtain accurate results. It is understood that stress concentrations are typically found around holes in a structure, therefore theoretical stress concentrations were calculated using Hertzian stress concentration factors (Eqs. C.4 - C.5) (Young, 1989). The analytical solution was obtained based on the dimensions used in the FE model of the screw hole in the locking plate. A load of 200N was used in the analytical calculation and the theoretical maximum tensile stress was found to be 36.935MPa which would provide a baseline for the FE model stress results to achieve.

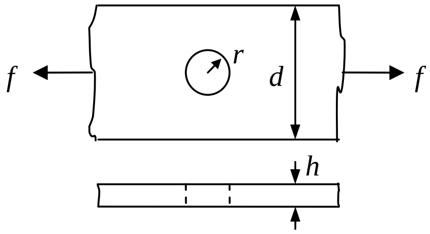

$$\sigma_{\max} = k \frac{f}{h(d-2r)} \tag{C.4}$$

$$K = 3 - 3.13\left(\frac{2r}{d}\right) + 3.66\left(\frac{2r}{d}\right)^2 - 1.53\left(\frac{2r}{d}\right)^3 \tag{C.5}$$

C.5.2 Element choice

The two element types under consideration were an 8-node linear or 20-node quadratic hexahedral elements (Fig. C.13). The linear 8-node element has a node at each corner of the brick, whereas the higher order quadratic 20-node element has a node at each corner as well as curved boundaries with an extra mid-side node at each side.

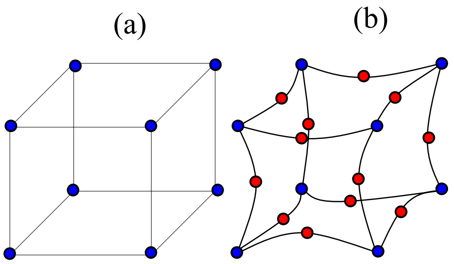

Figure C.13. (a) 8-node and (b) 20-node hex solid 3D elements.

C.5.3 Numerically predicted stress concentrations

To determine which element best simulated stresses at the screw holes, the maximum von Mises stress concentration was obtained using a one-quarter model of the locking plate screw hole (Fig. C.14). The maximum von Mises stress concentration was found at the edge of the hole. The von Mises yield criterion (Eq. C.6), which is based on the assumption that failure occurs when the energy of distortion reaches the same energy for yielding/failure in uniaxial tension. Both element types were used in the simulations. The method of strategically increasing the mesh density was by increasing the number of element divisions along the lines of the plate hole.

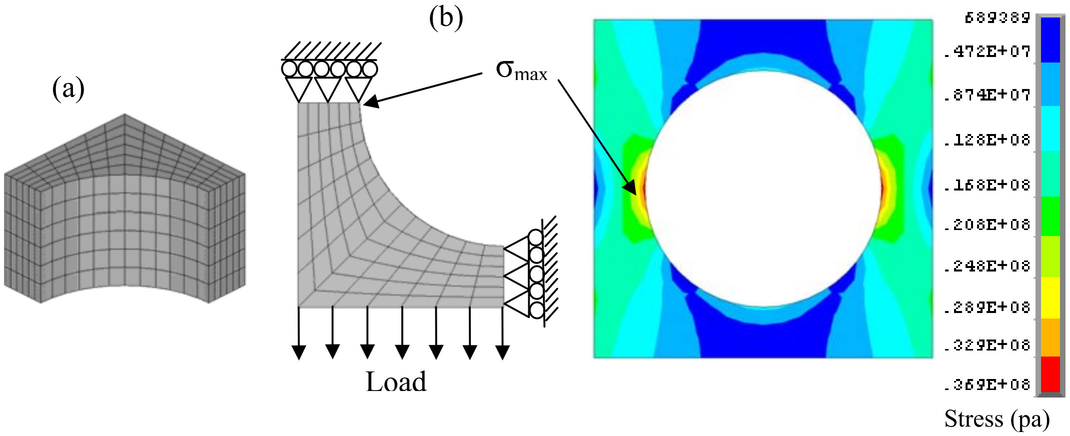

Figure C.14. (a) one quarter segment of hole in plate used for mesh convergence and (b) loading and boundary assumptions made to FE model and (c) von Mises stress concentration at edge of hole.

$$\sigma_y = \frac{1}{\sqrt{2}}\sqrt{(\sigma_1-\sigma_2)^2+(\sigma_2-\sigma_3)^2+(\sigma_3-\sigma_1)^2} \quad \text{(C.6)}$$

Where

σ_1 is the first principal stress

σ_2 is the second principal stress

σ_3 is the third principal stress

C.5.4 8-node element mesh convergence

The accuracy of the 8-node element was initially tested. Convergence began with only two element line divisions around the edges of the volumes, and was incrementally increased to nine divisions (Table C.1). This resulted in a typical convergence curve, however, even with a large number of nodes and elements, the numerically predicted stress did not reach the theoretical stress (Fig. C.15).

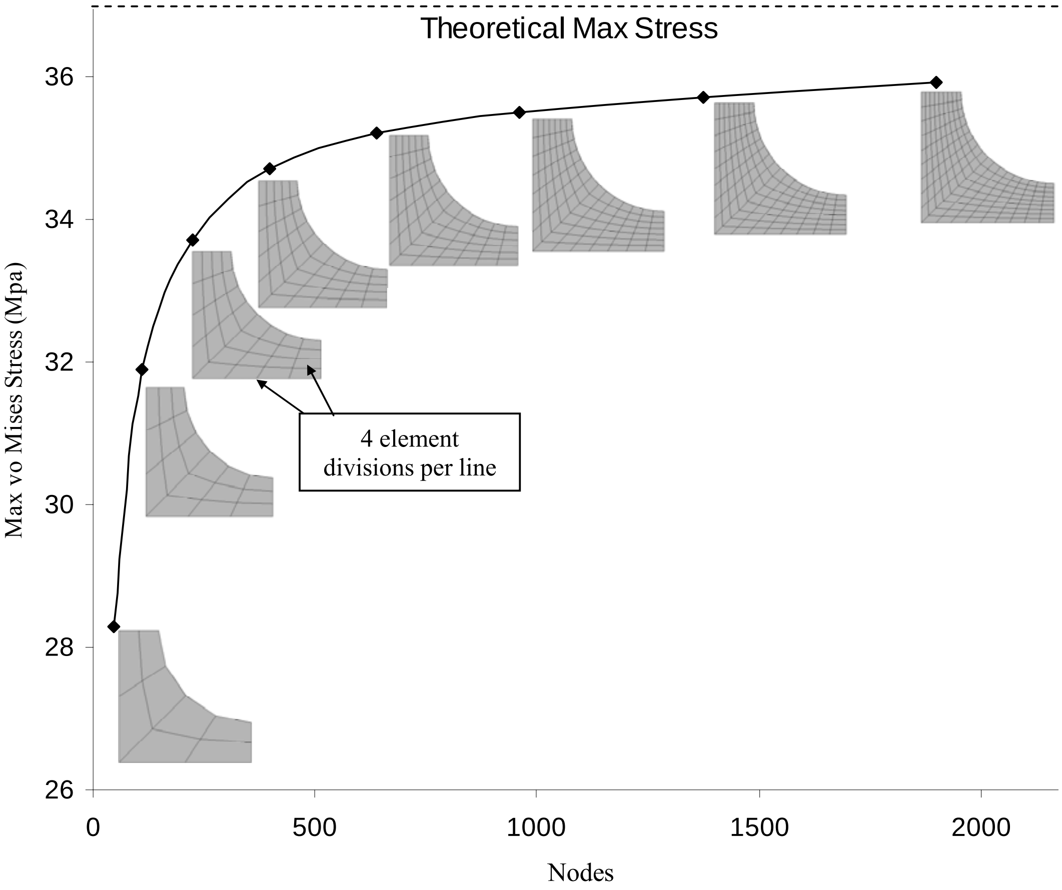

Figure C.15. Mesh convergence with solid45 8-node bricks.

Table C.1. Solid 45 8-node brick elements

Line division	Nodes	Elements	Max Stress (MPa)
2	45	16	28.3
3	112	54	31.9
4	225	128	33.7
5	396	250	34.7
6	637	432	35.2
7	960	686	35.5
8	1377	1024	35.7
9	1900	1458	35.9

C.5.5 20-node element mesh convergence

The same incremental line division method was again utilized. The number of elements increased, as was found in the 8-node elements, however, due to the mid-side nodes, the node count increased at a considerably greater rate (Table C.2). It was found that with the 20-node elements, the lowest mesh density (2 element divisions per line) produced the same stress as 8-node element with the greatest mesh density used in the study (9 element divisions per line). Also, the 20-node elements did converge to the theoretical stress (Fig. C.16).

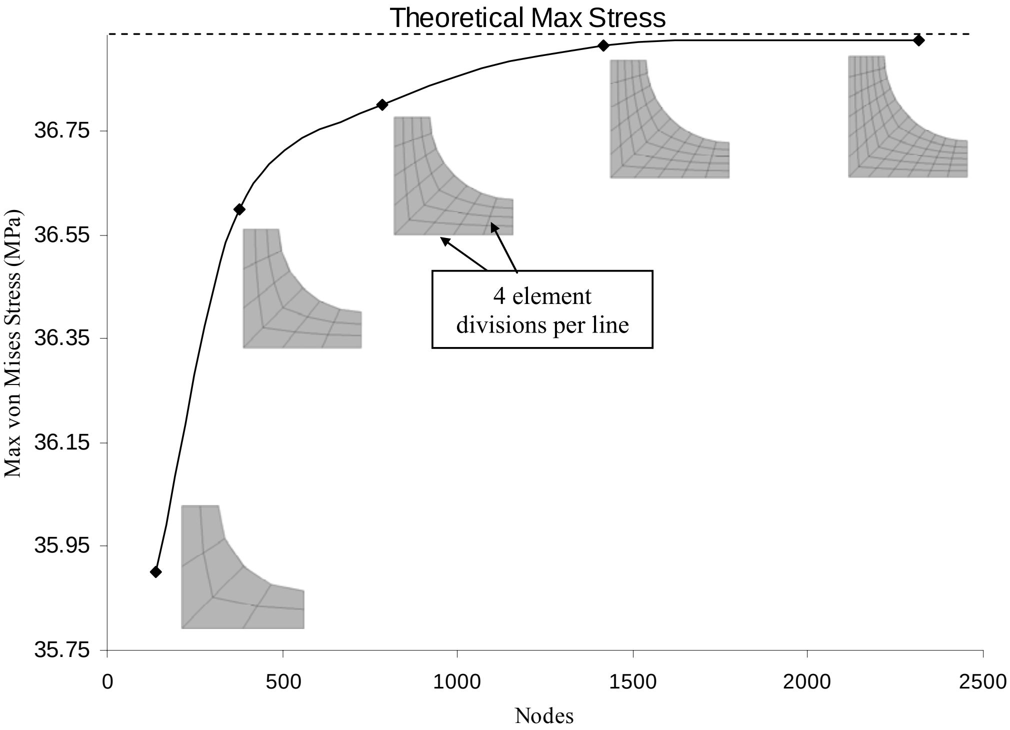

Figure C.16. Mesh convergence with solid95 20-node bricks.

Table C.2. Solid 95 20-node brick elements

Line division	Stress (MPa)	Nodes	Elements
2	35.9	141	16
3	36.6	376	54
4	36.8	785	128
5	36.91548	1416	250
6	36.92424	2317	432

There is always a trade-off between solution accuracy and solution time when using the FE method. The 20-node elements were more accurate, but with more elements, the node count increased correspondingly as does the solution time. It was found that four element divisions were defined around the screw holes in the plate thus ensuring high accuracy while maintaining a lower node count whether 8- or 20-node elements were to be used. In this appendix chapter, the verification was carried out with 20-node elements. As a result, the one-quarter FE model of the implant and bone assembly contained 74244 nodes and 15008 elements (Fig. C.17).

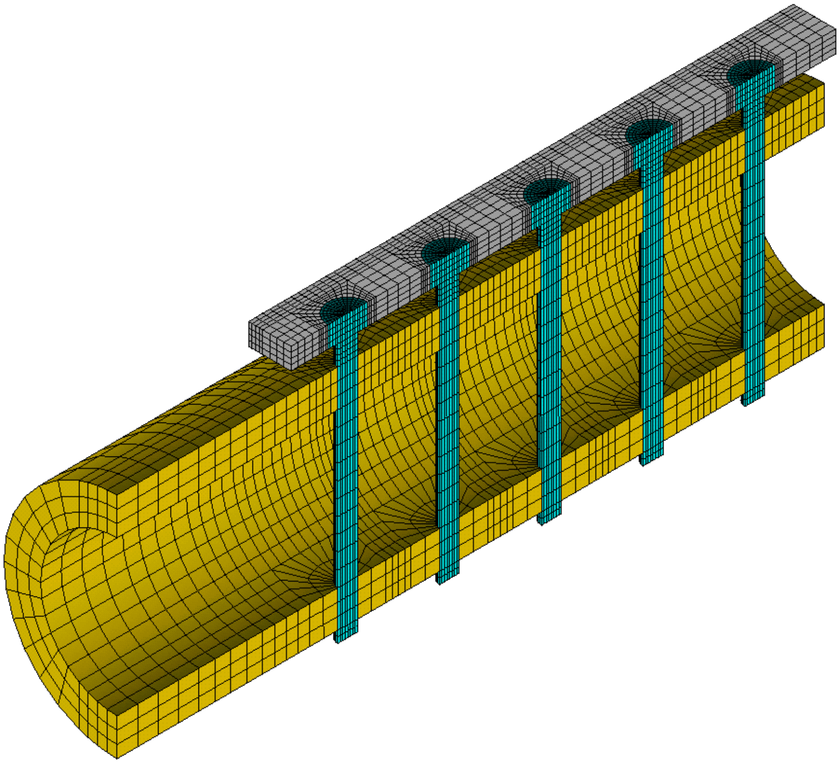

Figure C.17. One-quarter model of final mesh density used in whole model using 20-node bricks.

C.6 Results

The FE and experimental stiffnesses were compared for the cases when all screws were inserted, followed by the removal of the innermost screws, until two screws remained on each side of the plate furthest from the fracture. The average stiffness was found for each sample group and was compared to the FE models' elastic stiffness results (Figs. C.18 - C.20). The mean experimental stiffness results are also presented in the figures with the maximum to minimum stiffnesses, so that the full range of variation in results can be observed.

C.6.1 Axial stiffness

The FE models captured the same relationship between the number of screws and axial stiffness, as was found in the experimental tests (Fig. 3.22). It would appear that the FE simulation underestimated the stiffness of the implant construct, where there was an average discrepancy of 24% (SD 7.38) between FE and experimental results.

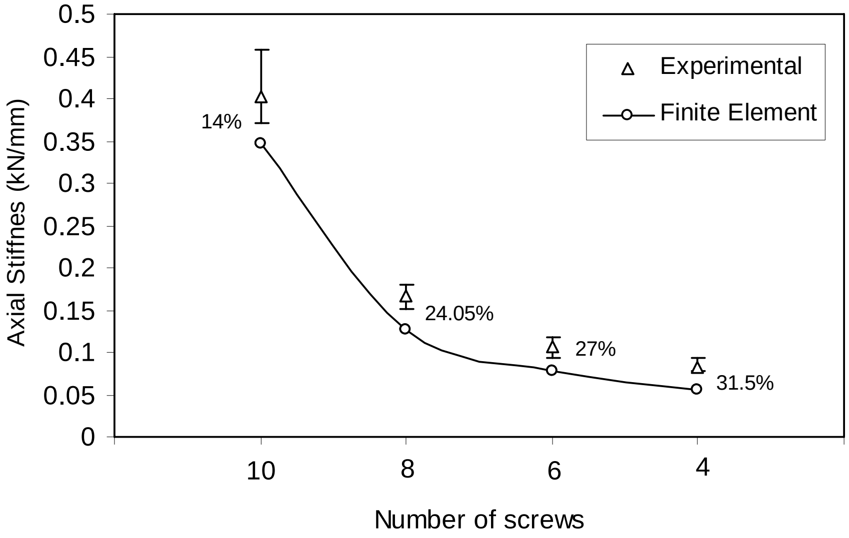

Figure C.18. Comparison of experimental and FE axial stiffness. Note, 10 – all screws inserted, 8 – two innermost screws removed, 6 – four innermost screws removed, and 4 – six innermost screws removed.

C.6.2 Bending stiffness

In the FE model, when all the screws were inserted, the average experimental stiffness was below the simulated stiffness. When screws were removed, the FE model simulated a stiffness which was in fact now less than the average experimental stiffness. It should be noted, however, that the simulated stiffness was still within the range of experimental results when not all screws were inserted (Fig. C.19). The average discrepancy between the experimental and simulated results was 15.5% (SD4.2).

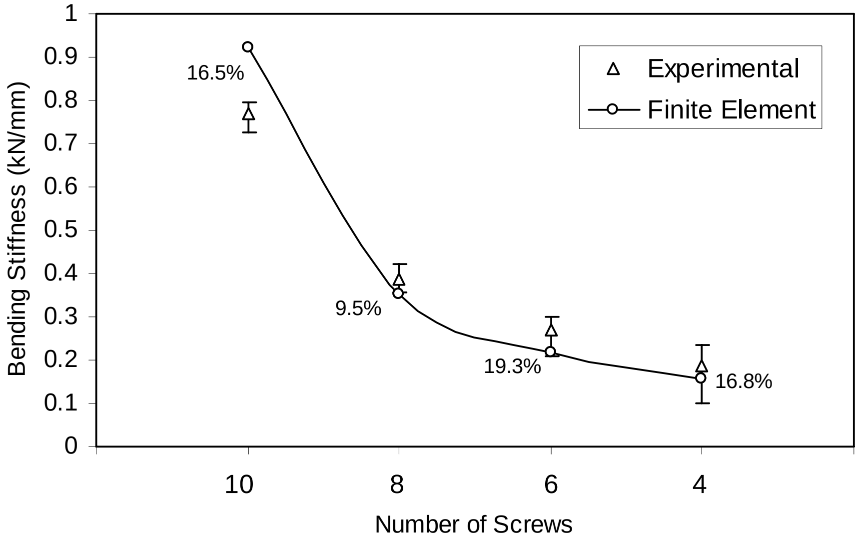

Figure C.19. Comparison of experimental and FE four-point bending stiffness.

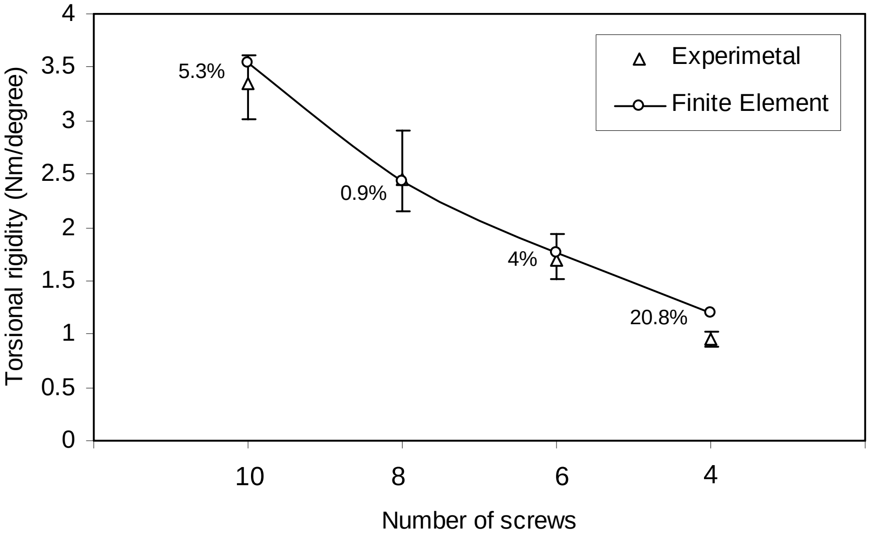

Figure C.20. Comparison of experimental and FE torsional rigidity.

C.6.3 Torsional rigidity

The correlation between the experimental and simulated torsional rigidities was most accurate, except when only 4 screws were inserted, where a discrepancy of 20.8% was found (Fig. C.20). Due to this anomaly the average discrepancy between experimental and simulated torsional rigidities was 7.75% (SD 8.87). Unlike the axial or bending scenarios, the relationship between number of screws and torsional rigidity was almost linear.

Appendix D

Callus formation imagery

Contents

D.1 Bending - anatomical views

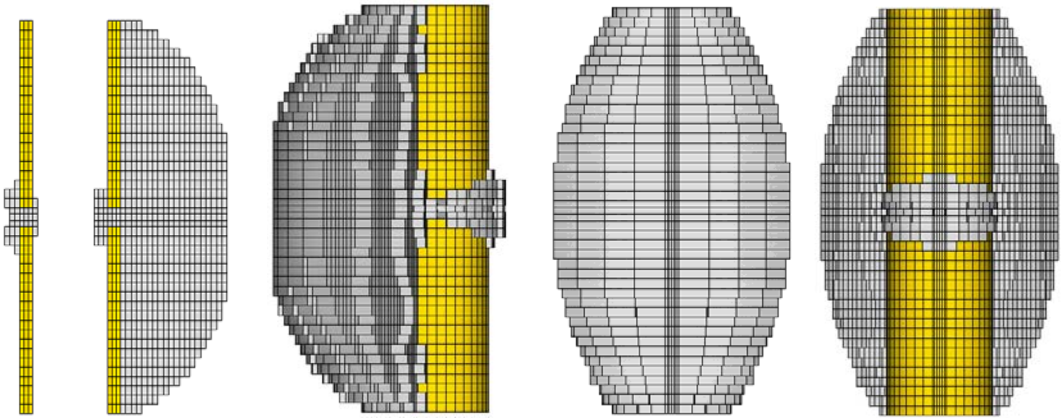

Figure D.1. Numerical approximation of final callus shape underasymertic loading - 9:1 ratio. (a) longitudinal section, (b) anteroposterior (A-P) view, (c) mediolateral (M-L) view, and (d) lateromedial (L-M) view.

D.2 Unilateral fixation – algorithm procedure

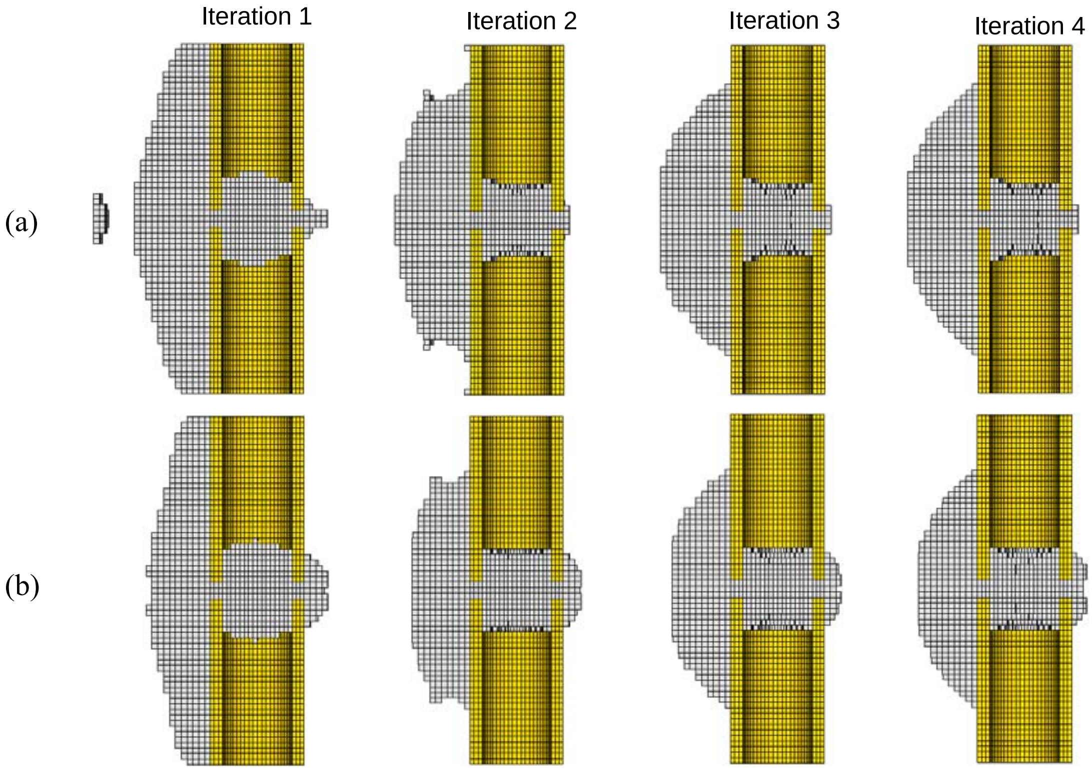

Figure D.2. Iterative removal of elements under locking plate fixation. Plate-bone distance: (a) 2mm, (b) 10mm.

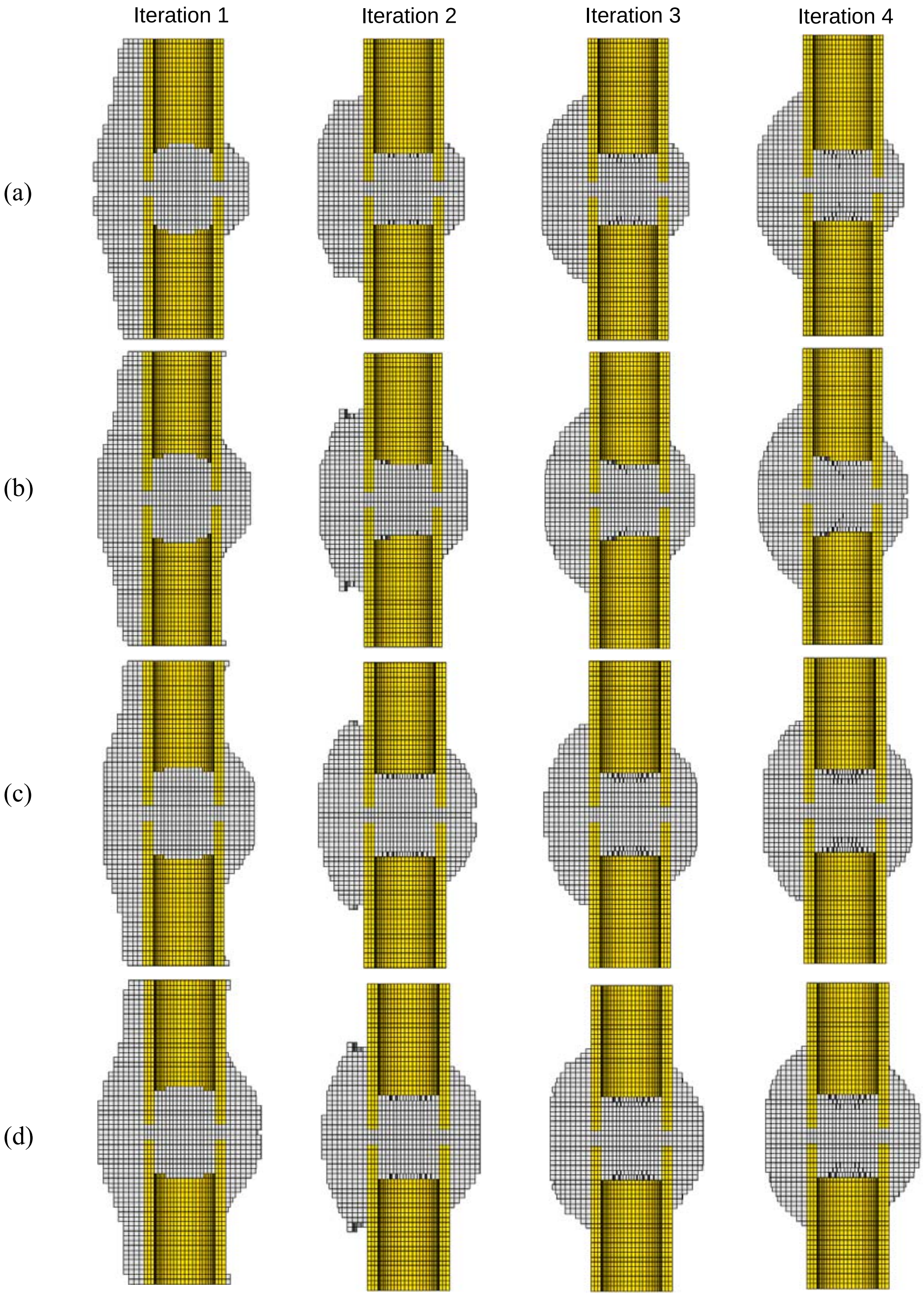

Figure D.3. Iterative removal of elements under locking plate fixation. Plate-bone distance: (a) 20 and (b) 30, (c) 40, and (d) 50mm

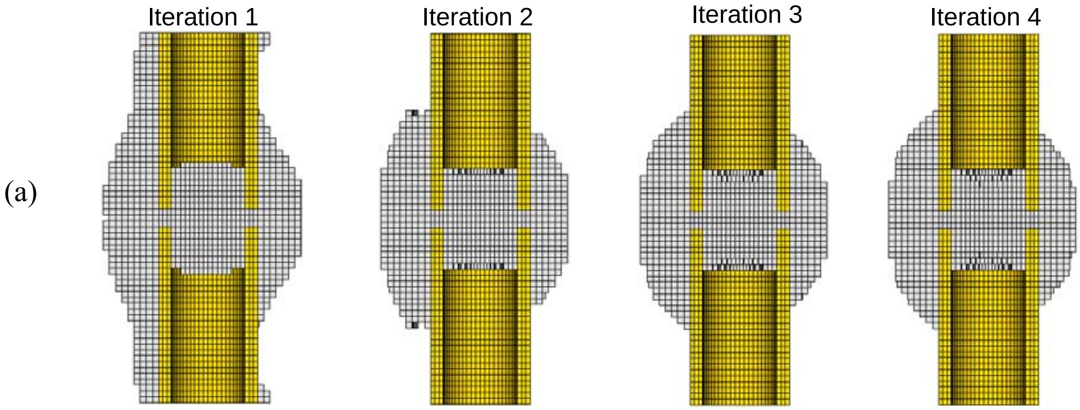

Figure D.4. Iterative removal of elements under locking plate fixation. Plate-bone distance: 60mm.

D.3 Unilateral fixation – anatomical views

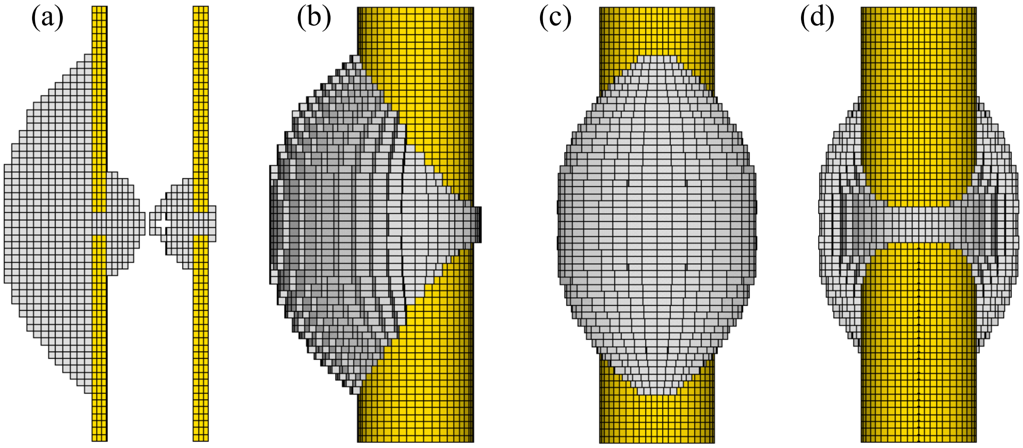

Figure D.5. Numerical approximation of final callus shape under unilateral fixation – Plate-bone distance:2mm (a) longitudinal section, (b) anteroposterior (A-P) view, (c) mediolateral (M-L) view, and (d) lateromedial (L-M) view.

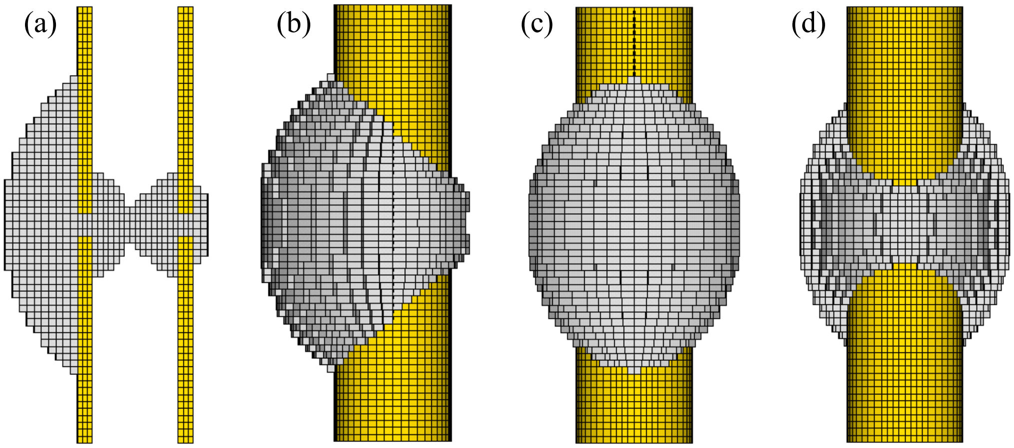

Figure D.6. Numerical approximation of final callus shape under unilateral fixation – Plate-bone distance:10mm (a) longitudinal section, (b) anteroposterior (A-P) view, (c) mediolateral (M-L) view, and (d) lateromedial (L-M) view.

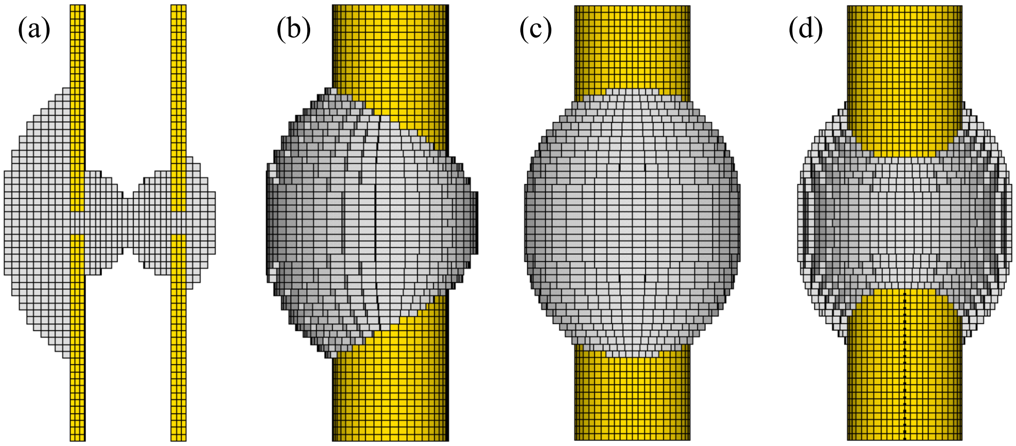

Figure D.7. Numerical approximation of final callus shape under unilateral fixation – Plate-bone distance:20mm (a) longitudinal section, (b) anteroposterior (A-P) view, (c) mediolateral (M-L) view, and (d) lateromedial (L-M) view.

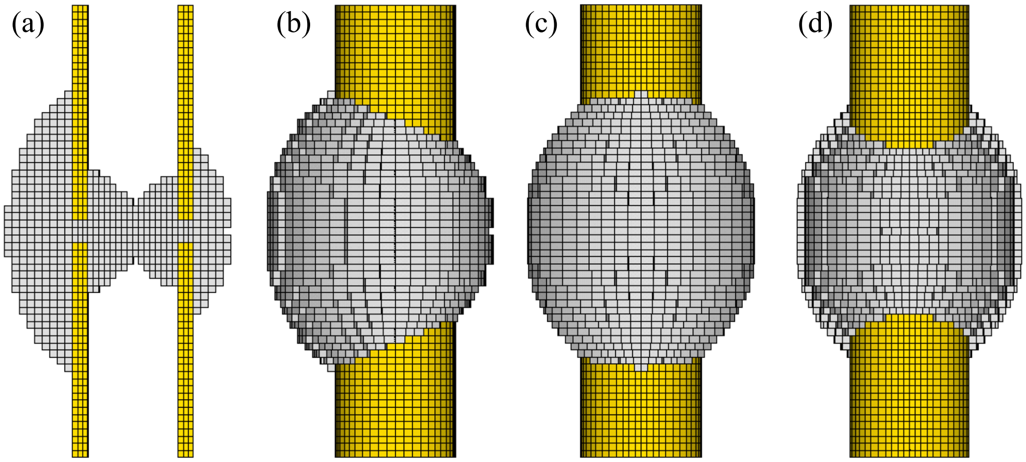

Figure D.8. Numerical approximation of final callus shape under unilateral fixation – Plate-bone distance:30mm (a) longitudinal section, (b) anteroposterior (A-P) view, (c) mediolateral (M-L) view, and (d) lateromedial (L-M) view.

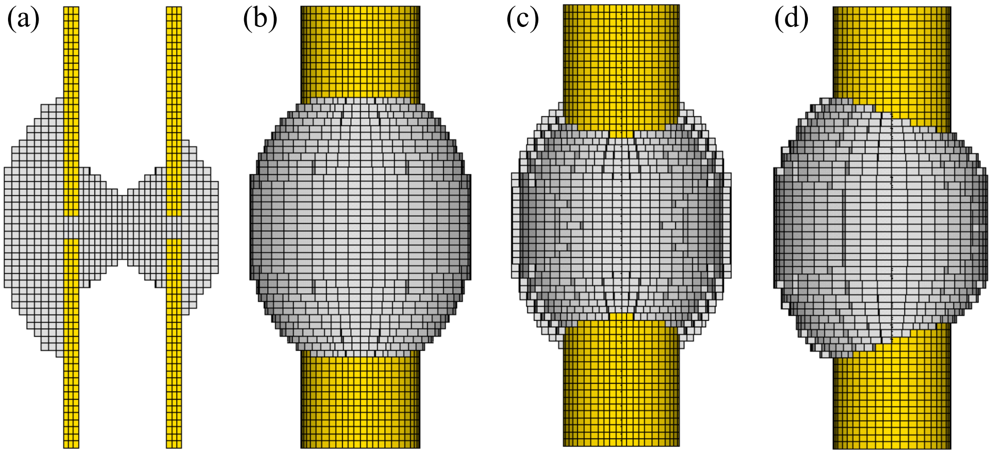

Figure D.9. Numerical approximation of final callus shape under unilateral fixation – Plate-bone distance:40mm (a) longitudinal section, (b) anteroposterior (A-P) view, (c) mediolateral (M-L) view, and (d) lateromedial (L-M) view.

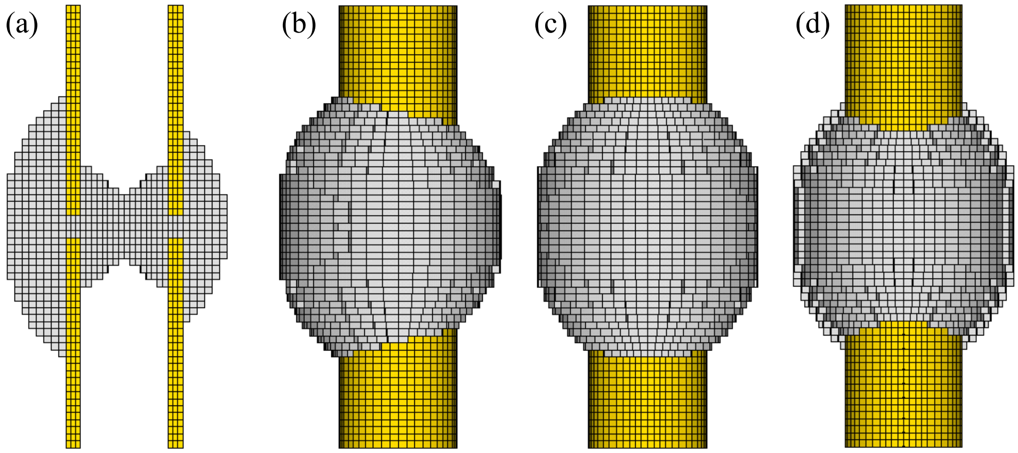

Figure D.10. Numerical approximation of final callus shape under unilateral fixation – Plate-bone distance:50mm (a) longitudinal section, (b) anteroposterior (A-P) view, (c) mediolateral (M-L) view, and (d) lateromedial (L-M) view.

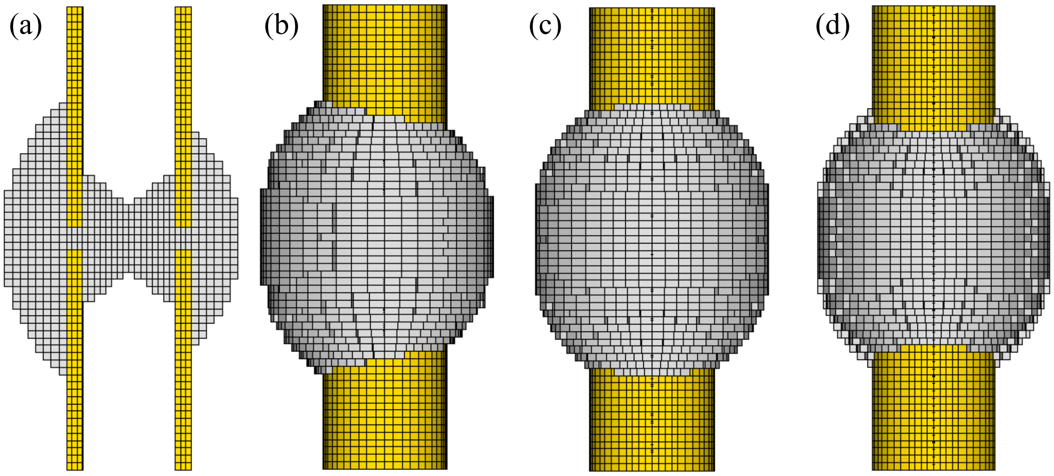

Figure D.11. Numerical approximation of final callus shape under unilateral fixation – Plate-bone distance:60mm (a) longitudinal section, (b) anteroposterior (A-P) view, (c) mediolateral (M-L) view, and (d) lateromedial (L-M) view.

Appendix E

Enhancement of radiographic imagery

Contents

E. 1 Case study 2 - Transversal fracture of the tibia with fragment misalignment

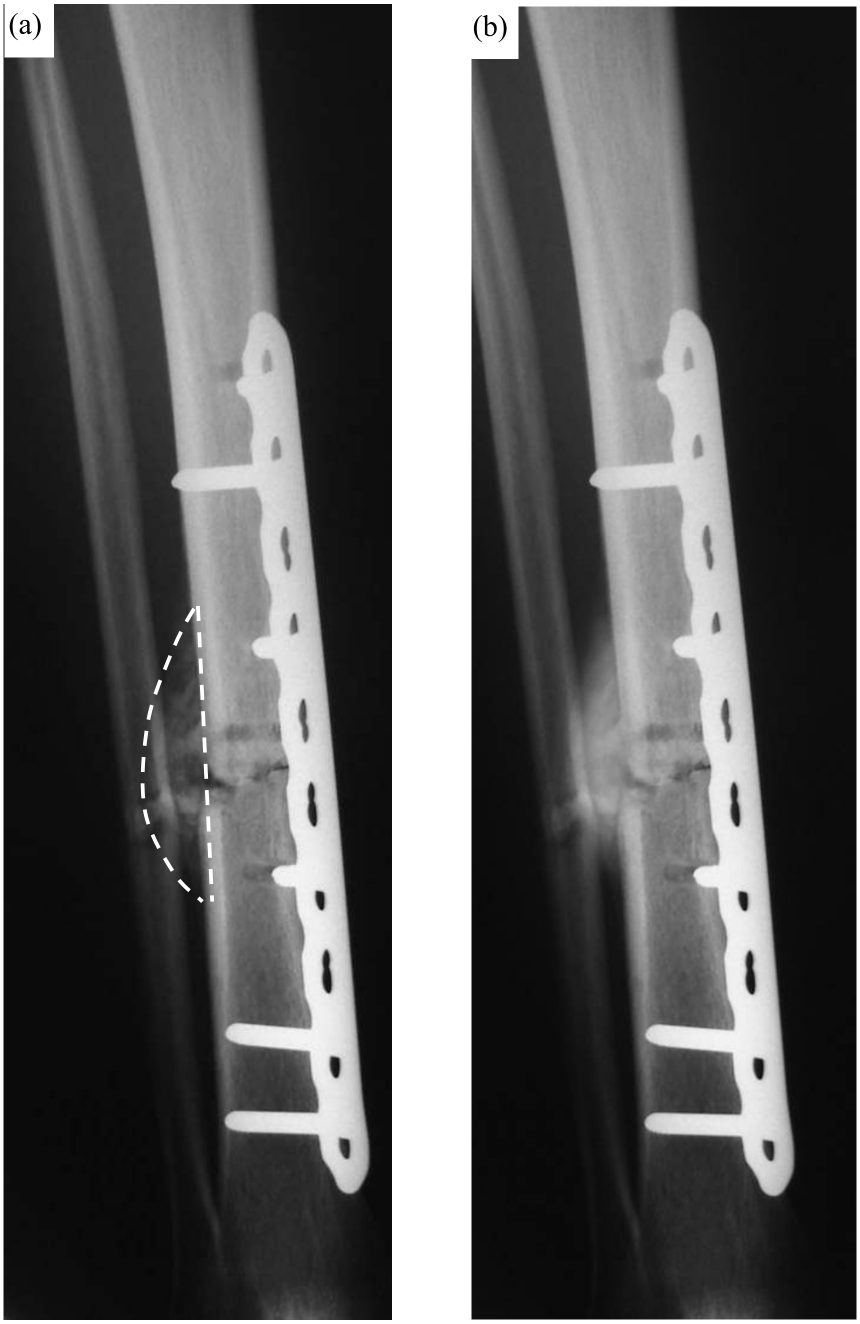

Figure E.1. (a) Anterio-posteriorl view of radiographic image of fracture tibia with callus formation 6 months postop (courtesy of Dr Nassiri and Mr David Cogley). Dashed line represents the callus, seen as a faint shadow. (b) Enhanced image. Callus was enhanced by altering the contrast and brightness levels within the area of the dashed line.

E. 2 Case study 4 - Spiral fracture of the femur

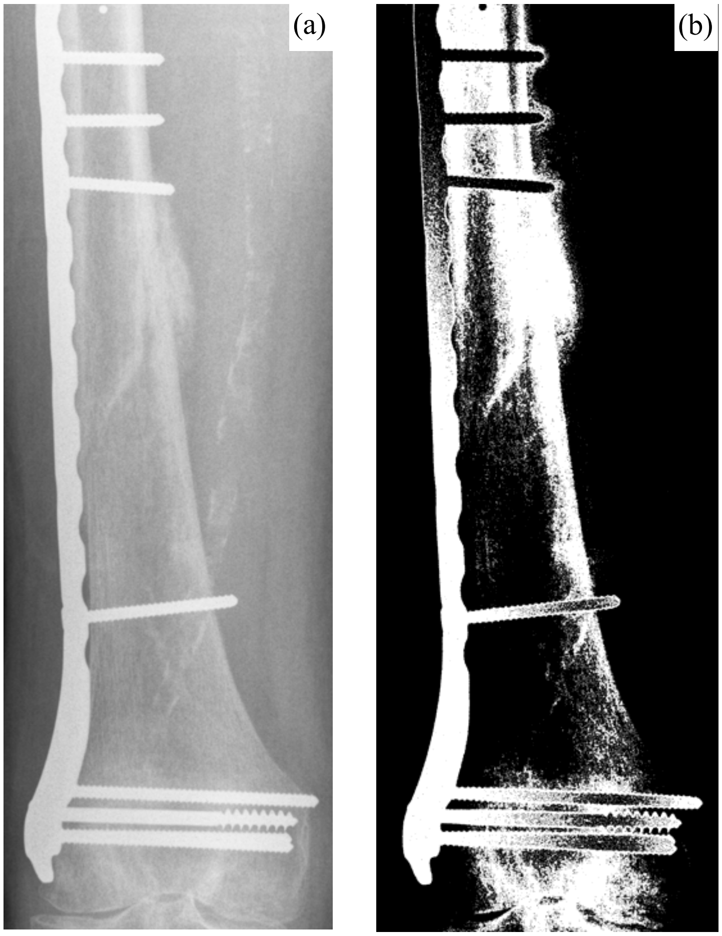

Figure E.2. (a) Anterio-posterior view of radiographic image of femur spiral fracture fixated with locking plate fixation, where callus formation is visible 2 months postop (courtesy of Dr. Nassiri). (b) Enhanced image of x-ray using thresholding methods to increase the contrast.

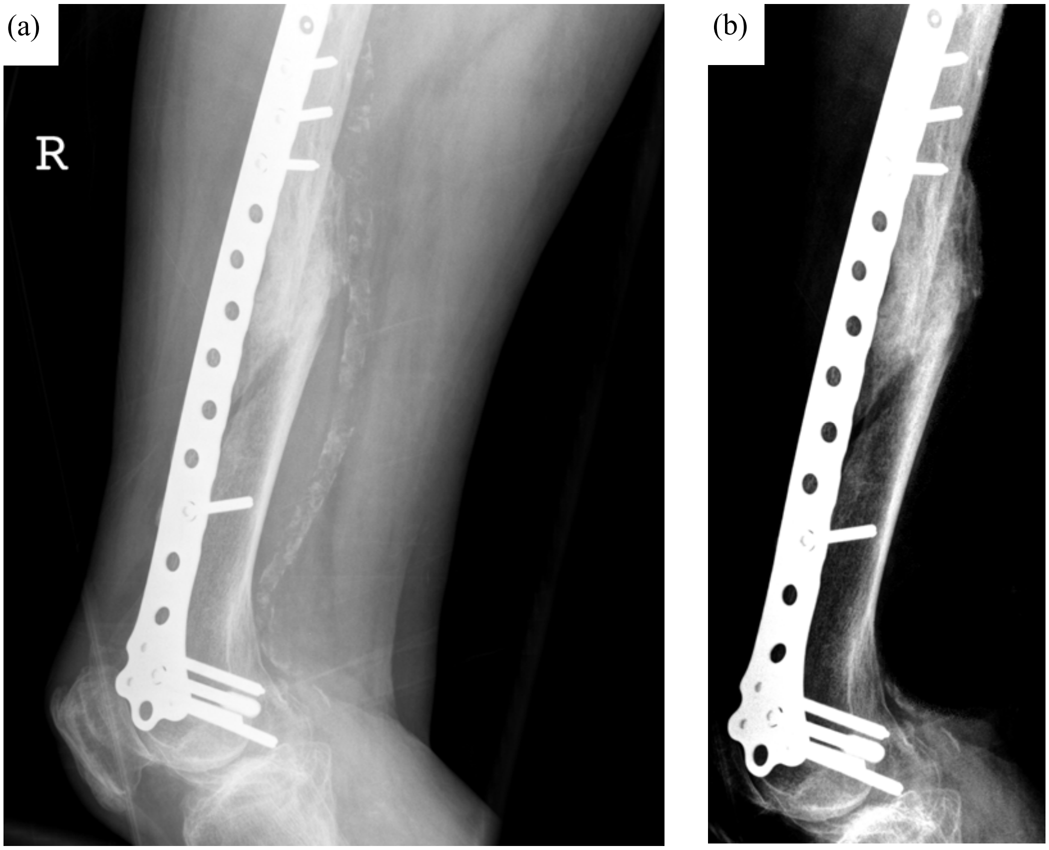

Figure E.3. (a) Latereo-medial view of radiographic image of femur spiral fracture fixated with locking plate fixation, where callus formation is visible 2 months postop (courtesy of Dr. Nassiri). Enhanced image of x-ray using thresholding methods to demarcate the callus tissues from the surrounding tissues, then surrounding tissues were removed from the image.

Appendix F

Combining modelling strategies

Contents

F.1 Introduction

It was proposed that the combination of the phenomenological model of healing rate and callus formation through mechano-regulation could be combined into a useful method of modelling healing in patient specific scenarios. In this study it is assumed that the callus is numerically modelled as an elastic homogenous isotropic solid model.

It is proposed in the present study that the initial interfragmentary strains at week one are responsible for the future progress of healing according to the mathematical model. If the loading applied to these initial tissues produce the appropriate tissue distribution using the mechano-regulated algorithm, then the callus structure and material properties should be able to calculate the IFS response. Following from this, by using the mathematical model, one could determine the future rate of healing.

F.2 A solid elastic homogeneous isotropic approach

It was assumed that the initial granulation tissues found at week one of healing behave as a homogenous, isotropic, solid pseudoelastic material for FE modelling purposes. To determine whether these modelling assumptions will provide the initial basis for reliable prediction of the future rate of bone healing, a comparison of the proposed computational and mathematical modelling methods with a previously generated inhomogeneous callus model (Claes and Heigele, 1999) is conducted.

The inhomogeneous model proposed by Claes and Heigele (1999) assumed that the granulation tissue found at week one of healing behaved as a Moony-Rivlin hyperelastic material. In the present study, a finite strain model, which allows large elastic deformations, was assumed. It should be noted that Claes manually built the callus model and the various tissues that become present during healing (Figs. F.1b-d). In the present study, however, it is conjectured that the combination of the computational and mathematical modelling will automatically produce the callus formation and then determine mathematically the rate of healing without the need to model the various tissues. Hence, the inhomogeneous manually constructed callus FE model by Claes and Heigele (1999) was compared with the simulated output of the modelling methods proposed in the present study.

For the sake of comparison, the same fracture geometry, and the same material properties were applied to the finite element model but without the hyperelastic component. Instead, finite strain or large deformations was assumed. Also, the model was loaded and constrained in the same manner as outlined by Claes and Heigele (1999). Firstly, the *in silico* callus was formed using the proposed mechano-regulated method (Fig. F.1a). Next, the *in silico* callus was re-loaded and the initial IFM, and subsequently IFS (34.6%), was recorded and the approximated rate of healing was calculated using the proposed mathematical model.

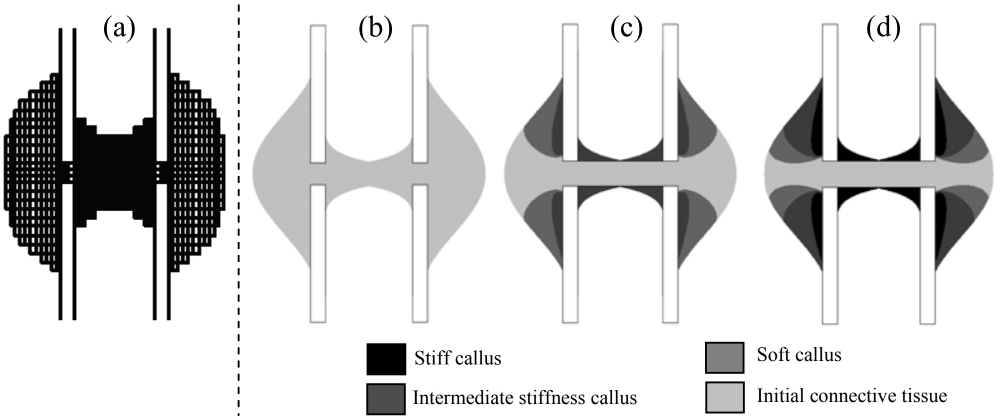

Figure F.1. (a) Predicted callus formation using proposed algorithm. Iidealized callus geometry and tissue locations based on histological examination used to develop FE models of calls formation and development at (b) week one, (c) week four and (d) week eight (adapted from Claes and Heigele, 1999).

F.3 Verification of homogeneous callus assumption

The relative increases in stiffness for the 34.6% initial IFS case was inputted in the proposed mathematical model. The simulated rate of healing was found to produce a good comparison with the *in vivo* increase in structural stiffness, but more importantly, the mathematically simulated rate of healing was more accurate than the inhomogeneous model (Fig. F.2). The hyper-elastic model by Claes and Heigele (1999) relied on intramembranous (connective tissue - bone) ossification and endochondral (cartilage - bone) ossification to model the increase in callus stiffness. That model however did not include the conversion of connective tissue to cartilage (chondrogenesis) within the central callus itself. This may have been the cause for the reduction in stiffness at week 8 in comparison to the *in vivo* results.

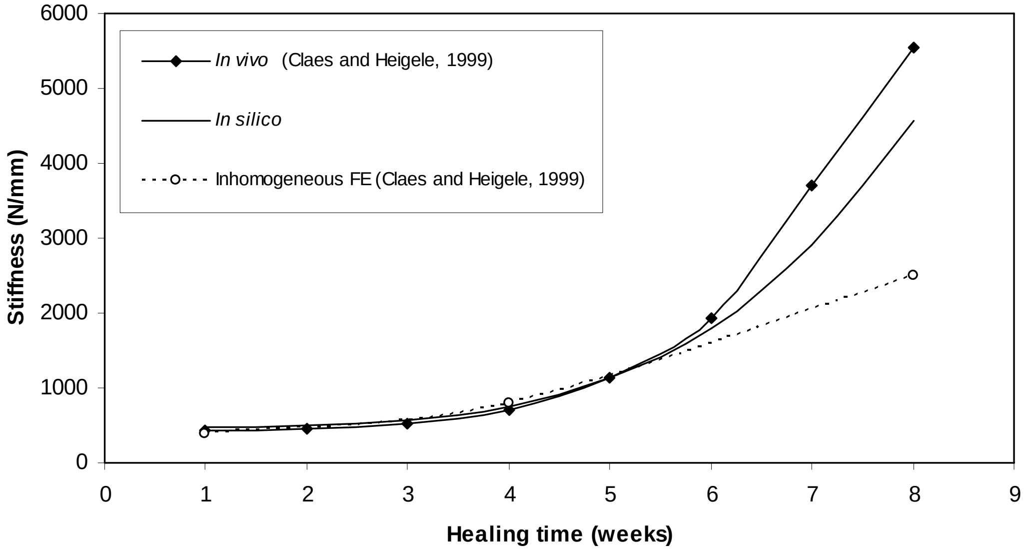

Figure F.2. Increase in stiffness for a 3mm gap with an initial IFS of 34.6%. The homogeneous, inhomogeneous and in-vivo results are compared.

Appendix references

Ahmad, M., Nanda, R., Bajwa, A.S., Candal-Couto, J., Green, S., Hui., A.C., 2007. Biomechanical testing of the locking compression plate: When does the distance between bone and implant significantly reduce construct stability? Injury 38, 358-364.

Mac Donald, B.J., Practical stress analysis with finite elements. Glasnevin Publishing, Dublin, 2007.

McCartney, W., Mac Donald, B.J., Hashmi, M.S.J., 2005. Comparative performance of a flexible fixation implant to a rigid implant in static and repetitive incremental loading. Journal of materials processing technology 169, 476-484.

Perren, S.M., 1999. Editorial: Trends in internal fixation - Potential, limits and requirements. Injury 30, 2-4.

Sommer, C., 2006. Biomechanics and clinical applications of locking plates. Suomen orthopedia ja traumatologia 29, 20-24.

Shütz, M., Südkamp, N.P., 2003. Revolution in plate osteosynthesis: new internal fixator systems. Journal of orthopaedic science 8, 252-258.

Stoffel, K., Dieter, U., Stachowiak, G., Gächter, A., Kuster, M.S., 2003. Biomechanical testing of the LCP – how can stability in locked internal fixators be controlled? Injury 34, 11-19.

Young, W.C., Roark's formulas for stress and strain (6th Ed.). McGraw-Hill, New York, 1989.

Website 1
http://www.rcsed.ac.uk/fellows/lvanrensburg/classification/surgtech/manuals/small%20fragment%20LCP.pdf (last accessed 25th of February 2005).